# Numerical Studies of Residual Stress in Cold Formed Steel Sigma Sections

by

**FEILIANG WANG**

A thesis submitted to the
University of Birmingham
for the degree of
**DOCTOR OF PHILOSOPHY**

# UNIVERSITYOF BIRMINGHAM

## University of Birmingham Research Archive

### e-theses repository

# Abstract

Cold-formed steel (CFS) sections are widely used for light-gauge structural beams and roof purlins due to their high strength-to-weight ratio and ease of installation on site. The commonly used profiles have a wide variety of cross-sectional shapes, e.g. C, Z, 'top hat' and sigma sections. Amongst these popular sections, the sigma section possesses several structural advantages, such as high cross-sectional resistance and large torsional rigidity compared with standard Z or C sections.

Residual stress is a self-balanced internal stress generated in the metal component when it is loaded beyond the elastic plateau and then unloaded. The existence of residual stress will be superimposed onto the external loadings to affect the stiffness and load resistance capacity of the structures. The most common sources of residual stress in CFS sections are cold working process and heat-treating operation. The cold working process can be divided into three primary categories: coiling-uncoiling, press braking and roll forming; and the residual stress induced by cold working mainly results from plastic deformation. Meanwhile, the welding process is the most prevalent heat-treating manufacturing procedure, and the residual stress will be introduced in the welding process due to uneven cooling.

Most of the conventional studies in residual stress were based on analytical solutions. Generally, analytical approaches are helpful for the simplified mechanical model, e.g. one-step pure bending model, but could rather complex and ineffective when comes to multi-steps analysis with nonlinear material properties like roll forming process. Hence, experimental methods were proposed as a supplement to theoretical analysis. Three primary approaches are commonly applied for measuring the residual stress in the laboratory: destructive method, semi-destructive method and non-destructive method. But the application of experimental methods also has limitations, for instance, sectioning and hole-drilling method ignore the effect of saw cutting vibration and X-ray diffraction method difficulty in detecting stress along the thickness of thin-walled sections. Finite element method (FEM) was thus proposed as a powerful tool for investigating residual stress. The computer-aided approach offers a possibility with lower cost and higher time efficient for predicting the cold forming residual stress and has a visualized interface that can better control the tolerances and defects during the production process.

The primary motivation of this thesis is to provide a numerical solution for exploring the distribution and effect of cold working and welding residual stress on CFS sigma sections. Initially, the magnitude and distribution of coiling-uncoiling, press braking, roll forming and welding residual stress in sigma sections are presented, and the

modelling details are discussed. Parametrical studies are conducted to investigate the influences of input parameters such as geometric dimensions and material properties on the numerical model. Numerical prediction validity is evaluated with analytical solutions and measured result from the X-ray diffraction measurement. Moreover, for investigating the influence of residual stress on structural beam in sigma sections, comparisons are performed based on the finite element (FE) analysis between the virgin model without cold work effects and modified model incorporated the effect of residual stress and strain hardening. The results obtained from the numerical simulation are again verified by the experimental and analytical data. Finally, some conclusions are proposed, and the recommendations for future works are presented.

# Acknowledgements

First and foremost, I would like to express my deepest gratitude to my supervisor, Dr Jian Yang for his persistent guidance, supports and encouragements throughout the whole period of my PhD study, without him this thesis would never been completed.

My appreciation to the Civil Engineering department of the University of Birmingham and Albion Ltd, for providing necessary assistance, facilities and supports throughout the research. My thanks also go to the EPRSC for providing the scholarship.

I am also grateful to my friends and colleagues in the School of Civil Engineering: Qiang Liu, Congxiao Zhao, Minxin Bao, Chong Ren, Haolin Su, Shunde Qin, Yu Hu, Wenxin Zuo, Hanwen Zhang, and Zijun Li, for providing helps to my living in the university and suggestions to the writing of this thesis.

My sincere thanks go to my parents, Ling Hu and Qungao Wang, there are no words can describe their love and encouragement to me, and I wish to dedicate this thesis to them.

# Table of Contents

# List of Figures

# List of Tables

# List of Definitions

| | |
|---|---|
| *AISC* | American Institute of Steel Construction |
| *AISI* | American Iron and Steel Institute |
| *AS* | Australia Standard |
| $A_g$ | Gross cross-sectional area |
| *BSI* | British Standards Institution |
| *CFS* | Cold-formed steel |
| *C* | The specific heat capacity |
| *DB* | Distortional buckling |
| *DSM* | Direct strength method |
| *E* | Young's modulus |
| *EWM* | Effective width method |
| *FE* | Finite element |
| *FEM* | Finite element method |
| $f_f, f_r$ | The fractions of the heat deposited in front and the rear parts |
| $F_y$ | Yield strength |
| $F_u$ | Ultimate strength |
| $h_c, h_r$ | The convection and radiation heat transfer coefficients |
| *I* | Current of arc welding |

| $k_x$, $k_y$ and $k_z$ | Thermal conductivities in the x, y and z directions |
| --- | --- |
| $LB$ | Local buckling |
| $LTB$ | Lateral torsional buckling |
| $LVDT$ | Linear variable displacement transducer |
| $M_E$ | Ultimate bending moment resistance |
| $M_{c,Rd}$ | Design moment resistance of a cross section |
| $M_{cr}$ | Critical elastic buckling moment of a flexural member |
| $M_{crd}$ | Critical elastic distortional buckling moment |
| $M_{cre}$ | Critical elastic lateral-torsional buckling moment |
| $M_{crl}$ | Critical elastic local buckling moment |
| $M_n$ | Nominal moment of a flexural member |
| $M_{nd}$ | Design moment for distorsional buckling |
| $M_{ne}$ | Design moment for lateral-torsional buckling |
| $M_{nl}$ | Design moment for local buckling |
| $M_{pp}$ | Pseudo-plastic bending moment |
| $My$ | First yield moment of a cross section |
| $N_x$, $N_y$ and $N_z$ | The direction cosine of the normal to the boundary |
| $PPDM$ | Pseudo-plastic design method |
| $P_e$ | The laser power |
| $Q$ | The magnitude of the heat input |

| | |
|---|---|
| $Q_{loss}$ | The heat flux loss |
| $q_1$, $q_2$ | The first yield load and excess load |
| $q_p$ | Ultimate load resistance |
| $q_s$ | The boundary heat flux |
| $r$ | The radial position |
| $r_e$ | The half width of welding line at the top surface |
| $r_i$ | The half width of the welding line on the bottom surface |
| S.D. | The standard deviation |
| $\Delta T$ | The difference between surface ( $T_s$ ) and ambient ( $T_0$ ) temperature |
| $T_r$ | The temperature of radiation |
| $T_\infty$ | The surrounding temperature |
| $t$ | The welding time |
| UDL | Uniformly Distributed Load |
| $U$ | Voltage of arc welding |
| $V$ | Travel speed of arc welding |
| $W_f$ | Gross section modulus |
| $x_0$ | The position of the heat source in the x-direction when t is zero |
| $\lambda$ | Non-dimensional slenderness |
| $\sigma_{yc}$ | Corner yield strength |
| $\sigma_{yf}$ | Flat yield strength |

| | |
|---|---|
| $\sigma_{0.2,c}, \sigma_{0.2,v}$ | Yield strength of the cold-formed and virgin steel |
| $\sigma'_{0.2,pb,c}$ | Predicted 0.2% proof stress of the corners of press-braked section |
| $\sigma'_{0.2,cr,c}$ | Predicted 0.2% proof stress of the corners of cold rolled box section |
| $\sigma_{x,c}, \sigma_{z,c}$ | The transverse and longitudinal stress after coiling |
| $\omega_c$ | Stress ratio for coiling process |
| $\omega_u$ | Stress ratio for uncoiling process |
| $y_{cy}$ | Distance when yielding occurs during coiling |
| $\sigma_{x,r}, \sigma_{z,r}$ | The final stress in the transverse and longitudinal direction |
| $\sigma_{x,u}, \sigma_{z,u}$ | The transverse and longitudinal stress after uncoiling |
| $k_{uy}$ | Coiling curvature when yielding occurs |
| $\eta$ | Efficiency of arc welding |

# 1. INTRODUCTION

## 1.1 Introduction of cold forming process

As an alloy of iron, carbon (less than 2%), manganese (less than 1%) and other elements, steel is by far the most important metal material in the world, with annual global production over 700 million tonnes. The high strength-to-price ratio of steel member makes it widely used in structural and mechanical applications. The manufacture of steel components includes seven steps: 1) iron ore preparation, 2) coke making, 3) iron making, 4) steel making, 5) casting, 6) rolling and 7) finishing. The $1^{st}$ to $4^{th}$ step is used to produce molten steel from raw materials such as iron ore, coke and limestone. During those steps, coke is used as a fuel and also a medium to reduce the oxide in the iron, and the limestone can react with other impurities like phosphorus and sulphur. In the $5^{th}$ step, molten steel will be cast into ingots or other special shapes by casting mould as the prototype preparing for direct use. The rolling process (the $6^{th}$ step) is the operation to reduce the thickness of cast product, which can be categorized into hot-rolling and cold-rolling. The former is used to produce hot rolled flat sheet, plate and structural profiles, etc., and the latter is the secondary operation to further reduces the thickness of hot-rolled products by annealing or acid washing process. The most common products from cold rolling are continuous metal sheets. Then, the rolled products will experience a variety of finishing processes such as painting, galvanising, tinning and plastic coating, to meet the market demands. The finished flat sheets will be initially coiled into a roll for storage and transportation

purpose and then uncoiled for further usage. This process is known as the coiling-uncoiling process. For manufacturing the components in cold-formed sections, the flat sheet from the coiling-uncoiling process will feed as the raw material to the subsequently cold forming operations.

Cold forming is a manufacturing process that can form the flat metal sheet to various structural profiles permanently without heating. The process involves two principal ways: press braking and roll forming. Press braking is the operation to fold the angle along the flat sheet between the top punch and bottom die. As a manually manufacturing process, press braking is suitable for forming simple configurations such as angle and channel sections. The deformation of the sheet in this method is accomplished simultaneously in one step. A typical press brake setup is shown in Fig. 1-1 (Yu 2000). The punch and die set in press braking process could with only a notch or with a complex V-shaped, U-shaped or channel-shaped profile.
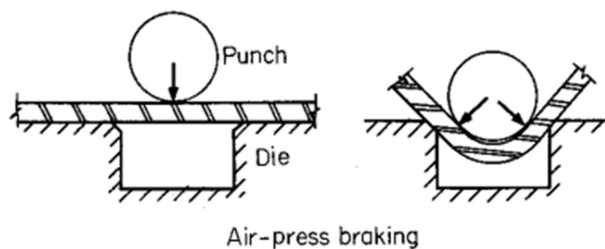


**Figure 1-1: Typical press brake setup (Yu 2000)**

Roll forming is an automatic process by using successive roll sets to form the flat sheet into desired profiles. The roll forming rolls, for the most part, can be re-arrangement for producing diverse required cross-section profiles. Each set of roll

brings the section progressively closer to its final shape, as showed in Fig. 1-2 (Yu 2000). The number of rolls depends on the material properties, shell thickness and the complexity of the target section.
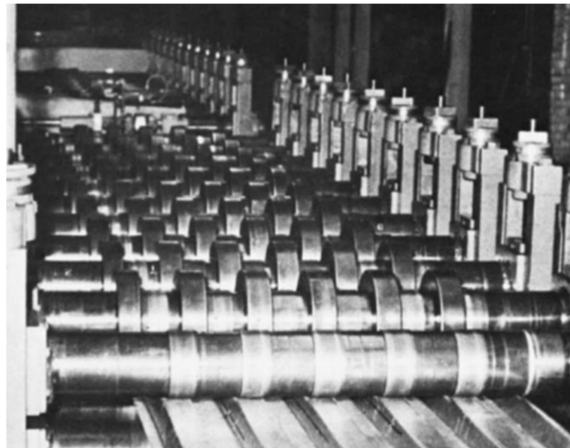


**Figure 1-2: Roll forming picture (Yu 2000)**

Roll forming process has a larger production capacity when compares to press braking process, which makes it an excellent choice for manufacturing large quantities of metal sheets or very long pieces. Furthermore, as the deformation behaviour of various parts of sheet at different positions in the transverse direction during the roll forming process is generally different, this process is thus competent for manufacturing complex sections and offers the user an adjustable approach to produce sections in accuracy and uniformly.

## 1.2 Background of welding process

As a widely used connection method, the research in welding was underdeveloped until the end of 19th century when a diversity of welding techniques emerged. The most prevalent welding methods are pressure welding and fusion welding. The

pressure welding approach, such as resistance welding, friction welding and ultrasonic welding, is a form of solid phase welding which utilize the pressure to create a tight connection between the parent metals at ambient or elevated temperature. Fusion welding, such as arc welding and laser welding can merge the weldment by moving a molten pool along the weld bead. The difference between arc welding and laser welding is the way to produce the molten pool. For instance, arc welding uses an electric arc between an electrode and the base material to melt the electrode at the joint while laser welding uses an intensive laser as heat sources to melt the filler in high-speed. More recently, the increasing interest in the industry is transferred to hybrid laser and arc welding method. The technique has shown high cost-effective when compared to separate arc welding or laser welding technique, and found can be applied for welding thick steel plates and difficult-to-weld materials like aluminium and magnesium (Kong et al. 2011).

During the welding process, a dynamic temperature cycle is introduced to produce a non-uniform heat distribution on the weldment. The residual stress is thus induced as a result of uneven cooling along welding bead and heat affected zone (HAZ).

**1.3 Residual stress and strain hardening**

Residual stress is generated in the metal component when it is loaded beyond the elastic plateau and then unloaded. If a steel member experiences a deformation beyond the elastic stage, the fibres that suffered a permanent set prevent the elastically stressed fibres from recovering their initial length after unloading, and in this way

4

some residual stresses are produced (Timoshenko 1956). Residual stress is commonly introduced during manufacturing processes involving cold working and heat treatment, the distribution of residual stress in the section greatly relies on the material properties and the production sequence. In the cold working process, residual stress is induced principally by plastic deformation and the distribution through the section is generally of the bending type. In the welding process, residual stress is induced by heating and subsequent rapid cooling process, and the distribution is distributed in localized. As a self-balanced internal force, residual stress has limited effect on the material strength but will lead to a modification of the stiffness of the steel component, because the superimpose of external loadings on residual stress can accelerate or decelerate the yielding of specific portions of the section. The occurrence of the residual stress is usually accompanied by strain hardening during roll forming and press braking process. Strain hardening, or know as work hardening, is induced when a steel structure is reloaded after loaded beyond the yield plateau and unloaded. The existence of strain hardening is considered can increase the yield and ultimate strength of the material.

The existence of residual stress will affect the service performance and fatigue life of the structural components. Those effects are of a complex nature and not yet well understood. Therefore, it is necessary to conduct a fundamental examination of the distribution and effects of residual stress on CFS members. In this thesis, the numerical solution is presented for predicting the cold working and welding residual stress on sigma sections. A series of theoretical studies and laboratory measurements

have been carried out to verify the FEM obtained. The effect of residual stress and strain hardening on steel beam in sigma sections is also discussed.

**1.4 Aims and objectives**

The primary aim of the thesis is to investigate the distribution and influence of residual stress on CFS sigma sections. The objectives of the thesis are:

1. To develop a numerical approach for predicting residual stress in coiling-uncoiling, press braking and roll forming process, and to find out the magnitude and distribution of residual stresses in sigma sections.

2. To measure the residual stress in roll formed sigma beam via laboratory approaches and compare the results from experimental obtained and numerical achieved for validation purpose.

3. To propose a FE approach for simulating the arc welding process in butt-welded sigma section. To achieve the heat induced residual stress by considering the thermal-mechanical coupled analysis.

4. Based on the obtained residual stress distributions, to investigate the effect of residual stress and strain hardening on the load resistance performance of sigma beams by carrying out extensive numerical and experimental studies.

**1.5 Methodology and the layout of the thesis**

In order to achieve the above aim and objectives, an extensive literature reviews are carried out to discuss the state of the art relevant to the research field. Knowledge gaps are identified and will be addressed in the following chapter. Numerical analysis using FEM is conducted for investigating the distribution of residual stresses. A series of analytical and experimental analyses are conducted to validate the numerical achieved results. For investigating the influences of residual stress and strain hardening, FE models are also proposed to reproduce the test results. Based on the comparison between the experimental and numerical results, the appropriate conclusions are thus summarized.

The thesis comprises a total of seven chapters, and the layout of the thesis is as follows:

Chapter 1 provides a brief introduction to the background knowledge of the cold forming process, welding process, residual stress, and strain hardening. It sets out the research scope, defines the aim and objectives, describes the research methodology and outlines the structure of the thesis.

Following the introductory chapter, Chapter 2 presents a literature review to document the existing approaches in the study of cold-formed sections, cold working and welding residual stress and the effect of initial imperfections. It includes the main

findings from existing published research and identifies knowledge gaps that lead to the subject of the thesis.

In Chapter 3, FEM investigations of the coiling-uncoiling and press braking residual stresses are presented. Parametric studies are carried out to investigate the impact of geometric variables and material properties on the model. The chapter also involves a comparison between numerical results and theoretical & experimental data for verifying the reliability of the FEM.

Chapter 4 presents the numerical and experimental investigations of residual stress distribution in roll formed sigma sections. Modelling details such as material properties, meshing schemes, interaction and boundary conditions are discussed. The laboratory test based on the X-ray diffraction method is introduced, and the measured residual stresses of sigma section are presented. Numerically achieved results are thus verified by using experimentally obtained data.

Chapter 5 presents the numerical approach for predicting the welding residual stress in sigma section. The study including two primary parts: the temperature field and thermally induced residual stress. Input parameters, such as the choice of element types, material properties, meshing sizes, loading and boundary conditions are introduced, and the magnitude and distribution of welding residual stress on the sections are depicted.

Chapter 6 concerns with the effect of cold work on the performance of sigma beam. The preceding achieved magnitude and distribution of cold working and welding residual stresses are imported into the FE model as initial stresses. The material properties are modified when considering the effect of strain hardening. The influences of residual stress and strain hardening on the load resistance of sigma beams are studied by comparing the virgin model that without cold work effects and the modified model that incorporated with the residual stress and strain hardening. The numerical method is also used for validation the analytical values obtained from the PPDM method.

Finally, in chapter 7, some conclusions are summarized, and recommendations for further works are critically discussed.

# 2. LITERATURE REVIEW

## 2.1 General

Before the maturity stage of the numerical techniques, most of the studies in residual stress were based on the analytical method and laboratory measurement. The research in this area has increased dramatically recently due to the growing applications of the computer-aided simulation approach. The occurrence of numerical technique presents a more efficient tool for predicting residual stress when compared with conventional analytical and laboratory approaches. This chapter introduces the literature reviews covering approaches and findings in the design of CFS sections and the investigation of distribution and influences of residual stress. The reviews are presented in several sections: the existing design and analysis approach for CFS sections are introduced in section 2.2; then, some important findings of cold working residual stress and welding induced residual stress are reviewed in section 2.3 and 2.4; section 2.5 concerns with the effects of initial imperfections, especially the cold work effect such as residual stress and strain hardening; finally, the knowledge gaps are presented in section 2.6.

## 2.2 Design of CFS sections

CFS sections offer a number of advantages over hot-rolled sections, with the principal appeal relating to their high strength to weight ratio and favourable versatility of the cross-sectional profiles, which will provide an economic and fast solution for design and construction. CFS sections are often used for single and multi-span beams in

roofing or cladding construction. For continuous beams, connections over the internal supports can be continuous (Liu et al. 2011a), lapped (Ho and Chung 2004) or sleeved (Yang and Liu 2012), each offering advantages on the structural and constructional performance, such as enhanced stiffness and ease of installation on site. Common shapes of CFS sections include C, Z, I and 'top hat'. More recently, sigma section, evolved from C-sections by adding two insets in the web as stiffeners, have been proposed. Sigma sections possess several advantages, such as high cross-sectional resistances, higher strength-to-weight ratio, and larger torsional rigidities, since the shear centre of a sigma section is closer to the centroid (Yu 2000). The manufacture of sigma sections could be press braking or roll forming, and the section can be found in a variety of latest applications as purlin and lattice beam.

Individual constituent elements of CFS members are usually slender, i.e., having a relatively small thickness-to-width ratio, and hence susceptible to buckling failure. Failure of CFS sections is normally associated with one or more of the following three buckling modes: local buckling (LB), distortional buckling (DB), lateral-torsional buckling (LTB). Moreover, the interaction between buckling modes frequently occurs (Rogers and Schuster 1997, Ye et al. 2002, Magnucki et al. 2010 and Cheng et al. 2013), which may further destabilize the system. The buckling of the constituent elements does not necessarily causes members to lose their full load bearing capacity immediately after their critical buckling loads are reached, instead the section may continue to carry increasing load in excess of the initial buckling load (Thomopoulos et al. 1995, Dubina and Ungureanu 2010, Zhang and Tong 2008). Thus, the utilization

of the post-buckling strength of cold-formed cross-sections can be one of the design considerations.

In order to take into account the effect of buckling on the cold-formed sections, two design methods: Effective Width Method (EWM) (BSI 2006) and Direct Strength Method (DSM) (AISI 2007) were presented. EWM was proposed by Karman (1932) to analyse the post-buckling and failure modes of steel plates. It was assumed that the total load is carried by a fictitious effective width, lead to a uniformly distributed stress, as showed in Fig. 2-1. The effective width is selected so that the area under the curve of the actual non-uniform stress distribution is equal to the sum of the two parts of the equivalent rectangular shaded area. Karman also suggested that when the elastic critical stress of the rectangular plate is equal to the yield strength of the material, then the failure of the plate occurs.
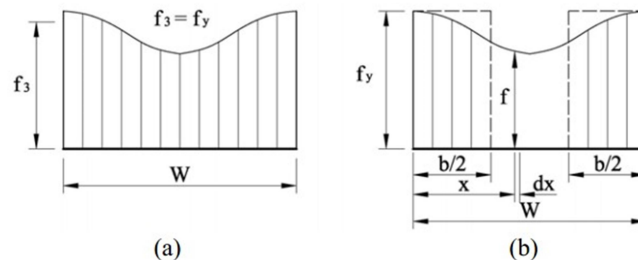


**Figure 2-1: Effective width of stiffened compression element (Karman 1932)**

DSM was developed by Schafer and Peköz (1998a), which can be used to achieve the post-buckling strengths for the entire cross section rather than an individual element. In this method, the initial buckling load and critical strength of the section can be evaluated by using following empirical formulas.

1) For lateral-torsional buckling:

For $M_{cre} \leq 0.56 M_y$               $M_{ne} = M_{cre}$                                                              (Eq. 2-1)

For $2.78 M_y > M_{cre} > 0.56 M_y$        $M_{ne} = \dfrac{10}{9}(1 - \dfrac{10 M_y}{36 M_{cre}}) M_y$                     (Eq. 2-2)

For $M_{cre} > 2.78 M_y$                  $M_{ne} = M_y$                                                                  (Eq. 2-3)

where

$M_{ne}$ is the design moment for lateral-torsional buckling;

$M_y$ is the yield moment, $M_y = W_f F_y$;

$W_f$ is the gross section modulus;

$F_y$ is the yield strength;

$M_{cre}$ is the critical elastic lateral-torsional buckling moment.

2) For local buckling:

For $\lambda_l \leq 0.776$                $M_{nl} = M_{ne}$                                                               (Eq. 2-4)

For $\lambda_l > 0.776$        $M_{nl} = \left[ 1 - 0.15(\dfrac{M_{crl}}{M_{ne}})^{0.4} \right] (\dfrac{M_{crl}}{M_{ne}})^{0.4} M_{ne}$        (Eq. 2-5)

where

$\lambda_l$ is the non-dimensional slenderness and $\lambda_l = \sqrt{M_{ne}/M_{crl}}$;

$M_{nl}$ is the design moment for local buckling;

$M_{crl}$ is the critical elastic local buckling moment.

3) For distortional buckling:

For $\lambda_d \leq 0.673$ $\qquad\qquad\qquad\qquad$ $M_{nd} = M_y$ $\qquad\qquad\qquad$ (Eq. 2-6)

For $\lambda_d > 0.673$ $\qquad$ $M_{nd} = \left[1\text{-}0.22(\frac{M_{crd}}{M_y})^{0.5}\right](\frac{M_{crd}}{M_y})^{0.5} M_y$ $\qquad$ (Eq. 2-7)

where

$\lambda_d$ is the non-dimensional slenderness and $\lambda_d = \sqrt{M_y / M_{crd}}$ ;

$M_{nd}$ is the design moment for distorsional buckling;

$M_{crd}$ is the critical elastic distortional buckling moment.

DSM was also validated and calibrated by Silvestre and Camotim (2006), Schafer (2008) and Pham and Hancock (2009), by comparing with EWM and laboratory test. Later on, an open source stability analysis program CUFSM was further developed by Schafer as an efficient supporting tool for the calculation of buckling load in DSM solutions (Schafer and Ádány 2006, Li and Schafer 2010).

More recently, the research by Liu et al. (2011) exhibited the local/distortional buckling failure governing sections (i.e. sigma section) which showed a reasonable level of ductility, and have a similar mechanism of the plastic hinge. In the case of multi-span beams system, failure of one section will not lead to an immediate collapse of the system. In fact, internal loads will be redistributed, and the system can continue to carry higher loads. Note that both EWM and DSM are based on elastic theory and ignore the effect of redistribution of moments on the failure loads. In order to improve the efficiency of design, the Pseudo-Plastic Design Method (PPDM) has been

proposed by Liu et al. for the design of indeterminate structures made by the cold-formed sections, i.e. sigma section.

As we know, the conventional plastic design method was normally applied for the hot-rolled steel sections, and can take advantage of rotation capacity of each plastic hinge in prior to the collapse of the structure (Davies and Brown 1996). PPDM method differentiates itself from the conventional plastic design method in that the moments at the plastic hinges are the reduced value of the elastic cross-sectional capacity, which was referred as pseudo-plastic moment (Liu et al. 2011). The PPDM method allows for the moment redistribution in the system, by considering the effect of a pseudo-plastic hinge at the internal supports and its resulting effect on the in-span bending moment. The design by employing this method will lead to a higher loading capacity for such systems, and will render a more economical design compared to elastic design methods.

## 2.3 Residual stress from cold working process

There was extensive literature in the study of cold working residual stress. Research methods were from theoretical methods to experimental and numerical methods. The applied measurement approaches were from hole-drilling to hybrid X-ray diffraction and sectioning method. Established numerical models were from simplified 2D pure bending model to complex 3D forming model. The materials considered in the model were from carbon steel to high strength alloy steel and stainless steel; material properties were from isotropic to anisotropic.

The analytical study of cold working residual stress was initially based on the cold bending process. In 1975, Ingvarsson presented an analytical solution for residual stresses in the cold bending process based on the bending theory proposed by Hill (1950). He discovered that the residual stresses caused by cold forming were not only in the circumferential direction but also in the length direction of channel members and the amount of the residual stress depended on the external circumstances during the cold-forming. Later on, Rondal (1987) suggested a similar theoretical method for predicting residual stresses due to cold rolling process, but his study was based on the assumptions that strain-stress relationship was represented by a tri-linear curve with an isotropic strain hardening in the corner. He noticed that an elastic springback phenomenon occurs subsequent to the unloading process led to a redistribution of residual stress in the cross section. The study also indicated that residual stress in the corner portion increased when the width-to-thickness ratio grew up and when the radius decreased, and the reverse conclusion was observed for the residual stresses in the flat portion. Tan et al. (1994) also formulated the distribution of residual stresses in bent sheets with considering the effect of springback, but incorporated with the bending curvature, thickness and material properties of sheet metals in the constitutive equations. Zhang and Hu (2008) extended Tan's et al. study to repeat bending, unbending and reverse bending cases. They developed a new analytical method for calculating the residual stress with springback effect and found cyclic material models had a considerable impact on the residual stress distribution in bending.

The above investigations were all concentrated on the analytical studies in cold bending operation. The theoretical solution was then introduced to the coiling-uncoiling process by Quach et al. (2004). They proposed a closed-form analytical solution for predicting the residual stresses in the coiling-uncoiling and flattening process. The study was based on the elastic-plastic plane strain pure bending assumption, and the results confirmed the through-thickness variations of residual stresses were non-linear. Moen et al. (2008) also presented the magnitude of residual stresses and effective plastic strains during coiling-uncoiling, flattening and cold forming process, and further derived an algebraic equation to predict the transverse and longitudinal residual stresses in roll formed sections. Their method was based on the elastic-perfectly plastic material, and the findings indicated that the stress and strain magnitudes increased with the decrease of yield stress and the increase of sheet thickness.

The distribution of cold forming residual stress not only depends on the procedure arrangement but also the material properties and cross-sectional geometric dimensions. However, conventional theoretical approaches of cold forming residual stress were mainly based on the simplified bending model and ignored the material nonlinearity and complex cross-sections. Hence, more investigations based on laboratory measurements were introduced into the subject.

Residual stress measurement methods can be divided into three categories: destructive, semi-destructive and non-destructive method. Destructive and semi-destructive

techniques, which are also known as the mechanical method, rely on the measurement of the resulting strains from the displacement incurred by completely or partially removed material. The typical destructive method is sectioning method while the commonly used semi-destructive method is hole drilling technique. Sectioning method has been extensively used for measuring residual stresses in structural carbon steel, aluminium and stainless steel sections. The method involves cutting the instrumented plate in strips to release the residual stress that is presented on the cutting line. The principle of the hole-drilling method is to measure the strain by relieving the locally residual stresses by drilling a hole on the material surface; and the approach can be applied to find the distribution of residual stress along the thickness. It is described as "semi-destructive" because the hole may not impair the structural integrity as both diameter and depth are quite limited. The sectioning method was adopted for measuring residual stress in hot-rolled sections by Huber and Beedle (1954), Lee and Ketter (1958), Beedle and Tall (1960), and Tebedge et al. (1973). An electrical discharge machining (EDM) technique, which evolved from conventional saw-cutting sectioning method, was presented by Weng and Peköz (1990) to measure residual stress in cold-formed sections. This technique can remove material by a series of discrete electrical discharge and will significantly reduce the external disturbance during the machining caused by heating, clamping and vibration. From the EDM test that the compression residual stresses on the inside surface and tension on the outside surface for both roll formed and press-braked sections were found. The magnitudes of residual stresses were found to be approximate between 25 to 70% of the yield strength of the material and the magnitudes of the residual stresses

on the corner regions were found to be higher than those on the flat portions. Almost in the same time, Weng and White (1990) used both sectioning and hole-drilling method for exploring the residual stresses in high-strength cold bending thick steel plates. They discovered that the tension residual stresses on the inside surface of the bending range was from 46% to 92% of the yield stress of the material, and the distribution of residual stress along the thickness showed a zigzag-type pattern. Cruise and Gardner (2008a) applied sectioning method in measuring the through thickness and cross-sectional residual stress on cold-rolled stainless steel hollow sections. They found that the membrane and bending residual stresses were below 10% and 20% of the material 0.2% proof stress, respectively, for the hot rolled sections; but for the press-braked sections, bending residual stresses in the corner were observed reached about 30% of 0.2% proof strength.

As the conventional destructive or semi-destructive methods will cause wastage of specimens and meanwhile will introduce vibration and heating during the measurement. In order to improve the accuracy and diminish the material wastage during the test, non-destructive measurement methods were thus proposed. Non-destructive techniques, including ultrasonic, X-ray diffraction and magnetic methods, etc., do not require the damage of specimens as it is based on the relationship between physical and crystallographic parameters and the stress. Li et al. (2009) also used the X-ray diffraction technique to require the residual stresses distribution along the thickness and inside surface of roll formed square hollow section. They found the maximum residual stress was occurred on the welding line and through thickness

variations of residual stresses came out typically as bi-linear, and the forming process had a significant effect on the distribution of longitudinal residual stresses on the outside surface of square hollow sections. Tong et al. (2012) conducted both hole-drilling and the X-ray diffraction test in measuring the magnitude and distribution of longitudinal residual stress on the cold-formed thick-walled square hollow sections. Based on the measured stress results, they also presented a series of predictive formulas to describe the distribution pattern of residual stress.

So far, the analytical solutions were proved efficiently and accurate for predicting coiling-uncoiling and press braking residual stress based on the pure bending model. However, the analysis would be quite complicated when it comes to multi-step roll forming of complex sections. The laboratory measurement methods are powerful for predicting the distribution of residual stress, but still with limitations, e.g. sectioning and hole-drilling method ignores the effects of vibration and heating, X-ray diffraction method is incapable in detecting residual stress along thickness of thin-walled components. Therefore, in order to overcome the limitations of theoretical and experimental methods, more and more studies were turned to use numerical approaches for investigating the residual stress. The application of computer-aided approach can not only offer a high-efficiency solution for predicting residual stress with visualized interface but also will dramatically reduce the number of prototypes and associated costs.

Recently, there were a number of applications of numerical approaches in the investigation of residual stress. Senanayake et al. (1994) adopted the computational simulation techniques for predicting the distribution of roll forming longitudinal plastic strain in the trapezoidal section. Heislitz et al. (1996) adopted a FE analysis in the study of deformed geometry and strain distributions in a three steps forming process. The study has shown that the explicit dynamic analysis in FEM can be used to simulate the roll forming process under certain approximations. Quach et al. presented a numerical model for simulating the press braking process in 2006, and further proposed an analytical method in 2009 for predicting residual stresses and co-existent equivalent plastic strains in stainless steel sections formed by the press-braking method. Lindgren (2007) established a numerical model to simulate the roll forming process of channel section, but his research was found the effect of deformation length on the peak longitudinal strain. Chinnaraj et al. (2014) conducted a numerical study on coiling-uncoiling residual stress and observed that the coiling-uncoiling residual stresses in longitudinal directions were predominantly in frame web and flange sections and it increases with a decrease in coil diameter.

According to the previous numerical studies, it can be concluded that the FEM is a valid and efficient solution for predicting residual stresses in roll forming sections, and the explicit dynamic analysis can be used for dealing with friction and contact problems in the roll forming simulation.

During the roll forming process, the levelled sheet will experience a highly complex behaviour such as longitudinal elongation and bending, transverse bending and shear. The quality of roll formed product can be influenced by varying factors such as the arrangement and sequence of roll sets, geometric dimensions, material properties and springback of the sheet during production. The defects generated during roll forming process including edge waving, twist, wrinkling, thinning, tearing, springback, etc. The tolerance control is thus a significant step in designing and optimising a roll system. The numerical method also stands as an ideal tool for conducting parametric studies during the forming process and finding the optimum forming configurations.

Zhu et al. (1996) investigated the effects of geometric variables in the roll forming process such as flange length, thickness, bend angle increment and roll diameter on the longitudinal strain of channel sections. According to their research, the peak longitudinal strain was found to increase with the increase in flange length and then drop when the flange length reaches a critical value; the peak longitudinal strain was found to rise with increased thickness; the increase of the bend angle increment was found to increase the peak longitudinal strain and the increase of the roll diameter was found to decrease the peak longitudinal strain. Brunet et al. (1996) and Zeng et al. (2008, 2009) performed an optimization design with FEM models for minimizing roll stands and eliminating product defects, respectively. The difference between their researches is that the former used boundary conditions as a function but the latter adopted springback angle as the objective function.

For achieving accurate and flawless products, Paralikas et al. (2009) presented a semi-empirical procedure to optimize the configuration of roll forming. It showed that the inter-distance between the roll stations played a dominant role for longitudinal strains in the roll forming process, followed by roll gap, velocity of the strip and rolls diameter (see Fig. 2-2).
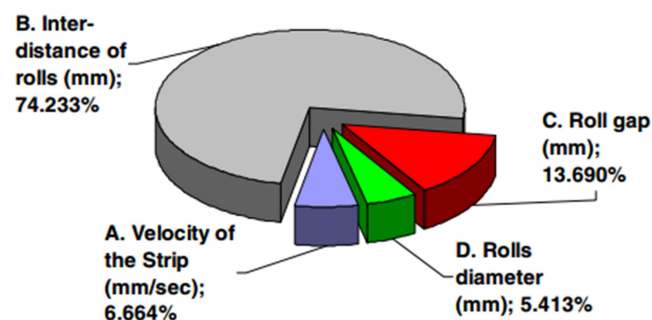


**Figure 2-2: Effect of each parameter to longitudinal strains at the strip edge (Paralikas et al. 2009)**

Wiebenga et al. (2013) used both numerical and experimental approaches in exploring the compensation of product defects while simultaneously minimizing the sensitivity to variation of material properties. They presented the robust optimization techniques to determine the roll forming stands and found that the adjustment of the tooling in the final roll stand leads to a significantly improved product quality by compensating for product defects and minimizing the deteriorating effects of scattering variables.

According to the previous reviews, it can be concluded that the hybrid use of experimental and numerical approaches are the best solution for exploring the cold worked residual stresses. Moreover, as most of the previous studies of the residual

stress were concerned with traditional sections, investigations on newly developed sections, e.g. sigma section, are still very limited. Therefore, in the present research, emphasis will be placed on the distribution of cold worked residual stress on sigma sections based on the explicit dynamic analysis and X-ray diffraction measurement.

## 2.4 Welding induced residual stresses

Hot rolling and welding process are the common sources of the thermal residual stress exist in steel members. The residual stress results from those processes are usually due to the uneven cooling phenomenon. Huber and Beedle (1954) from Lehigh University initially found that the magnitude of the maximum residual stress in hot-rolled shapes of moderate strength steels was approximately equal to 30% of the yield stress of the material. An idealized typical residual stress distribution pattern was presented by Weng and Peköz (1990) (Fig. 2-3). They found tensile stress occurred on the middle flange and compressive stress on the ends, and the stresses were assumed uniformly distributed through the plate thickness.
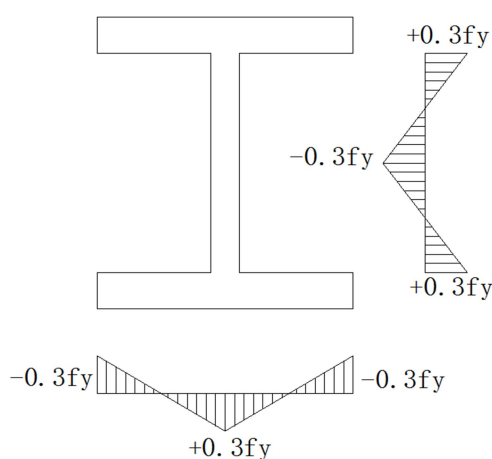
**Figure 2-3: Residual stress in hot-rolled section (Weng and Peköz 1990)**

During the welding process, a dynamic thermal cycle is introduced to generate a non-uniformly temperature distribution on the weldment. The residual stress is thus induced as a result of uneven cooling along welding bead and heat affected zone (HAZ). As the welding process involves with temperature-dependent material properties, short-term localized heating and cooling, metallurgical transformation and thermal-mechanical simulation, etc., the mathematical analyse of the process could be rather complicated. With the increasing power of computer processing capacity, increasingly numerical studies were applied to the simulation of the welding operation.

Brickstad and Josefson (1998) employed FEM in the study of multi-pass circumferential butt-welding of stainless steel pipes. They found the distribution of welding residual stress was sensitive to several factors such as structural restraint, wall thickness over diameter ratio, heat input, the number of weld passes and weld pass sequence. In the same year, Taljat et al. (1998) investigated the effect of solid-state phase transformations on residual stress from the gas tungsten arc (GTA) welding process by using numerical analysis. Later on, an "element birth and death" technique was introduced by Teng et al. (2003) in the analysis of welding sequences effect on residual stresses. The technique can deactivate and reactive the elements by multiplying their stiffness by a reduction factor for simulating the movement of the heat source. The same method was also adopted by Yaghi et al. (2006) for the study of the residual stresses in thin and thick-wall welded pipes. They found the peak tensile stresses occurred nearer to the inside surface and peak compressive stresses occur nearer to the outside surface of the pipe in thin-wall welded pipes; but converse

stress distribution can be seen in thick-wall welded pipes. The characteristics of residual stress distributions in the stainless steel pipe were stated by Deng and Murakawa (2006). They presented a detailed comparison of temperature field and residual stress between numerical and experimental results and found a good agreement between the two methods. Leggatt (2008) further illustrated that the controlling factors of the welding residual stress were the coefficient of thermal expansion, the yield strength and the phase change interaction.

More recently, Jameel et al. (2010) studied the single pass welding induced residual stresses in a welded steel pipe of 25.4mm radius by using mathematical and FE methods. It was found that the stresses changed from compression at the centreline of welding and tension away from the weld centreline at the end of welding to tension at the centreline and compression away from the weld centreline when it cooled. Moreover, a significant discrepancy between constant thermal material and temperature dependent thermal material was found. Kong et al. (2011) simulated the hybrid laser and gas metal arc (GMA) welding process by using SOLID 70 element for the thermal field based on ANSYS code. The model was heated by a double-ellipsoidal heat source and ignored the convection term. A good agreement was found between the experimentally obtained and numerically predicted residual stress in the study. Heinze et al. (2012) investigated the phase transformation and shrinkage restraint of six bead multi-pass gas metal arc welding by using FEM and laboratory tests. The extensive studies demonstrated that the experimental efforts can be reduced by adequate and deliberate application of FEM welding simulation technique.

In the papers mentioned above, the numerical simulation was encouraged to be used in the evaluation of welding residual stress as good agreements have been observed between the FE predictions and experimental results. However, the effort of the welding simulation in thin-walled sections was still limited. In the present research, predictions are made based on a thermal-mechanic coupled three dimensions (3D) FE model developed in ANSYS package (2010). Since the welding process is a coupling of dynamic thermal procedure and mechanical analysis, there are two major steps applied in the simulation: firstly, the non-linear transient heat conduction analysis is performed to obtain the thermal field; once the thermal analysis completed, the mechanical analysis is subsequently executed by using the temperature results as initial loading conditions.

## 2.5 Effects of initial imperfections

All cold formed structural members are working with imperfections. The main types of imperfection exist in steel structures including geometric imperfection, strain hardening and residual stress. The existence of such imperfections plays a significant role in determining the structural stiffness, load resistance capacity and fatigue life of components. Knowledge of their magnitude and distribution is, therefore, important for both structural design and numerical simulation. Extensive studies have been conducted before in the influences of initial imperfections on the behaviour of steel members.

Geometric imperfection refers to deviation such as bowing, warping, and twisting, of a member from 'perfect' geometry (Schafer and Peköz 1998b). As different imperfection types and their combinations affect the behaviour of structural members, Schafer and Peköz (1998b) found the magnitude of geometric imperfections is relevant to the various buckling modes of the member. They proposed suitable imperfection magnitudes for CFS beams based on numerous FE data. Dubina and Ungureanu (2002) also paid attentions on the characterisation and codification of imperfections for nonlinear FEM simulation. They pointed out that the crucial step in the analysis was to choose an appropriate imperfection shape and magnitude in connection with the relevant instability modes, because different shapes of local-sectional imperfections have a different effect on the member buckling strength. Recently, Liu et al. (2011b) proposed a most satisfactory geometric imperfection magnitude for sigma beams based on numerous tryouts in FEM.

## 2.5.1 Effects of residual stress

Residual stress is one of the main sources of material imperfections. The presence of residual stress in a component can either improve or impair its load resistance capacity and fatigue life, depending on the magnitude and distribution of the stress. The effects of residual stresses were veiled till the scholars from Lehigh University conducted a series of studies in the impacts of residual stress on steel members. Huber (1956) presented general formulas for residual stresses distribution in beams; Huber and Ketter (1958) theoretically studied the influence of residual stress on the strength of columns. Lee and Ketter (1958) illustrated the general stress-strain relationship in

respect to the influence of residual stress on column strength (Fig. 2-4). They found the maximum deviation due to residual stress would occur in relatively shorter members of the high strength material; residual stresses existed in high strength steels could affect the carrying capacity of compression members; and the maximum reduction due to residual stress would be 35% as compared to the full yield value.

Neglecting Residual Stress
Including Residual Stress
$E_t = \dfrac{d\sigma}{d\epsilon}$
E
Average σ – ε Curve of Section as a Whole
ε

Neglecting Residual Stress
Strong Axis
$\sigma_{cr} = \dfrac{\pi^2 (E)(\frac{E_t}{E})}{(\frac{L}{r})^2}$
Weak Axis
$\sigma_{cr} = \dfrac{\pi^2 (E)(\frac{E_t}{E})^3}{(\frac{L}{r})^2}$
Euler
$\dfrac{L}{r}$
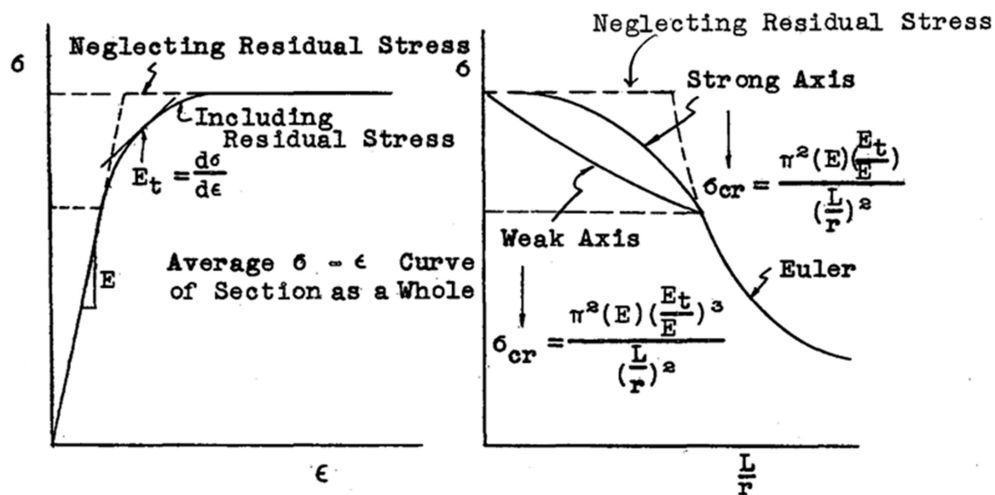
**Figure 2-4: Effects of residual stress on the column strength (Lee and Ketter 1958)**

Beedle (1960) investigated the strength of centrally-loaded columns as influenced by residual stresses. He found that for rolled or welded members, the part to cool last was usually in a tensile state of residual stresses. Residual stresses reduced buckling strength to about 25% because the occurrence of early localized yield when slenderness ratios range from 70 to 90. Later on, Weng (1991) proposed a "second reduction method" to quantify the effect of residual stresses on the local buckling behaviour of the component plate elements of a cold-formed section.

More recently, numerical methods were widely introduced to study the influence of residual stress. Real et al. (2004) determined the influences of residual stress on lateral-torsional resistance of steel I-beams at elevated temperatures by using a geometrically and materially non-linear FE model, and found the influence of the residual stresses is higher for intermediate slenderness of the beams (see Fig. 2-5).
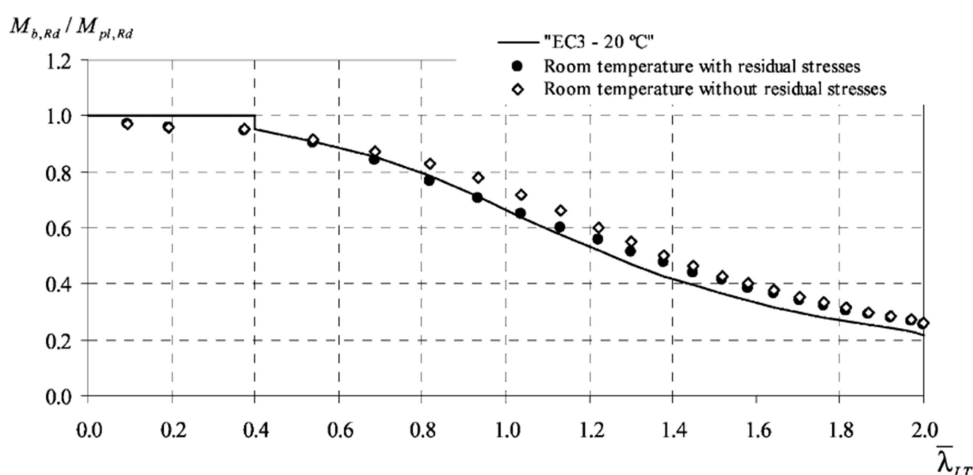


**Figure 2-5: Beam design curve at room temperature (Real et al. 2004)**

Quach et al. (2010) presented an advanced numerical approach for predicting the effect of cold work on press-braked thin walled steel columns in carbon steel lipped channels and stainless steel lipped channels, respectively. Both residual stresses and the equivalent plastic strains were considered in the FE model. It was found that strain hardening induced by cold work generally has a positive effect on the load-carrying capacity of a CFS member, but residual stresses generally have a negative impact. Whether the strength of a CFS column was enhanced or reduced depends on the balance between the effect of residual stresses and that of material strain hardening. The cold work in corner regions enhanced the column strength with the degree of

enhancement decreased as the column length increased. In the same year, Gao and Moen (2010) conducted a parametric study to explore the combined influence of isotropic hardening and kinematic hardening with residual stresses on the load-deformation responses of steel columns. They found the former was led to increasing the peak compression load and the latter was similar to the model without the effect of cold bending. Pastor et al. (2013) studied the influences of imperfections on cold-formed rack section by introducing an equivalent initial imperfection in the FE model. They found the effect of geometrical imperfection was not relevant for the prediction of the ultimate load of column when residual stresses are considered and the influence of residual stresses was relevant for distortional lengths and can be neglected for short columns. In the study of Jandera and Machacek (2014), the FEM was employed to determine the influence of forming-induced residual stresses in compressed members. It was concluded by the study that residual stresses led to an increase in load-carrying capacity of stainless steel square hollow sections in some cases.

Generally, the data of the distribution of cold working and welding residual stress on newly developed sections (e.g. sigma section) is quite limited, and the influence of residual stress in cold-formed beams is still not fully understood. The numerical method has proved an effective way to improve the efficiency and accuracy of the analysis in residual stress.

**2.5.2 Effects of strain hardening**

The effect of strain hardening during cold forming is also an inevitable topic when considering the impact of cold work. In 1881, Bauschinger reported a phenomenon that the yield strength was increased by reloading a plastically deformed specimen in the same direction or reduced by reloading it in the opposite direction, which is known as the Bauschinger effect.

Strength enhancement due to cold forming at the corners of carbon steel sections was first studied by Karren (1967). Nine specimens subjected to a simple type of cold work were tested to provide an understanding of the effects of cold-straining. These specimens, subjected to unidirectional permanent tensile prestrains, were tested in tension and compression both in and transverse to the direction of prestrain. Based on the strain hardening equation (Eq. 2-8) presented by Hollomon (1945) and substantial amount of test data, Karren established an empirical equation for predicting the corner yield strength $F_{yc}$ (Eqs. 2-9, 10, 11).

$$\bar{\sigma} = k(\bar{\varepsilon})^n \qquad\qquad \text{(Eq. 2-8)}$$

$$k = 2.80\,\sigma_u - 1.55\,\sigma_y \qquad\qquad \text{(Eq. 2-9)}$$

$$n = 0.225\,{\sigma_u}/{\sigma_y} - 0.120 \qquad\qquad \text{(Eq. 2-10)}$$

$$F_{yc} = \frac{B_c F_{yv}}{\left(R/t\right)^m} \qquad\qquad \text{(Eq. 2-11)}$$

where

k is the strength coefficient;

n is the strain-hardening exponent;

$\sigma_u$ is the virgin ultimate strength;

$\sigma_y$ is the virgin tensile yield strength;

$B_c$ is the constant, $B_c = 3.69 \frac{F_{uv}}{F_{yv}} - 0.819 \left(\frac{F_{uv}}{F_{yv}}\right)^2 - 1.79$;

$F_{yv}$ is the yield strength of the virgin steel;

$F_{uv}$ is the ultimate strength of the virgin steel;

R is the inside bend radius;

t is the thickness of the material;

m is the constant, $m = 0.192 \frac{F_{uv}}{F_{yv}} - 0.068$.

Karren and Winter (1967) further investigated the mechanical properties of the flat elements of sections and the mechanical properties of full sections. They found the increase in ultimate strength of the corner was considerably less than the increase in yield strength, and flats had smaller increases in strength than corners. The full section tensile yield strength was given by Eq. 2-12:

$$\sigma_{ys} = C\sigma_{yc} + (1 - C)\sigma_{yf} \qquad \text{(Eq. 2-12)}$$

where

C is the ratio of corner area to total cross-sectional area;

$\sigma_{yc}$ is the corner yield strength;

$\sigma_{yf}$ is the flat yield strength.

The equations introduced by Karren and Winter (1967) have been adopted by the AISI (1996) Specification to determine the full section yield strength and by the

Australian/New Zealand Standard AS/NZS 4600 (AS/NZS 1996) to decide average yield strength for cold formed carbon steel sections.

BSI (2006) also provided formulas to evaluate the increase in yield strength of CFS sections compared to the original material. In the specification, the average yield strength $f_{ya}$ of a cross section due to cold working should be determined by the following equations:

$$f_{ya} = f_{yb} + \left(f_u - f_{yb}\right)\frac{knt^2}{A_g} \text{ and } f_{ya} \leq \frac{f_u + f_{yb}}{2} \qquad \text{(Eq.2-13)}$$

where

$A_g$ is the gross cross-sectional area;

$f_{yb}$ is the basic yield strength;

k is a numerical coefficient that depends on the type of forming, k=7 for roll forming and k=5 for other methods of forming;

n is the number of $90^o$ bends in the cross section with an internal radius r≤5t;

t is the design core thickness of the steel material before cold forming.

Based on the nonlinear expression for stress–strain curve of metallic material introduced by Ramberg and Osgood (1943), Hill (1944) presented a modified formula (Eq. 2-14) by using 0.2% proof stress and the corresponding strain as the crucial factor. Chakrabarty (2006) developed a modified equation for plotting a stress-strain curve in the plastic stage (Eqs. 2-15, 2-16):

$$\varepsilon = \frac{\sigma}{E_0} + 0.002 \left(\frac{\sigma}{\sigma_{0.2}}\right)^n \qquad \text{(Eq. 2-14)}$$

$$
\begin{cases}
\sigma = E\varepsilon & (\varepsilon \le \frac{Y}{E}) \qquad\qquad \text{(Eq. 2-15)} \\[2ex]
\sigma = Y\left(\frac{E\varepsilon}{Y}\right)^{n} & (\varepsilon > \frac{Y}{E}) \qquad\qquad \text{(Eq. 2-16)}
\end{cases}
$$

where

$\sigma$ and $\varepsilon$ are engineering stress and strain, respectively;

$E_0$ is the material's Young's modulus;

$\sigma_{0.2}$ is the material's 0.2% proof stress;

n is a strain hardening exponent;

Y is the yield strength.


Van den Berg and Van der Merwe (1992) studied the degree of work hardening on stainless steel specimens 304, 409, 430 and Type 3CR12; and further proposed an modified equation (Eq. 2-17) for predicting the yield strength of comers based on Karren's methodology.

$$
F_{yc} = \frac{B_c F_y}{\left(R/t\right)^{m}} \qquad\qquad \text{(Eq. 2-17)}
$$

where

$B_c$  is the constant, $B_c = 3.289\frac{F_u}{F_y} - 0.861\left(\frac{F_u}{F_y}\right)^{2} - 1.34$;

$F_y$ is the yield strength of the virgin steel;

$F_u$ is the ultimate strength of the virgin steel;

R is the inside bend radius;

t is the thickness of the material;

m is the constant, $m = 0.06\frac{F_u}{F_y} + 0.031$.

Ashraf et al. (2005) proposed the recalibrated formulas for the evaluation of the enhanced strength of the corner regions of cold-formed stainless steel sections based on the equations presented by Van den Berg and Van der Merwe, illustrated in Eqs. 2-18 and 19:

$$\sigma_{0.2,c} = \frac{1.881\sigma_{0.2,v}}{\left(\frac{r_i}{t}\right)^{0.194}} \qquad \text{(Eq. 2-18)}$$

$$\sigma_{u,c} = 0.75\sigma_{0.2,c}\left(\frac{\sigma_{u,v}}{\sigma_{0.2,v}}\right) \qquad \text{(Eq. 2-19)}$$

where

$\sigma_{0.2,c}, \sigma_{0.2,v}$ is the yield strength of the cold-formed and virgin steel;

$\sigma_{u,c}, \sigma_{u,v}$ is the ultimate strength of the cold-formed and virgin steel;

r is the inside bend radius;

t is the thickness of the material.

Cruise and Gardner (2008b) studied the strength enhancement of cold-rolled box sections and press-braked angles, and presented the modified expressions Eqs. 2-20 and 2-21 for the corner regions shown in Fig. 2-9.

$$\sigma'_{0.2,pb,c} = \frac{1.673\sigma_{0.2,mill}}{\left(\frac{r_i}{t}\right)^{0.126}} \qquad \text{(Eq. 2-20)}$$

$$\sigma'_{0.2,cr,c} = 0.83\sigma'_{ult,f} \qquad \text{(Eq. 2-21)}$$

where

$\sigma'_{0.2,pb,c}$ is the predicted 0.2% proof stress of the corners of press-braked sections;

$\sigma'_{0.2,cr,c}$ is the predicted 0.2% proof stress of the corners of cold rolled box sections;

$r_i$ is the section corner radius;

t is the section thickness;

$\sigma_{0.2,mill}$ is the 0.2% proof stress given in inspection document or mill certificate;

$\sigma'_{ult,f}$ is the predicted ultimate stress for the central 50% of the faces of cold-rolled box.
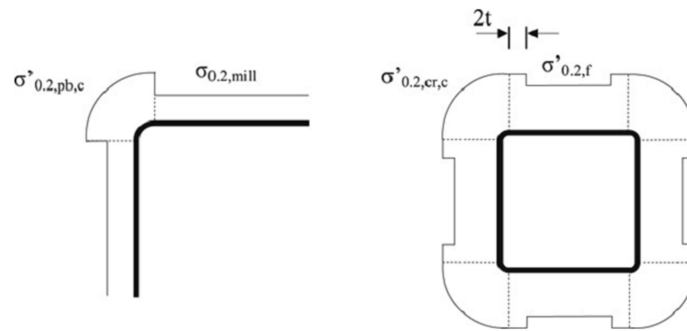


**Figure 2-6: Proposed 0.2% proof stress distributions for press-braked sections and cold-rolled boxes**

According to the extensive experimental data and formulas in previous studies, Rossi et al. (2009) proposed a new theory-based formula for predicting the enhanced mechanical properties of cold worked stainless steel structural members based on the virgin sheet material properties (Eq. 2-22). The formula was dependent on the curvature to thickness ratio and respected the assumption that no negative enhancement was allowed.

When $\varepsilon_{0.2} \leq \varepsilon \leq \varepsilon_u$

$$\frac{\sigma_u}{\sigma_c - \sigma_{0.2}} = \frac{\varepsilon_{0.2}}{r_2} \frac{\sigma_u}{\sigma_{0.2}} \frac{R}{t/2} + \frac{(r^*-1)\varepsilon_{0.2}}{r_2(\varepsilon_u - \varepsilon_{0.2})^{p^*}} \frac{\sigma_u}{\sigma_{0.2}} \left(\frac{R}{t/2}\right)^{1-p^*} \qquad \text{(Eq. 2-22)}$$

where

$\sigma_u$ and $\varepsilon_u$ are the ultimate stress and strain of the virgin material;

$\sigma_{0.2}$ and $\varepsilon_{0.2}$ are the 0.2% proof stress of the virgin material;

$\sigma_c$ is the enhanced proof stress in the corners of the cold formed sections;

R is the radius of the corner;

t is the thickness of the corner;

$r^* = E_2 \frac{\varepsilon_u - \varepsilon_{0.2}}{\sigma_u - \sigma_{0.2}};$

$r_2 = E_2 \frac{\varepsilon_{0.2}}{\sigma_{0.2}};$

$p^* = r^* \frac{1 - r_u}{r^* - 1}.$

Methods for predicting strength enhancement in CFS sections are summarized in Table 2-1:

**Table 2-1: Summary of strain hardening prediction method**

| Author | Year | Formulas | Note |
|---|---|---|---|
| Hill | 1944 | $\varepsilon = \dfrac{\sigma}{E_0} + 0.002 \left(\dfrac{\sigma}{\sigma_{0.2}}\right)^n$ | CS&SS |
| Hollomon | 1945 | $\bar{\sigma} = k(\bar{\varepsilon})^n$ | C, CS |
| Karren | 1967 | $\sigma_{yc} = \dfrac{kb}{\left(a/t\right)^m}$ | C, CS |
| Karren and Winter | 1967 | $\sigma_{ys} = C\sigma_{yc} + (1 - C)\sigma_{yf}$ | A, CS |
| Chakraberty | 2006 | $\sigma = Y \left(\dfrac{E\varepsilon}{Y}\right)^n$ | A, CS |
| BSI | 2006 | $f_{ya} = f_{yb} + \left(f_u - f_{yb}\right)\dfrac{knt^2}{A_g} \,, \; f_{ya} \leq \dfrac{f_u + f_{yb}}{2}$ | A, CS |
| Van den Berg and Van der Merwe | 1992 | $F_{yc} = \dfrac{B_c F_y}{\left(R/t\right)^m}$ | C, SS |

| | | | |
|---|---|---|---|
| Ashraf et al. | 2005 | $\sigma_{0.2,c} = \dfrac{1.881\sigma_{0.2,v}}{\left(\frac{r_i}{t}\right)^{0.194}}, \sigma_{u,c} = 0.75\sigma_{0.2,c}\left(\dfrac{\sigma_{u,v}}{\sigma_{0.2,v}}\right)$ | C, SS |
| Cruise and Gardner | 2008 | $\sigma'_{0.2,pb,c} = \dfrac{1.673\sigma_{0.2,mill}}{\left(\frac{r_i}{t}\right)^{0.126}}$ , $\sigma'_{0.2,cr,c} = 0.83\sigma'_{ult,f}$ | C, SS |
| Rossi et al. | 2009 | $\dfrac{\sigma_u}{\sigma_c - \sigma_{0.2}} = \dfrac{\varepsilon_{0.2}}{r_2}\dfrac{\sigma_u}{\sigma_{0.2}}\dfrac{R}{t/2} + \dfrac{(r^*-1)\varepsilon_{0.2}}{r_2(\varepsilon_u - \varepsilon_{0.2})^{p^*}}\dfrac{\sigma_u}{\sigma_{0.2}}\left(\dfrac{R}{t/2}\right)^{1-p^*}$ $\varepsilon_{0.2} \le \varepsilon \le \varepsilon_u$ | C, CS&SS |

*Note:* *C – Only consider corner enhancement;*

*A – Consider average enhancement for cross section;*

*CS – Carbon steel;*

*SS – Stainless steel.*

## 2.6 Knowledge gap

Despite substantial findings were presented in the study of residual stress, some issues are still not fully understood and need further investigations. The knowledge gaps are presented in following:

1. Most of the analytical models of coiling-uncoiling and press braking process were simplified as the static bending processes. The dynamic nature of those processes was ignored. Moreover, most of the previous numerical simulations of coiling-uncoiling and press braking process were based on 2D models. Although the results achieved from 2D model can fulfil the requirement of time-efficiency and accuracy. However, 2D models ignored the edge effect and cannot fully describe the residual stress distribution along the section. Therefore, a 3D model based on dynamic analysis is needed to validate the previous founding.

2. Some researchers have investigated the roll forming process in conventional profiles such as channel section and I section. However, very limited data is available to the roll sets arrangement, processing analysis and residual stress distribution of newly developed profile such as sigma section. The present research is concentrated on the numerical prediction of residual stress in roll formed sigma section, and the FE results are validated by X-ray diffraction experiment.

3. Previous studies in welding process were mainly focused on the hot-rolled sections, the knowledge in welding induced temperature field and residual stress distribution in thin-walled sigma section were limited and needed to be further studied.

4. Prior studies have shown that the impact of residual stress on the columns was significant, and the strength enhancement during cold working was also a critical factor to the load resistance capacity of the steel component. The study on the combined effect of residual stress and work hardening on beams in sigma sections is still rarely. Furthermore, it is also necessary to investigate the combined influence of press braking and welding residual stress on sigma beams.

The present study will address the above mentioned gaps by using theoretical, experimental and numerical methods. The residual stress distribution in sigma sections during coiling uncoiling, press braking, roll forming and welding process will be presented. The influences of residual stress and strain hardening on cold-formed

sigma beams will be studied by using FEM. The theoretical and experimental

approaches will be further proposed for validation purpose.

# 3. COILING-UNCOILING AND PRESS BRAKING RESIDUAL STRESS

## 3.1 Introduction

The continuous metal sheet feed to cold forming is usually provided with unwound coils from the coiling-uncoiling process. The coiling process is used to bend the flat sheet to roll for storage and transportation purpose, and the uncoiling process is to force the rolled sheet to be flat again for further usage. Therefore, prior to the investigation of the press braking and cold forming process, the residual stress from the coiling-uncoiling process has to be studied in advance.

Press braking is a semi-manually bending process that only requires punches and dies for angle folding. The process has strong operability when compares with roll forming approach but limited in member length and production capacity. During the process, the sheet is placed between a set of top punch and bottom die (see Fig. 3-1); the angle is then achieved along the sheet when the punch moves downward to meet the shape of the die.
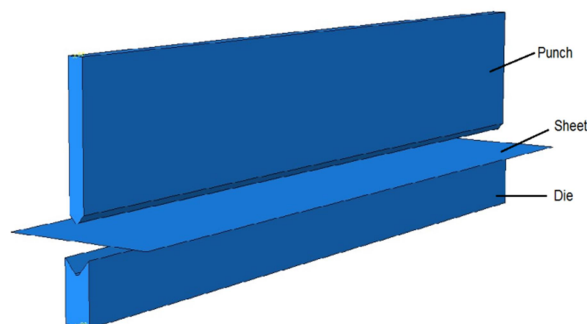


**Figure 3-1: Sketch of press brake tools**

The residual stress induced in the coiling-uncoiling and press braking process is studied numerically in this chapter. The stress development of the sheet during the dynamic processes is visualized, and the final residual stress distributions are presented. Furthermore, to validate the present model, the residual stress achieved in FEM is compared with that obtained from the theoretical and experimental method. A series of parametric studies are conducted to illustrate the influence of input parameters on the model.

## 3.2 Analytical solution for coiling-uncoiling residual stress

An analytical study is conducted herein to quantify the residual stress during the coiling-uncoiling process. The calculation process (Eq. 3-1to 3-10) is according to the approach presented by Quach et al. (2004).

The residual stress after coiling process:

For $|y| \leq y_{cy}$ (in elastic stage)

$$\boldsymbol{\sigma}_{z,c} = \frac{E}{(1-v^2)} \boldsymbol{k}_c \boldsymbol{y} \qquad \text{(Eq. 3-1)}$$

$$\boldsymbol{\sigma}_{x,c} = \frac{vE}{(1-v^2)} \boldsymbol{k}_c \boldsymbol{y} \qquad \text{(Eq. 3-2)}$$

For $|y| > y_{cy}$ (in plastic stage)

$$\boldsymbol{\sigma}_{z,c} = \pm \frac{\sigma_y}{\sqrt{1-\omega_c+\omega_c^2}} \qquad \text{(Eq. 3-3)}$$

$$\sigma_{x,c} = \pm \frac{\omega_c \sigma_y}{\sqrt{1 - \omega_c + \omega_c^2}} \qquad \text{(Eq. 3-4)}$$

where

$k_c$ is the coiling curvature;

E is the Elastic modulus;

$\sigma_{x,c}$, $\sigma_{z,c}$ is the transverse and longitudinal stress after coiling;

$\omega_c$ is the stress ratio for coiling process, $\omega_c = {\sigma_{x,c}}/{\sigma_{z,c}}$ ;

 y is the distance from the neutral axis,

$$|y| = \frac{\sigma_y(1-v^2)}{Ek_c\sqrt{1-v+v^2}} + \frac{\sigma_y}{Ek_c}\left[\frac{\omega_c(1-2v)}{\sqrt{1-\omega_c+\omega_c^2}} + \frac{\sqrt{3}}{2}coth^{-1}(\sqrt{\frac{4(1-\omega_c+\omega_c^2)}{3}})\right]_v^{\omega_c} \; ;$$

$y_{cy}$ is the distance when yielding occurs during coiling,

$y_{cy} = \sigma_y(1-v^2)/(Ek_c\sqrt{1-v+v^2})$;

$v$ is the Poisson's ratio.

The residual stress after uncoiling process:

$$\sigma_{z,r} = \sigma_{z,c} + \sigma_{z,u} \qquad \text{(Eq. 3-5)}$$

$$\sigma_{x,r} = \sigma_{x,c} + \sigma_{x,u} \qquad \text{(Eq. 3-6)}$$

For $k_c \le |k_{uy}|$

$$\sigma_{z,u} = -\frac{E}{(1-v^2)}k_c y \qquad \text{(Eq. 3-7)}$$

$$\sigma_{x,u} = -\frac{vE}{(1-v^2)}k_c y \qquad \text{(Eq. 3-8)}$$

For $k_c > |k_{uy}|$

$$\sigma_{z,u} = \mp\left(\frac{\sigma_y}{\sqrt{1-\omega_c+\omega_c^2}} + \frac{\sigma_y}{\sqrt{1-\omega_u+\omega_u^2}}\right) \qquad \text{(Eq. 3-9)}$$

$$\sigma_{x,u} = \mp\left(\frac{\omega_c\sigma_y}{\sqrt{1-\omega_c+\omega_c^2}} + \frac{\omega_u\sigma_y}{\sqrt{1-\omega_u+\omega_u^2}}\right) \qquad \text{(Eq. 3-10)}$$

where

$\sigma_{x,r}, \sigma_{z,r}$ is the final stress in the transverse and longitudinal direction;

$\sigma_{x,u}, \sigma_{z,u}$ is the transverse and longitudinal stress after uncoiling;

$\omega_u$ is the stress ratio for uncoiling process, $\omega_u = {\sigma_{x,r}}/{\sigma_{z,r}}$;

$k_{uy}$ is the coiling curvature when yielding occurs,

$k_{uy} = -\sigma_y(1-v^2)[2-v+(2v-1)\omega_c]/(E|y|(1-v+v^2)\sqrt{1-\omega_c+\omega_c^2})$ ;

y is the distance from the neutral axis,

$$|y| = \frac{\sigma_y}{E(k_c+k_{uy})}\left[\frac{\omega_u(1-2v)}{\sqrt{1-\omega_u+\omega_u^2}} + \frac{\sqrt{3}}{2}coth^{-1}\left(\sqrt{\frac{4(1-\omega_u+\omega_u^2)}{3}}\right)\right]_{\omega_{uy}}^{\omega_u} .$$

It needs to be noted that in Quach's et al. study, the coiling-uncoiling process was considered as a plastic plane strain pure bending problem that obeyed to the von Mises criterion. It also assumed that any residual stresses prior to the coiling-uncoiling process have been removed in the annealing furnace and strain hardening effect was not involved in the process.

## 3.3 Numerical analysis of coiling-uncoiling process

### (1) Dynamic explicit analysis method

The numerical analysis in this chapter is based on the dynamic explicit method in ABAQUS package. Explicit dynamic method can be used to solve highly discontinuous, high-speed dynamic problems and quasi-static problems. It allows the definition of very general contact conditions for complicated contact problems, and without generating numerical convergence difficulties. Also, an explicit dynamic solver uses a consistent large-deformation theory that can model large rotations and large deformations. Therefore, the metal forming process, which is considered as the quasi-static problem with one or more of the discontinuities parts and complex contacts, is a good candidate for explicit analysis.

The explicit dynamics analysis procedure is based upon the implementation of an explicit integration rule together with the use of diagonal element mass matrices. The equations of motion for the body are integrated using the explicit central-difference integration rule:

$$\dot{u}^N_{(i+\frac{1}{2})} = \dot{u}^N_{(i-\frac{1}{2})} + \frac{\Delta t_{(i+1)} + \Delta t_{(i)}}{2} \ddot{u}^N_{(i)} \qquad \text{(Eq. 3-11)}$$

$$u^N_{(i+1)} = u^N_{(i)} + \Delta t_{(i+1)} \dot{u}^N_{(i+\frac{1}{2})} \qquad \text{(Eq. 3-12)}$$

where $u^N$ is a degree of freedom (a displacement or rotation component) and the subscript i refers to the increment number in an explicit dynamics step. The central-

difference integration operator is explicit in the sense that the kinematic state is advanced using known values of $\dot{u}^{N}_{(i-1/2)}$ and $\ddot{u}^{N}_{(i)}$ from the previous increment.

The explicit central-difference operator satisfies the dynamic equilibrium equations at the beginning of the increment t; the accelerations calculated at time t are used to advance the velocity solution to time $t + \Delta t/2$ and the displacement solution to time $t + \Delta t$. The dynamic equilibrium equation for explicit analysis is:

$$M\ddot{u} = P - I \qquad\qquad \text{(Eq. 3-13)}$$

where

**M** is the mass matrix;

$\ddot{u}$ is the acceleration;

**P** and **I** are the external and internal force.

The explicit dynamic solver provides an efficient solution procedure when compared to the direct-integration dynamic analysis procedure available in Abaqus/Standard because there is no solution for a set of simultaneous equations. In a static analysis, for each load increment, the continuity of the contact states is checked first. In an explicit dynamic solver, a kinetic contact algorithm is used, in which the model moves into a predicted configuration without considering the contact conditions. The explicit analysis is also has an advantage over the implicit analysis as the former only related to the time step and without iteration and convergence problem; while the latter requires Newton-Raphson iterations to enforce equilibrium of the internal structure at each increment and has convergence problems. When applying explicit dynamics to

model quasi-static events (such as metal forming process), it is expedient to reduce the computational cost by scaling the mass. Mass scaling has exactly the same effect on inertia forces as speeding up the time of simulation. Mass scaling is attractive because it can be used in rate-dependent problems, but it must be used with care to ensure that the inertia forces do not dominate and change the solution.

**(2) Geometric model**

The numerical model of the coiling-uncoiling process is a two-stage manufacture process consists of metal sheet and coil roll. At the first stage, the sheet moves horizontally to the roll and be coiled in the anti-clockwise direction (see Fig. 3-2a). Then, the roll rotates in the reverse direction for flatting the sheet as a uncoiling process (see Fig. 3-2b). In the model, the radius of the roll was assumed as 120mm, and the geometric dimension of the sheet was 1300mm × 190 mm × 1.2mm (length × width × thickness). The FE model was established based on the sign convention that tension in positive and compression in negative. In the model, the longitudinal direction was assumed along the length of sheet and transverse direction along the width of the sheet.



(a) Coiling          (b) Uncoiling
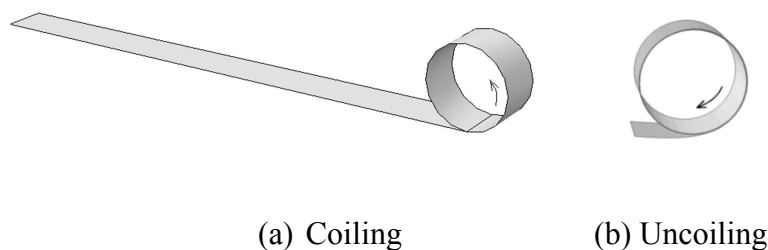
**Figure 3-2: FE model of coiling-uncoiling process**

**(3) Material properties**

The multi-linear material was considered for the steel sheet with the stress-strain curve shown in Fig. 3-3 (**Liu et al. 2011b**). The young's module for the material was 207GPa, Poisson's ratio was 0.3, density was 7850 kg/m$^3$ and the nominal yield strength was 450Mpa.
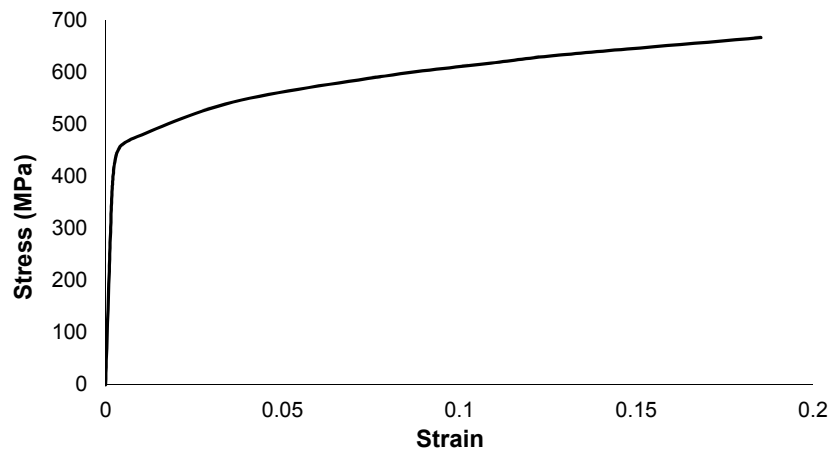


**Figure 3-3: Stress-strain curve used in the FE model (Liu et al. 2011b)**

**(4) Boundary conditions**

During the coiling process, the sheet was restrained in lateral movement and the end edge of sheet was fixed in vertical direction to avoid edge-waving effect; the roll was fixed in all movements except the anti-clockwise rotation, with the angular velocity was 25rad/s. The angular velocity was selected as no unintended deformations of the sheet occurred while the minimum CPU time was required. When coiling operation finished, the rolled sheet was unwinded to flat by imposing a rotation to the roll in the clockwise direction with the same velocity.

**(5) Meshing and interaction**

In the FE model, the roll was modelled using 4-node 3D discrete rigid shell element (R3D4) as it made of high-strength alloy steel and has limited deformations during the process. The sheet was simulated using 4-node 3D deformable shell elements (S4R) with reduced integration. As the meshing assignation plays a significant role in the modelling process, the selection of mesh size was selected based on the following mesh sensibility analysis shown in the Table 3-1.

**Table 3-1: Comparison of different mesh size**

| Element size (mm) | Total number of elements | CPU time (s) | Maximum longitudinal stress | |
|---|---|---|---|---|
| | | | S11 (MPa) | Diff. (%) |
| 30 | 444 | 2301 | 462.3 | -7.15% |
| 25 | 728 | 3770 | 483.3 | -2.93% |
| 20 (selected) | 1110 | 5604 | 497.3 | -0.12% |
| 15 | 1963 | 9901 | 497.9 | 0.00% |

It can be seen from Table 3-1 that the discrepancy in longitudinal stress between the coarse mesh (30mm and 25mm) and finer mesh (15mm) is -7.15% and -2.93%, respectively, but the difference between medium mesh (20mm) and finer mesh is insignificant (-0.12%). In the meanwhile, the CPU time required for medium mesh (5604s) reduces 77% when compared with finer mesh (9901s). Therefore, the medium mesh size was selected for the model based on combined consideration of stress result and CPU time.

In the model, the movement of the sheet during the coiling process was driven by tie contact between the roll and the front part of the sheet. Hard contact was applied as the general interaction between surfaces of sheet and roll. This interaction can resist the penetration of surfaces in the normal direction and allows separation when contact finished. The summary of input parameters such as geometric dimensions, material property, mesh size and rotation speed is shown in Table 3-2.

Table 3-2: Summary of input parameters

| | |
|---|---|
| Sheet thickness | 1.2mm |
| Sheet length | 1.3m |
| Sheet width | 190mm |
| Roll radius | 120mm |
| Yield strength | 450MPa |
| Density | 7850 kg/m$^3$ |
| Poisson's ratio | 0.3 |
| Young's modulus | 207Gpa |
| Sheet element | S4R |
| Roll element | R3D4 |
| Mesh size | 20mm |
| Angular velocity | 25rad/s |

## 3.4 Results discussions

The contour of von Mises stress during the coiling process is demonstrated in Fig. 3-4a and stress contour after uncoiling is shown in Fig. 3-4b.
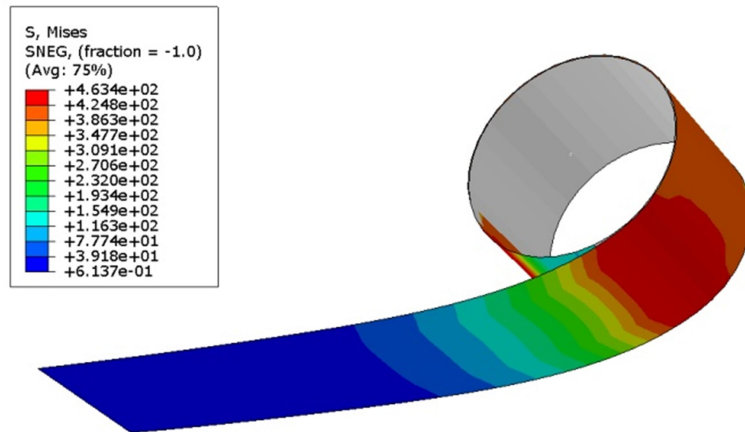
(a) Coiling stress contour
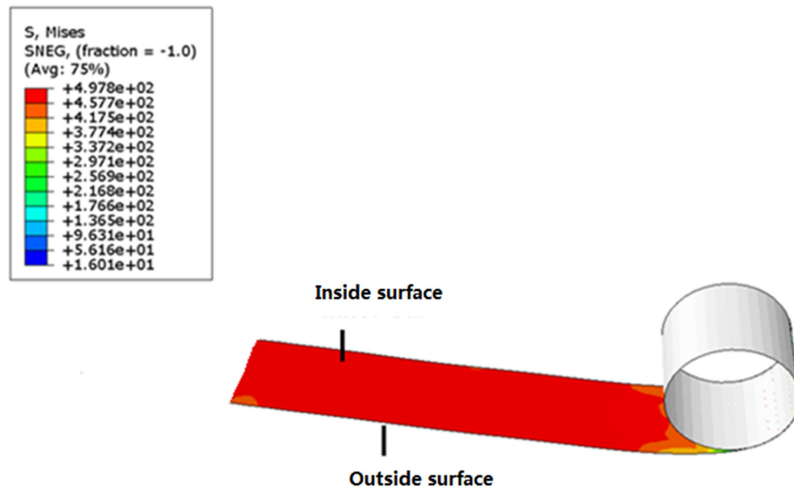


(b) Uncoiling stress contour

**Figure 3-4: Coiling-uncoiling von Mises stress contours**

It can be seen from Fig. 3-4a that the sheet is coiled on the bottom of the roll, and the stress is ascended as the increases of the bending angle. The maximum stress during the coiling process is 463MPa, which located on the bottom of the roll where sheet and roll are fully contacted. In Fig. 3-4b, it can be found that the maximum uncoiling stress is 498MPa, and the distribution of uncoiling stress is uniform along the sheet.

In order to investigate the residual stress distribution along shell thickness, nine integration points were assigned to the shell element. To keep the same sign convention with the output in ABAQUS, the Y-coordinate of each integration point was normalized by t/2. The schematic graph of the coordinate along thickness is shown in Fig. 3-5.
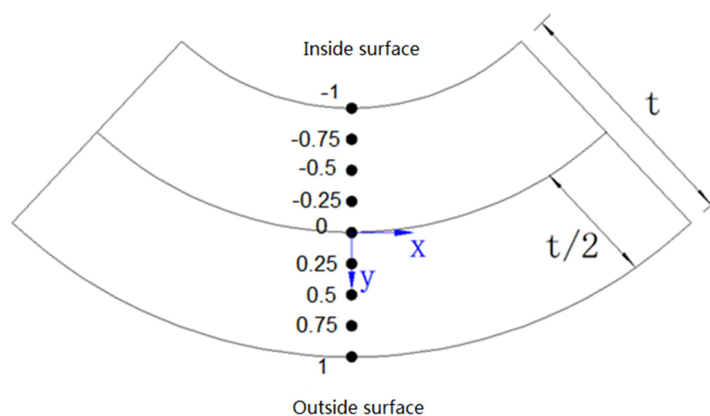


**Figure 3-5: Coordinate along thickness**

The distribution of residual stress along the thickness after the coiling and uncoiling process is shown in Fig. 3-6a and Fig. 3-6b, respectively. In the figures, the Y-axis represents the normalized coordinate along thickness and X-axis is the ratio between residual stress and nominal yield strength. The theoretical results presented in the figure are calculated based on Quach's et al. formulas (Eqs. 3-1 to 3-10).
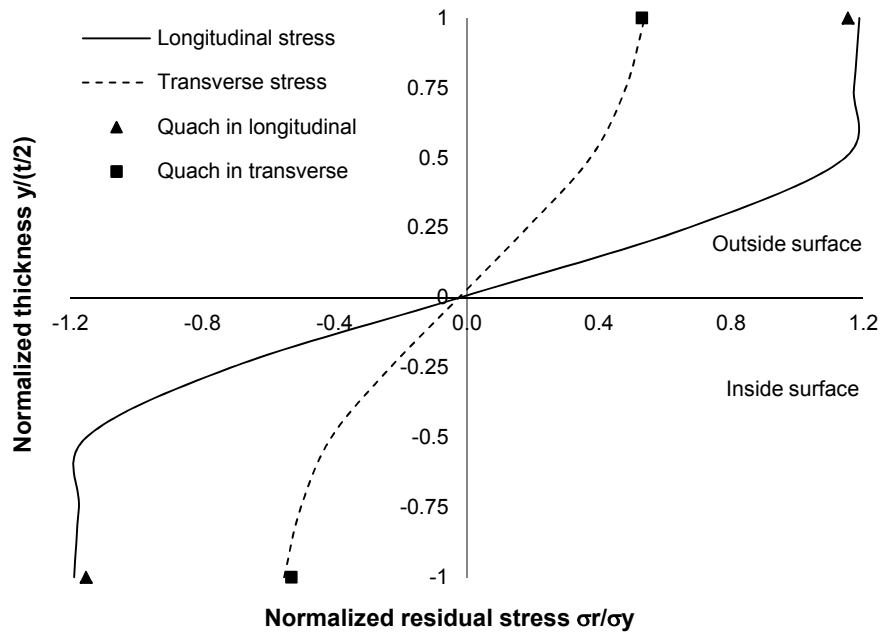
(a) Coiling residual stress
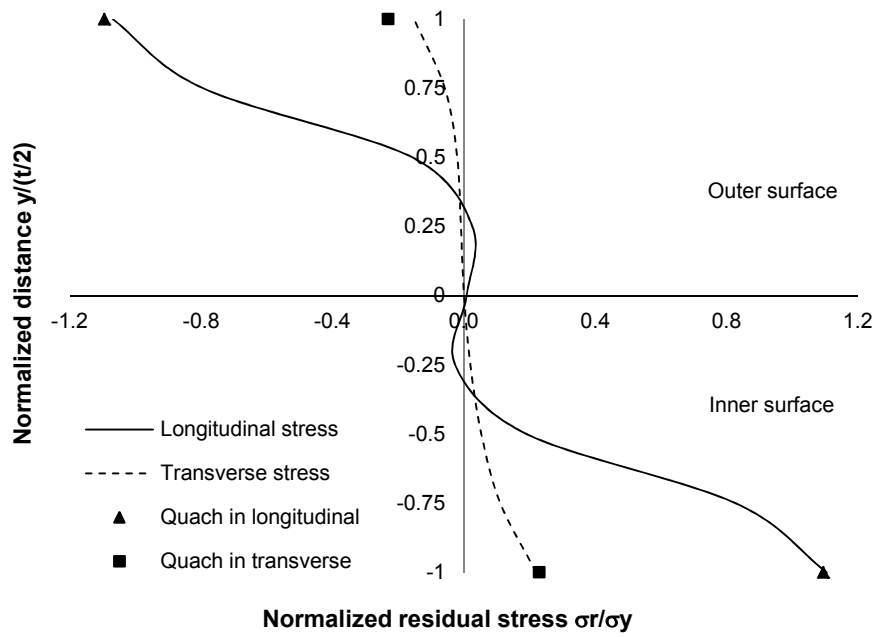


(b) Final residual stress after the uncoiling

**Figure 3-6: Residual stresses along thickness**

The following conclusions can be found from Fig. 3-6:

(1) The distribution of coiling and final residual stress is nonlinear along the shell thickness, and the curves are asymmetrical about the neutral axis in both directions.

(2) After the coiling process, the tensile stress is shown on the outside surface and compression on the inside surface. The longitudinal coiling stress ($1.19\sigma_y$) is greater than transverse stress ($0.54\sigma_y$) on the outside surface, and a good agreement can be found between FEM results and analytical values ($1.15\sigma_y$ in longitudinal and $0.53\sigma_y$ in transverse direction) with the gap is 3.5% and 1.9%, respectively.

(3) At the final stage of the uncoiling process, the longitudinal residual stress in FEM is $1.11\sigma_y$ on the inside surface, which also acts as the dominated stress when compared with the transverse stress ($0.22\sigma_y$). The discrepancy is also insignificant when compare FEM results with theoretical results ($1.09\sigma_y$ in longitudinal and $0.23\sigma_y$ in transverse direction), while the difference is only 1.8% and -4.3%, respectively.

(4) The outside surface of the sheet is subjected to tension during the coiling process but turns to compression after uncoiling, which proves the coiling-uncoiling process is similar to a loading-unloading operation.

The final longitudinal residual stress along the width of the sheet is presented in Fig. 3-7, where Y-axis is the ratio between longitudinal residual stress and nominal yield stress and X-axis represents the transverse distance of the sheet.
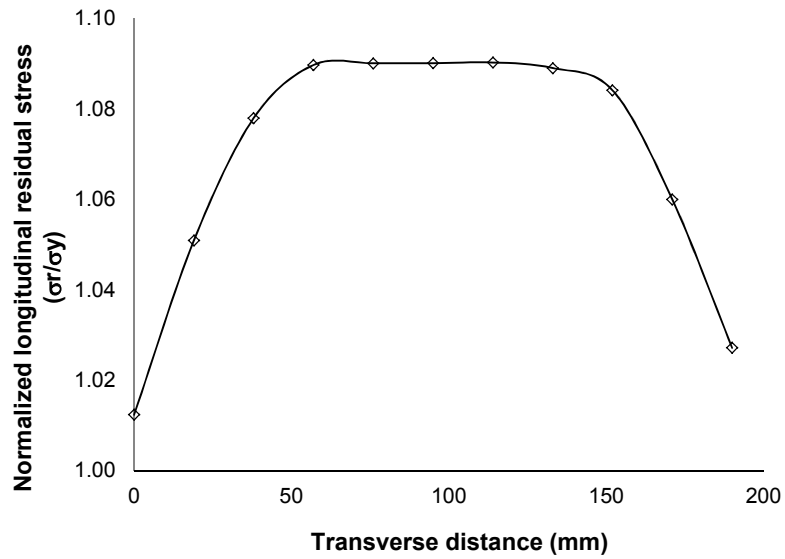
**Figure 3-7: Residual stresses along transverse direction**

It can be seen from Fig. 3-7 that the distribution of normalized longitudinal stress is symmetrical about the mid-width axis of the sheet and the stress ratio on middle portion of sheet (1.09) is slightly greater than side portion (1.01), which is an evidence of the occurrence of the edge waving on side portion.

The predicted through thickness equivalent plastic strain (PEEQ) of the sheet after the uncoiling process is shown in Fig. 3-8.
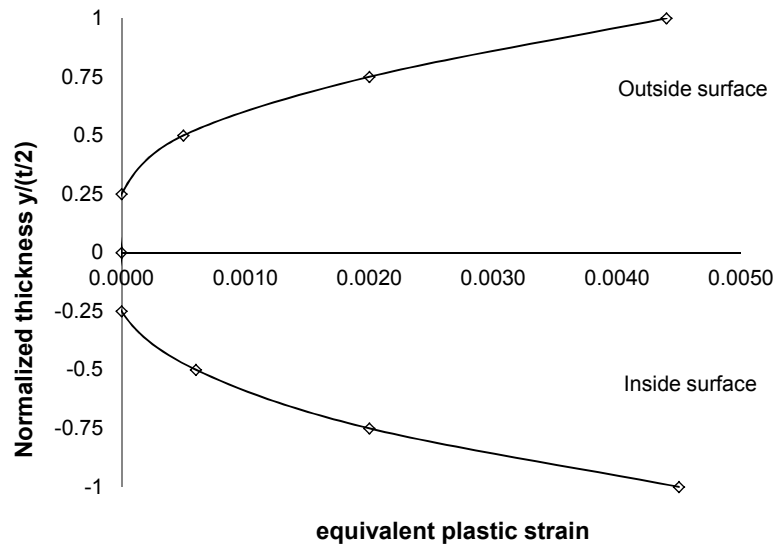
**Figure 3-8: Through-thickness equivalent plastic strains**

From the figure, it shows that the PEEQ is nonlinear along the shell thickness and symmetrical to the neutral axis. It also indicates that there are no plastic strains occurs in the core region (-0.25 to 0.25) of the sheet after the uncoiling process. The PEEQ is found increases along the normalized thickness and the maximum value is 0.0045.

## 3.5 Parametric studies

Parametric studies are further conducted to investigate the influence of yield strength, sheet thickness and roll radius on the coiling-uncoiling residual stress. The input variables for the standard model are: 450MPa for yield strength, 1.2mm for sheet thickness and 120mm for roll radius, and only one variable is changed at a time during the following parametric studies.

**(1) Effect of yield strength**

The comparison of final residual stress between different yield strengths: 250MPa, 350MPa and 450MPa, is shown in Fig. 3-9. In the figure, the X-axis is the normalized ratio between residual stress and named yield strength, and Y-axis represents the normalized coordinate along shell thickness.
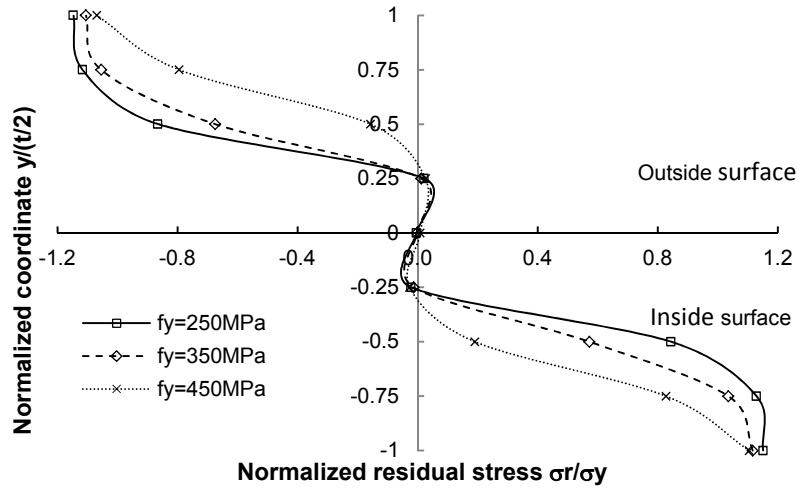


(a) Longitudinal residual stress
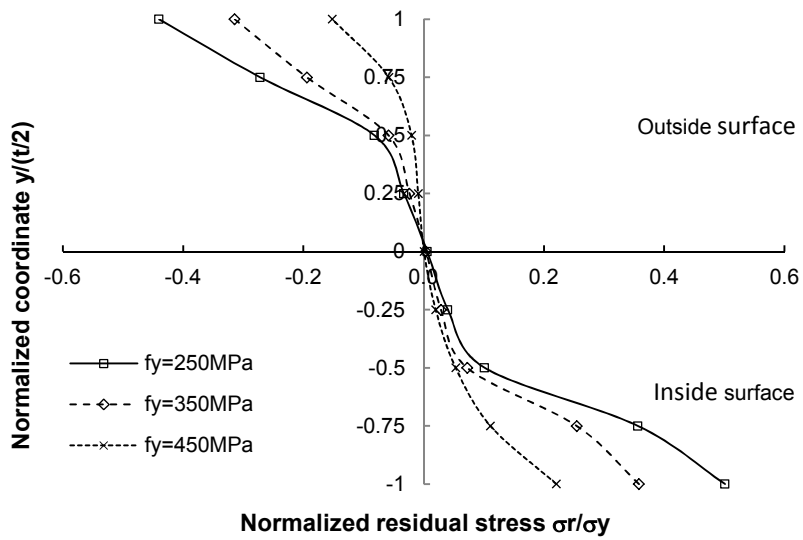


(b) Transverse residual stress

**Figure 3-9: Comparison of models with different material strengths**

## (2) Effect of sheet thickness

Three different thicknesses: 1.0mm, 1.2mm and 1.8mm, are chosen for the sheet to reveal the effect of sheet thickness on residual stress. The comparison of residual stress between models is shown in Fig. 3-10.
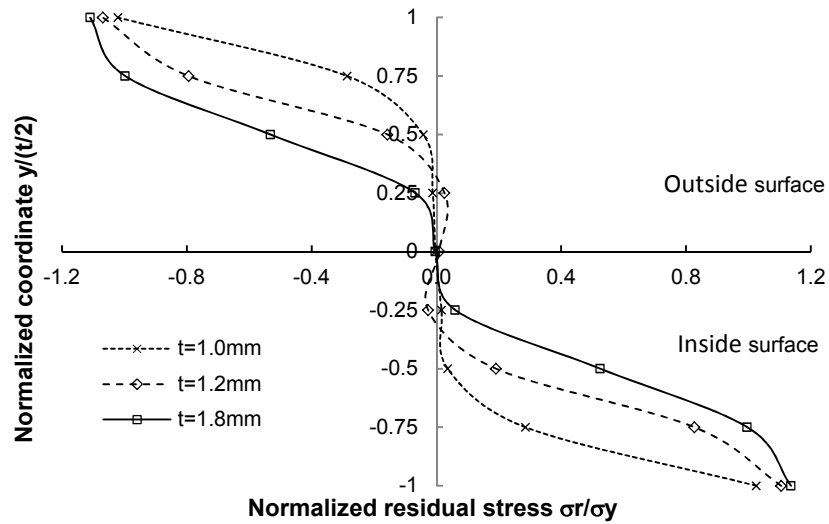


(a) Longitudinal residual stress
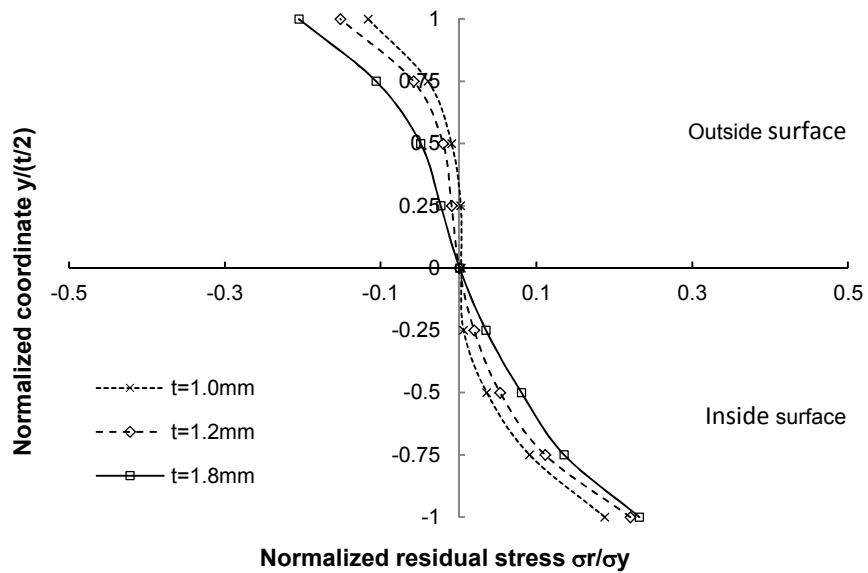


(b) Transverse residual stress

**Figure 3-10: Comparison of models with different thicknesses**

**(3) Effect of roll radius**

There are four different coiling radiuses: 120mm, 360mm, 600mm and 1200mm with the same shell thickness 1.2mm, are selected to investigate the effect of the coiling curvature on final residual stress. The curves from different models are compared in Fig. 3-11.
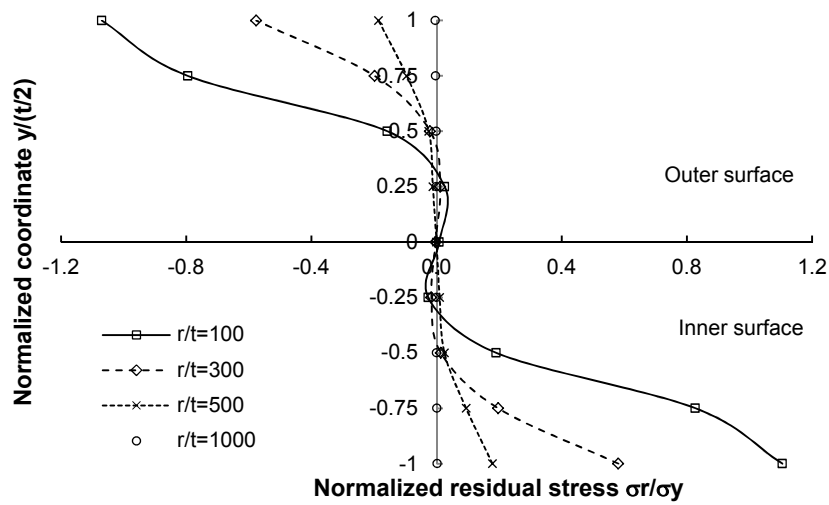


(a) Longitudinal residual stress
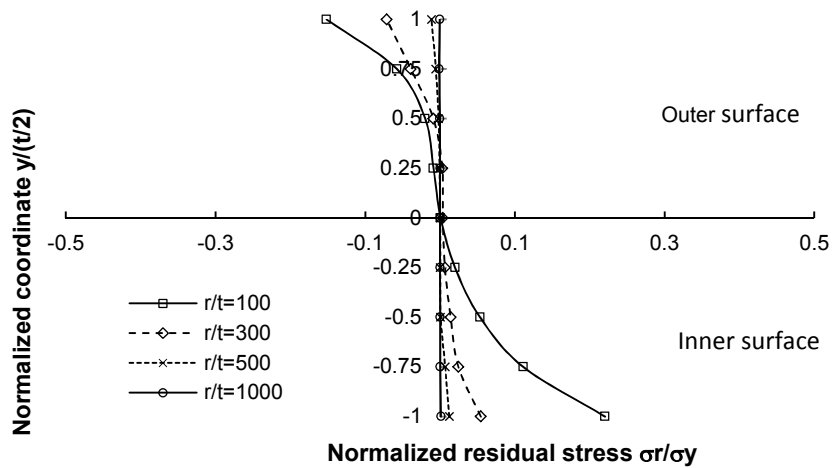


(b) Transverse residual stress

**Figure 3-11: Comparison of models with different roll radiis**

The following conclusions can be drawn from the parametric study:

(1) As shown in Fig. 3-9, the residual stress in both directions reduces when the yield strength increases from 250MPa to 450MPa. The final longitudinal residual stress at the inside surface decreases 2.6% from 250MPa ($1.15\sigma_y$) to 350MPa ($1.12\sigma_y$) and 0.9% from 350MPa ($1.12\sigma_y$) to 450MPa ($1.11\sigma_y$). In the transverse direction, the residual stress is $0.50\sigma_y$, $0.36\sigma_y$ and $0.22\sigma_y$ for the model in 250MPa, 350MPa and 450MPa, respectively.

(2) It can be found form Fig. 3-10 that the residual stress in both directions increases with increasing thickness. The longitudinal residual stress on inside surface is $1.03\sigma_y$ (t=1.0mm), $1.11\sigma_y$ (t=1.2mm) and $1.14\sigma_y$ (t=1.8mm), with the growth being 7.8% and 2.7%, respectively.

(3) In Fig. 3-11, it exhibits that the final longitudinal residual stress reduces 48%, 69% and 94% as the roll radius to sheet thickness ratio raises from 100 to 300, 300 to 500 and 500 to 1000, respectively. As the radio approach to 1000 the residual stress in both directions close to zero, which means that no plastic deformation occurs under such condition.

(4) According to the parametric studies, it shows that effect of roll radius is the dominant factor to the coiling-uncoiling residual stress, followed by the effect of sheet thickness, and the change of yield strength has the least impact on the final residual stress.

## 3.6 Residual stress in press braking sigma section

In the following section, the FE simulation is proposed to obtain the magnitude and distribution of residual stress in the press-braked sigma section. Prior to that, a comparison of longitudinal strain on channel section between numerical and experimental results is conducted to validate the numerical method. The coiling-uncoiling induced residual stress is ignored herein as the roll radius is assumed to be sufficiently large.

### 3.6.1 Modelling of channel section

For verifying the FE simulation method, a numerical model of channel section P16 was established and compared with experimental data measured by Wend and Peköz (1990). The geometric dimensions of the specimen are demonstrated in Fig. 3-12a. In the test, the specimen P16 was saw-cut from the column with press-braked channel sections, with the yield strength of 221MPa and the ultimate strength of 311MPa. The electric discharge machining (EDM) method was adopted to measure the press-braked strain on the inner and outer surfaces of the specimen along the longitudinal direction. The arrangement of each strain gauge is illustrated in Fig. 3-12b. The corresponding parameters were kept the same in the numerical model for validation purpose.
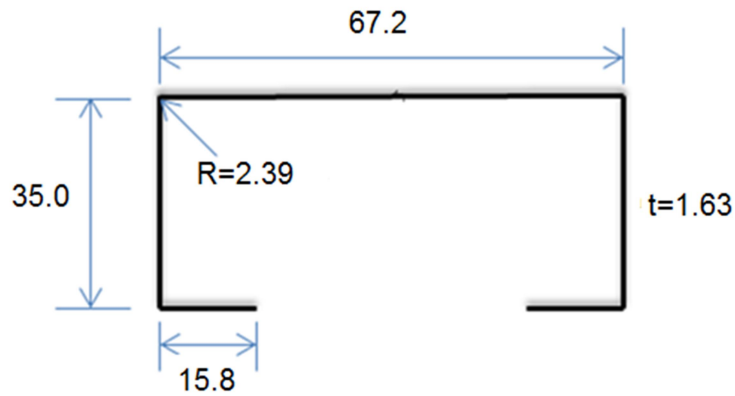
(a) The cross-sectional geometric dimensions of P16 (unit: mm)
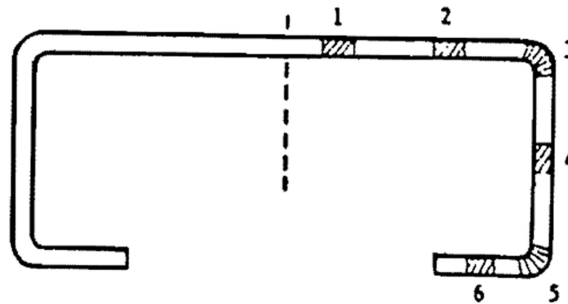


(b) The location of strain gauges of P16

**Figure 3-12: Cross-sectional geometric dimensions and the location of strain gauges of the specimen P16 (Wend and Peköz, 1990)**

As shown in Fig. 3-13, the press braking simulation of the channel section includes two steps: the first step is to bend flange to lip corner, and the step-2 is used for bending web to flange corner. Each step was established with three parts: sheet, top punch and bottom die. For reducing the effects of spring back, $2^0$ over-bend was considered on the flange of punch and die at the second step.
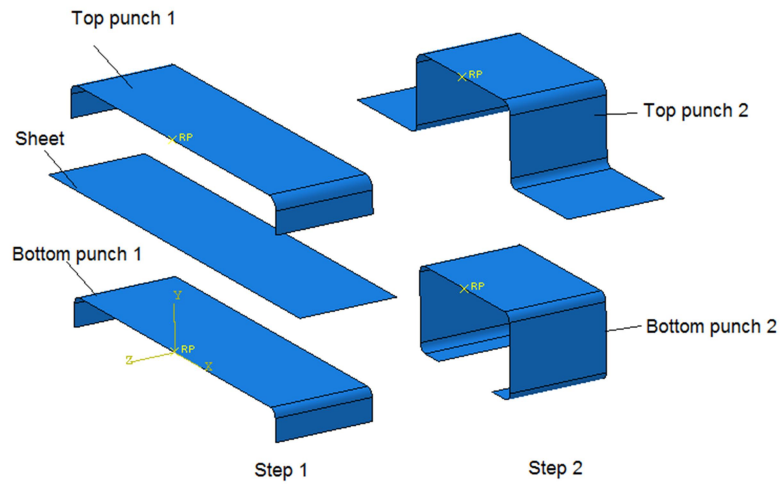
**Figure 3-13: Press braking model for channel section**

The element types used in the model were the same to the coiling-uncoiling model, with shell element S4R for the sheet and rigid element R3D4 for the punch and die. The mesh size of the sheet was 2mm, and mesh size of the punch and die was 5mm with finer mesh (3mm) on the corner. It needs to be noticed that the mesh density of the shell element should always be greater than the rigid element to prevent the penetration between surfaces. The meshed press braking model is shown in Fig. 3-14.
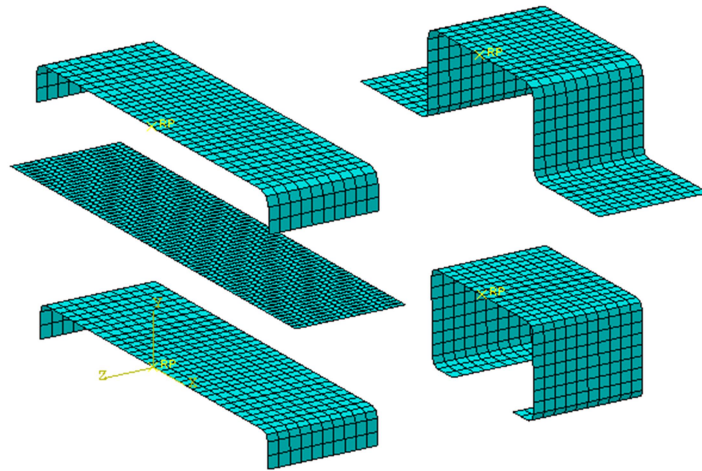
**Figure 3-14: Meshed press braking model**

An explicit analysis was conducted in the analysis for simulating the dynamic press braking operation. The hard contact was adopted as the normal interaction between tools and sheet to control the overclosure. There was no friction applied in the tangential direction on the interacted surfaces as it may cause extra surface stresses and strains.

The boundary conditions applied to the model are introduced in the following. At the first step, the top punch was restrained to prevent any other movements but the downward pressing. In the meanwhile, the bottom die was fixed in all directions, and the sheet was free to move. During the step, the flat sheet was pushed by the top punch to meet the shape of the lower counterpart, and the clearance between the punch and die was set as the thickness of the sheet. After this step, a horizontal displacement was applied to the sheet to position for the second step, and the same boundary conditions were then applied to the tools in the second step.

The comparison of normalized strain in the longitudinal direction between experimental and numerical results is demonstrated in Fig. 3-15. In the graph, the FEM represents the results from the numerical model and P16 is the test value achieved by Wend and Peköz (1990) for specimen P16.
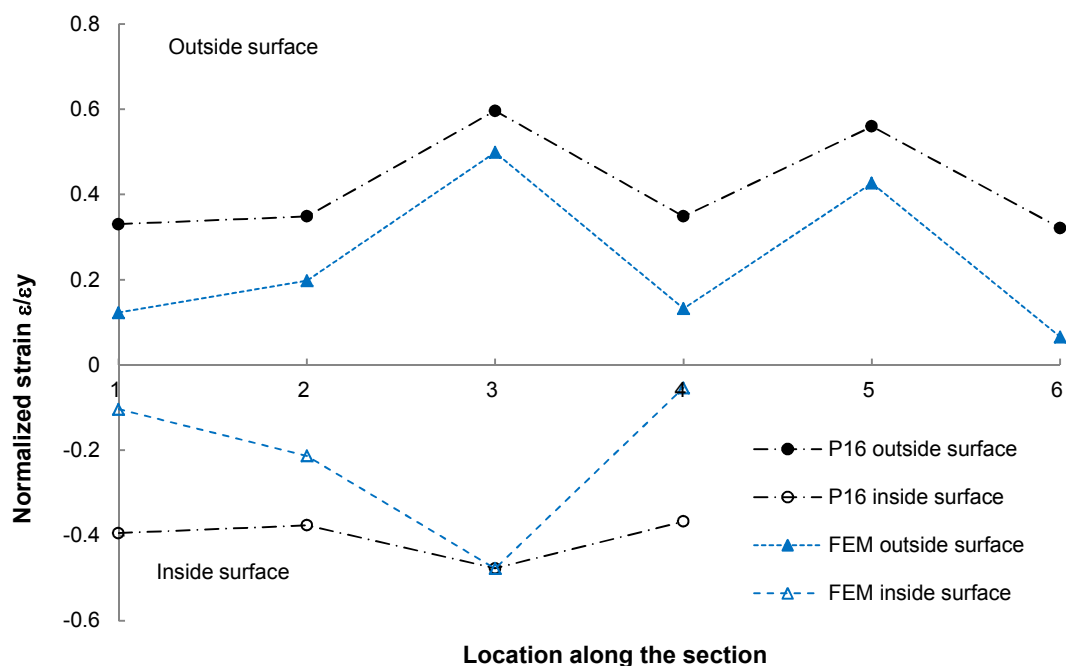


**Figure 3-15: Comparison of the longitudinal strain**

From Fig. 3-15, it shows a good agreement at the corner portion (see point 3 and point 5) between FEM and test results. The cross-sectional distributed longitudinal strain from numerical model is found symmetrical with respect to the neutral axis of the shell-thickness, and it is obvious that the longitudinal strain on the corner region is greater than that on the flat region. The longitudinal strains are in tension on the outside surface, with the numerical and experimental results at corner point 3 and 5

are $0.50\varepsilon_y$, $0.43\varepsilon_y$ and $0.59\varepsilon_y$, $0.55\varepsilon_y$, respectively. The FEM achieved values of longitudinal strain at flat point 1, 2, 4 and 6 are $0.12\varepsilon_y$, $0.20\varepsilon_y$, $0.13\varepsilon_y$ and $0.07\varepsilon_y$, respectively, which is lower than laboratory measurement ($0.33\varepsilon_y$, $0.35\varepsilon_y$, $0.36\varepsilon_y$ and $0.32\varepsilon_y$, respectively). The numerical longitudinal strain on flat portion is less than test results because the residual strain on flat portion was mainly induced from coiling-uncoiling process, but the effect of coiling-uncoiling was ignored in the press braking modelling process.

### 3.6.2 Modelling of sigma section

The same modelling method is further used for simulating the press braking process of sigma section. The geometric dimensions of the target profile are illustrated in Fig. 3-16, with the depth of the section is 200mm and the thickness is 1.6mm. The press braking model for sigma section is shown in Fig. 3-17.
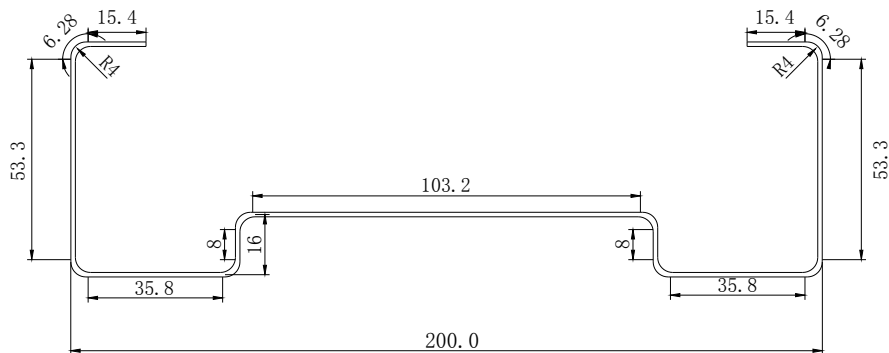


**Figure 3-16: Geometric dimensions of sigma section (unit: mm)**
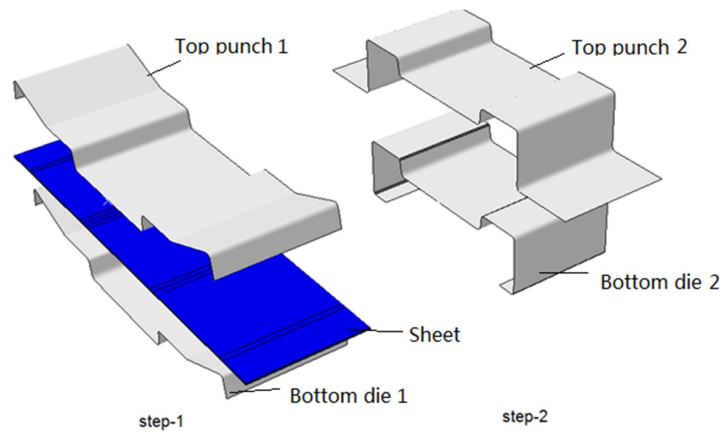
**Figure 3-17: Press braking model for sigma section**

As shown in Fig. 3-17, the press braking simulation for sigma section also designed in two steps: the first step is to bend innerweb to outerweb corner and flange to lip corner, and step-2 is used for bending outerweb to flange corner.

The mesh pattern and boundary conditions used in this model were the same to the channel section model. An explicit analysis was also conducted for simulating the press braking operation of sigma section. The stress-strain curve used in the model was obtained by tensile test introduced in Appendix 2 (Fig. 3-18), with the Young's module of 206GPa, and Poisson ratio of 0.3. It was assumed that the shell thickness remains the same during the press braking process, and the effect of material anisotropy was insignificant.
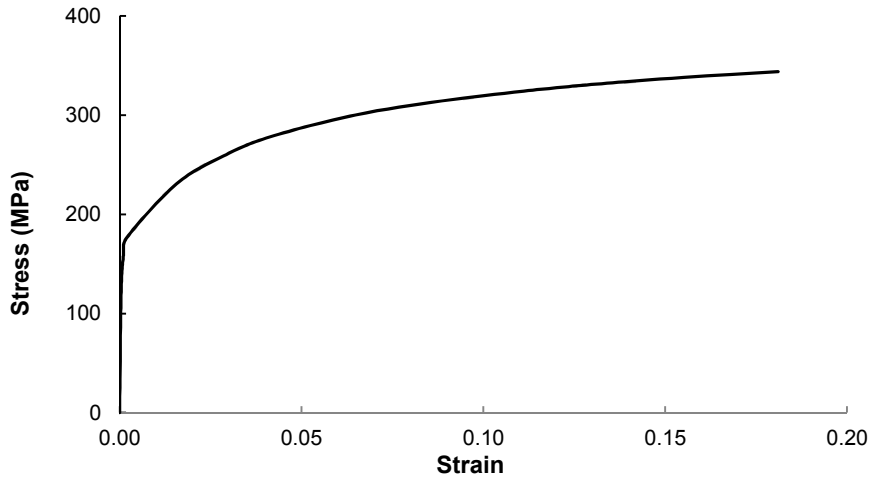
**Figure 3-18: Stress-strain curve applied in the model**

### 3.6.3 Result discussions

The distribution of stress and strain after press braking process is presented herein. The stress result follows the sign convention that positive for tension and negative for compression. It assumes that the transverse direction is the direction along the cross-sectional. The contour plot of transverse residual stress after press braking process is shown in Fig. 3-19.
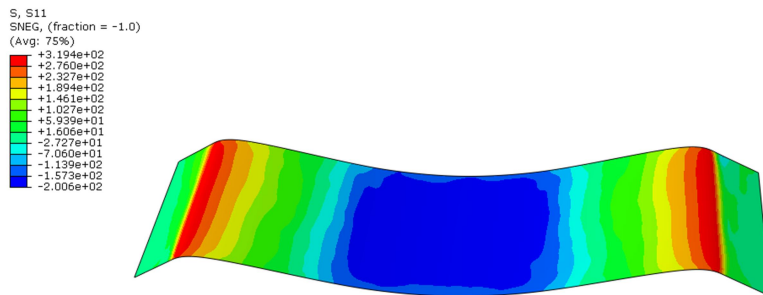


(a) Stress contour at step 1
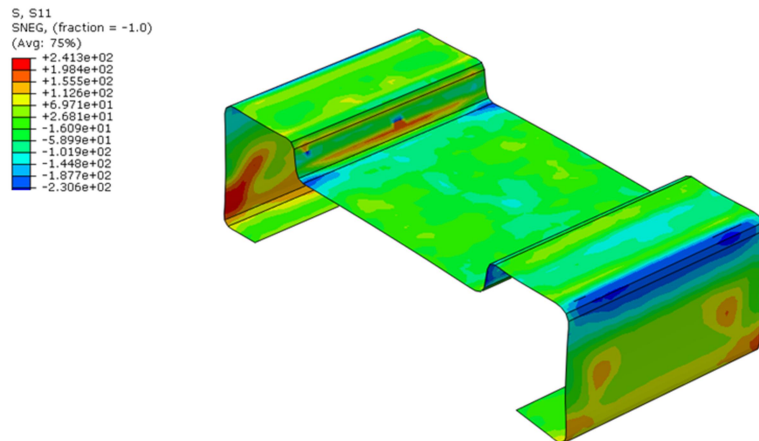
(b) Stress contour at step 2

**Figure 3-19: Transverse residual stress contour**

According to the figure, it can be seen that at the first step, the maximum transverse stress (319MPa) is located on the flange to lip corner as the bending mainly occurs in this area. Then, after the press braking at step 2, the maximum compressive stress (-231MPa) happens on outerweb to flange corner, and the residual stress on the flat portions is relatively small.

In Weng and Peköz's (1990) test, the distribution of residual stress along shell thickness was not measured as the limitation of laboratory devices. However, the through-thickness variation of residual stress can be easily achieved by using numerical method. In Fig. 3-20, the distribution of longitudinal and transverse residual stresses along thickness in the corner and flat portion are presented.
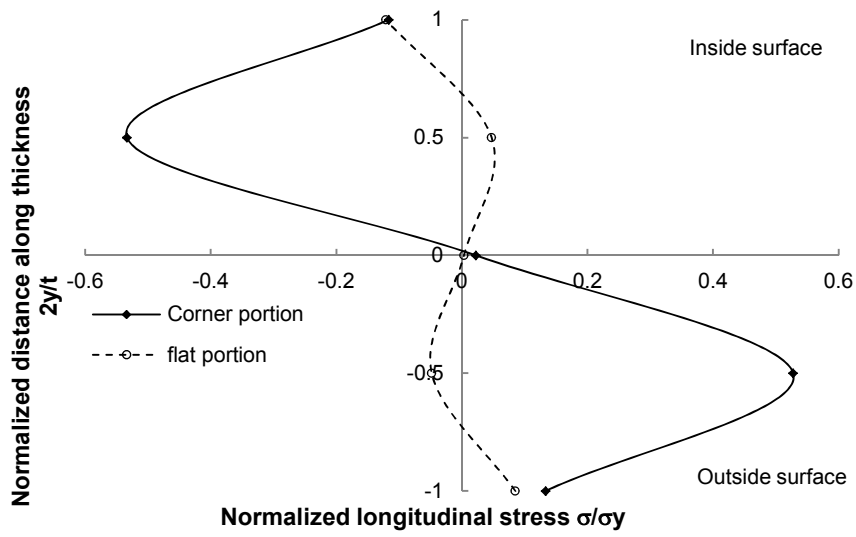
(a) In longitudinal direction
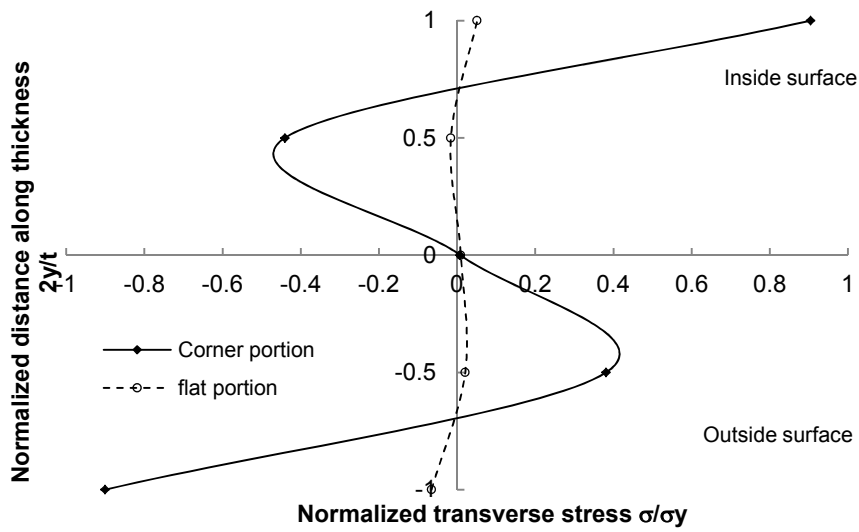


(b) In transverse direction

**Figure 3-20: Residual stress along thickness**

It can be seen from Fig. 3-20 that the residual stress distribution in both directions is non-linear along shell thickness and asymmetric to the neutral axis. For the corner portion, the maximum longitudinal residual stress is $0.6\sigma_y$, and the max value located

on the ¼ thickness; the peak transverse residual stress is $-0.9\sigma_y$ occurs on the surface. For the flat region, the discrepancy of residual stress in two directions is insignificant while the longitudinal stress is in tension ($0.1\sigma_y$) and the transverse residual stress is in compression ($-0.1\sigma_y$). The transverse residual stress on the corner portion is found greater than that in the flat portion while the gap is quite limited for longitudinal residual stress. From the figure, it also reveals that the measurement of the surface residual stresses in the laboratory may underestimate the magnitude of the residual stress.

In order to further investigate the sensibility of the numerical model to input parameters, a series of parametric studies are also conducted herein.

**(1) Effect of yield strength**

The press braking models with three different yield strengths: 235MPa, 345MPa and 450MPa, respectively, are compared. The comparisons of residual stress in two directions on the corner are shown in Fig. 3-21.
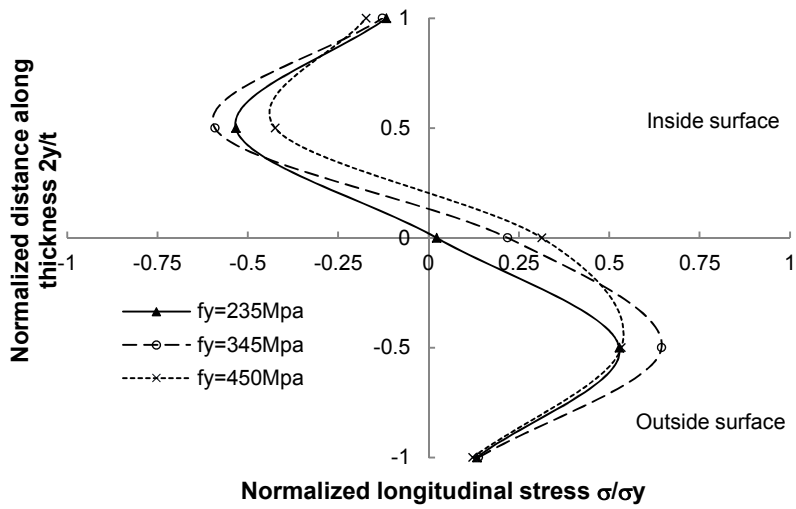
(a) Longitudinal residual stress on corner portion
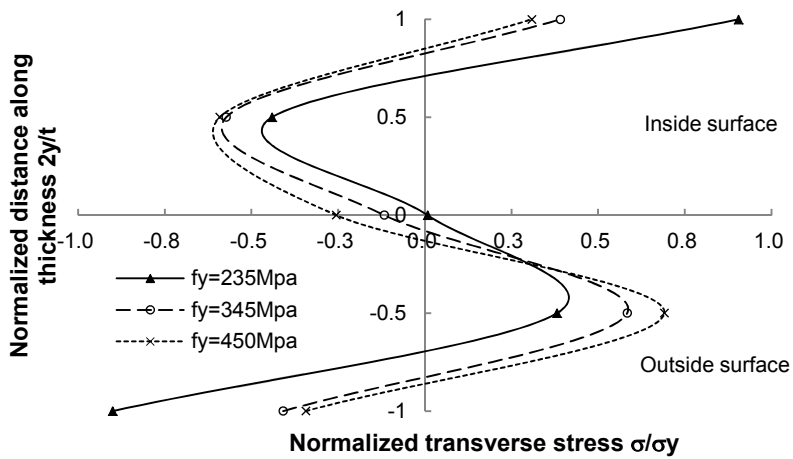


(b) Transverse residual stress on corner portion

**Figure 3-21: Stress results with different yield strengths**

## (2) Effect of sheet thickness

Fig. 3-22 shows the comparisons of press braking residual stress with different sheet thicknesses from 1.6mm, 2.5mm to 3.0mm.
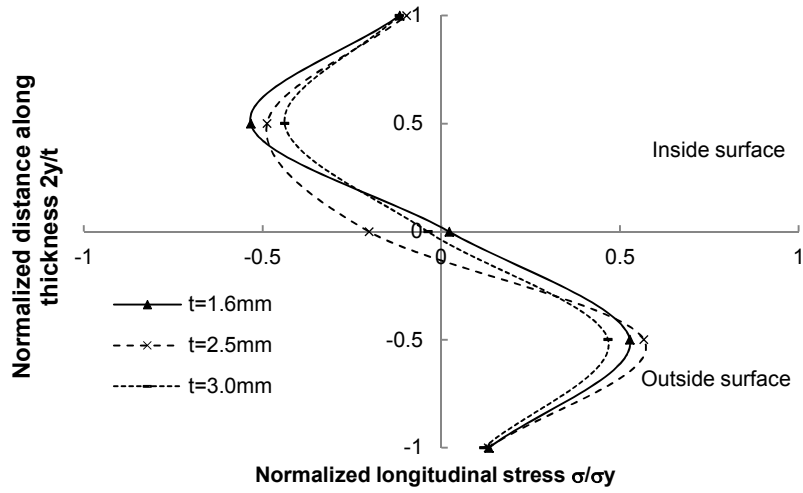
(a) Longitudinal residual stress on corner portion
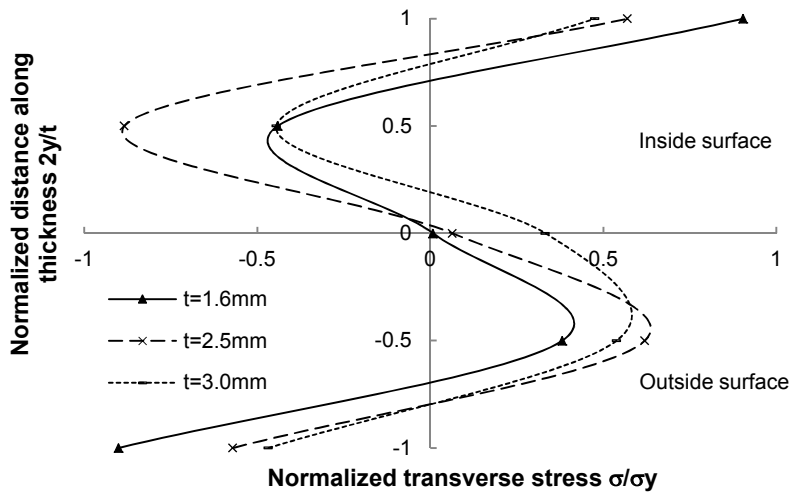


(b) Transverse residual stress on corner portion

**Figure 3-22: Residual stress along thickness**

According to Fig. 3-21, for the corner portion, the effect of yield strength on residual

stress in the longitudinal direction is insignificant; the transverse residual stress on the

inside surface are $0.9\sigma_y$, $0.4\sigma_y$ and $0.3\sigma_y$ for the yield strength 235MPa, 345MPa and

450MPa, respectively, and this reduces by 56% and 25% with increasing yield strength.

From Fig. 3-22, it shows that the effect of thickness on longitudinal residual stress on the surface of the corner portion is also insignificant. The transverse residual stress on the corner portion reduces as the increase of shell thickness, the values for thicknesses of 1.6mm, 2.5mm and 3.0mm are $-0.90\sigma_y$, $-0.6\sigma_y$ and $-0.5\sigma_y$, respectively, which lead to a reduction by 33% and 17%, respectively.

### 3.7 Summary

In this chapter, FE simulations of coiling-uncoiling and press braking induced residual stress have been performed. The following observations can be made based on the previous findings and discussions:

1. The distribution of coiling and uncoiling residual stress is nonlinear along the shell thickness, and the curves are not symmetrical about the neutral axis in both directions.

2. After the coiling process, the tensile stress is found on the outside surface and compression on the inside surface. The longitudinal residual stress is greater than the stress in the transverse direction. At the final stage of the uncoiling process, the longitudinal residual stress acts as the dominant stress when compared with the transverse stress. The outside surface of the sheet is subjected to tension during the coiling process but turns to compression after uncoiling, which proves the coiling-

uncoiling process is similar to a loading-unloading operation. A good agreement can be found between FEM results and analytical values.

3. The coiling-uncoiling residual stress in both directions decreases as the yield strength increases from 250MPa to 450MPa and as the thickness increases from 1.0mm to 1.8mm. The increasing of the roll radius will decrease the coiling-uncoiling residual stress in both directions. As the roll radius to sheet thickness radio approaches to 1000 the residual stress in both directions close to zero, which means that no plastic deformation occurs under such a condition.

4. The effect of rolling radius is found to be the dominant factor in the coiling-uncoiling residual stress, followed by the effect of sheet thickness, and the change of yield strength has the least impact on the final residual stress.

5. In the press braking process, the residual stress along the thickness is non-linear along the shell thickness and asymmetric to the neutral axis. For the corner portion, the maximum longitudinal residual stress occurs at 1/4 thickness position while the peak transverse residual stress occurs on the surface. For the flat region, the discrepancy of residual stress in two directions is insignificant. The transverse residual stress on the corner portion is found greater than that in flat portion while the gap is quite limited for longitudinal residual stress.

6. The effect of yield strength on residual stress in the longitudinal direction is insignificant, the transverse residual stress on the inside surface decreases with increasing yield strength. The effect of thickness on longitudinal residual stress on the surface of the corner portion is also insignificant while the transverse residual stress on the corner portion reduces as the increase of shell thickness.

# 4. NUMERICAL PREDICTION OF ROLL FORMING RESIDUAL STRESS

## 4.1 Introduction

Roll forming and press braking are two common approaches in the cold forming manufacturing process. Press braking process is a semi-manually operation requires only limited set of punches and dies for shaping simple profiles but with limited production capacity. Meanwhile, roll forming is a more advanced mass-production process used to fold the complex sections with a continuous roll set system. The roll forming system can work as an integral machine for manufacturing and each roll set functions individually as a guide or bending tool.

In the roll forming process, as the metal sheet is fed into the machine, each set of roll bends the sheet a little more than the previous one until the final profile is achieved, and the sheet will experience a repeated loading and unloading process. The transverse bending residual stress and longitudinal membrane residual stress will hence be induced by the plastic deformation when the sheet is loaded beyond the elastic limit. The existence of residual stress will be superimposed onto the external loadings to affect the stiffness and load resistance capacity of the steel structures.

Most of the conventional studies in residual stress were based on analytical solutions. Generally, analytical approaches are helpful for the simplified mechanical model, e.g. one-step pure bending model, but could be rather complex and ineffective when

comes to multi-steps roll forming process with nonlinear material properties. Hence, experimental methods were proposed as a supplement to theoretical analysis. The residual stress measurement techniques can be divided into three categories: destructive method, semi-destructive method and non-destructive method. All methods are considered to be cost-consuming and with limitations. In order to achieve a higher design efficiency and tighter tolerance, the numerical simulation is, currently, widely used for optimising the roll forming process and investigating roll forming induced residual stress.

In this chapter, a 3D model was developed by using the explicit dynamic analysis to explore the roll forming residual stress in sigma section. Modelling details including the setup of roll stations, material properties of sheet, element types, mesh size, boundary conditions and interactions, are introduced. The distribution of residual stress during and after the roll forming process is also discussed. The X-ray diffraction test is further conducted to validate the FEM method.

## 4.2 Modelling process

Cold roll forming is a complicated production process involving elastic-plastic deformation of metal sheet and the interaction between sheet and rolls. During the process, the metal sheet experiences a series of dynamic actions imparted from each roll set so that once it comes off the last roll a desired cross section will be formed. In this study, explicit analysis with 3D FE model (see Fig. 4-1) was employed to simulate the manufacturing process of the sigma section. There were two main parts

in the model: sheet and roll sets, the former was initially flat and then formed to a desired profile, whereas the latter was a governing factor to a successful numerical modelling. The numerical model was established based on the following assumptions:

1) It assumes there is no deformation happens on roll sets during the forming process as the materials of the roll was much stiffener than that of the sheet.

2) The shell thickness was assumed to remain the same during the roll forming process.

3) The effect of material anisotropy was ignored, and the material was assumed to follow the von Mises yielding criterion.

4) The radius of the roll during the coiling-uncoiling process was assumed sufficiently large and the residual stress induced before roll forming can be neglected.
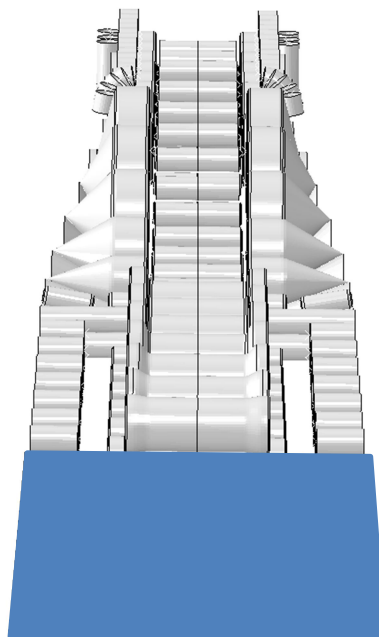


**Figure 4-1: Overall view of the entire model**

## 4.2.1 Geometric parameters

Roll forming process usually consists of multi-step roll sets and the design of each roll set is a deciding factor to the final profile. When the sheet is fed into roll sets continuously from a coil, it will pass those rolls at a constant speed. Each set of rolls brings the section progressively closer to its final shape. The distance between the top and bottom roll is in accordance to the thickness of the sheet. The number of forming steps depends not only on the geometric dimensions but also on the material properties and desired dimensional precision of the profile. The symmetrical model is shown in Fig. 4-2. Since the computing process in ABAQUS could be time-consuming, only half of the model was established in order to reduce the computation time. The forming process works as following: the rolls rotate with a constant velocity while the metal sheet is moved with an initial loading. When the front edge of the sheet enters the gap of the first roll set, the top and bottom roll will meet the sheet and the contact function is turned on. The sheet is then driven by the friction and bent into the plastic phase to fit the shape of rolls. As soon as the sheet leaves the first set of rolls, the contact function will be turned off and the sheet will encounter with the second set of rolls and repeat the forming process.
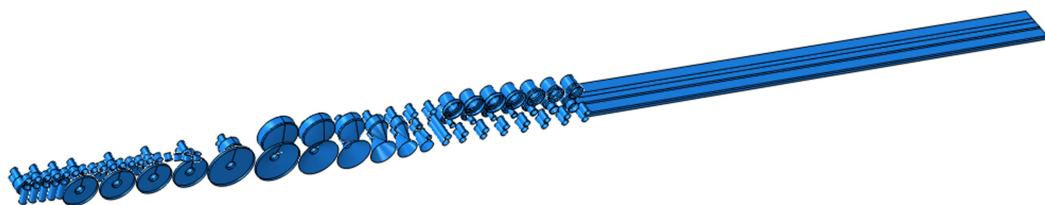


**Figure 4-2: Numerical model**

Sigma section 20012 was taken as a target profile to demonstrate the roll forming process, the symbol of the section is represented by the depth of the section of 200mm and the thickness of 1.2mm. The geometric dimensions of the section are depicted in Fig. 4-3.
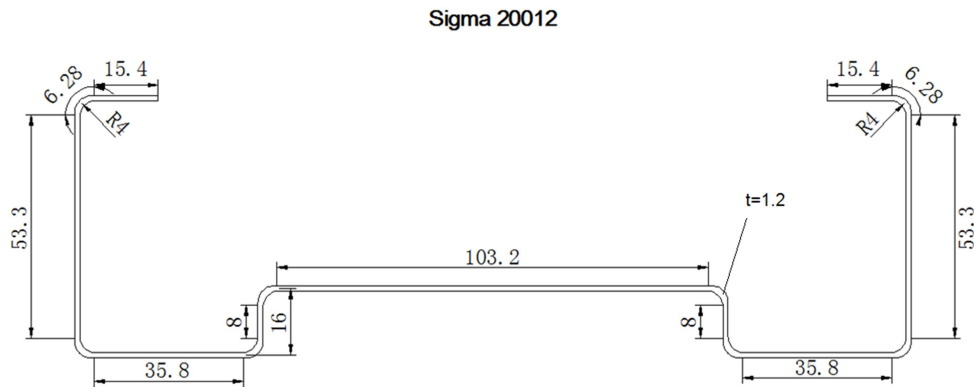


**Figure 4-3: Dimensions of sigma section 20012 (unit: mm)**

The design of roll forming system starts from roll flower and roll sequence; the former is used to decide the increment angle and the latter is used for achieving rolling distance. The program COPRA (2012) was used to generate the roll flowers of the sigma section. COPRA allows the user to design simple profiles as well as highly complex open or closed sections in a professional way. It is cost-effective for planning, designing and controlling of the whole process chain from the flower design to quality control. Roll flower of the sigma section is demonstrated in Fig. 4-4. The roll flower diagram was drawn as a sequence of one roll bending step superimposed on others.
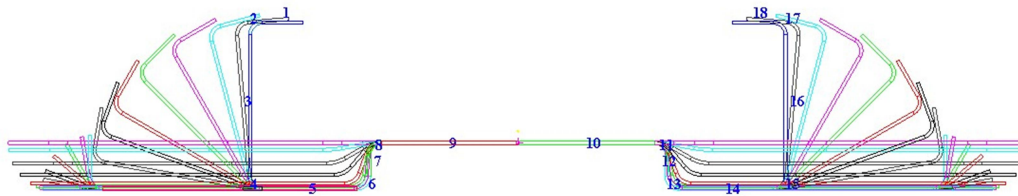
**Figure 4-4: Roll flowers diagram for sigma section**

According to the roll flowers diagram, the sigma section 20012 was divided into 18 parts. There are three main bending regions for the section: the inset (plate No. 7 and 12), the flange (plate No. 3 and 16) and the lip (plate No. 1 and 18). The bending of inset has seven steps with angles from 10°, 30°, 45°, 65°, 75°, 80° and 90°, respectively. Eight steps are utilized to bend the flange, and the angles for each step is from 10°, 20 °, 30 °, 45 °, 60°, 70 °, 80 ° to 90°. The lip of sigma section is formed by six forming steps with bending angles of 15°, 30°, 45°, 60°, 75° and 90°, respectively.

Based on the roll flowers, 22 roll sets were required for the roll forming of the sigma sections (see Fig. 4-5). In Fig. 4-5a, it provides an illustration of the arrangement of roll sets (RS) which are numbered from RS1 to RS22 from the right-hand side to the left. Each forming set consists of four to five rolls and only half of the model is established due to symmetry. There are three stages in the system: the first stage (RS 1 to RS 7) is for the forming of inset (innerweb to outerweb corner); the second stage from RS 8 to RS15 is used to bend outerweb to flange junction and rest roll stands are final stage for forming lip. The roll sets include two main categories: guide roll and forming roll, the guide roll is used to ensure the successively of the forming process

(as right part in Fig. 4-5b and left part in 4-5c, d) and the forming roll undertakes the section forming task (see left part in Fig. 4-5b and right part in 4-5c, d).
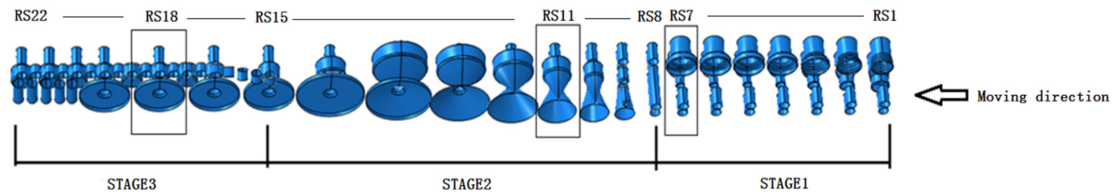


(a) Overall roll system
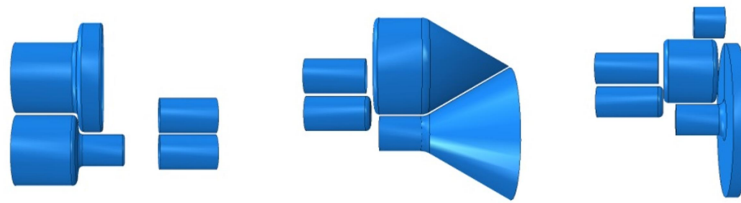


(b) RS-7          (c) RS-11          (d) RS-18

**Figure 4-5: Roll set sequences and typical roll sets**

The dimension of the flat sheet for sigma 20012 was 190x2500x1.2mm (width × length × thickness). The length of the sheet was chosen to ensure the continuous forming process i.e. the end of sheet is still in contact with the first roll set while the front edge of the sheet just coming out of the last roll stand, (see Fig. 4-6).
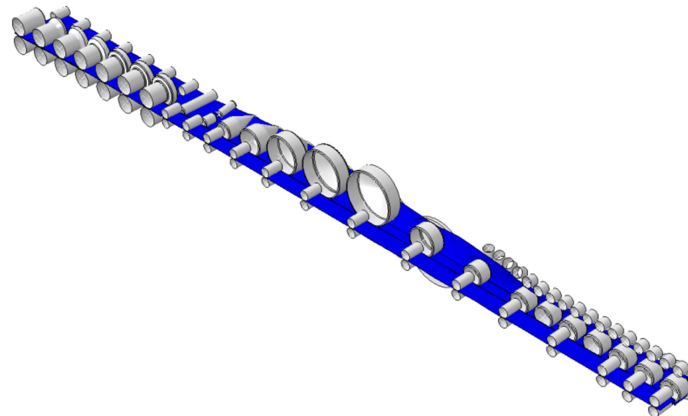


**Figure 4-6: Sheet to rolls contact**

## 4.2.2 Material and geometric parameters

For achieving a better accuracy, the material nonlinearity and isotropic hardening rule of the sheet were considered in the model. The young's module of the sheet was 207GPa, and Poisson's ratio was 0.3, and 0.2% proof stress 450Mpa was taken as norminal yield strength. The stress-strain curve shown in Fig. 4-7 is according to the tensile test result presented by Liu et al. (2011b).
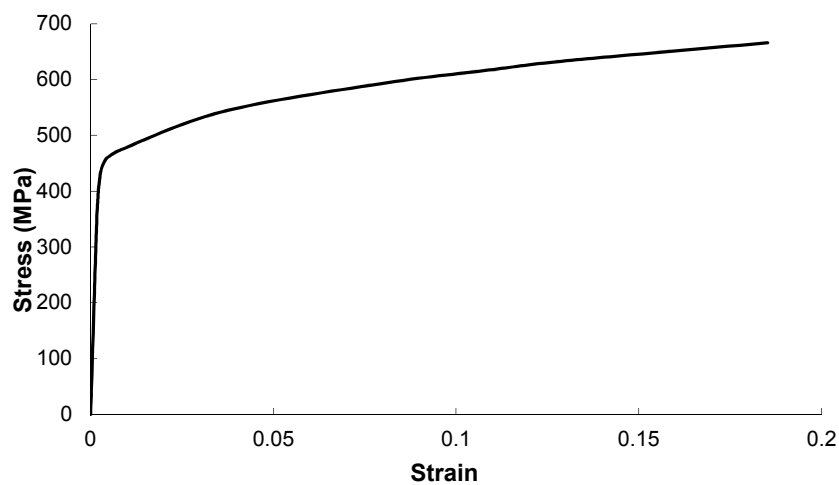


Figure 4-7: Stress-strain curves for steel sheet

## 4.2.3 Mesh convergence study

In the model, rolls were meshed by R3D4 rigid element and sheet by S4R shell element. Nine integration points were applied to the shell element to investigate the residual stress distribution along the thickness.

Since the mesh size may have a significant impact on the roll forming residual stress and reduce the size will decrease the computation times but may lead to an inaccuracy

result. Five different mesh sizes are compared in Table 4-1 to investigate the meshing sensitivity of the model. Note that the mesh size of the sheet should be always less than rolls to prevent penetration between surfaces, and a finer mesh pattern is assigned to the corner portions of the sheet as indicated in the bracket in Table 4-1.

**Table 4-1: Mesh sensitivity study**

| Mesh No. | Mesh size for sheet (mm) | Mesh size for rolls (mm) | Total number of elements | CPU time (h) | Maximum transverse stress S11 (MPa) | Relative difference (%) |
|---|---|---|---|---|---|---|
| 1 | 4 (3) | 6 | 112510 | 25.9 | 274.2 | 3.69% |
| 2 | 3 (2) | 4 | 162314 | 40.2 | 280.1 | 1.62% |
| 3(selected) | 2 (1.5) | 3 | 236906 | 44.6 | 284.5 | 0.07% |
| 4 | 1.5 (1.0) | 1.5 | 365418 | 65.5 | 285.1 | -0.14% |
| 5 | 1 (0.8) | 1 | 448326 | 74.8 | 284.7 | 0.00% |

The comparison in the table indicates that the minimum differences (0.07%) of residual stress can be found between mesh 3 and mesh 5. In considering the CPU times and accuracy of residual stresses, Mesh 3 with the element size $2 \times 3 \times 1.5$mm was chosen for the model. The meshed model was shown in Fig. 4-8 with a total element number of 236906 and the running time of one analysis is about 45 hours.
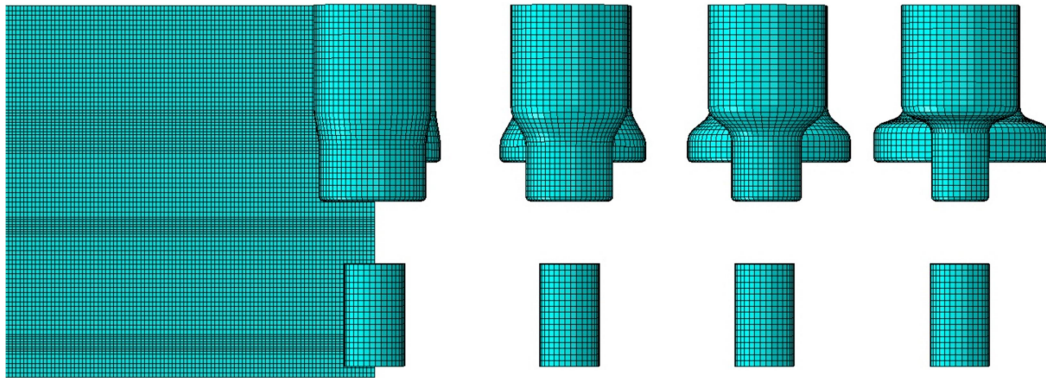
**Figure 4-8: Mesh details**

### 4.2.4 Interactions and boundary conditions

In the model, the hard contact was applied as a surface to surface interaction in the normal direction to determine the successive contact- separate-contact process between sheet and rolls, and the penalty friction was used to simulate the contact in the tangential direction.

For the sheet, boundary conditions were applied along the plane of symmetry to prevent the edge waving effect. The movement of the sheet was firstly motivated by an initial velocity and then driven by friction between sheets and rolls. Rolls were restrained for all movements, except the authorized rotation in accordance with the moving direction of the sheet. The summary of the input parameters is listed in Table 4-2.

**Table 4-2: Summary of input parameters**

| | |
|---|---|
| Sheet thickness | 1.2mm |
| Distance of roll sets | 0.1m |
| Sheet length | 2.5m |
| Sheet width | 190mm |
| Sheet element type | S4R |
| Roll element type | R3D4 |
| Rotate velocity | $\pm$ 20rad/s |
| Friction coefficient | 0.05 |
| Young's modulus | 207GPa |
| Poisson's ratio | 0.3 |
| Norminal yield strength | 450MPa |

## 4.3 Numerical results

In this part, the development of stress and strain during the forming process is presented, and the distribution of final residual stress is predicted. It is worth noting that the longitudinal direction mentioned herein refers to the direction along the length of sheet and transverse direction is along the width of the sheet.

### 4.3.1 Strain development

The sheet has two regions during the roll forming process: non-contacted region and contacted region. The distance between contacted regions is named as the deformation length. When the sheet comes into the gap of the first roll set, it experiences both horizontal friction force and lateral bending moment. The sheet moves forward with

the surface kept attaching to the rotating top and bottom rolls due to friction on contact surfaces. During this process, the deformation of the sheet is elastic-to-plastic and will lead to a sudden increasing of strain. The strain is mainly concentrated on the bending line and the value increases as the enhancement of the bending angle. Fig. 4-9 demonstrates the equivalent plastic strain contour of the sheet during the first stage (see RS 1-7 in Fig. 4-5).



a)  Before bending                              b) After bending
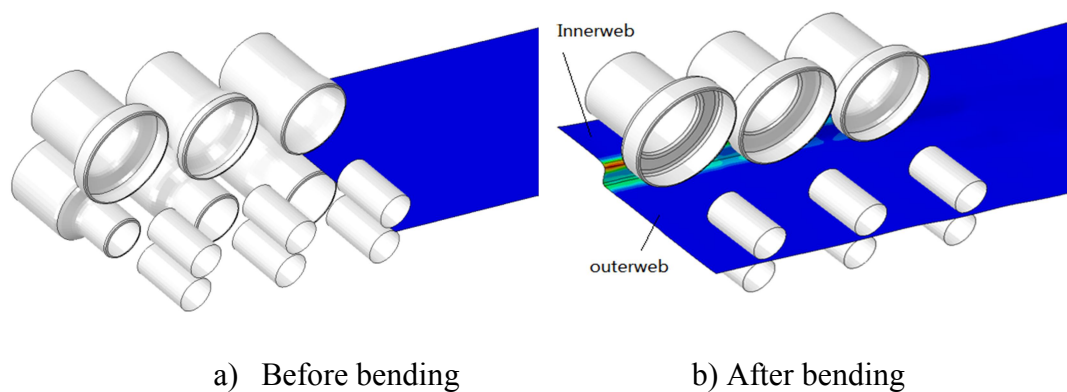
**Figure 4-9: Equivalent plastic strain contour in the first stage**

It can be observed from Fig. 4-9 that the equivalent plastic strain is mainly occurred on the bending zone between innerweb and outerweb; the strain in the rest part is insignificant. The development of the longitudinal strain in the first stage is shown in Fig. 4-10. In the figure, the X-axis represents the number of roll set and the Y-axis is the strain in the longitudinal direction, the strain values are captured from the flat region.
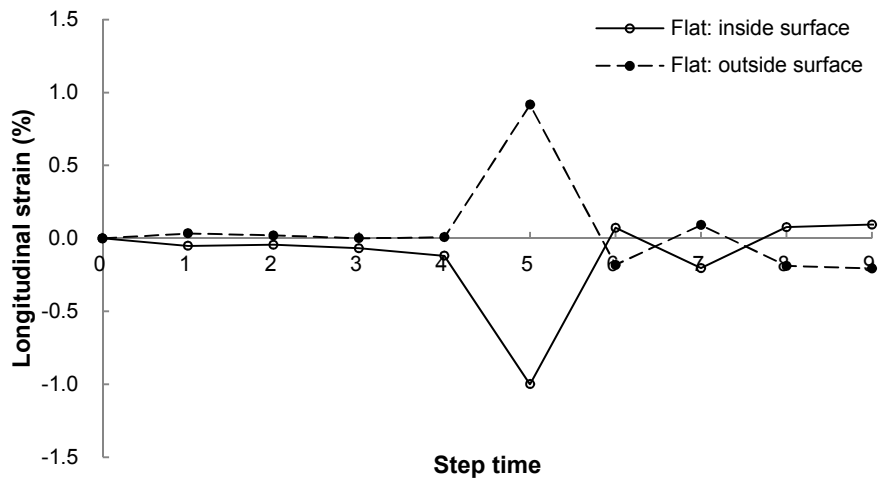
**Figure 4-10: The development of longitudinal strain in the first stage**

According to Fig. 4-10, the longitudinal strain keeps at a low level except a crest is found at $5^{th}$ roll set, which may be due to the effect of friction between surfaces. The maximum strain during the first stage is 0.9% and then steady at 0.1% after RS8. The development of longitudinal strain indicates that the arrangement of roll set in the longitudinal direction is acceptable as the elongation is insignificant on the flat portion during the forming process.

### 4.3.2 Stress development

Fig. 4-11 plots the contour of the transverse stress at the second stage (see RS 8-15 in Fig. 4-5), the roll sets in this stage are used to bend the outerweb to flange corner from $0^{o}$ to $90^{o}$.
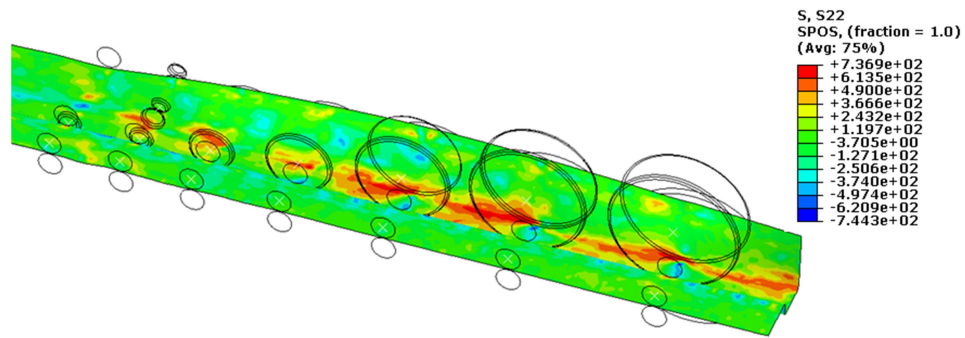
**Figure 4-11: Stress contour in transverse direction**

It can be observed from Fig. 4-11 that during the second stage, the tensile stress is gradually distributed on the outerweb to flange corner, with the maximum transverse residual stress that exists on the main deforming region below the roll gap line. The figure also indicates that the transverse stress region will increase continually as the rise of the bend angle. When the sheet moves away from the last roll station of the second stage, a springback will occur at the corner, and the tensile stress is reduced.

Fig. 4-12 illustrates the development of the stress on the outerweb to flange corner during the entire roll forming process. In the graph, the residual stress is taken as the Y-axis, and the X-axis represents the number of roll set.
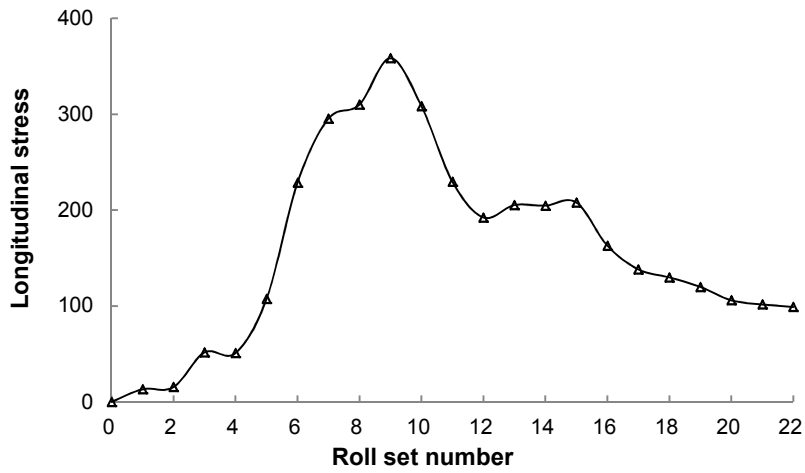
(a) The develpoment of longitudinal stress
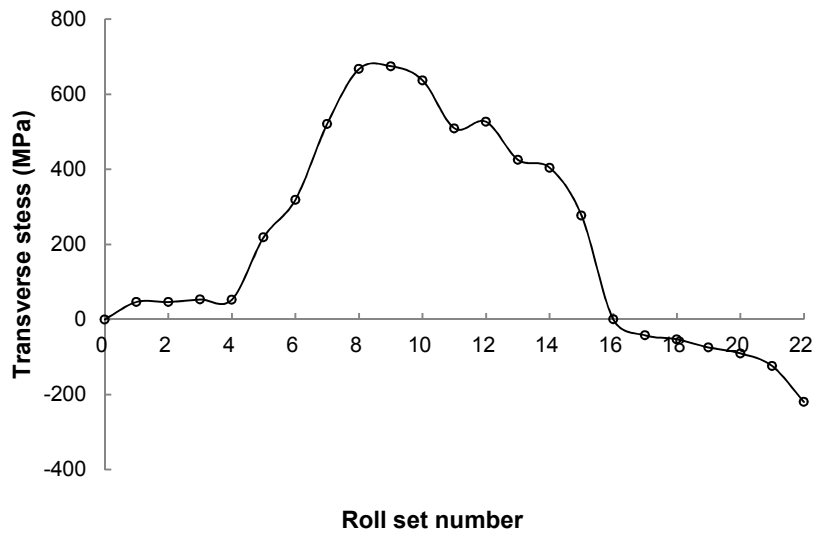


(b) The development of transverse stress

**Figure 4-12: The development of residual stresses on outerweb to flange corner**

From Fig. 4-12, it can be found that in the first stage, both longitudinal and transverse stress on the outerweb to flange corner stays at a low level. When the sheet enters the second stage (RS8), the corner is under bending, and a concentrated tensile stress occurs. The maximum value in the transverse direction is around 700MPa at the 10th

roll set, in the meanwhile, the maximum longitudinal stress is also reached around 350MPa. The stress in both directions then has a decrease when the springback occurs at the final stage. It is interesting to note that the final residual stress in the transverse direction is 280MPa in compression while the longitudinal residual stress is about 100MPa in tension.

### 4.3.3 Springback study

The occurrence of the springback may control the final geometric dimensions of the formed section and affect the distribution of final residual stress. In order to precisely predict the magnitude of springback in the FE model, the geometric dimension of a roll formed sigma section 20012 is measured as the specimen, as shown in Fig. 4-13.



**Figure 4-13: Springback of the specimen**

It can be seen from Fig. 4-13 that the measured distance centreline of flange-to-lip corners is 211mm. As the processing of explicit dynamic analysis needs to be terminated manually, the measured value is then used to control the final step of FEM simulation.

The final deformation contour of the formed sigma section is performed in Fig. 4-14a and the comparison between FEM and standard geometric dimensions of sigma 20012 is displayed in Fig. 4-14b.
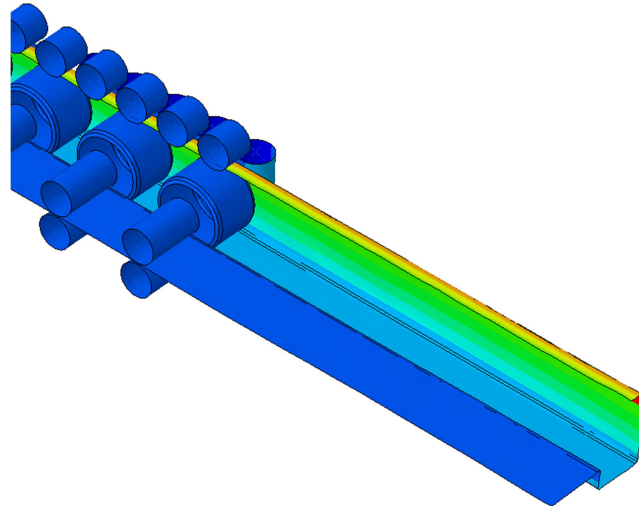


(a) The deformation contour
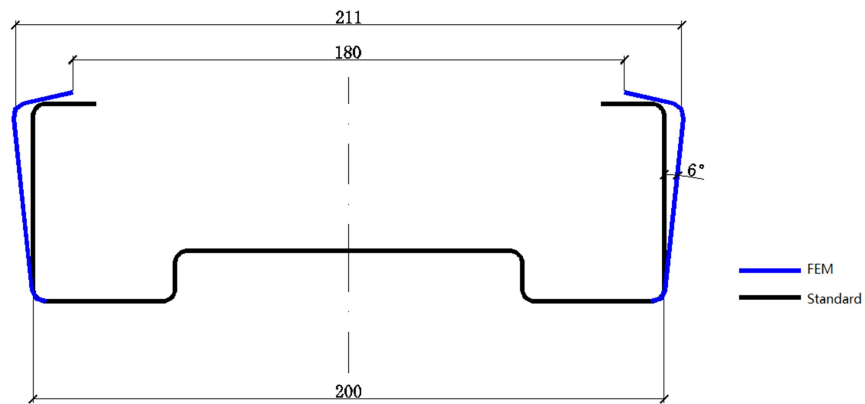


(b) The comparison between FEM and standard profile of 20012 (unit: mm)

**Figure 4-14: The final deformation contour**

Figure 4-14a shows that the maximum springback after roll forming process happens on the outerweb to flange and flange to lip corner. The springback of the innerweb and outerweb is insignificant because the regions are restrained by top and bottom

rolls all the time during the forming. From Fig. 4-14b, it is obvious that the springback of the flange is $6^0$ when the measured dimension is reached. The distribution of the final residual stress after springback is presented in the following section.

### 4.3.4 Distribution of residual stress

Two representative reference points located at outerweb to flange corner portion and mid-outerweb flat portion are chosen to elaborate the distribution of roll forming residual stress, as shown in Fig. 4-15a, b. The X-axis in the figure is the normalized residual stress by nominal yield strength $\sigma_y$, and the Y-axis represents the normalized coordinate of nine integration points along shell thickness.
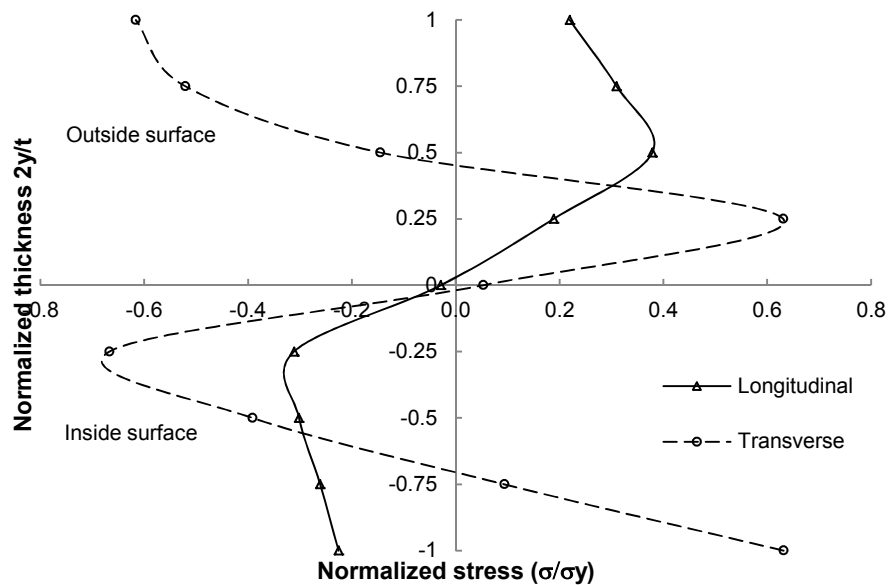


(a) Reference point at outerweb to flange corner portion
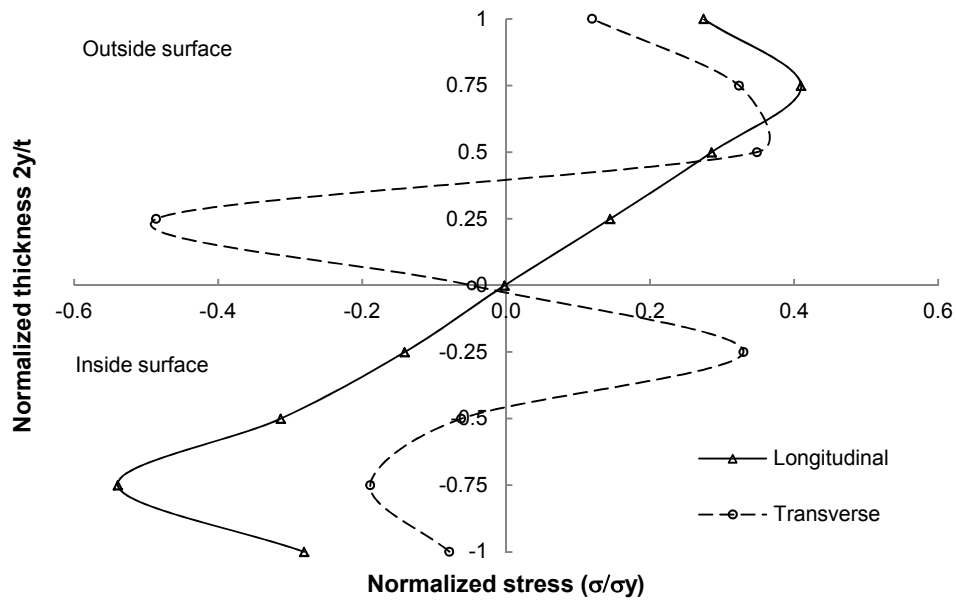
(b) Reference point at mid-outerweb flat portion

**Figure 4-15: Stress against thickness graph**

It can be seen from the figures that the residual stress of two reference points is nonlinear distributed along the thickness and the curves are asymmetrical about the neutral axis. The peak value of transverse residual stress ($0.7\sigma_y$) is higher than longitudinal residual stress ($0.4\sigma_y$) at corner portion as the deformation mainly occurs in the transverse direction. The maximum longitudinal residual stress ($-0.6\sigma_y$) is found to exceed the transverse stress ($-0.5\sigma_y$) at the flat portion and the location of maximum stress along the thickness is located on $\pm0.25$ of normalized thickness. The residual stress of the corner portion on the outside surface is $-0.6\sigma_y$ in transverse and $0.2\sigma_y$ in longitudinal, and the value is $0.1\sigma_y$ and $0.3\sigma_y$ on the flat regions.

## 4.4 Experiment studies

In order to validate the predicted residual stress in FEM, a laboratory measurement is further conducted to quantify the residual stress in roll formed sigma section 20012.

The X-ray method is currently the most frequently used non-destructive measurement method. The technique utilizes the lattice spacing as the strain gauge to measure residual stresses on the surface of crystalline materials such as metallic and ceramic. The advantage of this method is that residual stresses can be measured without destruction of the specimen, and the measurement procedure can be conducted quickly. However, this method is difficult to determine the residual stresses in large member as the geometry dimensions of the specimen have to be such that an X-ray can both hit measurement area and still be diffracted to the detector without hitting any obstructions. The X-ray diffraction method is also used in this paper to measure the residual stresses of cold-formed sigma beams.

The details of the experimental process are presented herein, and the comparisons between numerically achieved and experimentally obtained data are also conducted. The experiment was conducted in the Materials Laboratory of Shanghai Jiaotong University in China.

### 4.4.1 X-ray diffraction measurement

The X-ray diffraction method is by far the most efficient technique for measuring surface residual stress. This method uses the distance between crystallographic planes,

which can be obtained from Eq.4-1 based on Bragg's Law (Bragg 1912), as a strain gauge to measure the residual stress (Eq. 4-2).

$$\lambda = 2d\sin\theta \qquad\qquad \text{(Eq. 4-1)}$$

$$\sigma_\alpha = \frac{E}{(1+\mu)\sin^2\varphi}\left(\frac{d_\varphi - d_n}{d_n}\right) \qquad\qquad \text{(Eq. 4-2)}$$

where

$\lambda$ is the wavelength of X-ray;

d is the distance between crystallographic planes;

$\theta$ is the angle between the crystal surface and incident rays;

$\sigma_\alpha$ is the stress at $\alpha$ angle with the principal stress in the plane stress state;

E and $\mu$ are material elastic modulus and Poisson's ratio;

$\varphi$ is the angle between the normal direction of the specimen surface and the reflective crystal surface;

$d_\varphi$ and $d_n$ are the distance between the reflective crystal surfaces spacing indirection specified and the distance between crystal surfaces parallel to the specimen surface.

The tested sigma specimen is also manufactured from the roll forming process with the length of one meter. The nominal yield strength of specimens is 450MPa and it has the same stress-strain curve used in the previous numerical model. The zinc coating of each measured point is removed in advance by acid washing process (see Fig. 4-16) and the measurement is performed at ambient temperature.
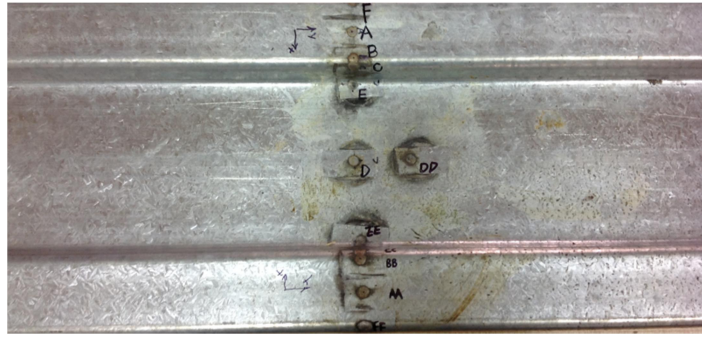
**Figure 4-16: Specimen after acid washing**

The measurement device used in the experiment is IXRD-GR40 portable residual stress & retained austenite measurement system (see Fig. 4-17). This system offers a 40mm focal distance with standard 30mm x-ray tube, which makes it capable of measuring the bore diameter within 120mm. The penetration depth of X-ray diffraction in the experiment is 20 µm and the wavelength is 2.291nm. The residual stress on the surface of the specimen is obtained in both transverse and longitudinal directions, and it is assumed that the transverse direction (X-axis) along the cross-section and longitudinal direction (Y-axis) along the length of the specimen. The measurement setup is shown in Fig. 4-18.
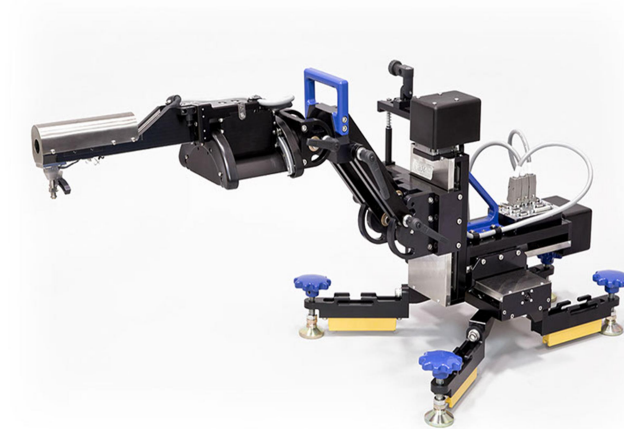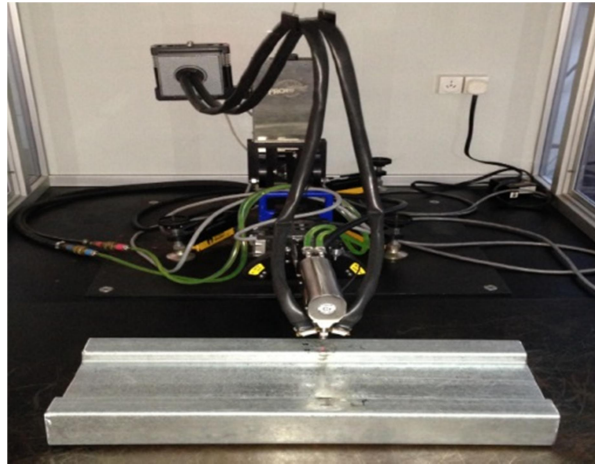
Figure 4-18: Test setup

Twelve points are measured in this X-ray diffraction experiment, and each point has been tested twice for data verification. The position of each point is demonstrated in Fig. 4-19; all points are on the outside surface and located on the corner or flat portions. The measured residual stress of each point is presented in Table 4-3.
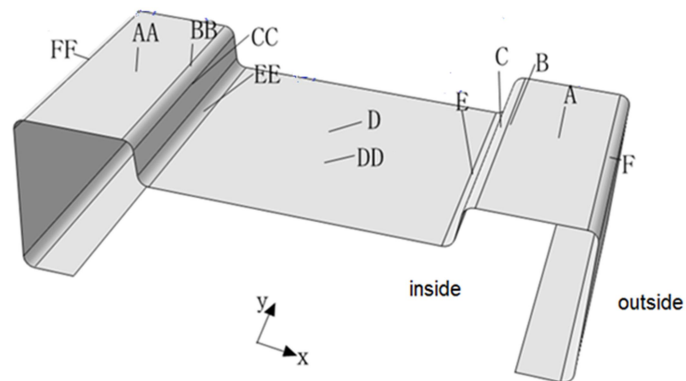


Figure 4-19: Location of measured points

Table 4-3: Measured residual stresses

| Poin t | Transverse stress (X) $\sigma_T$ (MPa) | | $\dfrac{\sigma_{T1}}{\sigma_{T2}}$ | $\sigma_T/\sigma_y$ | | Averag e $\sigma_T/\sigma_y$ | Longitudinal stress(Y) $\sigma_L$ (MPa) | | $\dfrac{\sigma_{L1}}{\sigma_{L2}}$ | $\sigma_L/\sigma_y$ | | Average $\sigma_L/\sigma_y$ |
|---|---|---|---|---|---|---|---|---|---|---|---|---|
| | Test 1 | Test2 | | Test 1 | Test2 | | Test 1 | Test2 | | Test 1 | Test2 | |
| A | -20.5 | -12 | 1.71 | -0.046 | -0.027 | -0.037 | 60.9 | 74.3 | 0.82 | 0.136 | 0.165 | 0.151 |
| B | 51.0 | 50.8 | 1.00 | 0.113 | 0.113 | 0.113 | 203.3 | 220.0 | 0.92 | 0.452 | 0.489 | 0.471 |
| C | -237.7 | -240.9 | 0.99 | -0.528 | -0.535 | -0.533 | -107.5 | -100.1 | 1.07 | -0.238 | -0.223 | -0.231 |
| D | -63.4 | -54.3 | 1.17 | -0.140 | -0.120 | -0.130 | -159.7 | -143 | 1.12 | -0.355 | -0.32 | -0.340 |
| E | N/A | N/A | N/A | N/A | N/A | N/A | 50.6 | 31.7 | 1.60 | 0.115 | 0.075 | 0.095 |
| F | -328.3 | -323.6 | 1.01 | -0.730 | -0.720 | -0.725 | 114.3 | 116.5 | 0.98 | 0.25 | 0.26 | 0.260 |
| FF | -236.1 | -234.8 | 1.01 | -0.525 | -0.520 | -0.525 | -3 | -6.9 | 0.43 | -0.007 | -0.015 | -0.011 |
| EE | -82.7 | -73.5 | 1.13 | -0.180 | -0.165 | -0.175 | 79.3 | 82.8 | 0.96 | 0.176 | 0.184 | 0.181 |
| DD | -44.7 | -53.9 | 0.83 | -0.095 | -0.120 | -0.110 | -134.3 | -125.8 | 1.07 | -0.295 | -0.28 | -0.288 |
| CC | -227.7 | -251.5 | 0.91 | -0.506 | -0.560 | -0.534 | -129.7 | -113.3 | 1.14 | -0.288 | -0.253 | -0.271 |
| BB | 15.2 | 19.5 | 0.78 | 0.034 | 0.045 | 0.040 | 294.1 | 297 | 0.99 | 0.404 | 0.662 | 0.658 |
| AA | 4.25 | 16.4 | 0.26 | 0.010 | 0.036 | 0.023 | 80.6 | 83.1 | 0.97 | 0.180 | 0.185 | 0.183 |
| Mean | | | 0.98 | | | | | | 0.92 | | | |

*Note: N/A occurs when points are immeasurable due to the limitation of the experimental apparatus and test conditions.*

It can be seen from Table 4-3 that the average ratio of two tests is found close to 0.92 in longitudinal direction and 0.98 in the transverse direction. The corner regions (C, CC, F and FF) have the maximum transverse residual stress, with the values of -0.533$\sigma_y$, -0.725$\sigma_y$, -0.534$\sigma_y$ and -0.525$\sigma_y$, respectively. The table also exhibits that the maximum compressive residual stress in transverse directions (-0.725$\sigma_y$) is found on outerweb to flange corner point F and maximum tensile stress in longitudinal is 0.658$\sigma_y$ on point BB. The residual stress of point E is not measured as the limitation of the experimental apparatus and conditions.

## 4.4.2 Results comparison

The comparison of residual stresses between experimental and the numerical method

is shown in Fig. 4-20. The ID and location of each point on the X-axis are depicted in

Fig. 4-19.
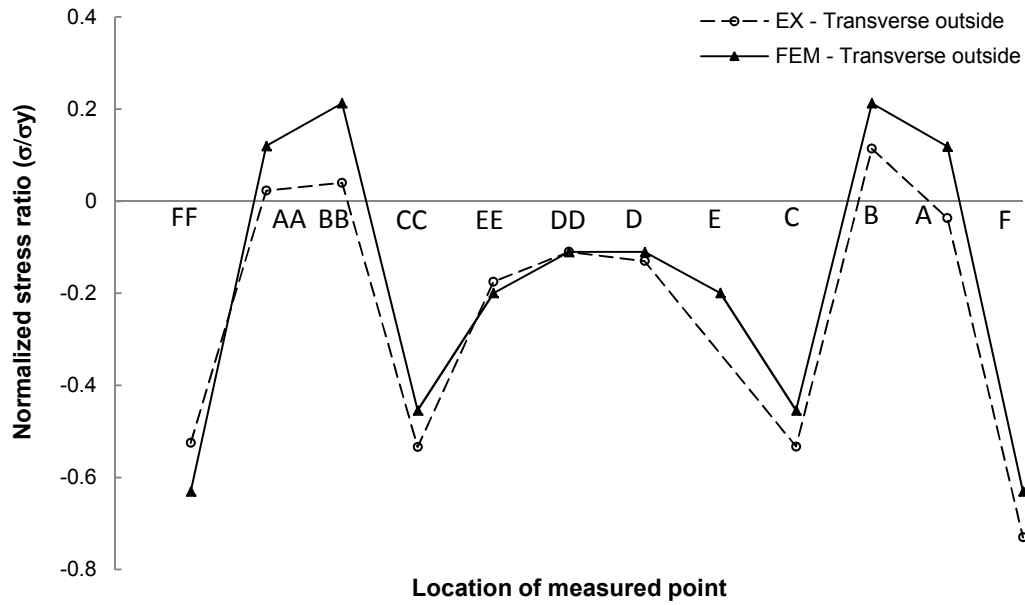


(a) Transverse direction
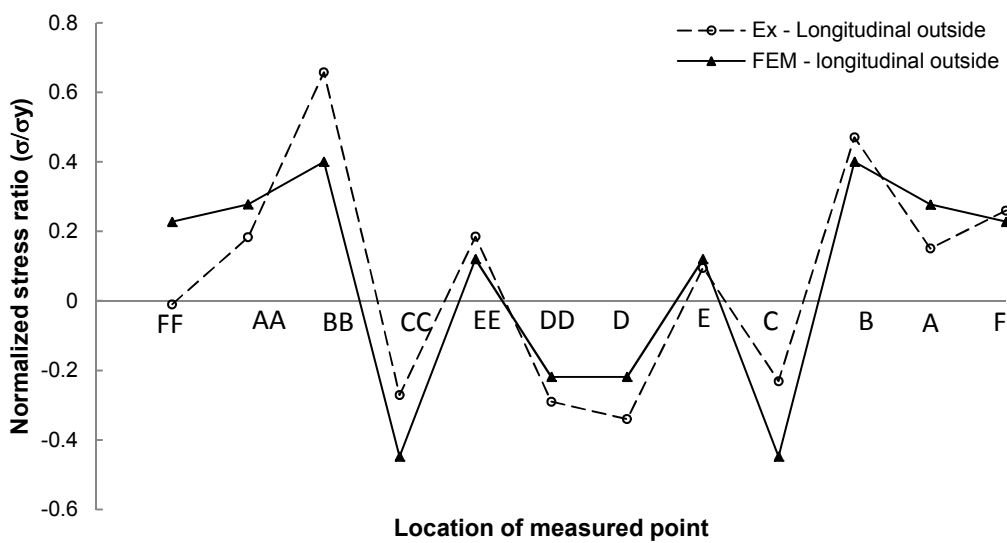
(b) Longitudinal direction

**Figure 4-20: Comparison of experiment and FEA results**

It can be observed that in the transverse direction (see Fig. 4-20a), the trend of experimental and numerical residual stresses is observed to follow the similar pattern. The FE predicted residual stresses are found to be greater than the experimentally measured residual stresses on regions A (AA) and B (BB). The maximum gap is $0.17\sigma_y$ on point B and BB. In the longitudinal direction (see Fig. 4-20b), the numerically predicted residual stresses are in good agreement with the experimentally measured results. The experimental stresses at FF and BB are not symmetric to F and B, which may be due to the device error and external turbulence during measurement. If ignore the difference at those two points, then the maximum gap is located on point C, with the test value $-0.23\sigma_y$ and FE value $-0.45\sigma_y$. The numerical curves are observed symmetric to the centre line in both directions. In general, the comparison demonstrates the reliability and accuracy of the numerical model.

In order to have a clear plot of the FE predicted residual stress for further investigation, the magnitudes and distributions of residual stress in roll formed sigma section are elaborated in Fig. 4-21. In the figure, the residual stress in two directions on the outside surface and mid-normalized thickness is presented. The distribution of residual stresses in the graph is based on the following assumptions:

(1) The maximum through-thickness residual stress is assumed as the mid-thickness residual stress in the graph. The residual stress at the neutral axis is assumed to be zero.

(2) It is assumed that the small area around reference points has the same stress pattern to the point.
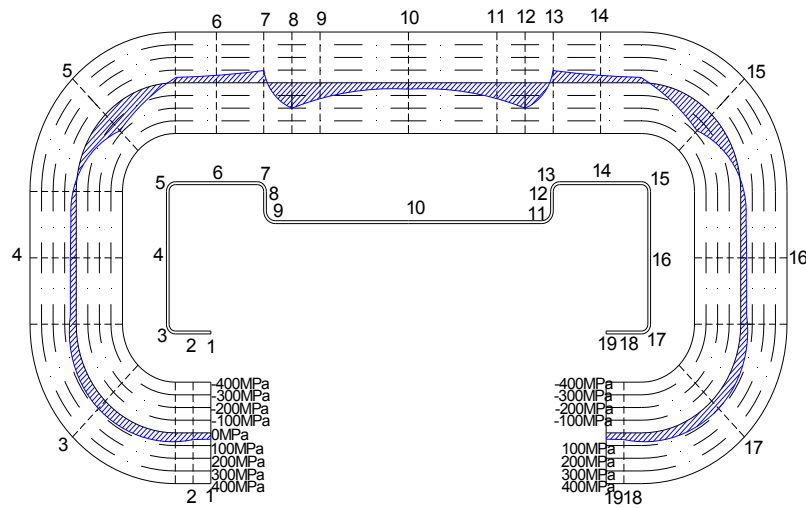


(a) Transverse (outside surface)
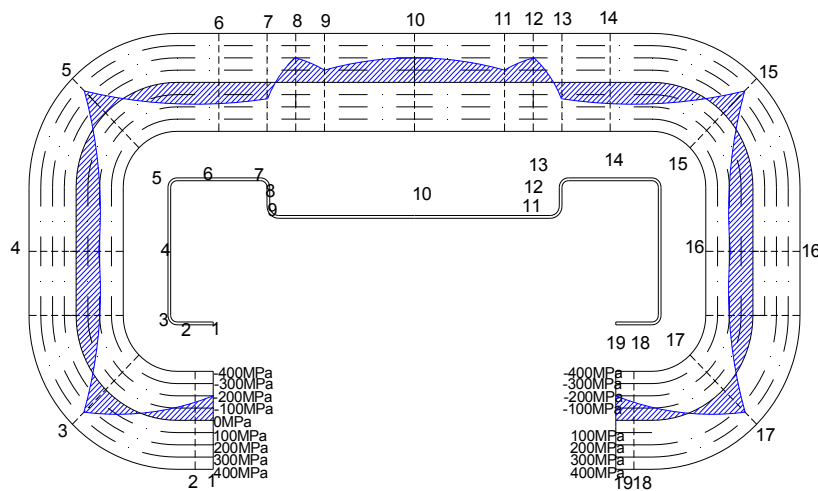


(b) Transverse (mid-thickness)
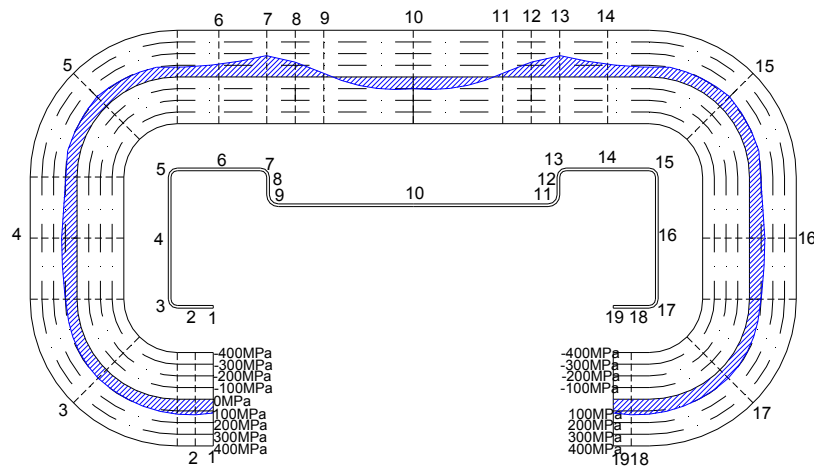
(c) Longitudinal (outside surface)
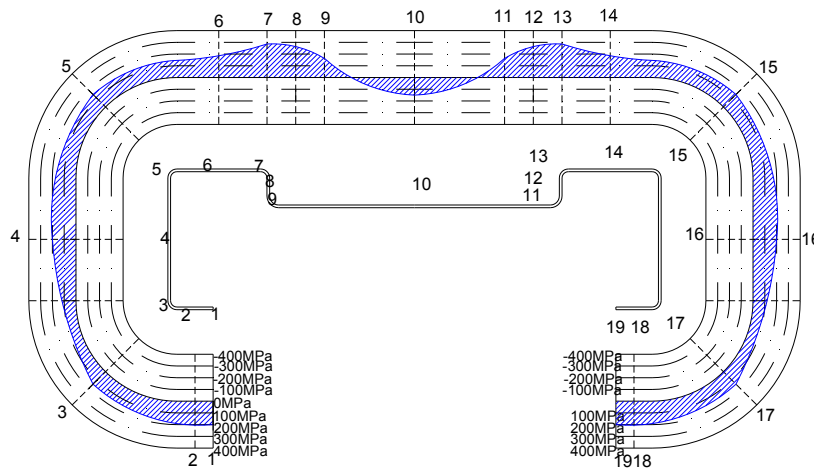


(d) Longitudinal (mid-thickness)

**Figure 4-21: Distribution of residual stress on sigma section 20012**

## 4.5 Summary

In this chapter, FE simulations of cold forming induced residual stress have been performed. The proposed FE model is based on the roll flowers and takes material nonlinearity and isotropic hardening into account. The distribution and magnitude of

residual stress are predicted and compared with experimental results. The following conclusions can be drawn:

1. During the forming process, the equivalent plastic strain is mainly occurred on the bending zone between innerweb and outerweb; the strain in the rest part is insignificant. The development of longitudinal strain indicates that the arrangement of roll set in the longitudinal direction is acceptable as the elongation is insignificant on the flat portion during the forming process.

2. The transverse stress of the sheet increases continually as the increase of the bend angle in roll forming. The stress in both directions then has a decrease when the springback occurs at the final stage.

3. In both corner and flat portions, the residual stress is nonlinearly distributed along the thickness and the curves are asymmetrical about the neutral axis. The peak value of transverse residual stress is higher than longitudinal residual stress at corner portion as the deformation mainly occurs in the transverse direction. The maximum longitudinal residual stress is found to exceed the transverse stress at the flat portion and the location of maximum stress along the thickness is located on $\pm 0.25$ of normalized thickness.

4. A good agreement is found between the FE achieved residual stress and experimental data obtained by using X-ray diffraction method. The comparison has demonstrated the reliability and accuracy of the numerical model.

# 5. SIMULATION OF WELDING RESIDUAL STRESS

The welding process is a widely used manufacturing technique in the production of structural members and the construction of steel structures. As one of the often used welding methods, arc welding can join weld pieces by using the molten of filler metal. During arc welding process, a dynamic temperature cycle is introduced to generate a non-uniformly distributed temperature field on the weldment. As the result of uneven cooling at the weld bead and heat affected zone (HAZ), the residual stress is thus induced.

The occurrence of residual stress may either be beneficial or detrimental to the weldment, for instance, the tensile residual stress may contribute to fatigue failure, promote brittle fracture and stress corrosion cracking on welded member (Dattoma et al. 2006, Deng 2009). However, the effect of welding residual stress is still not well understood as the distribution of welding residual stress is of a time-dependent nature and the theoretical and experimental prediction of welding residual stress can be rather challenging. Therefore, finite element simulation of the welding process has been commonly adopted in recent literature as a cost and time-efficient tool for accurate evaluating welding induced temperature field and residuals stress.

In this chapter, a simplified approach for simulating single-pass welding process in sigma section is introduced by using the finite element package ANSYS (2010). The simulation procedure is verified with temperature and residual stress measurements found in the literature. A parametric study is further conducted to investigate the

effect of shell thickness on the residual stress distribution. The data of welding residual stress is taken as the pre-stress condition for the simulation of sigma beam in the following chapter.

## 5.1 FEM simulation process

During the simulation, a heat conduction analysis was initially carried out based on the temperature dependent material properties to obtain the temperature history and field; then, achieved thermal results were used as initial loading to gain stress distribution. The essence of this simulation procedure is the "birth-and-death" technical, which allows the element active and inactive at the specific time step to imitate the movement of heat flux.

In the thermal analysis, the finite element formulation is based on the governing equation for transient nonlinear heat transfer (Peric et al. 2014)

$$\frac{\partial}{\partial x}\left(k_x \frac{\partial T}{\partial x}\right) + \frac{\partial}{\partial y}\left(k_y \frac{\partial T}{\partial y}\right) + \frac{\partial}{\partial z}\left(k_z \frac{\partial T}{\partial z}\right) + Q = \rho C \frac{\partial T}{\partial t} \qquad \text{(Eq. 5-1)}$$

where $k_x$, $k_y$ and $k_z$ are the thermal conductivities in the x, y and z directions, respectively; T is the current temperature; Q is the heat generation; $\rho$ is the density; C is the specific heat; and t is the time. A general solution of Eq. 5-1 is achieved by introducing the following initial and boundary conditions:

$$T(x, y, z, 0) = T_0(x, y, z) \qquad \text{(Eq. 5-2)}$$

$$\left(k_x \frac{\partial T}{\partial x} N_x + k_y \frac{\partial T}{\partial y} N_y + k_z \frac{\partial T}{\partial z} N_z\right) + q_s + h_c(T - T_\infty) + h_r(T - T_r) = 0 \qquad \text{(Eq. 5-3)}$$

where $N_x$, $N_y$ and $N_z$ are the direction cosine of the normal to the boundary; $h_c$ and

$h_r$ are the convection and radiation heat transfer coefficients; $q_s$ is the boundary heat

flux; $T_r$ is the temperature of radiation; and $T_\infty$ is the surrounding temperature.

The simulation procedure is illustrated in the subsequent flowchart (see Fig. 5-1).
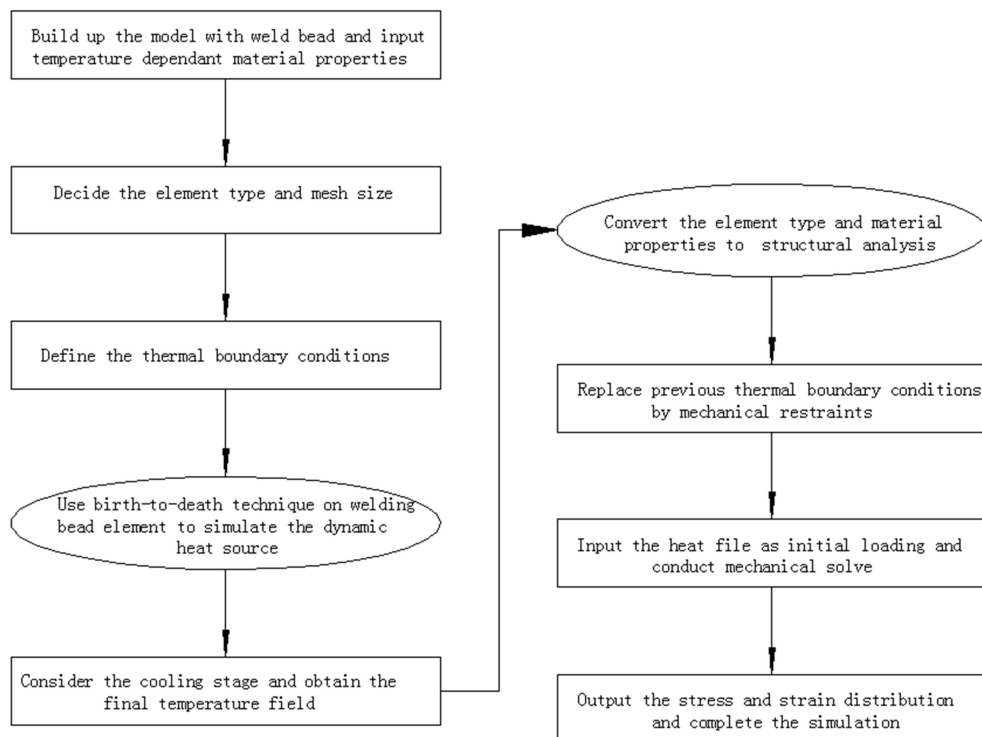


**Figure 5-1: Schematic diagram of welding simulation procedure**

The numerical analysis is based on the following assumptions:

1) In the model, the effect of work hardening prior to welding is removed by setting

the equivalent plastic strain to zero;

2) It is assumed that the effect of solid phase transformation and multi-pass welding is

insignificant for thin walled section;

3) The distortions induced in the welding process are ignored as assuming sufficient restraints are offered during the procedure.

### 5.1.1 Geometric model

As mentioned before, this welding simulation is conducted as the preparation of the bending test simulation in the following chapter. The specimen in the test is a sigma beam 20012 (see Fig. 4-3) which was butt-welded by using arc welding method. The weld bead and HAZ are depicted in Fig. 5-2.
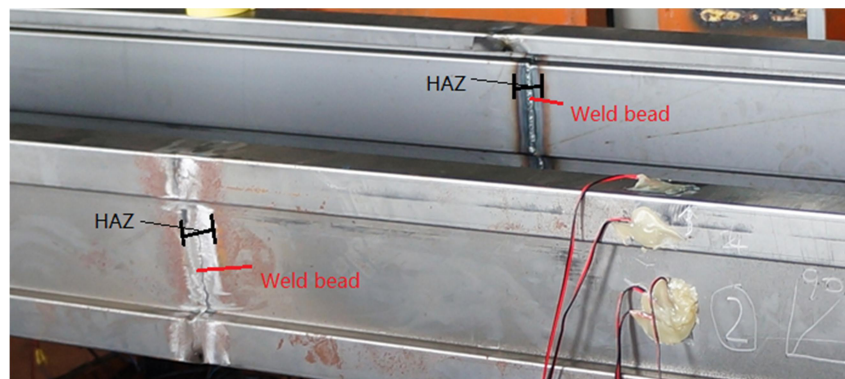


**Figure 5-2: The picture of weld bead and HAZ**

The FEM model is shown in Fig. 5-3, it is assumed that the weld bead is located on the mid-span section, and the width of HAZ is 60mm on both sides of the weld bead.
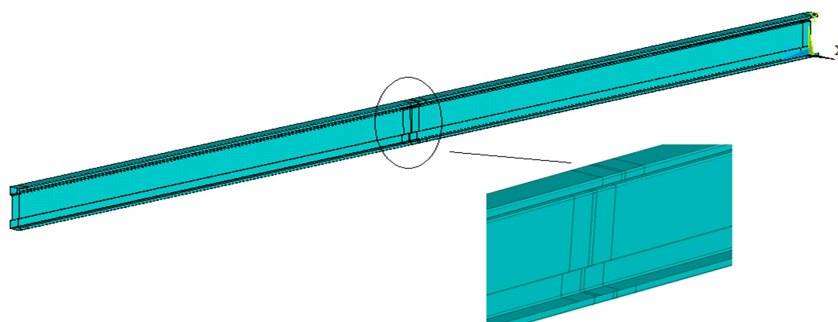


**Figure 5-3: Overall view of model**

The welding direction is shown in Fig. 5-4a by the arrow line and a bottom to top sequence should be noted. One reference point located on the mid-bottom flange and one reference path cross the mid-innerweb were selected to characterise the distribution of temperature and residual stress, as shown in Fig. 5-4b.



(a) Welding direction        (b) Reference point & path
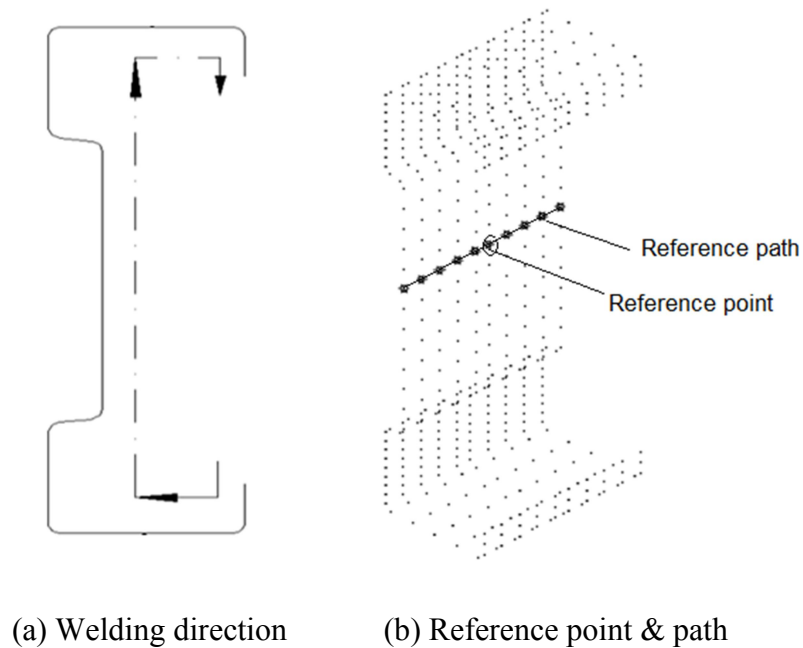
**Figure 5-4: Welding direction and reference point & path**

### 5.1.2 Material properties

The material properties in the thermal–mechanical analysis are related to the metallurgical conditions of the weldment. The yield strength of the welded specimen is 235MPa, in order to keep the similarity, the temperature dependent material properties listed in Deng and Murakawa's (2006) paper were used for the model. The input material properties include temperature-dependent conductivity, specific heat,

thermal expansion coefficient, Young's modulus, Poisson's ratio, density and yield strength. The summary of the material properties is shown in Fig. 5-5.
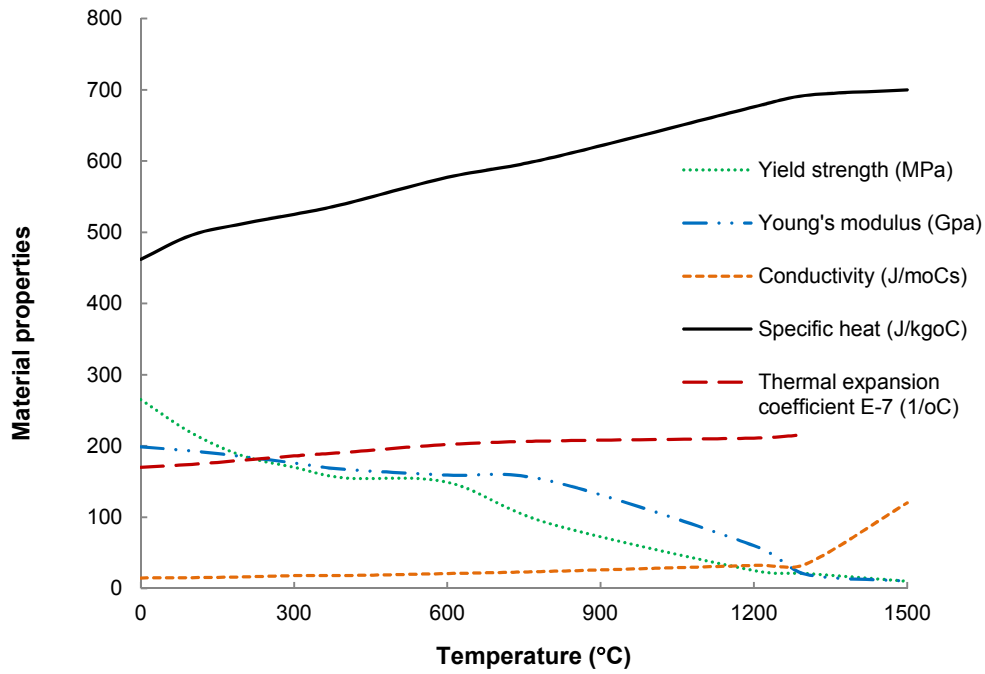


(a)
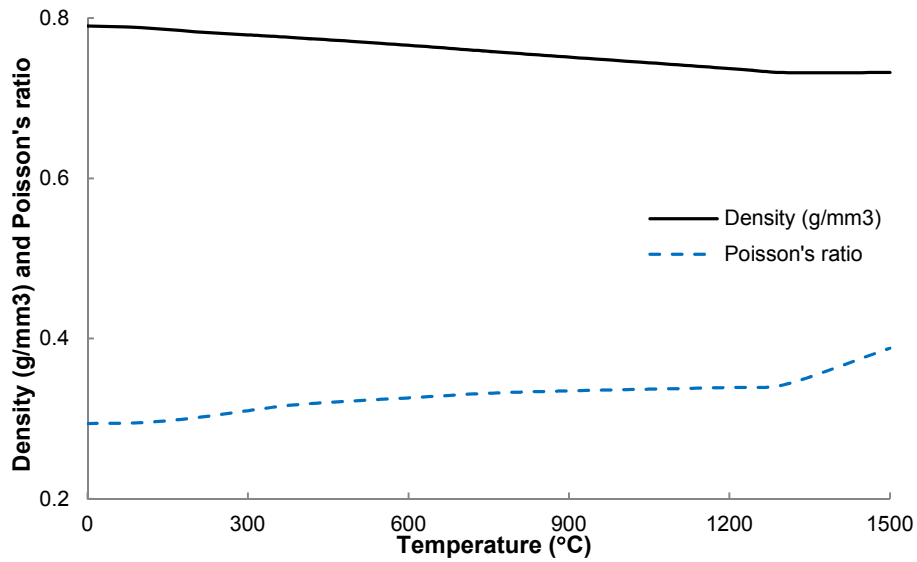


(b)

**Figure 5-5: Temperature-dependent material properties (Deng and Murakawa 2006)**

As showed in the figure, there is a descent trend found for yield strength, young's modulus and density as the temperature ascends from 0 ℃ to 1500 ℃; and specific heat, thermal expansion coefficient, conductivity and Poisson's ratio increase with increasing temperature.

### 5.1.3 Meshing

In spite of the development of faster computers, the time duration of 3D numerical simulations of welding processes remains a substantial challenge. To reduce the computation time needed for numerical analysis, a simplified shell model was proposed herein instead of the solid model. This model can minimise the requirement of CPU capacity by ignoring the solid phase transformation, and will not affect residual stress for low carbon steel (Deng 2009).

In order to adopt the thermal to mechanical conversion during analysis, the sigma beam was initially meshed by shell element SHELL57 in the thermal analysis and then by shell element SHELL181 in the stress analysis. The former is a three-dimensional element having in-plane thermal conduction capability and the latter is a 4-node element which is well-suited for large rotation and large strain nonlinear applications (ANSYS 2010). A relatively finer mesh (5mm) was assigned to the HAZ (see Fig. 5-6) as high temperature and flux gradients were anticipated around the welding bead and HAZ, and relatively coarse mesh (20mm) was applied to the rest regions for reducing the computational cost.
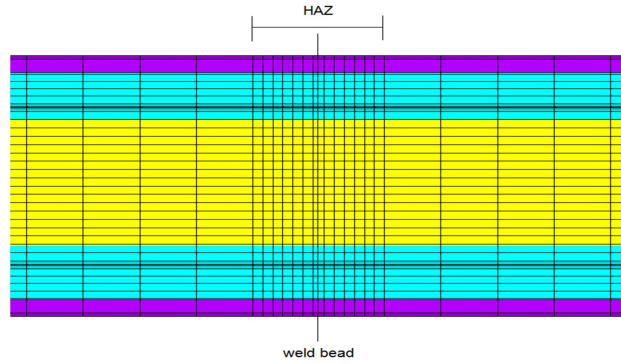
**Figure 5-6: Schematic meshed model**

### 5.1.4 Thermal boundary conditions

Welding heat flux is of the localized and dynamic features and has a significant effect on the temperature and stress distribution. There are three heat sources often used in the finite element simulation.

(1) Gaussian heat flux

The Gaussian heat is distributed as a cone-shaped volumetric heat source and given by following equations (Ferro et al. 2005)

$$Q(x, y, z) = \frac{2\eta P_e}{\pi r_e^2 H} \exp\left(\frac{-r^2}{r_0^2}\right) \qquad \text{(Eq. 5-4)}$$

$$r^2 = x^2 + y^2 \qquad \text{(Eq. 5-5)}$$

$$r_0 = r_i + \frac{(r_e - r_i)z}{H} \qquad \text{(Eq. 5-6)}$$

where $\eta$ is thermal efficiency; $r_e$ is the half width of welding line at the top surface; $P_e$ is the laser power; $r_i$ is the half width of the welding line on the bottom surface; r is

the radial position; H is the welding penetration, for full penetration laser welding, it can be considered as the thickness of the plate.

(2) Double ellipsoidal heat flux

The double ellipsoidal distribution was proposed by Goladk et al. (1984); the equations are presented in the form

For the front heat source

$$q(x, y, z, t) = \frac{6\sqrt{3}f_f Q}{a_1 bc\pi\sqrt{\pi}} e^{-3(x-vt-x_0)^2/a_1^2} e^{-3y^2/b^2} e^{-3z^2/c^2} \qquad \text{(Eq. 5-7)}$$

For the rear heat source

$$q(x, y, z, t) = \frac{6\sqrt{3}f_r Q}{a_2 bc\pi\sqrt{\pi}} e^{-3(x-vt-x_0)^2/a_2^2} e^{-3y^2/b^2} e^{-3z^2/c^2} \qquad \text{(Eq. 5-8)}$$

where $f_f$ and $f_r$ are the parameters which give the fractions of the heat deposited in front and the rear parts, respectively. Q is the magnitude of the heat input per unit time; v is the welding speed; t is the welding time; and $x_0$ is the position of the heat source in the x-direction when t is zero. The parameters $a_1$, $a_1$, b and c are related to the characteristics of the welding arc.

(3) Line energy heat flux

The line energy input of welding is based on the following equation (Brickstad and Josefson 1998):

$$Q = \eta \frac{UI}{V} \qquad \text{(Eq. 5-9)}$$

where Q is the net line energy; $\eta$ is the arc efficiency; V is the travel speed; U and I are the arc voltage and current. It is obviously from the equation that the increases of welding speed will decrease the input energy.

Both Gaussian and double ellipsoidal heat distributions are commonly applied in thick-walled solid models for considering flux transferring through the thickness. The line energy equation is a simplified distribution pattern suitable for shell model with thin-walled sections, and this heat source was adopted in the present study. In the ANSYS, the energy generated rate was input based on the net line energy Q, the area of meshed element and time step. It was assumed that the current is 140A, voltage is 9.5V, heat torch is travelling at a speed of 80 mm/min (Deng and Murakawa 2006), and $\eta$ is 0.5 for thin-walled sections (Brickstad and Josefson 1998).

In the simulation, it was assumed that the temperature of parent metal was equal to ambient temperature (20°C) before welding, the entire heating time was 100s and the total cooling time from the end of the heating phase to the cooling down stage was about 900s. The convection and radiation heat transfer boundary conditions have been employed in all regions except the weld bead. The heat loss through convection was taken into account according to the Newton's law, and the heat loss due to radiation was modelled using Stefan–Boltzman law (Deng and Kiyoshima 2012):

$$q_c = -h_c(T_s - T_0) \qquad\qquad \text{(Eq. 5-10)}$$

$$q_r = -\varepsilon_0\sigma_0[(T + 273.15)^4 - (T_0 + 273.15)^4] \qquad \text{(Eq. 5-11)}$$

where $q_c$ is the heat flux loss due to convection, $h_c$ is the heat transfer coefficient, $T_s$ is the surface temperature of the weldment, $T_0$ is the ambient temperature, $\varepsilon_0$ is the emissivity, and $\sigma_0$ is the Stefan–Boltzmann constant.

## 5.2 Thermal analysis

In the thermal analysis, the torch was moved from bottom to top based on "birth-and-death" cycle syntax, and the visualized temperature flow is demonstrated in Fig. 5-7. Figs. 5-7a, b, c depict the temperature field as torch moves at 20s, 50s and 100s, respectively, and 5-7d shows the final thermal field after cooling down (1000s).



|       |       |       |
|-------|-------|-------|
| a) 20s | b) 50s | c) 100s |



d) 1000s
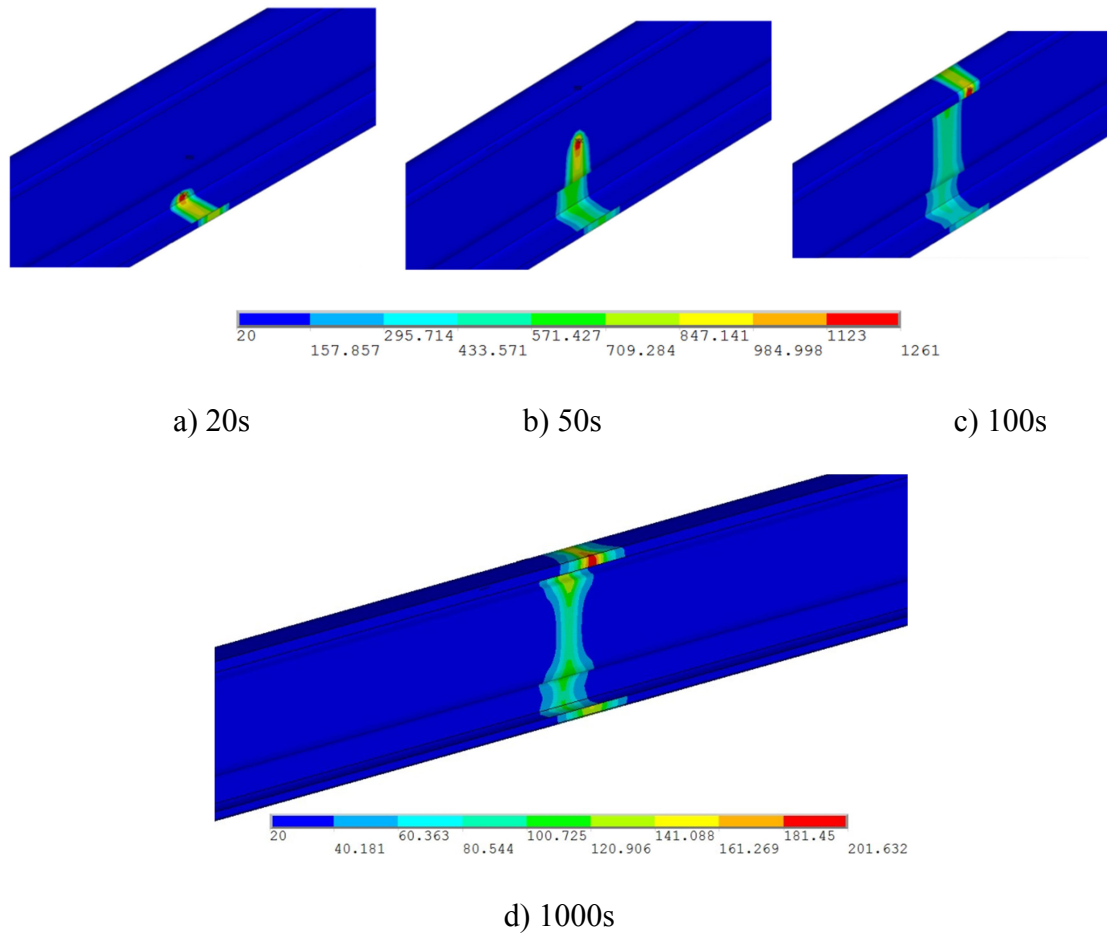
**Figure 5-7: Temperature contours during welding process**

The temperature contours in Figs. 5-7a, b, c indicate that the weldment is heated localized by the heat flux and temperature in the vicinity of the weld bead are not uniformly distributed but changes with distance from the weld centreline. It can be seen that the maximum temperature during welding is 1261℃ and then drop to 202℃ after cooling down. The highest value at 1000s occurs at the last torch point on the top lip (Fig. 5-8d). The numerical and experimental obtained temperature history curves during welding and cooling process is illustrated in Fig. 5-8.
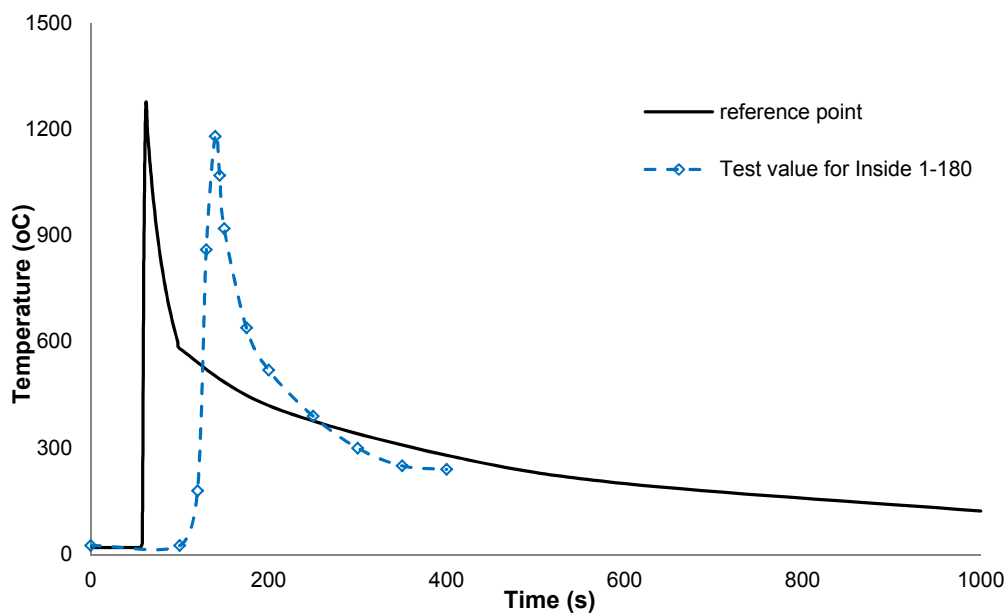


**Figure 5-8: Numerical and experimental obtained temperature history curves**

According to Fig. 5-8, it shows that the temperature of all reference point increases dramatically as approaching of the torch and then falling slowly as torch leaves. During the welding process, the numerical achieved peak temperature is 1261℃ at reference point and decreases to 580℃ when heat source removed at 100s, then, the

descend trend continue due to convection, the temperature at 400s is 280 °C and the finally temperature after cooling down is 120°C. In order to validate the temperature result, the experimental data achieved by Deng and Murakawa (2006) were also introduced in the Fig. 5-8. The test curve was the thermal cycle of the point on the inside surface during the first welding pass and the recorded time history was from 100s to 400s. The temperature history of the reference point shows a good agreement when compared to the test curve, while the experimental curve increases to peak temperature around 1190°C at 140s and then reduces to 240°C at 400s.

The thermal history along reference path is demonstrated in Fig. 5-9 for investigating the temperature development on HAZ.
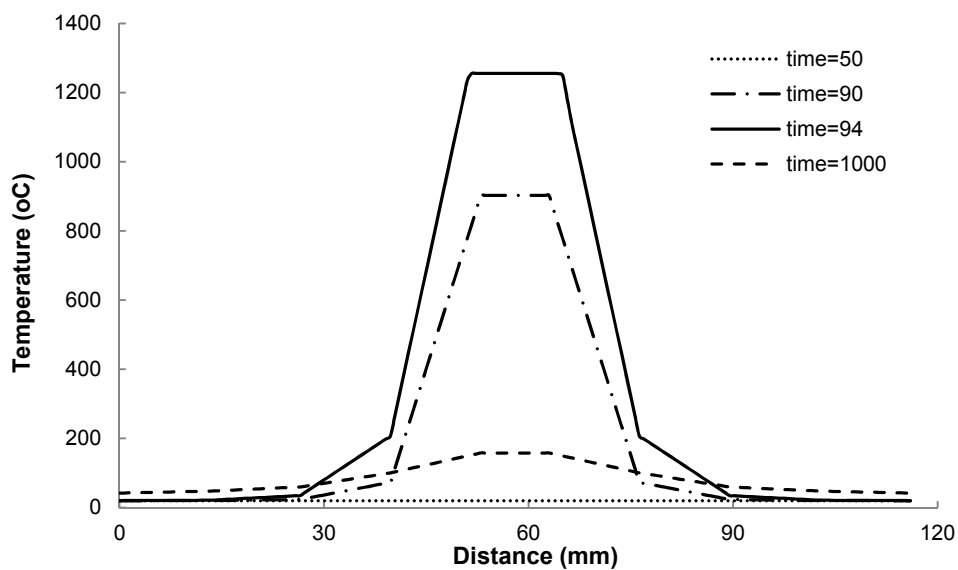


**Figure 5-9: Temperature history along path1**

It can be seen from Fig. 5-9 that the range of HAZ caused by torch is only 60mm in width from (30mm to 90mm). For areas 30mm far from the weld bead, the value of

the temperature is reduced to zero. Moreover, the stress distribution at four critical moments 50s, 90s, 94s and 1000s shows that the temperature distribution along reference path remains at a low level till a rapidly ascent happens from 50s to 94s and reaches the maximum value at 94s, then, the temperature drops to about 120℃ at 1000s due to cooling convection.

## 5.3 Mechanical analysis

Mechanical analysis was conducted based on the achieved thermal field. During the study, the element type should change to SHELL 181 to fulfil the requirement of mechanical analysis. It is assumed that the direction normal to the weld bead is the transverse direction and the direction of the weld bead is the longitudinal direction. Figs. 5-10 and 5-11 exhibit the distribution of longitudinal and transverse residual stress along the reference path after cooling down. The test curve in the figures is according to Deng and Murakawa's (2006) study.
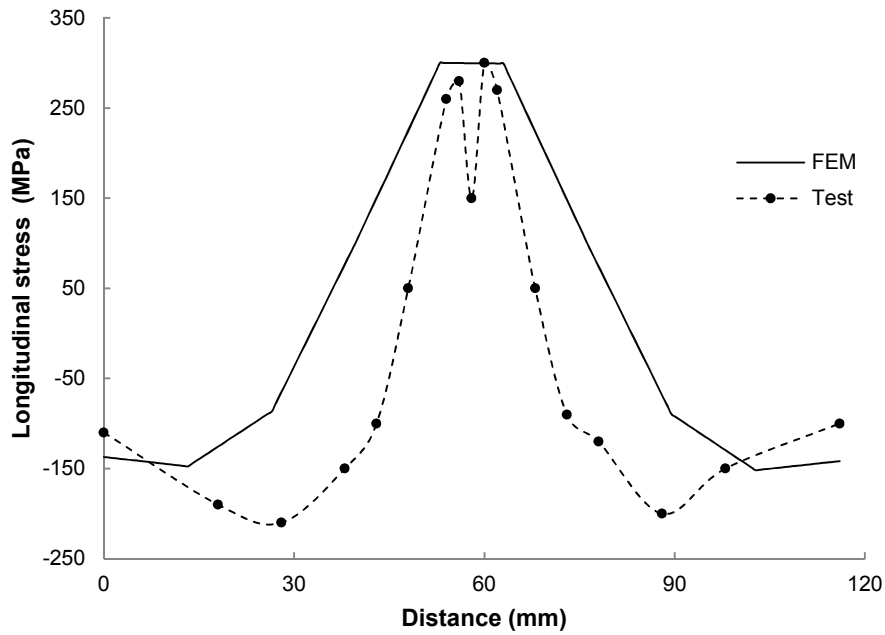
**Figure 5-10: Longitudinal residual stress along reference path after cooling down**
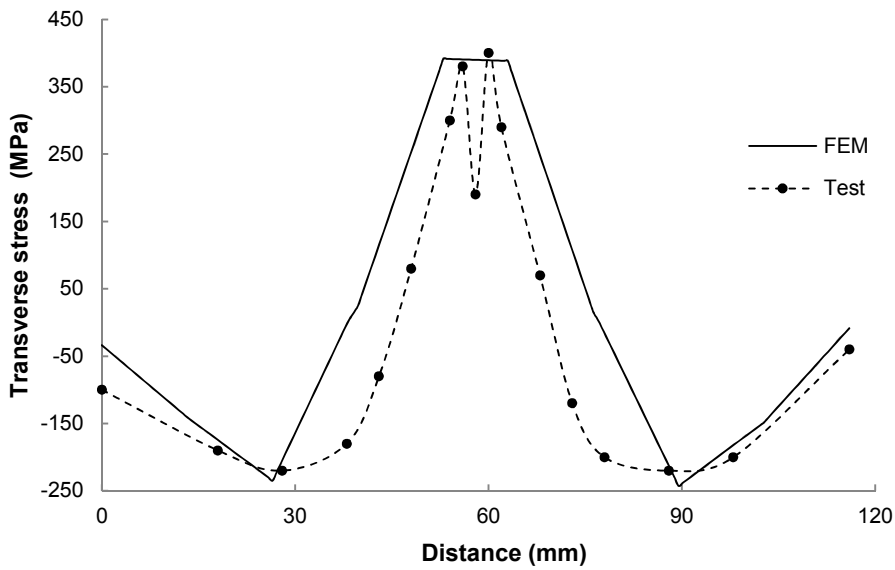


**Figure 5-11: Transverse residual stresses along reference path after cooling down**

It can be concluded from Fig. 5-10 that the longitudinal residual stress is symmetric with respect to the centreline of the weld bead and the stress decreases drastically with

increasing distance from the weld bead. The maximum longitudinal stress is in tension and the max value is 300MPa. The maximum compressive longitudinal stress is approximately 150MPa that happens at 10mm and 100mm. The width of the longitudinal tensile residual stress zone is about 50mm from 35mm to 85mm. Fig. 5-11 illustrates the transverse residual stress along the reference path. It can be seen that the maximum tensile transverse residual stress (400MPa) is greater than longitudinal stress (300MPa) on the weld bead, while the maximum compressive transverse residual stresses (230MPa) occurs at 30mm and 90mm. The curve approaches to zero value almost 25mm away from the welding centreline; then tensile stress reverses to compressive residual stress.

The distribution of longitudinal stress along shell thickness is explored by using nine integration points along the thickness. The location of each point is from $-t/2$ (inner surface) to $t/2$ (outer surface) and the coordinate of each point is normalized by $t/2$ (Fig. 5-12a). The distribution of longitudinal residual stress along thickness at the reference point is shown in Fig. 5-12b, where the y-axis represents the normalized coordinate along thickness and the x-axis is the longitudinal residual stress.
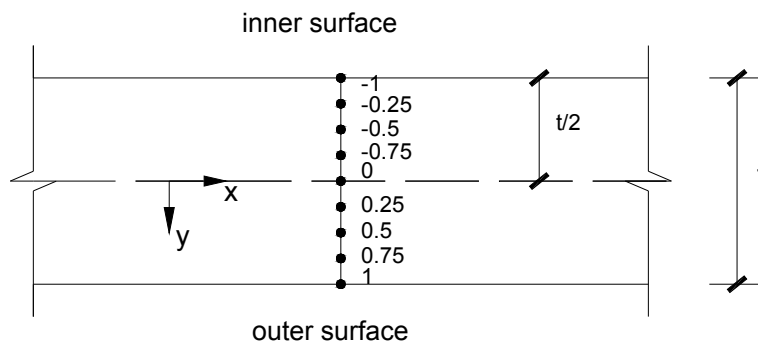
(a) Coordinate along thickness
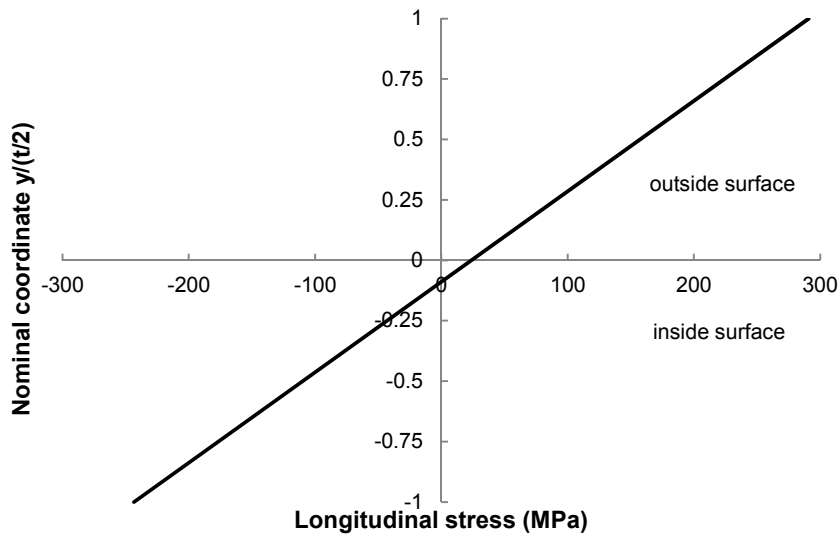


(b) Residual stresses along thickness

**Figure 5-12: Coordinate and residual stresses along thickness at reference point**

Fig. 5-12 exhibits that the distribution of longitudinal stress along the thickness is linear and the curve is anti-symmetric to the neutral axis. The maximum tensile longitudinal stress is 300MPa which occurs on the outside surface and the maximum compression on the inside surface.

A parametric study is also conducted herein to explore the influence of shell thickness on welding residual stress distribution. The curves of longitudinal stress distribution at reference path with different thickness (t) from 1.2mm to 3.0mm are shown in Fig. 5-13.
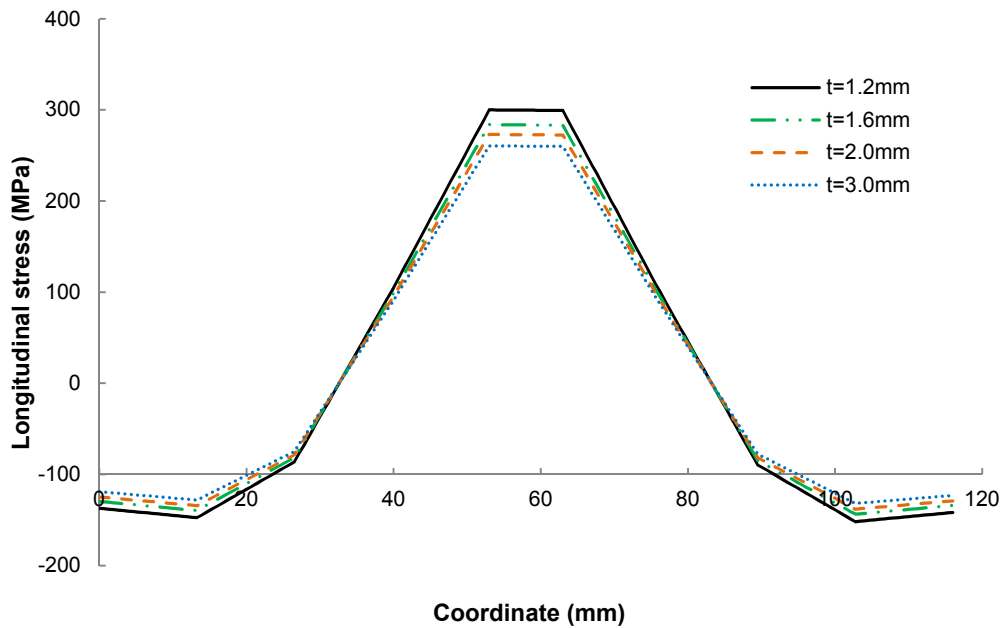
**Figure 5-13: Longitudinal residual stress along path1 with different thicknesses**

It can be seen from Fig. 5-13 that the maximum tensile stress and compressive stress decrease with the increases in shell thickness. The maximum tensile stress for thickness from 1.2mm to 3.0mm are 300MPa, 284MPa, 273MPa and 260MPa, respectively, and the value drops 5.3%, 3.9% and 4.8% as the thickness increases from 1.2mm to 1.6mm, 1.6mm to 2.0mm, and from 2.0mm to 3.0mm respectively. The occurrence of this phenomenon because the increases in thickness will benefit to the convection process and thus lead to a lower temperature field and residual stress.

## 5.4 Summary

In this chapter, a 3-D finite element model was presented to simulate the temperature field and residual stress distribution in butt-welded sigma section during arc welding

process. Meanwhile, numerical results were compared with experimental data delivered by Deng and Murakawa (2006). Based on the findings and discussions mentioned above, the following conclusions can be drawn:

1. The temperature of weldment increases dramatically as torch approaches and then falling as torch leaves. The maximum temperature during heating is 1261℃, and the thermal field predicted by FEM is in good agreement with experimental measurement.

2. The range of HAZ caused by torch is about 60mm in width, and the temperature on regions 30mm away from the HAZ is reduced to zero.

3. It is found that welding may introduce residual stress in weldment of the higher magnitude than the yield strength of the base material. The maximum longitudinal residual stress is in tension and the value is 300MPa on the weld bead; the longitudinal stress decreases drastically with increasing distance from the weld centreline. The maximum transverse residual stress (400MPa) is also in tension and greater than longitudinal stress around the weld bead; the value approaches zero almost 25mm away from the welding centreline and then tensile stress reverses to compressive stress.

4. The distribution of longitudinal stress along shell thickness is anti-symmetric with respect to the neutral axis. The maximum tensile longitudinal stress occurs on the outside surface and the maximum compressive stress happens on the inside surface.

Increases in shell thickness will lead to a decrease of the maximum tensile and compressive stress.

Overall, from Chapter 3 to Chapter 5, the magnitude and distribution of cold working and welding residual stresses on sigma sections are investigated. In the following chapter, the emphasis is given to the effect of residual stress and strain hardening on the loading resistance capacity of sigma beams.

# 6.  INFLUENCES OF RESIDUAL STRESSES ON SIGMA BEAM

In the previous studies, it shows that the residual stress is usually induced in sigma sections during cold forming and welding process. The existence of residual stress will lead to a modification of the stiffness of the steel component because the superimposition of external loadings on residual stress can accelerate or decelerate the yielding of specific portions of the section. The occurrence of the residual stress is usually accompanied by strain hardening during roll forming and press braking process, which is also considered to be able to increase the yield and ultimate strength of the material. As a result, the mechanical properties of the steel member are, to various degrees, different from those of the sheet prior to forming. In order to achieve a better understanding of the effect of residual stress and strain hardening on cold-formed sigma beams, a series of numerical studies were conducted in ANSYS. The comparisons are further provided between the virgin model without cold work effects and modified model with the effect of residual stress and strain hardening. The results obtained from the numerical simulation are again verified by the experimental and analytical data.

## 6.1 Sigma beams with roll forming effects

The effects of cold work were usually ignored in the conventional design because it was assumed that the negative effects induced by residual stress can be balanced by the positive effects of strain hardening. In the meanwhile, the impact of residual stresses are often excluded in the design and FE analysis as the cold working induced

residual stress is of a complex nature and the distribution will not only depend on the type of manufacturing but also the properties of steel material. However, the existence of residual stress will influence the stiffness of the member and the combined effect of residual stress and strain hardening can affect the materials properties and the stability of components. Therefore, the effects of roll forming on structural beams in sigma sections are investigated herein. The numerical simulation is conducted in the present study for achieving the effect of roll forming on sigma beams. The numerical models are established based on the bending test of roll formed sigma section conducted by Liu et al. (2011a)

In the test, the simply supported sigma purlin was subjected to a concentrated load to simulate the response of two-span continuous beam near the internal support, as showed in Fig. 6-1. The central point load was applied to represent the reaction at the internal support while the purlin was constructed to represent the hogging moment region near an internal support. The load was applied to the purlin via a rigid universal beam section (UBS) and a stiffened loading cleat. The loading cleat was bolted to the sigma purlin by using four bolts. Because the loading jack was sufficiently rigid, the sigma purlin was laterally and rotationally restrained at the loading section. The purlin was supported on beams with square hollow section (SHS) at both ends. The ourtweb of purlin was connected to the cleat by grade 8.8 M12 bolts for the 200 and 240 series sections, and grade 8.8 M16 bolts for the 300 series sections.
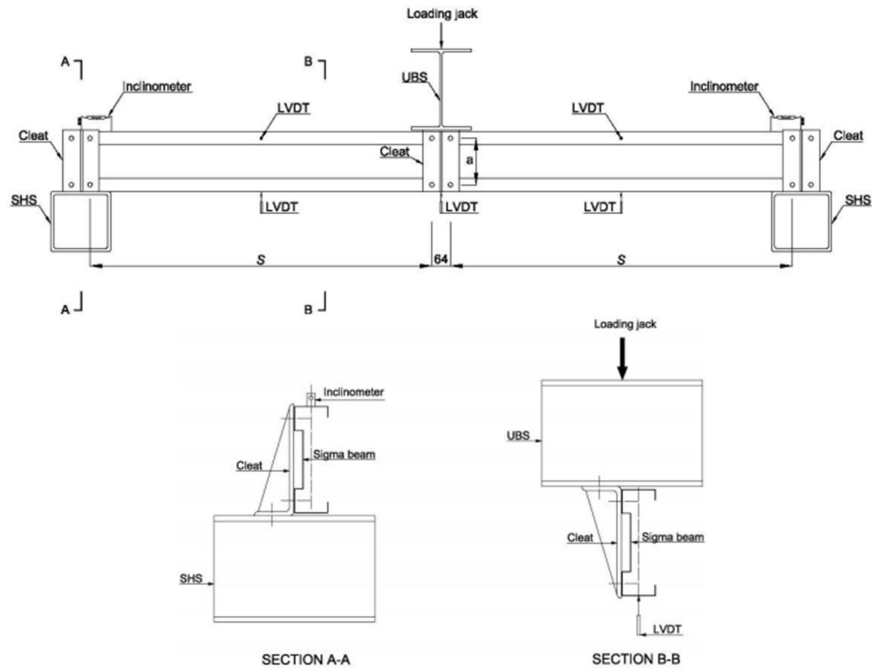
**Figure 6-1: Test set-up (Liu et al. 2011a)**

The geometric dimensions of each specimen are summarized in Table 6-1with the span length was 1.2m and 2m, respectively, which taken as the 1/5 span length (assumed as the distance between two inflexion points) of full-scale purlin.

**Table 6-1: List of sigma sections (Liu et al. 2011a)**

| Section | Depth mm | Flange mm | Lip mm | Outer Web mm | Thickness mm | Corner radius mm |
|---------|----------|-----------|--------|--------------|--------------|------------------|
| 20012 | 200 | 62.5 | 20 | 45 | 1.2 | 4 |
| 20016 | 200 | 62.5 | 20 | 45 | 1.6 | 4 |
| 20025 | 200 | 62.5 | 20 | 45 | 2.5 | 4 |
| 24015 | 240 | 62.5 | 20 | 50 | 1.5 | 4 |
| 24023 | 240 | 62.5 | 20 | 50 | 2.3 | 4 |
| 24030 | 240 | 62.5 | 20 | 50 | 3.0 | 4 |
| 30018 | 300 | 75 | 20 | 60 | 1.8 | 4 |
| 30025 | 300 | 75 | 20 | 60 | 2.5 | 4 |
| 30030 | 300 | 75 | 20 | 60 | 3.0 | 4 |
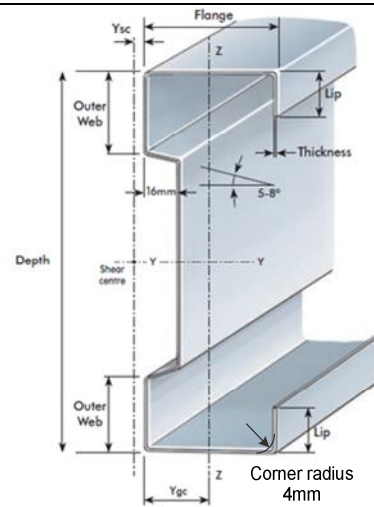


## 6.1.1 Numerical modelling process

In the model, shell element, namely SHELL181 and SHELL63 were employed to model the cross-section of the sigma beam and the bolt elements respectively. The primary difference between these two types of the shell element is that the former is suitable for nonlinear analysis and the latter is only designed for linear elastic analysis. The nominal yield strength of the tested sigma beam was 450N/mm$^2$ and the nonlinear plastic properties were adopted by using the tensile test curve presented in Liu's et al. (2011b) study. The mesh size for numerical analysis also followed the suggestion in that study, namely 2 elements in the lip, 8 elements in the flange, 8 elements in the outerweb, 12 elements in the innerweb and 1 element in the rounded corners.

Downwards loadings were applied on the four bolt holes at the mid-length section. As the element SHELL63 was incompatible with the residual stress import file, the bolt element was ignored in the model and bolt restraints were applied to bolt-holes. For eight bolt holes on the beam, the upper quarter of circular arc of each bolt-hole were restrained in both vertical and lateral direction and other nodes were only restrained in lateral to simulate bolt to beam interaction and the support of cleats (see Fig. 6-2b). Two nodes on the mid-section were restrained in the longitudinal direction to resistance the overall movement in this direction. The meshed model and applied boundary conditions are presented in Fig. 6-2a.



(a) Meshed model of specimen 24-20012        (b) Detail of bolt-hole restraints
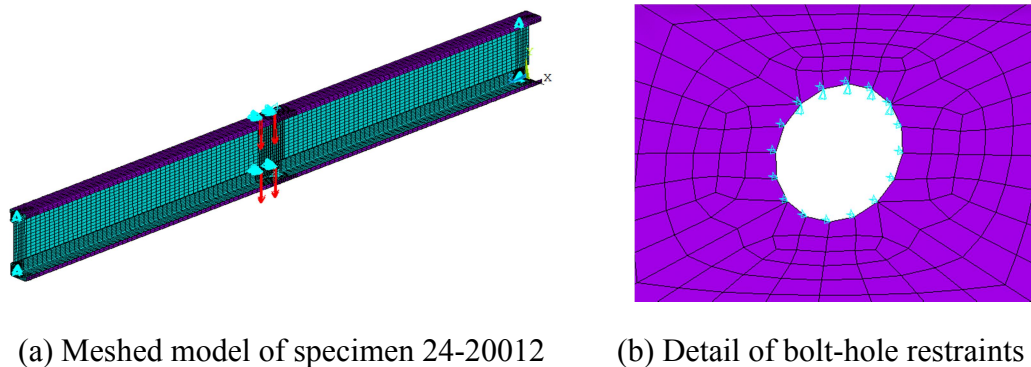
**Figure 6-2: Meshed model and boundary conditions**

The applied geometric imperfection magnitude for LB, DB and LTB mode was 0.5t 1.0t and1.5t (Liu et al. 2011b), respectively, where t represents the shell thickness. The characteristic buckling modes obtained by linear elastic buckling analysis for the specimen 24-20012 are illustrated in Fig. 6-3.

(a) LB            (b) DB            (c) LTB
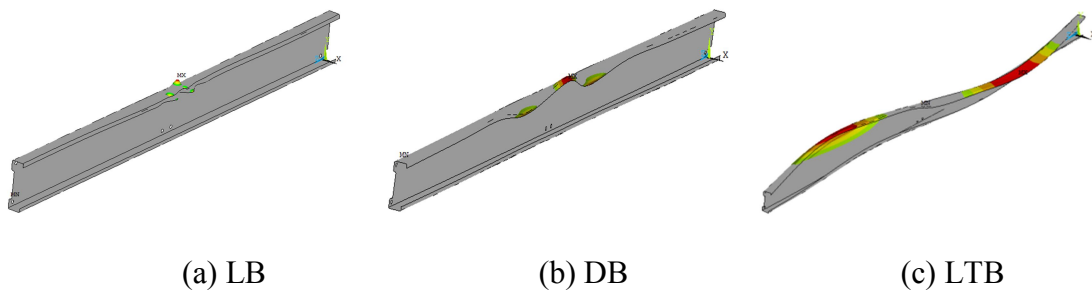
**Figure 6-3: Buckling modes of specimen 24-20012**

There are two steps to import the residual stress to the model:

In the first step, to establish the geometrical model and fix all nodes in all degrees of freedom to avoid undesired deformations induced by residual stress. Import initial stress file and run the linear static analysis, to achieve the reaction force of each support. The purpose of this step is to obtain the reaction file of all nodes as a preparation for the second step.

Step 2: Clear all restraints and apply the real load and boundary conditions. Input the reaction file and initial stress file, the application of reaction file can eliminate the unexpected deformations induced by initial stress. Then, to conduct a linear elastic buckling analysis (i.e. an eigenvalue analysis) to obtain the eigenvalue-type buckling modes. The local and distortional buckling modes of their lowest orders are selected as the components to make the geometric imperfection shapes of the beam. Finally, define the nonlinear material properties and conduct the nonlinear analysis.

The distribution of residual stress was based on the numerical achieved results of sigma section 20012 illustrated in Fig. 4-21. The input residual stress on the outside surface is shown in Fig. 6-4.
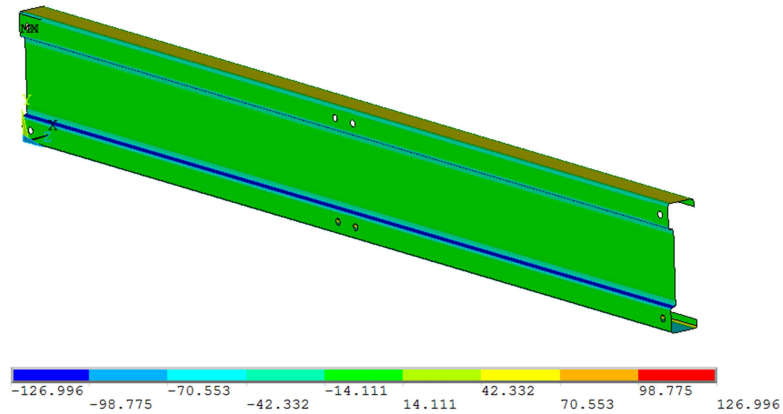


(a) Transverse residual stress
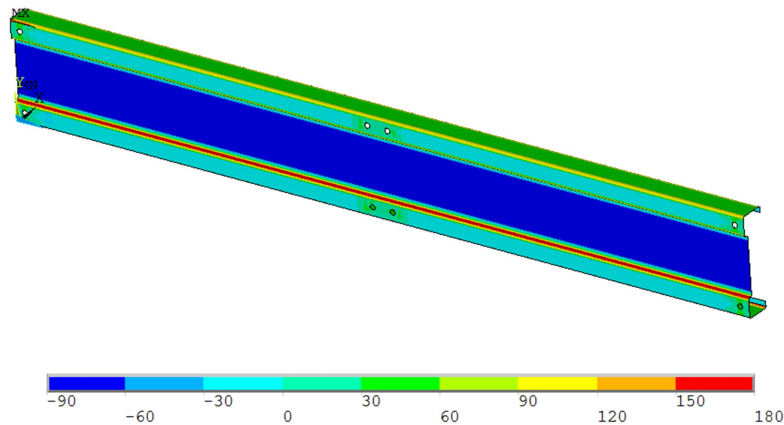


(b) Longitudinal residual stress

**Figure 6-4: Stress contours on the outer surface of the sigma section 20012**

It was assumed that the effect of shell thickness and section width was insignificant as the occurrence of springback, the residual stress distribution of sigma section 20012 can be applied to all specimens in the simulation. It was also assumed that there were no plastic deformations occurred during the coiling-uncoiling process as the roll

radius was sufficiently large and the residual stresses prior to roll forming stage can be ignored.

## 6.1.2 Effect of strain hardening

In order to consider the effect of strain hardening on the material strength of the cold-formed specimens in the model. A series of tensile tests were conducted to determine the enhancement of yield and tensile strength of flat and corner portions of the section. The test coupons were prepared from various positions of sigma section 20012 (200mm in depth and 1.2mm in thickness) by using sectioning method, shown in Figs. 6-5, 6. The nominal length and thickness of each sample were 250mm and 1.2mm, respectively. For increasing the accuracy of the testing result, the actual width and length of each sample were measured before each testing was taken. The geometric dimensions and measured results of the test specimens are summarized in Appendix 1.
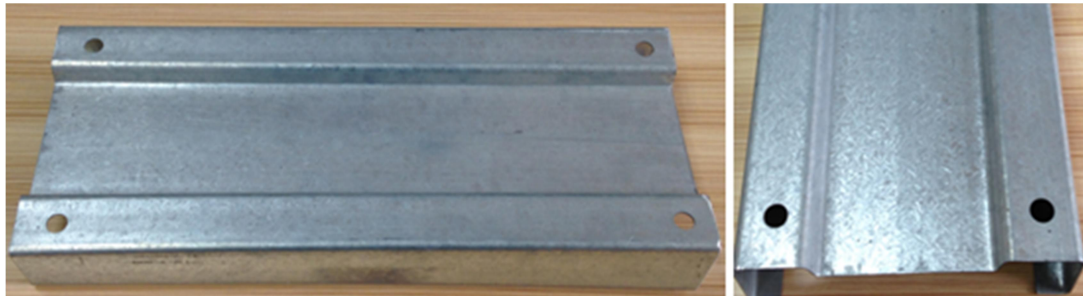


**Figure 6-5: Roll formed sigma section 20012**

(a) Flat specimens



(b) Corner specimens

**Figure 6-6: The pictures of test specimens**

The comparison of 0.2% proof stress and ultimate tensile stress between flat and corner portions is illustrated in Fig. 6-7. In the figure, the strength of the flat portion is shown in the blue line and strength of the corner portion is shown in the red triangle. The X-axis of the graphs is the cross-sectional distance and it is divided into flat and corner part according to the sectioning location. The tested strengths presented in the graphs are summarized in the Table A-1-1 and A-1-2.
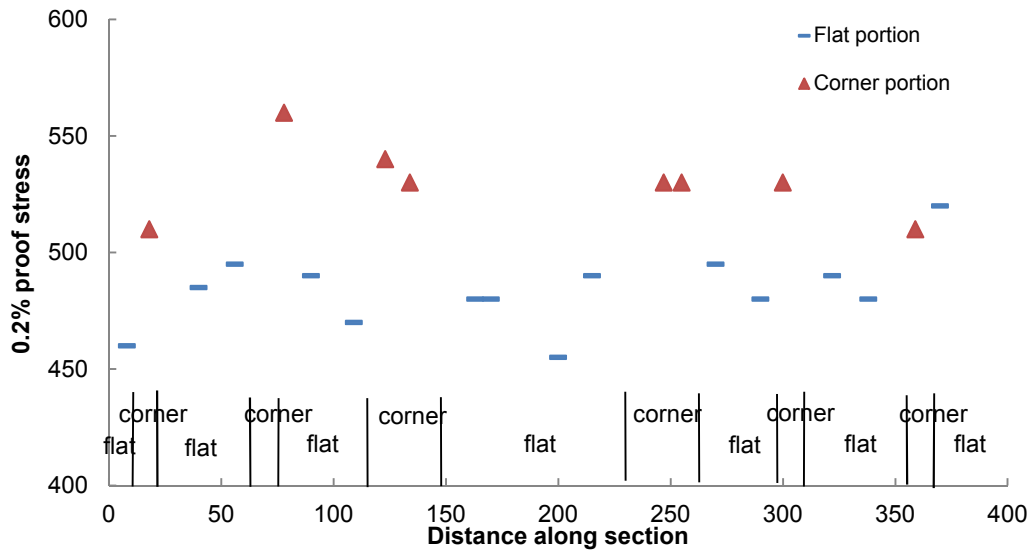
(a) Test results of 0.2% proof stress
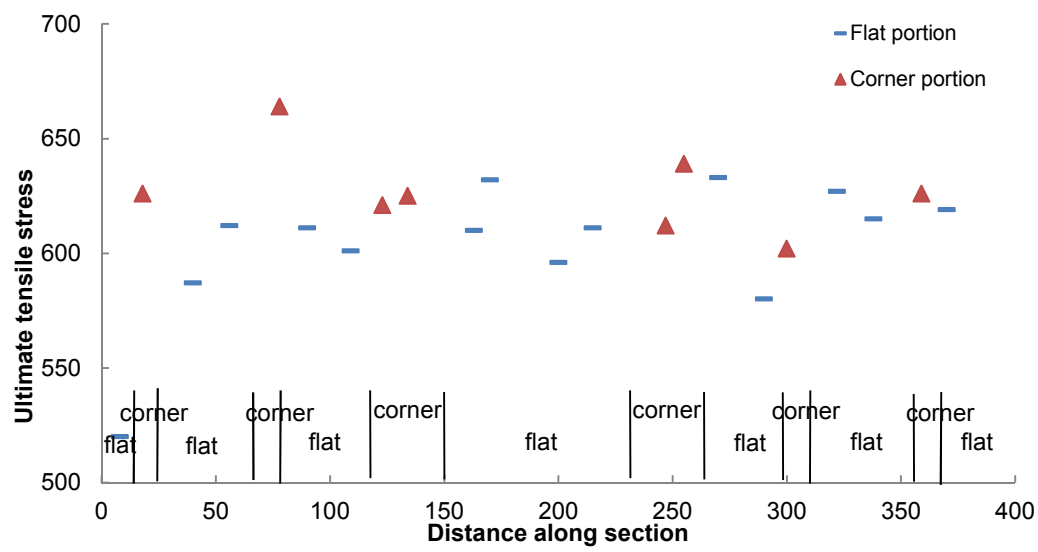


(b) Test results of ultimate tensile stress

**Figure 6-7: Comparisons of 0.2% proof stress and ultimate tensile stress**

According to the figure, the average 0.2% proof stress of corner portions is 533MPa and the strength enhancement is 10.2% when compare to the flat portion (the average 0.2% proof stress is 484MPa). Ultimate tensile stress also experiences an increasing

trend from 604MPa (average value of flat portions) to 627MPa (average value of

corner portions) with the enhancement is 3.8%. It is obvious that both 0.2% proof

stress and ultimate tensile stress of the sigma section have an enhancement during the

roll forming process, and the enhancement of the yield strength is considerably higher

than the ultimate strength.

In the model, the utilization of the strength enhancement in the material properties

that result from cold forming operation was considered. The true stress-strain curve

(Liu et al. 2011a) was adopted for the virgin model, and the modified stress-strain

curves were used for the models with the strain hardening effect. The true and

modified stress-strain curves of each specimen are summarized in Fig. 6-8. In the

figures, the enhanced curve of each section is according to the modified Ludwik

equation (Eqs. 2-15, 16) presented by Chakrabarty (2006), and the selection of value n

is to let the modified curve fitting the enhancement yield strength $f_{ya}$ calculated by

equation  (Eq. 2-13) in BSI (2006).
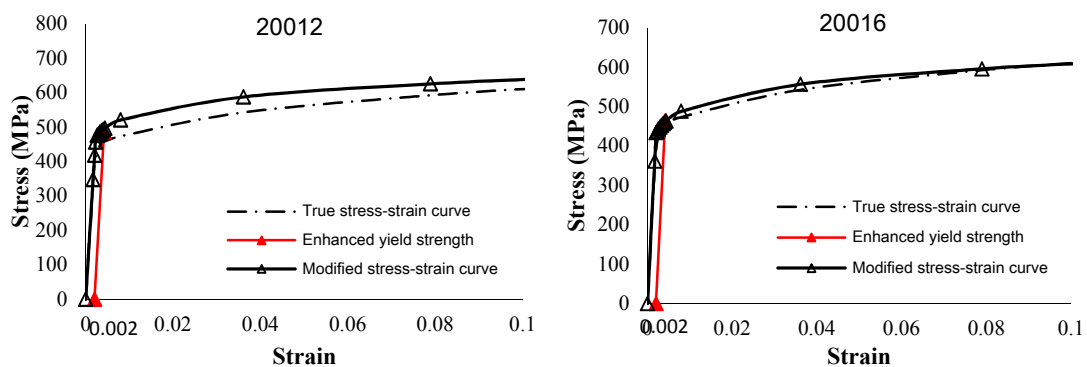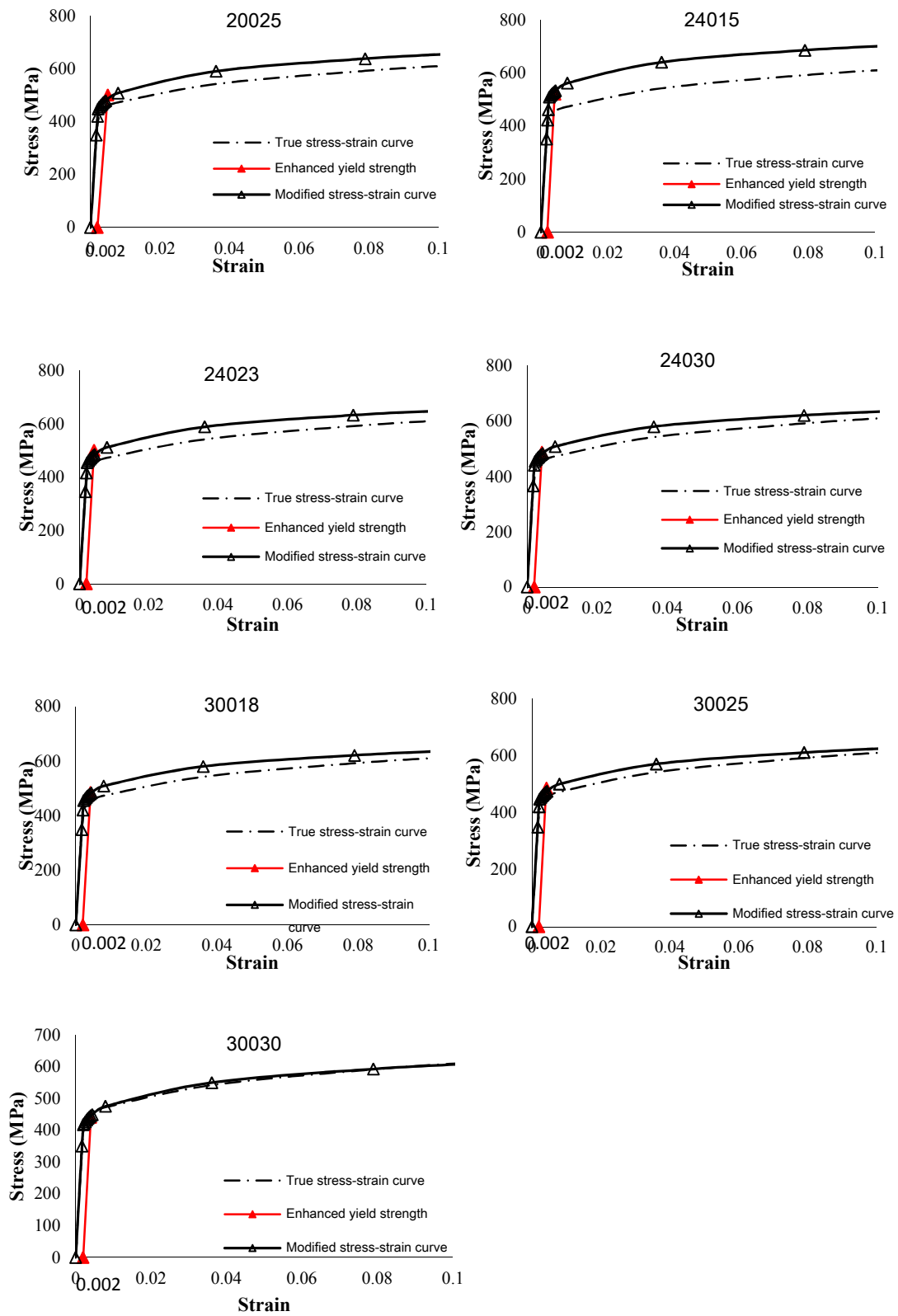
**Figure 6-8: True and modified stress-strain curves**

### 6.1.3 Result comparisons

In the FE model, the residual stress and strain hardening induced in roll forming is introduced to the model. In order to verify the FEA, the comparison is carried out between experimental data obtained by Liu et al. (2011a) and numerically obtained.

The comparison of experimentally and numerically achieved results is presented in Fig. 6-9 while the load versus deflection curves for each specimen in different cases is illustrated. The curves can be divided in four categories: (a) test result; (b) FE model with virgin stress-strain relationship (virgin); (c) FE model with the effect of residual stress (RS); (d) FE model with the effect of strain hardening (SH); (e) FE model with combined effect of residual stress (RS) and strain hardening (SH).
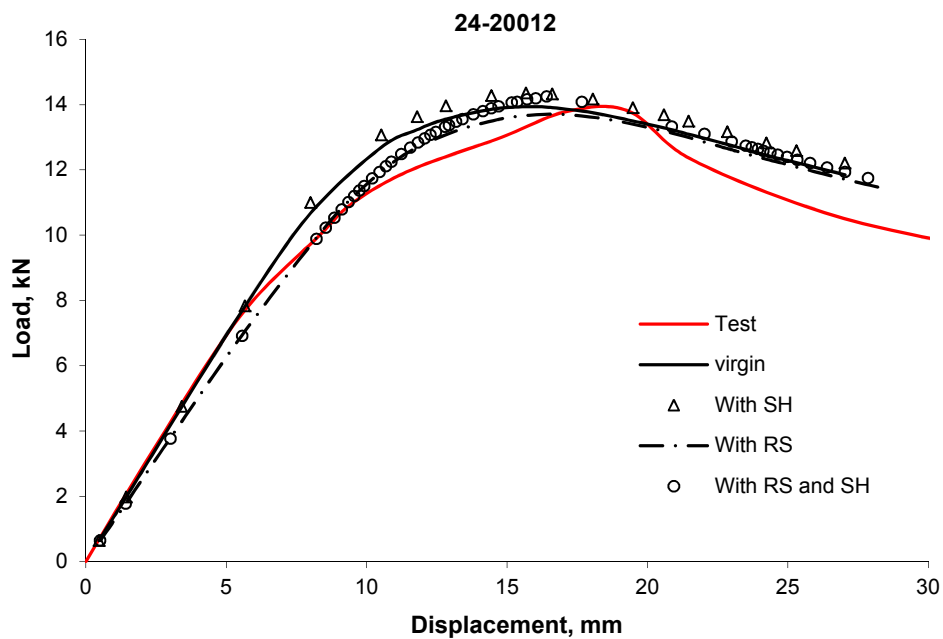


(a) 24-20012

(b) 24-20016



(c) 24-20025

(d) 24-24015



(e) 24-24023

(f) 24-30018



(g) 24-30025

**40-20025**



(h) 40-20025

**40-24030**



(i) 40-24030

144
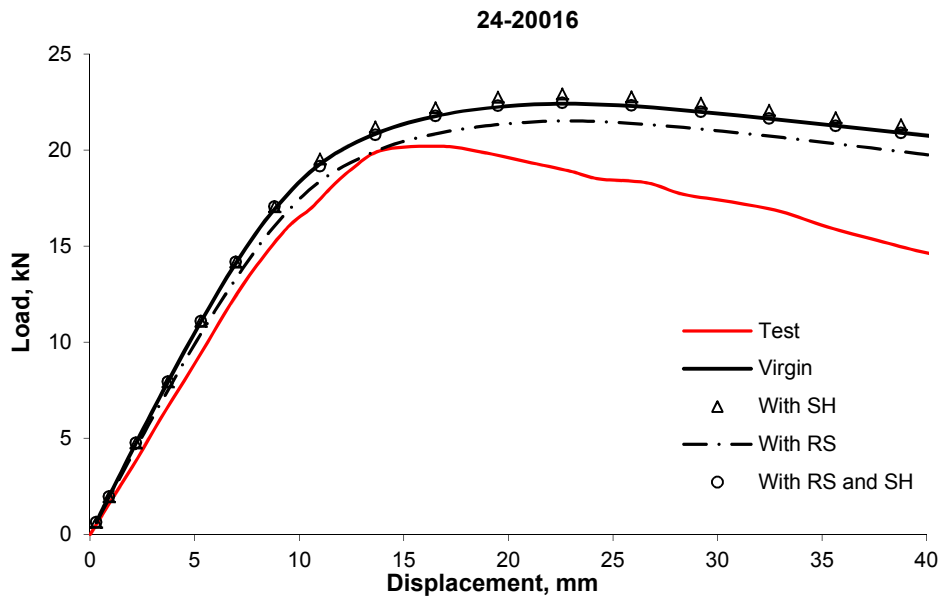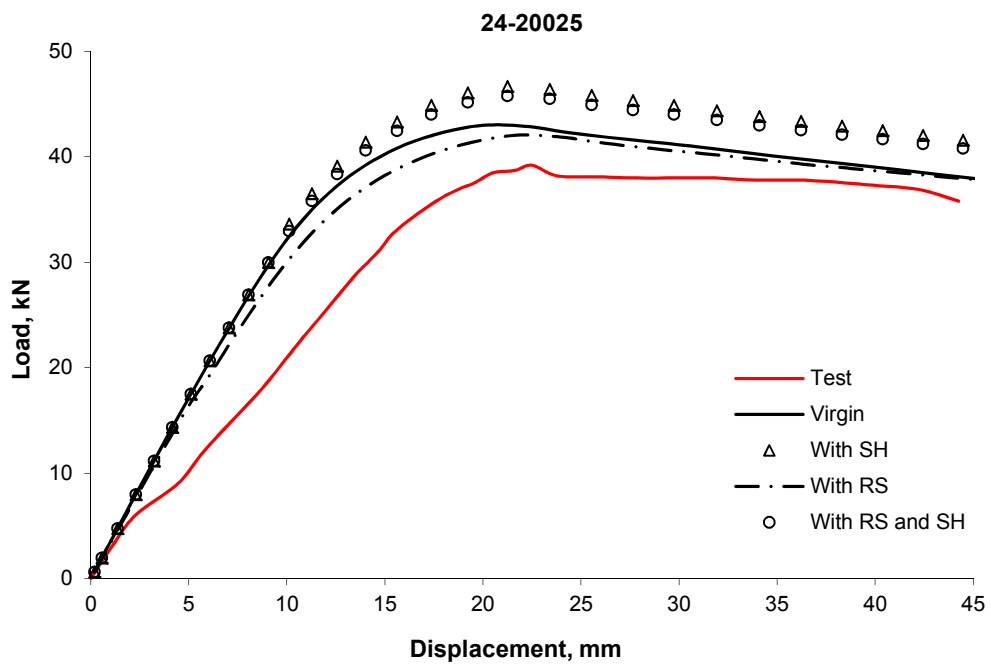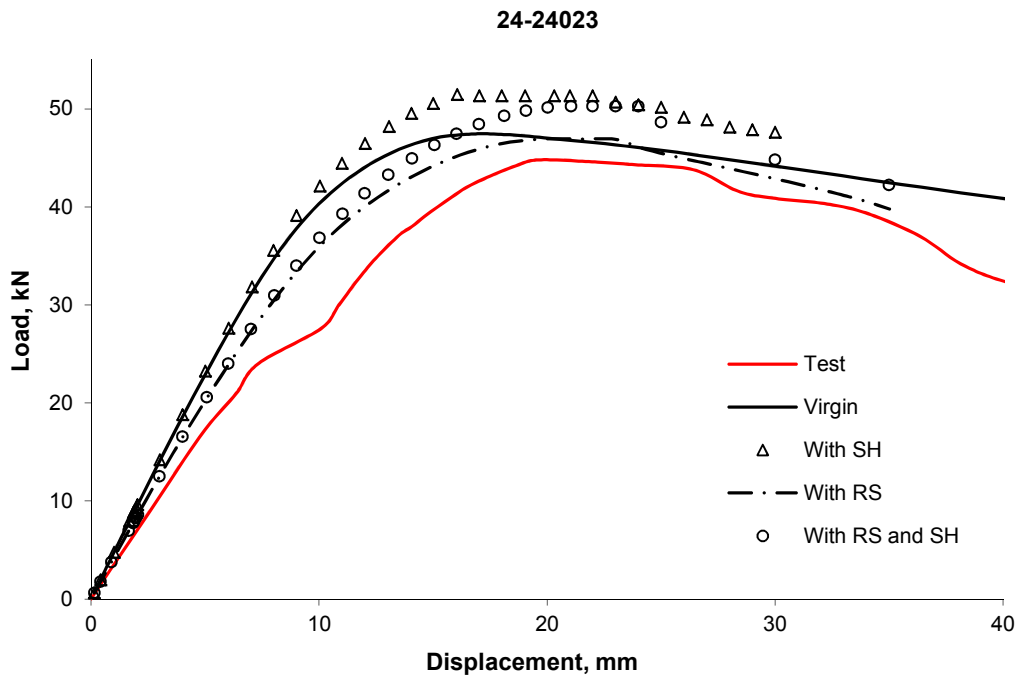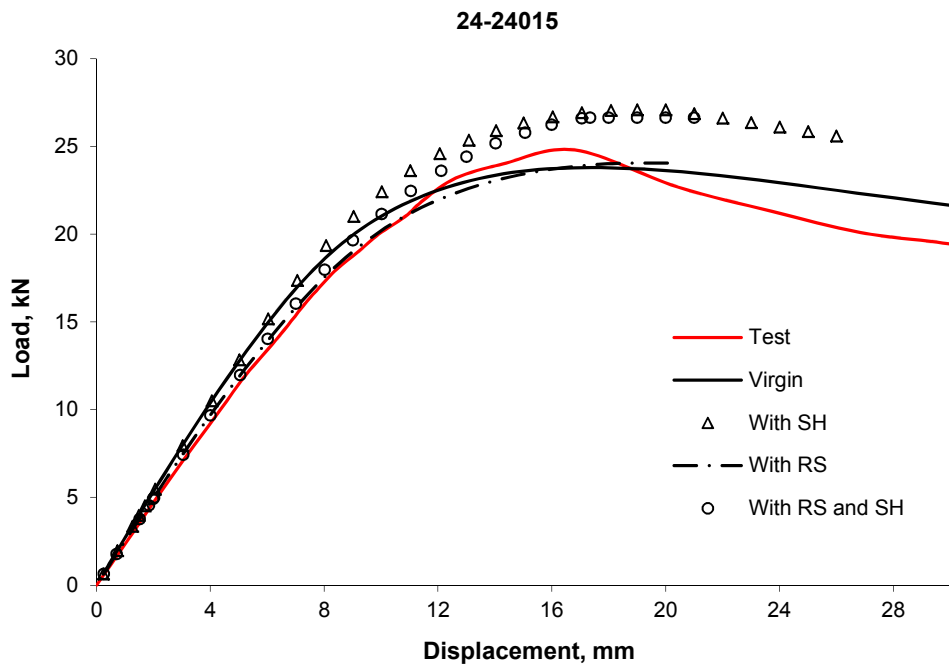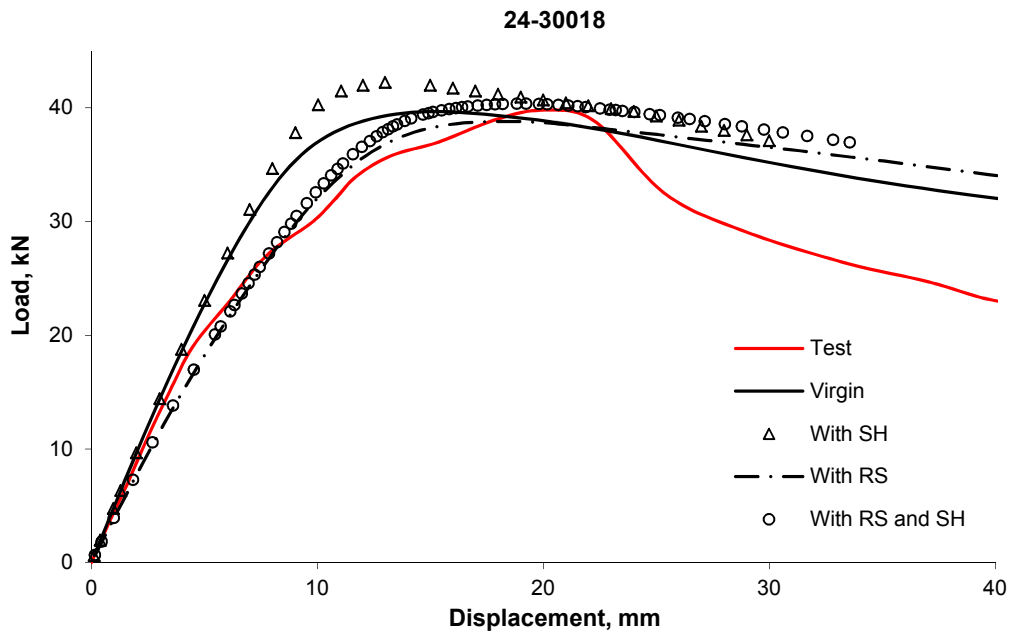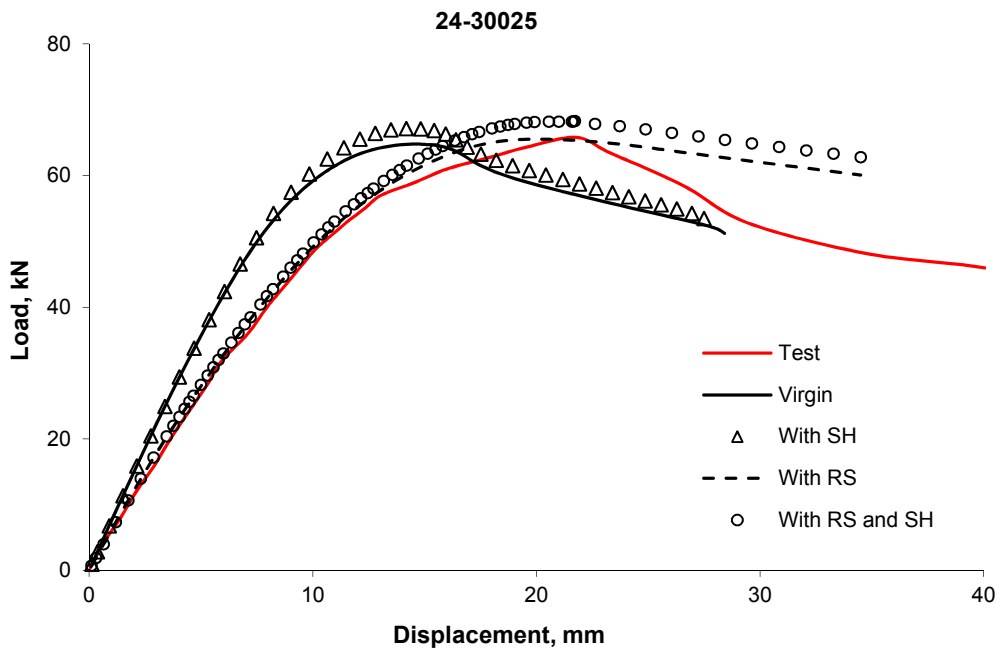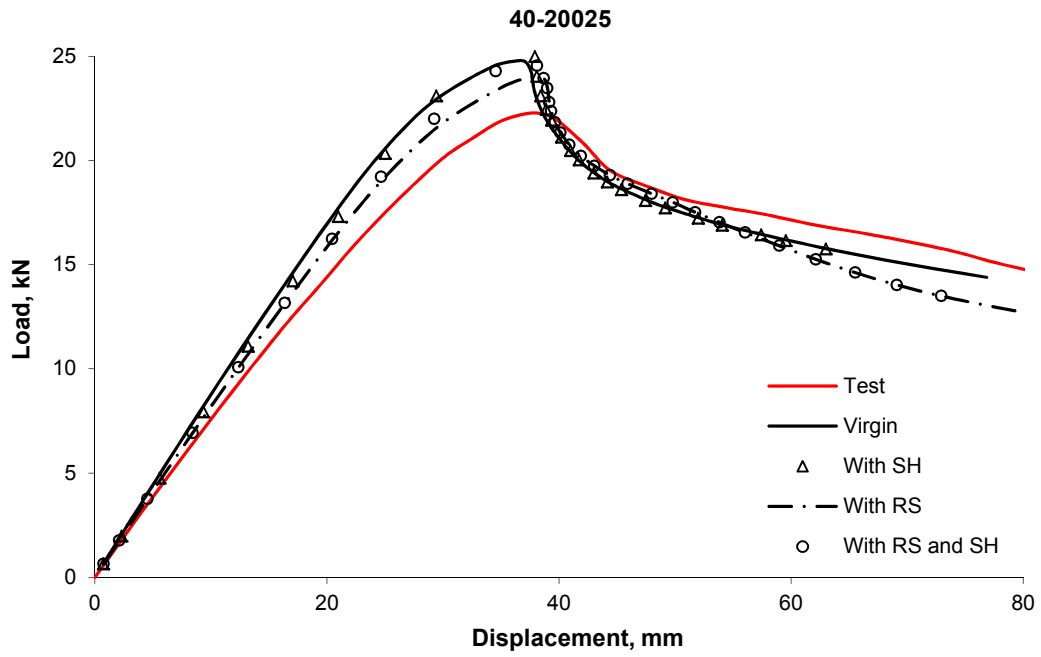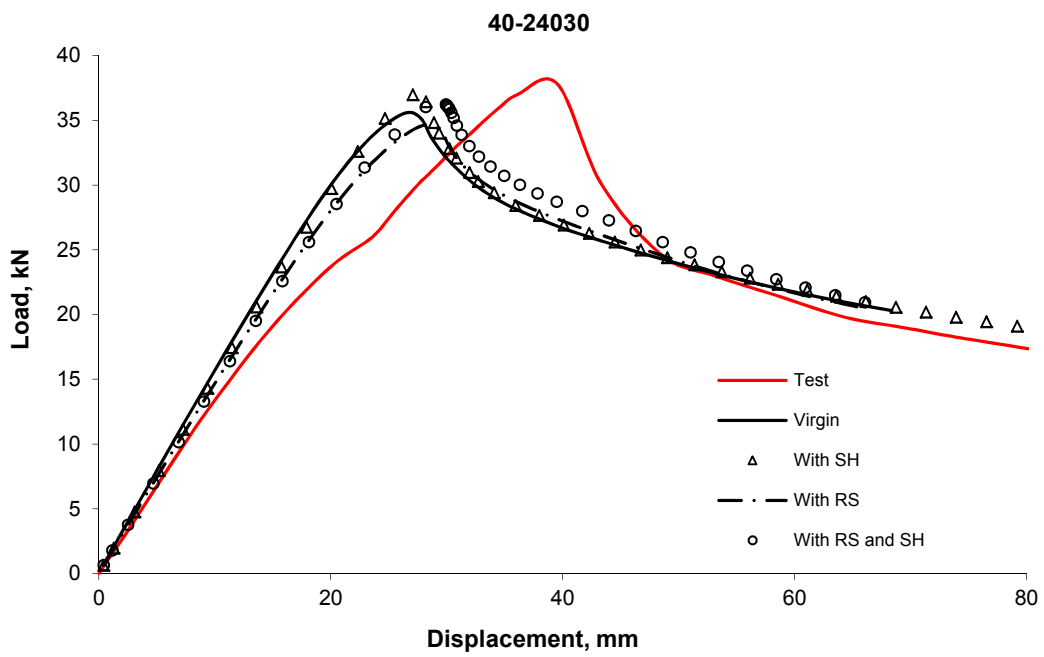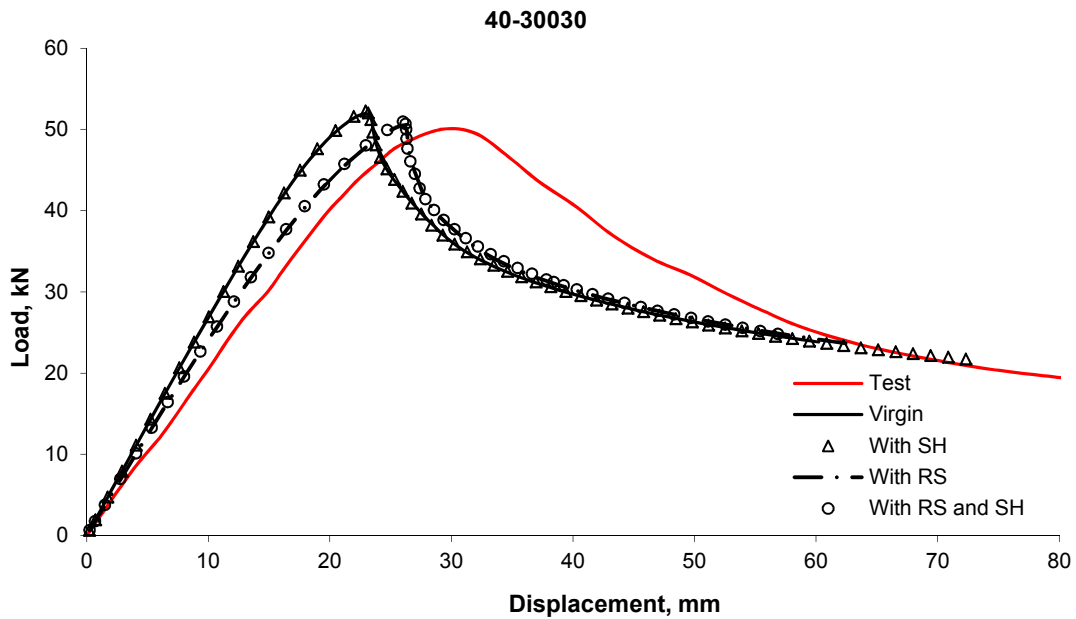
**40-30030**

(j) 40-30030

**Figure 6-9: Comparison of load-deflection curves**

Inspection of the Fig. 6-9 shows that the load-deflection response is sensitive to the residual stress and strain hardening. The existence of residual stress can decrease the stiffness and failure load of the virgin beam. A combined effect of residual stress and strain hardening can increase the peak load of sigma beams when compared with the model only consider the effect of residual stress. A better agreement can be achieved between the test result and the FE model with both RS and SH, which also indicate the ignorance of cold work during design should lead to an inaccuracy outcome.

In order to further investigate the effect of each variable, the test and predict failure loads from different models are summarized in Table 6-2.

**Table 6-2: List of failure loads**

| Specimen | $P_{cr,t}$ (kN) | $P_{FE,V}$ (kN) | $P_{FE,SH}$ (kN) | $P_{FE,RS}$ (kN) | $P_{FE,RS,SH}$ (kN) | $\dfrac{P_{FE,V}}{P_{cr,t}}$ | $\dfrac{P_{FE,RS}}{P_{cr,t}}$ | $\dfrac{P_{FE,SH}}{P_{FE,V}}$ | $\dfrac{P_{FE,RS}}{P_{FE,V}}$ | $\dfrac{P_{FE,RS,SH}}{P_{FE,RS}}$ |
|---|---|---|---|---|---|---|---|---|---|---|
| 24-20012 | 13.80 | 13.9 | 14.4 | 13.7 | 14.2 | 1.01 | 0.99 | 1.04 | 0.99 | 1.04 |
| 24-20016 | 20.20 | 22.41 | 22.91 | 21.51 | 22.46 | 1.11 | 1.06 | 1.02 | 0.96 | 1.04 |
| 24-20025 | 39.20 | 42.99 | 46.69 | 42.07 | 45.78 | 1.10 | 1.07 | 1.09 | 0.98 | 1.09 |
| 24-24015 | 24.80 | 23.79 | 27.1 | 24.05 | 26.64 | 0.96 | 0.97 | 1.14 | 1.01 | 1.11 |
| 24-24023 | 44.80 | 47.47 | 51.46 | 46.96 | 50.26 | 1.06 | 1.05 | 1.08 | 0.99 | 1.07 |
| 24-30018 | 39.80 | 39.68 | 42.24 | 38.8 | 40.36 | 1.00 | 0.97 | 1.06 | 0.98 | 1.04 |
| 24-30025 | 65.80 | 64.77 | 67.16 | 65.51 | 68.25 | 0.98 | 1.00 | 1.04 | 1.01 | 1.04 |
| 40-20025 | 22.20 | 24.77 | 25.72 | 24.01 | 24.55 | 1.12 | 1.08 | 1.04 | 0.97 | 1.02 |
| 40-24030 | 37.80 | 35.59 | 36.98 | 34.62 | 36.23 | 0.94 | 0.92 | 1.04 | 0.97 | 1.05 |
| 40-30030 | 50.00 | 51.59 | 52.28 | 50.48 | 50.94 | 1.03 | 1.01 | 1.01 | 0.98 | 1.01 |
| **Mean** | | | | | | **1.03** | **1.01** | **1.06** | **0.98** | **1.05** |

From the table, it can be seen that the average ratio between FE virgin result and test result is 1.03 while the ratio between RS model and test result is 1.01, which shows that a closer agreement can be obtained when considering the effect of RS in the model. The ratio of the failure load between SH model and FE virgin model is 1.06, which represents the effect of strain hardening in the failure load is not negligible. The ratio between RS model and FE virgin model is 0.98 and between RS-SH model and FE virgin model is 1.05, which indicates the enhancement induced by strain hardening is the dominate factor.

**6.2 Sigma beams with press braking and welding effects**

In this part, the influence of welding and press braking process on the behaviour of simply supported single-span sigma beams is studied numerically. In the model, the preceding achieved distribution of press braking and welding residual stress is imported into FE program as initial stress file. The effects of geometric imperfection and strain hardening are also considered simultaneously. The numerical results are further validated by values obtained from laboratory test and analytical method.

**6.2.1 Purlin-sheeting bending test under UDL**

In the test, a vacuum box was introduced to simulate the uniformly distributed load (UDL) downward loading condition. The purpose of using such a loading pattern was to avoid the local bearing effect caused by concentrated loads. The dimension of the box was 2m in width, 7m in length and 0.76m in height. The downward UDL was applied to purlin-sheeting system representing the actions of wind pressure. A pair of simply-supported identical sigma purlins with 6m length was placed in parallel with opposing faces. The purlins were bolted by four steel angle cleats placed on two steel stands at both ends. The steel stand was welded to the vacuum chamber and the strength was assumed far beyond the purlins so the deformation of the steel stand can be ignored. Connections between cleats and purlins were through Grade 8.8 M12 bolts for section series 200 and 240 and M16 for section series 300. The test setup is shown in Fig. 6-10.

**Figure 6-10: Overall test assemblies**

As the length of the press-braked machine in the factory is only two meters, in order to achieve a six meters beam, three short purlins were butt-welded together by arc welding. The location of the weld bead is shown in Fig. 6-11, it can be seen that there are two weld beads located on the quarter-span sections on each purlin (see Fig. 6-11).



**Figure 6-11: The purlin with weld beads**

The sheet used in the test was 1.2m in width, 1m in length and 0.6mm in thickness. It was fastened onto purlins by using self-drilling screws applied at predefined intervals about 400mm (see Fig. 6-12a). There were six sheets used for each test and 36 self-drilling screws were used for the sheet to purlin connection. The diameter of the screw

was 5.5mm while the diameter of the washer was 1mm larger than the screw. The geometric dimensions of the sheeting are shown in Fig. 6-12b.



(a) Sheets to purlin connection
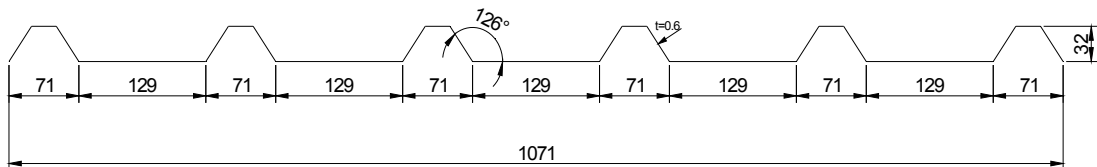


(b) Dimensions of sheeting (unit: mm)

**Figure 6-12: Details of sheeting**

The specimens used in the test were press-braked sigma section 20012, 20014, 20024, 24014, 24024, 30020 and 30030, all in 6m length. The cross-sectional geometric dimensions of each specimen can refer to the Table 6-1. It needs to be noted that the

thickness of each specimen in this test is 1.2mm, 1.4mm, 2.0mm, 2.4mm and 3.0mm, respectively.

Seven linear variable displacement transducers (LVDTs) were placed for purlins to measure the vertical and horizontal deflections. The arrangement of LVDTs for this purlin was like this: five LVDTs were used for the purlin with greater initial geometric imperfection, three of them were placed at the mid-span and both quarter-span points on the free flange to measure vertical deflections, and two were placed on the lower outerweb at the mid-span and quarter-span cross section to measure the horizontal deflection; the other two LVDTs were applied to measure the vertical and horizontal deflections at the mid-span point of the second purlin. The setup of LVDTs for mid-span and quarter-span section is shown in Fig. 6-13. As the same setup to LVDT, strain gauges were mounted on the middle and quarter span sections, with strain rosettes on the innerweb and unidirectional strain gauges on the outerweb and flange.



**Figure 6-13: The setup of test instruments**

When completed the test assembly inside the vacuum box, a membrane was used on the top of the box to seal the open side. The membrane was bolted to all edges of the box (see Fig. 6-14) with the bolt diameter was 16mm. Then, the air inside the box was exhausted by using an air pump with the maximum pressure was 26kPa. The pressure difference between the outside and inside of the box will lead to a uniformly downward load applied to the sheeting through the membrane. The pressure of the box was controlled by an adjustable one-way valve as showed in Fig. 6-15. The valve can only be opened when air was pumped from outside to inside. The initial load increment was 0.5KPa and reduced to approximately 0.1KPa when 50% of the predict peak load was reached. The pressure, displacement and strain were recorded at all load increments until the failure occurs.



**Figure 6-14: Membrane to chamber connection**

**Figure 6-15: One-way valve**

## 6.2.2 Material properties

The nominal yield strength for test specimens was 235MPa. In order to obtain the stress-strain curve for each specimen, a series of tensile tests (see Appendix 2) were conducted for the coupons shown in A-2-1. The strength enhancement for each specimen was also considered as the same to the previous section. The virgin and strain hardening modified stress-strain curves with enhanced yield strength (BSEN) is shown in Fig. 6-16 and the tested and enhanced strength is summarised in Table 6-3.

t=1.2



t=1.4

**t=2.0**



**t=2.4**
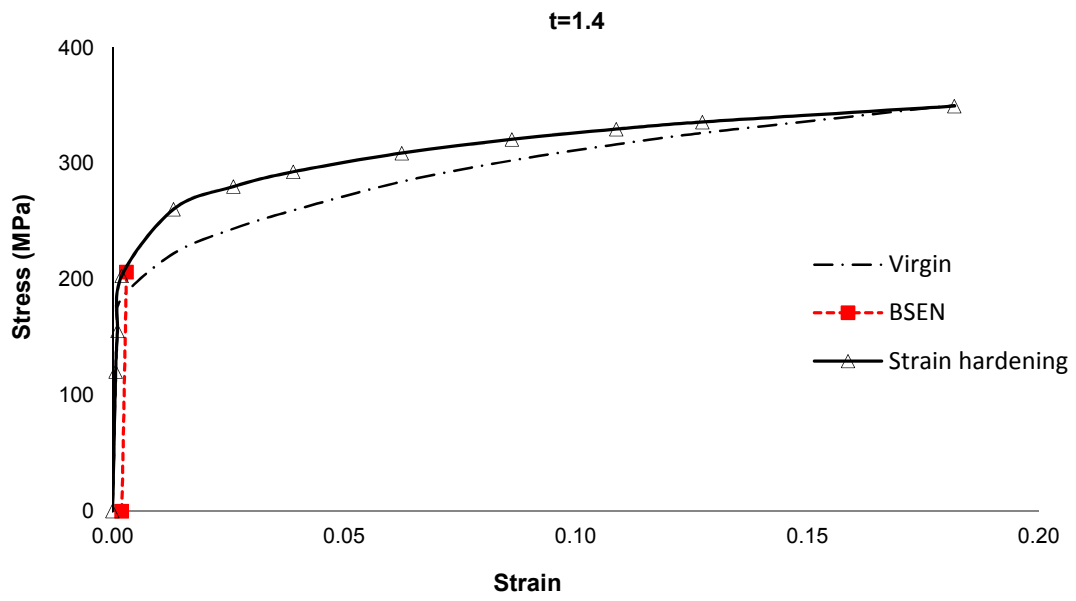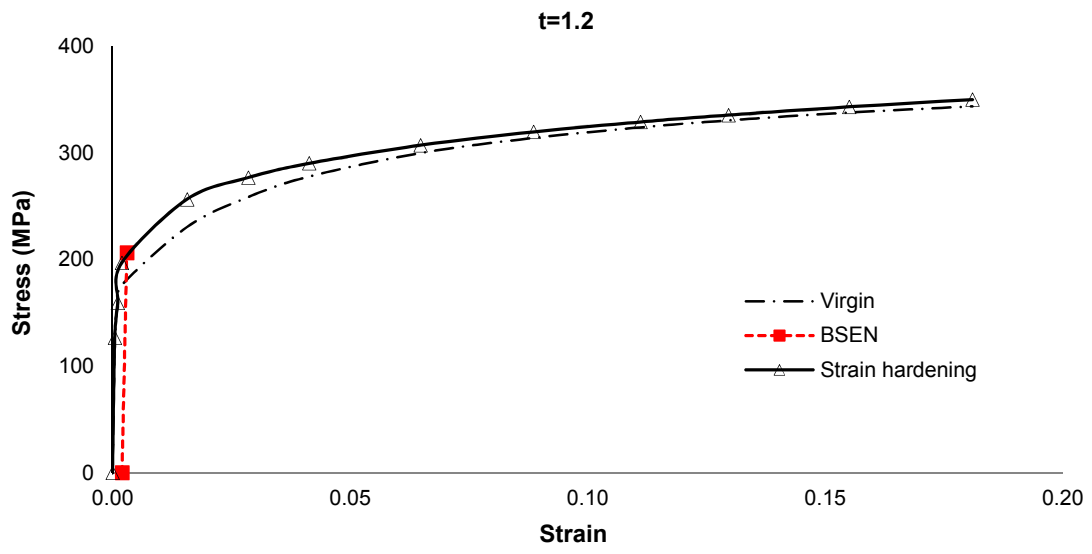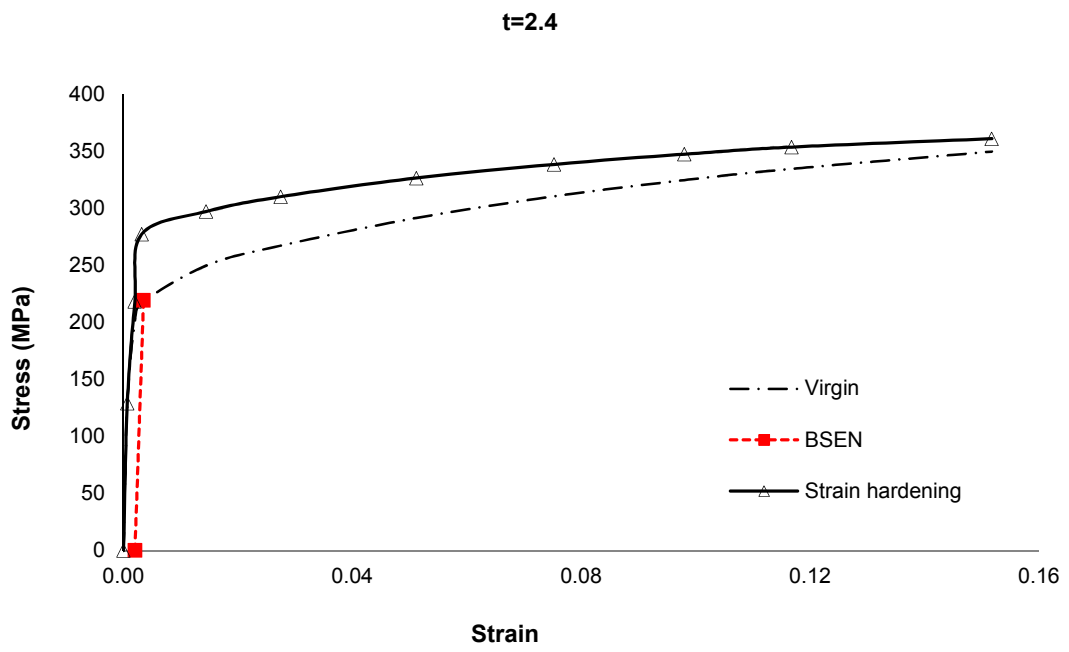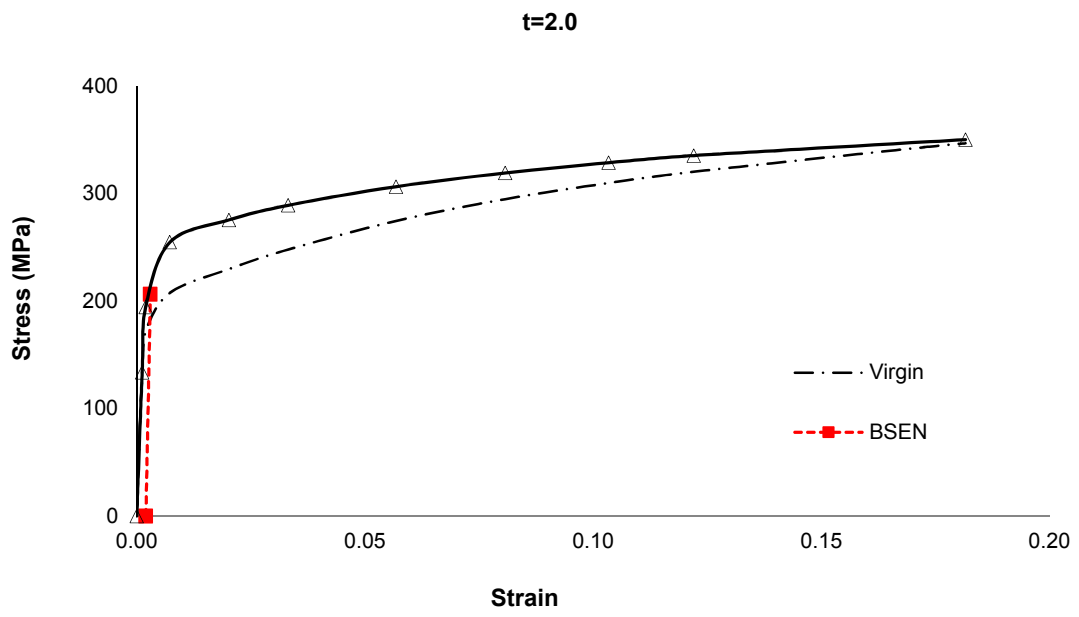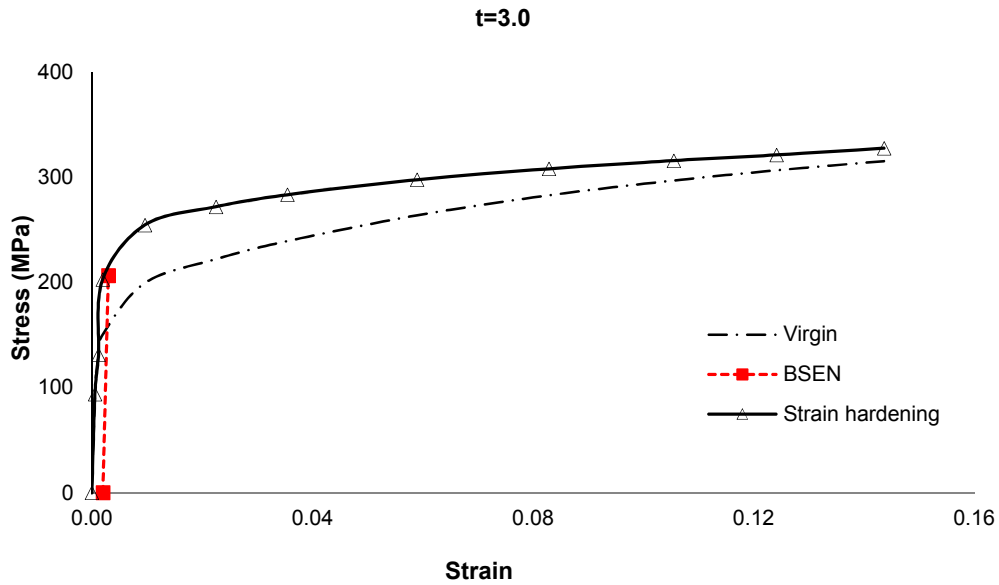
**Figure 6-16: Stress-strain curves**

The summarized test results are shown in the Table 6-3.

**Table 6-3**: **Summary of the test results**

| Specimen No. | Associated section thickness (mm) | Elastic modulus (GPa) | 0.2% Proof strength (MPa) | Ultimate tensile strength (MPa) | Enhanced yield strength (MPa) |
|---|---|---|---|---|---|
| 60-20012 | 1.2 | 203 | 178 | 344 | 206 |
| 60-20014 | 1.4 | 207 | 185 | 350 | 219 |
| 60-20024 | 2.4 | 213 | 201 | 352 | 255 |
| 60-24014 | 1.4 | 207 | 185 | 350 | 214 |
| 60-24024 | 2.4 | 213 | 201 | 352 | 252 |
| 60-30020 | 2.0 | 201 | 175 | 347 | 210 |
| 60-30030 | 3.0 | 206 | 186 | 324 | 233 |

### 6.2.3 Numerical modelling

The geometrical imperfections, residual stresses and strain hardening due to the welding and press braking process were all considered in the following simulations. The true stress-strain curves were adopted for the virgin model, and the enhanced stress-strain curves were used for the models with the strain hardening effect.

In the model, the shell element and mesh size were followed the previous internal supported model, only with the finer mesh was applied to weld beads located on the quarter-span sections of the beam (see Fig. 6-17a). The vertical bolt supports were applied on the upper quarter of the circular arc of four bolt holes and lateral restraints were applied to all bolt holes as the bolt to beam interaction (see Fig. 6-17b). The outerweb to flange junction line was fully restrained in lateral direction, represented the restraint of roof sheeting to the purlin. The UDL was applied along the middle of top-flange as the compression from sheeting.
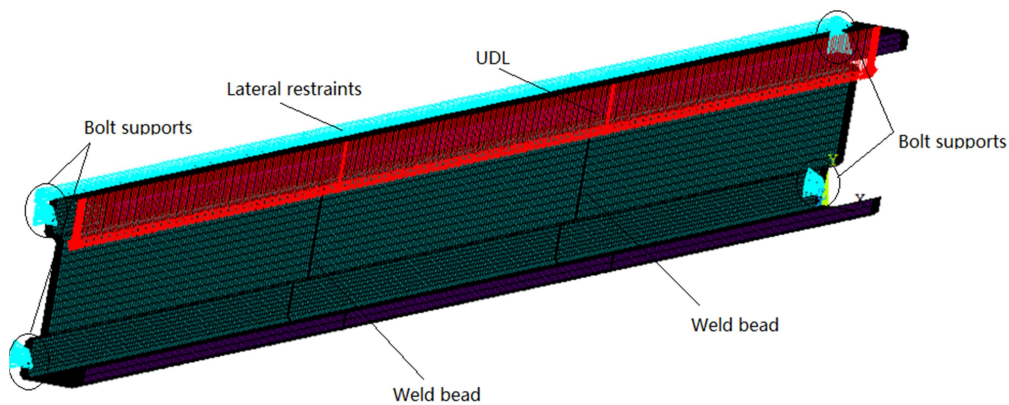


(a) Overall view of specimen 60-20014
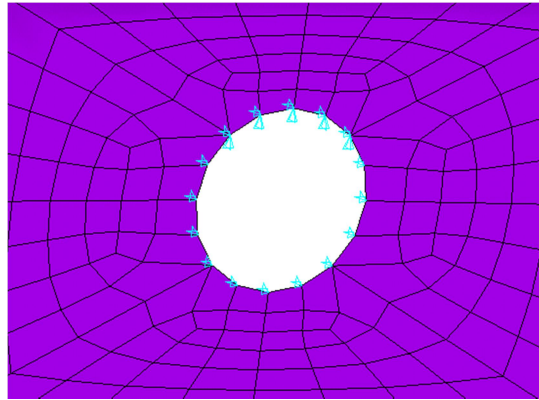
(b) Restraint details on bolt-hole line

**Figure 6-17:  Model of simply supported sigma beam**

Before carrying out the nonlinear analysis, a linear elastic eigenvalue buckling analysis was performed based on the same model with the same restraints conditions to obtain the eigenvalue-type buckling modes. The local and distortional buckling modes of their lowest orders were selected as the components making the geometric imperfection shapes of the beam and their magnitudes were 0.5t and1.0t, respectively (Liu's et al. 2011b).

Both press braking and welding residual stresses were considered as the initial input stress. The welding residual stress was only applied to weld bead and HAZ while redistribution of press braking residual stress during heat treatment was ignored. The distribution of welding residual stress in the longitudinal direction is shown in Fig. 6-18, and the combined welding and press braking residual stress in the longitudinal direction is shown in Fig. 6-19.

-400  -311.111  -222.222  -133.333  -44.444  44.444  133.333  222.222  311.111
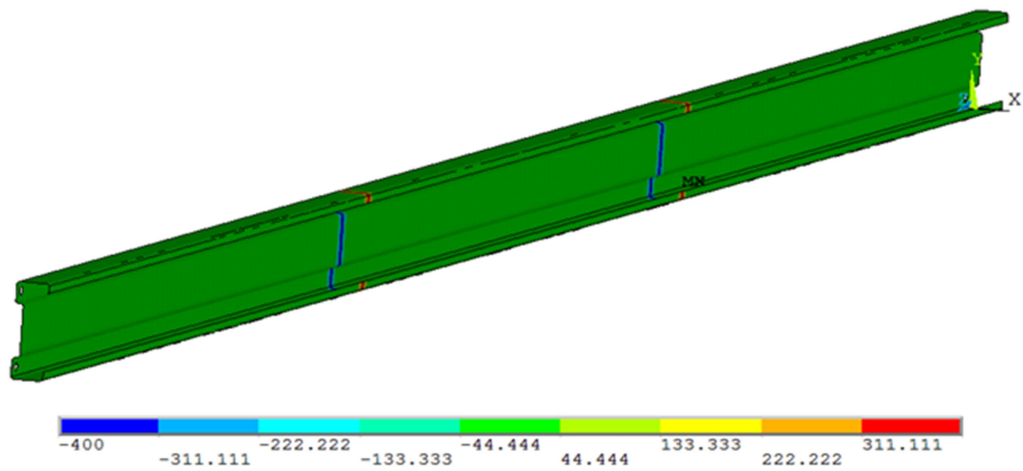
**Figure 6-18: The distribution of welding residual stress**



47.222  94.444  141.667  188.889  236.111  283.333  330.556  377.778  425
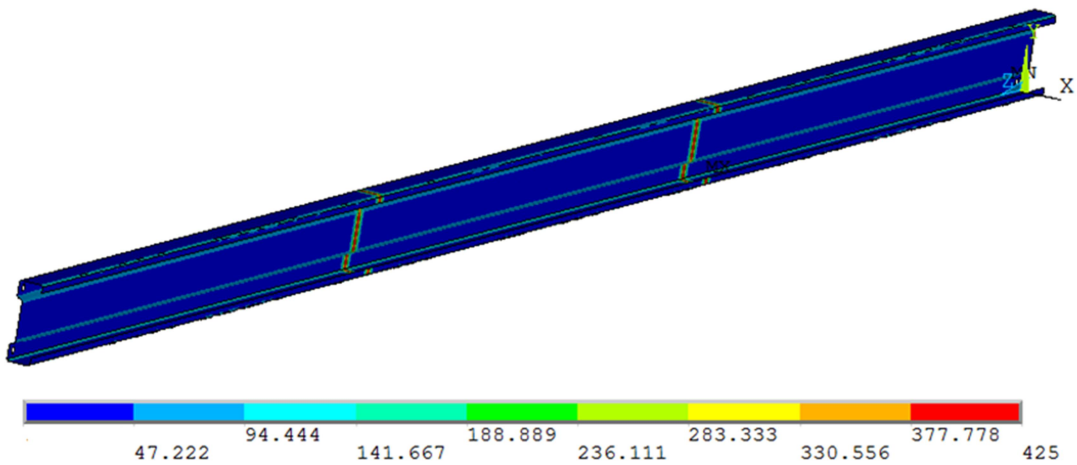
**Figure 6-19: The distribution of combined welding and press braking residual stress**

### 6.2.4 Result discussions

The failure modes of specimen 20012 and 30030 are shown in Figs. 6-20 and 6-21. It can be seen that in the section with a relatively small thickness (i.e. 20012), the

combination of local buckling and distortional buckling modes was mainly found on the left purlin. The local buckling was occurred on the top flange and the distortional buckling on the flange-to-lip junction at the mid-span (see Fig. 6-20). The mode of failure for the section with a relatively large thickness (i.e. 30030), as shown in Fig. 6-21, was described as the failure located on the sheeting (near the edges of the crest) with the distortional buckling occurred on the top flange of purlin at the mid-span. A good agreement can be found in the comparison between the numerical deformation contours with the failure modes captured from the test.
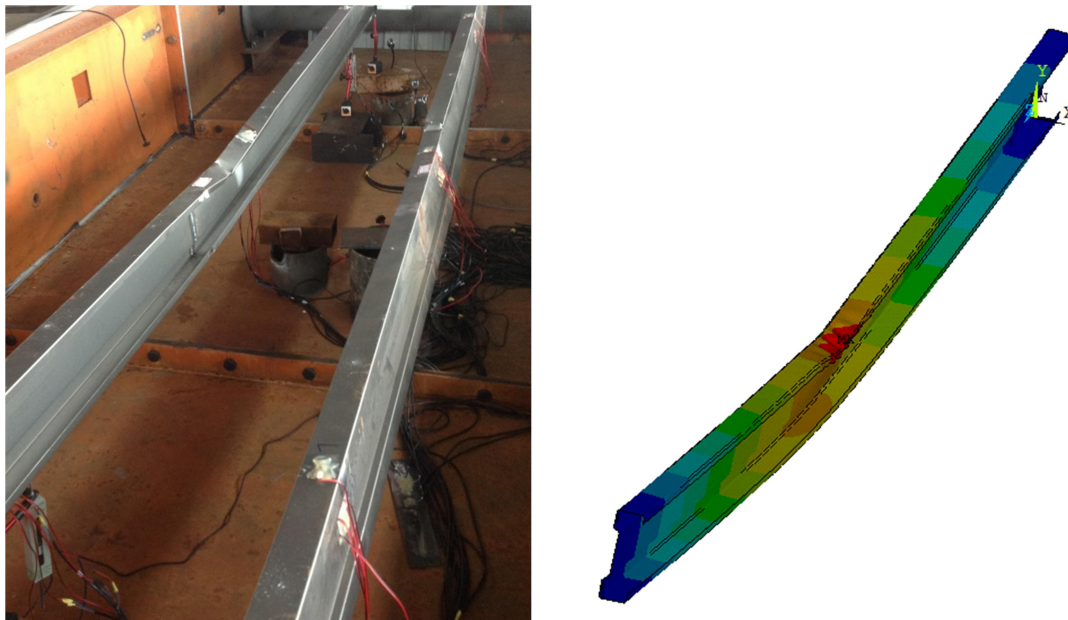


**Figure 6-20: The failure mode of sigma 20012**
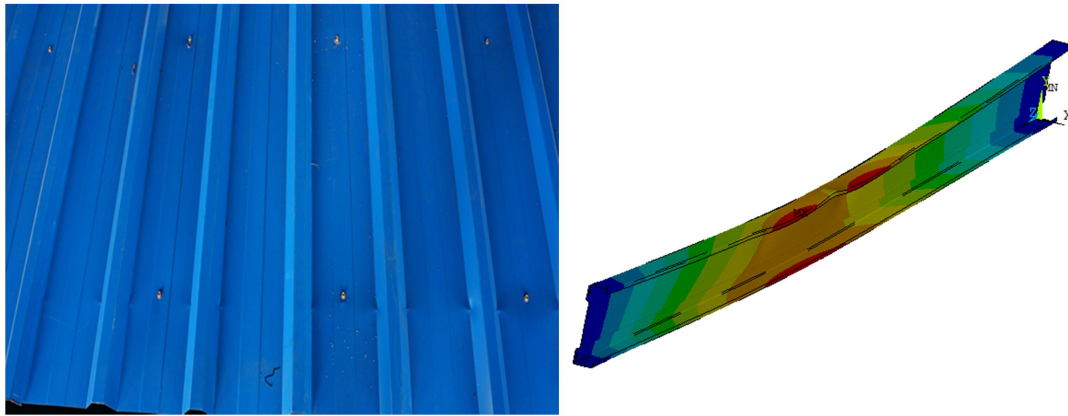
**Figure 6-21: The failure mode of sigma 30030**

The difference in failure mode is because the section with a relatively small thickness tends to have a lower local buckling resistance than the distortional buckling; when the section thickness increases, their local buckling resistance also increases, and existence of the stress concentration at the connection between purlin and sheeting lead to the tendency to distortional buckling of the purlin flange.

According to the recorded data of pressure and strain at every increment, the load-to-deflection curve can be achieved in the test. The experimental, numerical and theoretical load to deflection curves are shown in the Fig. 6-22. For the theoretical analysis, the virgin and enhanced values were achieved based on the effective and gross sectional modulus multiply by virgin yield strength and enhanced yield strength, respectively. The model only with welding residual stress (only W) and the model with combined press braking residual stress and welding residual stress (PB and W) are all presented in the figure. It should be noted that only the test results of sigma 20012 and 20014 were presented herein.

**60-20012**



**60-20014**

**60-20024**

*Load, kN/m* vs *Displacement, mm*

- Virgin
- PB and W
- Theoretical virgin
- Theoretical enhanced



**60-24014**

*Load, kN/m* vs *Displacement, mm*

- Virgin
- PB and W
- Theoretical virgin
- Theoretical enhanced

**60-24024**

Load, kN/m vs Displacement, mm

Legend:
- Virgin
- pb and w
- Theoretical virgin
- Theoretical enhanced



**60-30020**

Load, kN/m vs Displacement, mm

Legend:
- Virgin
- PB and W
- Theoretical virgin
- Theoretical enhanced

**Figure 6-22: Load to deflection curves for simply supported sigma beam**

By comparing the curves of virgin model and model with welding residual stress of specimen 60-20012 and 60-20014, it can be concluded that the effect of welding residual stress is insignificant on the load resistance capacity of sigma beam. Meanwhile, the load-deflection curves for all the specimens are enhanced by the effect of strain hardening during press braking. A good agreement can be found on the failure load of specimens between the theoretical curves and numerical curves. The theoretical curves show a greater stiffness than numerical curves when exceeding the yield stress due to the ignore of residual stress in the theoretical analysis.

In order to further investigate the effects of cold work, the failure loads of theoretical model with virgin material ($q_{T,v}$), theoretical model with press braking effect ($q_{T,pb}$),

FE model with virgin material ($q_{FE,v}$) and FE model with effect of press braking and welding ($q_{FE,pb,w}$) are summarized in Table 6-4.

**Table 6-4: List of failure loads**

| Specimens | Failure load (kN/m) | | | | $q_{T,v}/q_{FE,v}$ | $q_{T,pb}/q_{FE,pb,w}$ | $q_{FE,pb,w}/q_{FE,v}$ |
|---|---|---|---|---|---|---|---|
| | $q_{T,v}$ | $q_{T,pb}$ | $q_{FE,v}$ | $q_{FE,pb,w}$ | | | |
| 60-20012 | 1.05 | 1.20 | 1.16 | 1.29 | 0.91 | 0.93 | 1.11 |
| 60-20014 | 1.11 | 1.48 | 1.34 | 1.41 | 0.83 | 1.05 | 1.05 |
| 60-20024 | 2.45 | 2.89 | 2.59 | 2.76 | 0.95 | 1.05 | 1.07 |
| 60-24014 | 1.69 | 1.90 | 1.68 | 1.79 | 1.00 | 1.06 | 1.07 |
| 60-24024 | 3.15 | 3.63 | 3.57 | 4.18 | 0.88 | 0.87 | 1.17 |
| 60-30020 | 3.39 | 3.58 | 3.56 | 4.08 | 0.95 | 0.88 | 1.15 |
| 60-30030 | 5.40 | 6.51 | 5.28 | 6.81 | 1.02 | 0.96 | 1.29 |
| **Mean** | | | | | **0.93** | **0.97** | **1.13** |
| **S.D.** | | | | | **0.07** | **0.08** | **0.08** |

It can be found in Table 6-4 that the ratio between theoretical and FEM values with virgin model is 0.93, and the ratio between theoretical and FEM values with press braking and welding effect is 0.97, which indicates the reliability of the numerical approach. The enhancement of press braking process on failure load is achieved by comparing the FE enhanced model ($q_{FE,pb,w}$) with the virgin model ($q_{FE,v}$), and the average ratio is 1.13 with the maximum ratio is 1.29.

For exploring the effect of residual stress, more sensitivity studies are conducted by FEM. In the study, the effect of strain hardening is ignored and the virgin model is compared with two different models: the model with residual stress on both corner portion and flat portion (C+F) and the model only with corner residual stress (C). The failure loads for each model are listed in Table 6-5.

Table 6-5: List of failure loads

| Specimens | Failure load (kN/m) | | | $q_{C+F}/q_V$ | $q_C/q_V$ |
|---|---|---|---|---|---|
| | $q_V$ | $q_{C+F}$ | $q_C$ | | |
| 60-20012 | 1.16 | 1.10 | 1.17 | 0.95 | 1.01 |
| 60-20014 | 1.34 | 1.30 | 1.36 | 0.97 | 1.01 |
| 60-20024 | 2.59 | 2.51 | 2.62 | 0.97 | 1.01 |
| 60-24014 | 1.68 | 1.62 | 1.73 | 0.96 | 1.03 |
| 60-24024 | 3.57 | 3.51 | 3.59 | 0.98 | 1.01 |
| 60-30020 | 3.56 | 3.47 | 3.73 | 0.97 | 1.05 |
| 60-30030 | 5.28 | 5.22 | 5.52 | 0.99 | 1.05 |
| **Mean** | | | | **0.97** | **1.02** |
| **S.D.** | | | | **0.01** | **0.02** |

It can be found that the cold work in corner regions can enhance the load resistance of sigma beam, as the average enhancement of the failure load is 1.02. While the residual stress in flat portions lead to reduce the failure load of each specimen. The average ratio of the failure load between the model with combined residual stress and virgin model is 0.97. The conclusion can be drawn that the effect of strain hardening is

dominant for the enhancement of load resistance capacity of sigma beam with simply supported. The residual stress on the corner portion can increase the failure load while the cross-sectional residual stress will decrease the failure load.

## 6.3 Sigma beams without residual stresses

In this section, loading behaviour of continuous sigma beams without the impact of cold forming is explored. Comparisons are conducted between the numerical results and PPDM method to validate the reliability of the analytical method. The structural response during the entire loading history subjected to various loading scenarios and collapse behaviours is characterized. Parametric studies are also carried out to investigate the influence of geometric dimensions and materials properties on the collapse behaviours of sigma beams.

### 6.3.1 Geometric models

A two-span continuous beam made of sigma section, having a span length of 6m and a total length of 12m, a section depth of 300mm and a thickness of 1.8mm was considered as an example to illustrate the FEM modelling and analysis process. The cross section designation of this beam was 30018 and the geometric dimensions are referred to Table 6-1. The beam was subjected to a downward uniformly distributed load (UDL) along its entire length and was connected to the primary structures via stiffened angle brackets as indicated in Fig. 6-23.
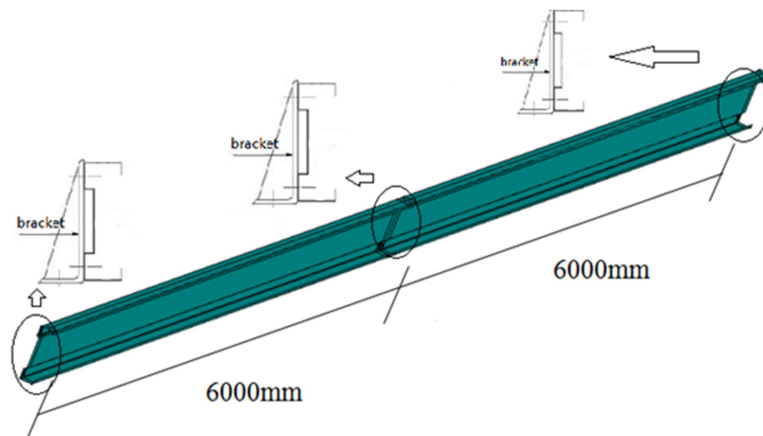
**Figure 6-23: Geometric model of a two-span continuous sigma beam**

## 6.3.2 Analytical solution

In according with the proposed PPDM (Liu et al. 2011), it is assumed that the development of bending moment resistance of continuous beam can be divided into two stages (see Fig. 6-24): the first stage is the elastic range and it can be predicted that the section near the internal support will reach a "yield" level initially, and the first plastic hinge will form at this section. It is worth noting that the term "yield" may not necessarily only refer to the material yield but also include a combined effect of local and distortional buckling. Continuously increasing the applied load will lead to the formation of a second plastic hinge in the mid-span and introduce mechanism, which then was considered as the second stage. Meanwhile, the distance between the inflection point and the internal support reduces from S to S' (see Fig. 6-24); and the bending moment at mid-length shifted to $M_{pp}$ which indicates the redistribution of moments in the continuous beam. The final load capacity of the continuous beam

should consider the superposition of the load resistances from both stages. In order to validate the assumption, an internal support test with cold-formed beams of sigma sections was conducted and a semi-empirical approach (Eq. 6-1 to 6-4) was further proposed for calculating the pseudo-plastic load capacity.
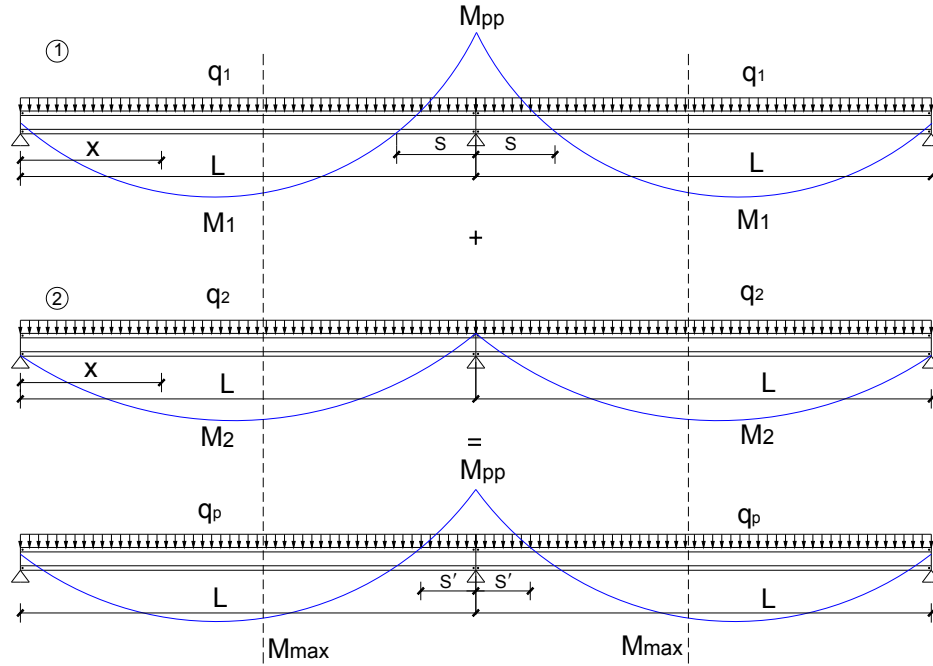


**Figure 6-24: Development of bending moment diagram to PPDM**

$$\frac{M_{pp}}{M_E} = 1.9\frac{M_y}{M_{cr}} - 4.2\sqrt{\frac{M_y}{M_{cr}}} + 2.9 \qquad \text{(Eq. 6-1)}$$

$$q_1 = \frac{8M_{pp}}{L^2} \qquad \text{(Eq. 6-2)}$$

$$q_2 = \frac{M_E\left(4 - \frac{6M_{PP}}{M_E} + 4\sqrt{\frac{M_{PP}}{M_E} + 1}\right)}{L^2} \qquad \text{(Eq. 6-3)}$$

$$q_p = q_1 + q_2 \qquad \text{(Eq. 6-4)}$$

where

$M_E$ is the ultimate bending moment resistance;

$M_y$ is the first yield bending moment of the gross cross section;

$M_{cr}$ is the critical elastic buckling bending moment of the beam;

$M_{pp}$ is the pseudo-plastic bending moment;

$q_1$, $q_2$ are the first yield load and excess load;

$q_p$ is the ultimate load resistance.

The calculated failure loads based on the PPDM for all specimens are shown in Table 6-6.

**Table 6-6: Ultimate load resistance in PPDM**

| Specimens* | $f_y$ (MPa) | I (cm⁴) | $M_E$ (kNm) | $M_y$ (kNm) | $M_{cr}$ (kNm) | $M_{pp}$ (kNm) | Buckling mode | $q_1$ | $q_2$ | $q_p$ |
|---|---|---|---|---|---|---|---|---|---|---|
| 120-20012 | 450 | 262.68 | 7.95 | 11.82 | 11.1 | 4.68 | LB | 1.04 | 1.22 | 2.26 |
| 120-20016 | 450 | 347.61 | 11.4 | 15.64 | 24.3 | 8.59 | LB | 1.91 | 1.51 | 3.42 |
| 120-20025 | 450 | 533.99 | 20.2 | 24.03 | 57.2 | 19.70 | DB | 4.38 | 2.11 | 6.49 |
| 200-20025 | 450 | 533.99 | 17.35 | 24.03 | N/A# | N/A | LTB | N/A | N/A | N/A |
| 120-24015 | 450 | 504.02 | 13.9 | 18.90 | 24.5 | 9.41 | LB | 2.09 | 1.98 | 4.07 |
| 120-24023 | 450 | 762.45 | 22.7 | 28.59 | 56.8 | 19.90 | DB | 4.42 | 2.66 | 7.08 |
| 200-24030 | 450 | 982.76 | 26.9 | 36.85 | N/A | N/A | LTB | N/A | N/A | N/A |
| 120-30018 | 450 | 1129.44 | 21.65 | 33.88 | 41.3 | 14.16 | DB | 3.15 | 3.14 | 6.29 |
| 120-30025 | 450 | 1553.24 | 33.2 | 46.60 | 76.0 | 25.76 | DB | 5.72 | 4.31 | 10.03 |
| 200-30030 | 450 | 1850.74 | 36.75 | 55.52 | N/A | N/A | LTB | N/A | N/A | N/A |

**Note:** (1) * The specimens number 120- and 200- refer to the total length of the beam being 12m and 20m respectively.

(2) N/A# means the PPDM is not applicable when the failure involves LTB.

### 6.3.3 Modelling process

The two-span continuous beam had an internal support comprising of the connection between the bracket and the web of the section through four bolts. Standard bolt hole sizes were adopted, namely, 2mm larger than the bolt size and they were located on the outer web of the sigma section. This type of bolt connection arrangement facilitated the free movement of the section in relation to the connecting brackets thereby providing a simple connection nature. In the model, the connecting bolts were modelled with quarter circular plates that had the same thickness as the cross-sectional thickness. The selection of material properties, shell element and mesh size were the same to the section 6.1.

Due to edge clearance between the bolts and bolt holes, the longitudinal movement of the beam was anticipated. As such only the mid-span section was restrained in the numerical model to allow for the beams' symmetric behaviour. The outerweb to flange junction line was fully restrained both laterally and rotationally, representing the effective restraining effect of roof sheeting to the purlin (see Fig. 6-25a). The central node in each bolt plate was vertically restrained and other nodes on the plate were laterally restrained. The nodes on the upper quarter of the bolt hole and the external circumferential surface of the bolt plate were coupled together (see Fig. 6-25b).
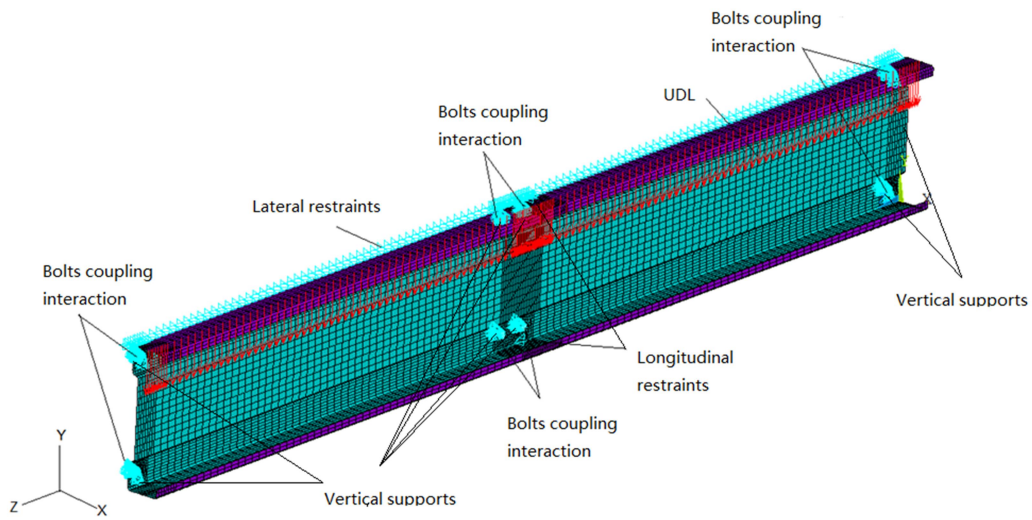
(a) FE mesh and boundary conditions
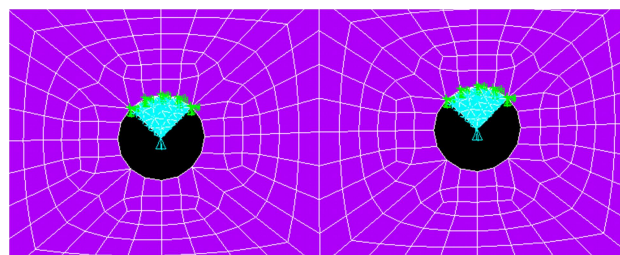


(b) Bolts coupling interaction

**Figure 6-25: FE boundary conditions**

Before carrying out the nonlinear analysis, a linear elastic eigenvalue buckling analysis was performed based on the same model with the same restraining conditions to obtain the eigenvalue-type buckling modes. The local and distortional buckling modes of their lowest orders (see Fig. 6-26) were selected for the initial imperfection of the beam; with their magnitudes being 0.5t and1.0t, respectively (Liu et al. 2011b).
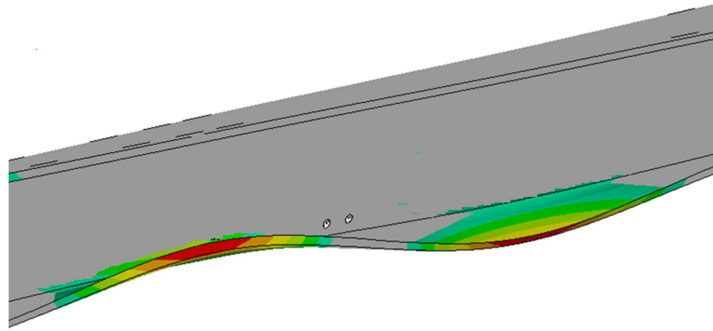
(a) The lowest distortional buckling modes
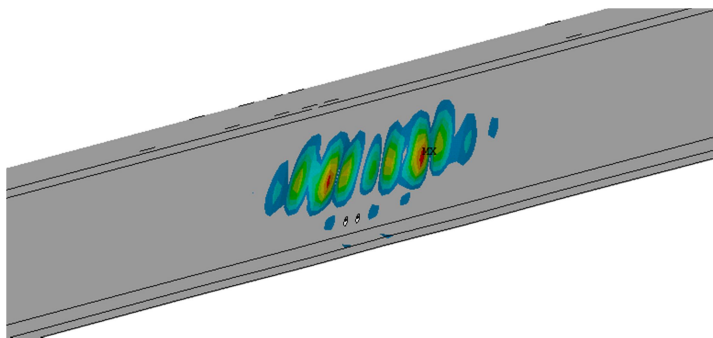


(b) The lowest local buckling modes

**Figure 6-26: Buckling modes for specimen 30018**

### 6.3.4 Results discussions

The plot of deflection against UDL at the mid-span section (captured at the centre of the top flange) of the left span of 120-30018 is shown in Fig. 6-27. It can be seen that the yield load was 6.0kN/m and the failure load was 6.4kN/m. A good agreement is observed between the PPDM failure load (6.29kN/m) and the FEM (6.46kN/m) failure load for 120-30018, with a discrepancy of 2.7%.
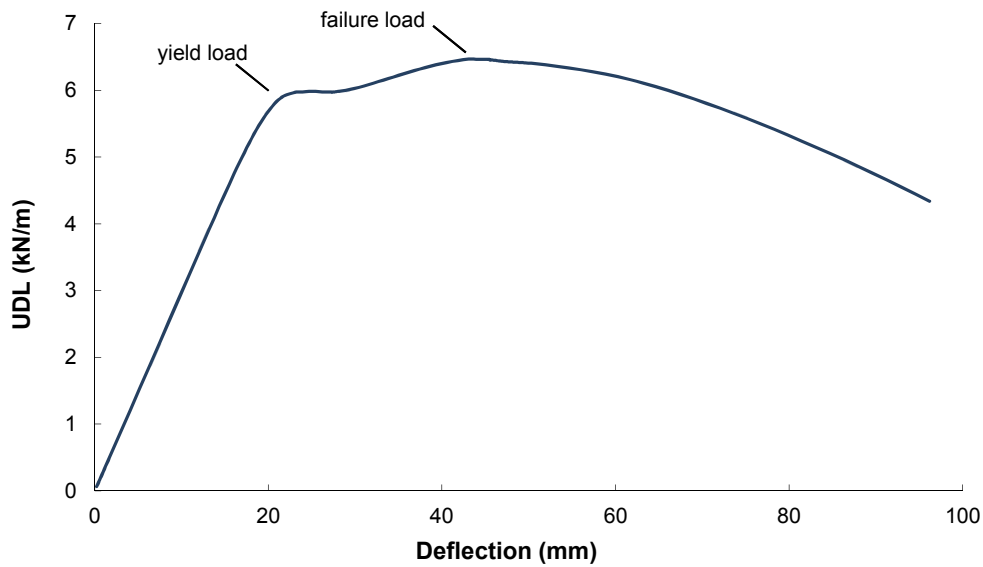
**Figure 6-27: Load-deflection curve of the mid-span section in the left span**

A common trend has been observed in Fig. 6-27 where the UDL and deflection curve shows two distinct phases, that is, prior to and after the formation of the plastic hinge at the internal support. In the first phase, the UDL and deflection maintain an almost linear relationship and the gradient of the curves rapidly reduces once it enters the second phase.

Fig. 6-28 presents the contour plots of von Mises stress at the yield and failure loads. It also shows the corresponding deformation patterns.
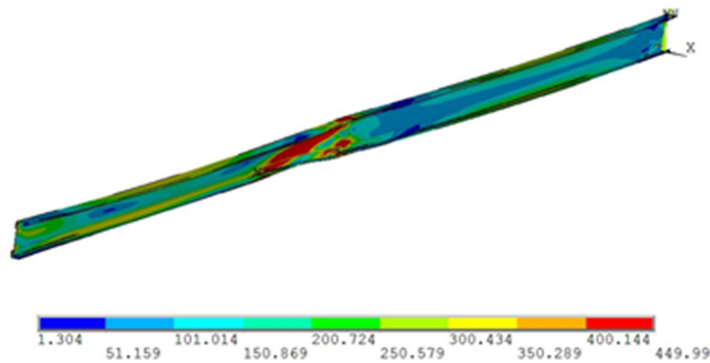
(a) von Mises stress contour plot at the yield load (MPa)
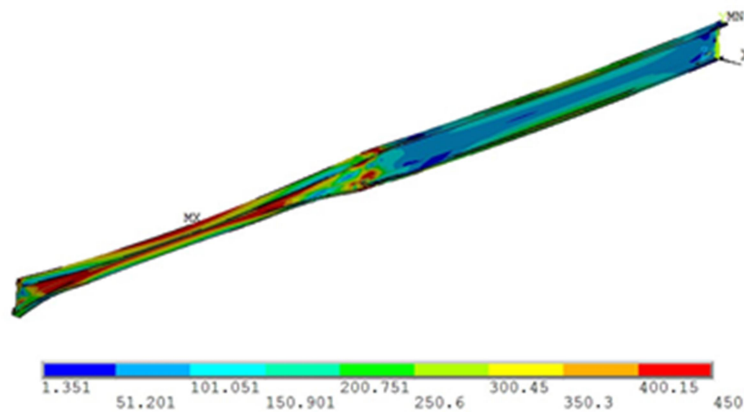


(b) von Mises stress contour plot at the failure load (MPa)

**Figure 6-28: von Mises stress contour plot in specimen 30018**

Fig. 6-28a shows that the yield stress (450MPa) occurred at the internal support at the yield load and then moved to the left mid-span point at the failure load (Fig. 6-28b). This indicates that the plastic hinge was initially formed at the internal support sections when the yield load was reached. Then, the occurrence of plastic hinge relaxed the fixity of the supports and rendered the moment redistribution of the beam.

After this stage, the deflection at the left mid-span section continued to increase until the failure occurred at the section.

In order to further examine the developments of bending moment and the plastic hinge, the curves of bending moment versus UDL for the left mid-span and internal support section are plotted, as shown in Fig. 6-29.
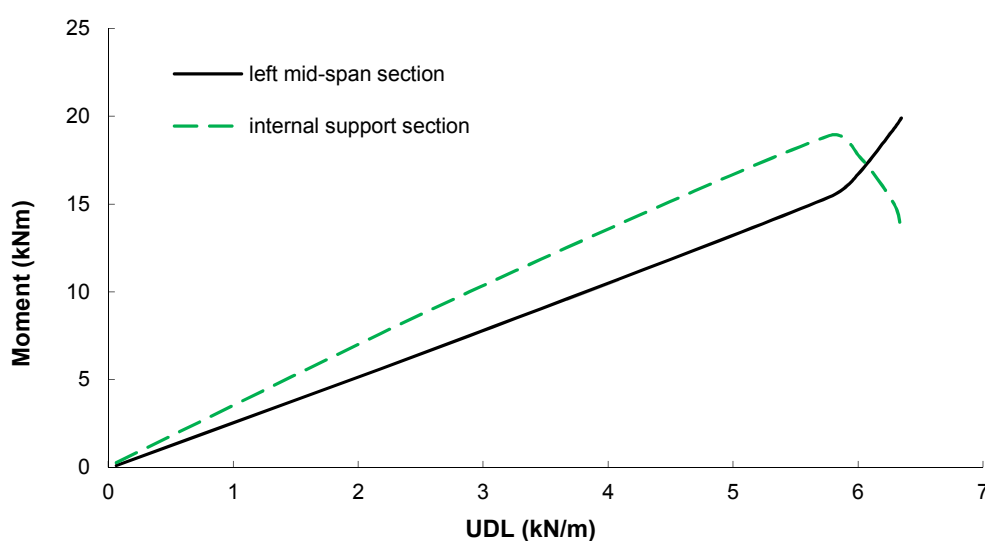


**Figure 6-29: Applied bending moments vs. UDL at various cross sections**

It can be seen from Fig. 6-29 that once the yield load (6.0kN/m) is reached, the bending moment at the internal support (in absolute value) reached its maximum value (18.9kNm) and it is then followed by a non-linear descending curve indicating its post-failure reduction in loading resistance. However, the bending moment at the mid-span section is still increasing, and the increase rate rises considerably after the yield load is reached. This observation confirms the occurrence of the moment redistribution.

The movement of the inflection point is shown in Fig. 6-30, where the vertical axis represents the distance between the inflection point and the internal support point ($S$ and $S'$ in Fig. 6-24); and the horizontal axis shows the corresponding applied UDL at which this distance is captured. The sections where the bending moment value is nearly zero are denoted as the inflection point of the beam.
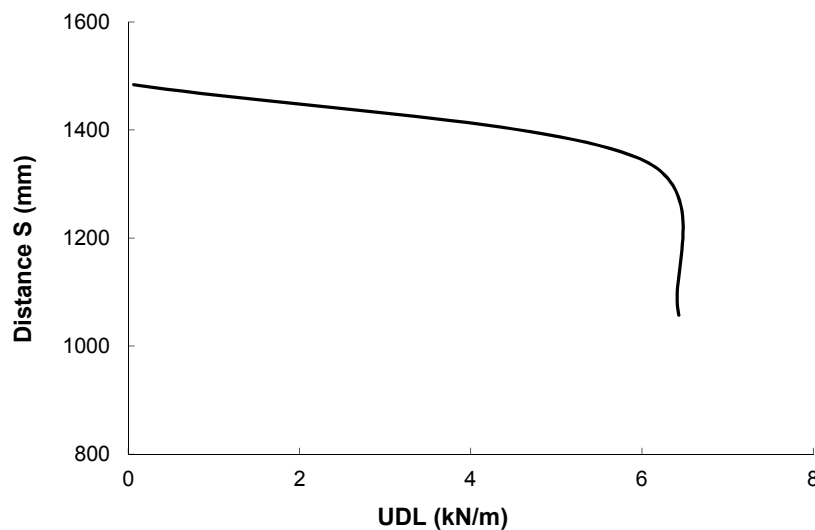


**Figure 6-30: Location of the inflection point**

Fig. 6-30 exhibits that as the load increased up to 6.0kN/m, the inflection point has a slight movement. This distance decreases dramatically as the structure enters the yield phase (when UDL is greater than 6.0kN/m), which indicates the occurrence of the plastic hinge and the resulting moment redistribution commencing.

## 6.3.5 Parametric studies

A series of parametrical studies of additional models with various yield strengths, cross-sectional properties, span numbers and span lengths are analysed herein.

## (1) Effect of yield strength

The specimen 120-30018 with three yield strengths 350MPa, 450MPa and 550MPa, is analyzed herein. The UDL- mid-span deflection (left span) curves, up to the failure load, are shown in Fig. 6-31. It can be seen that the low strength specimen exhibits the greatest ultimate/first yield ratio in deflection, which demonstrates a higher ductility in low strength steel. In addition, the increase in strength will not proportionally increase the load capacity if the cross section remains the same.
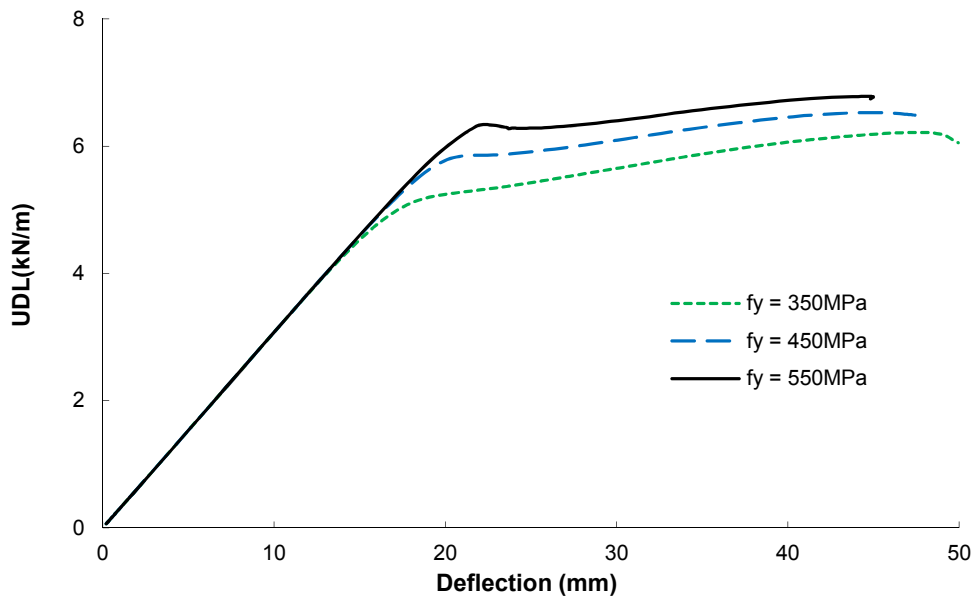


**Figure 6-31: Comparison of different yield strengths**

The comparison of failure loads between PPDM and FEM is presented in Table 6-7:

**Table 6-7: Comparison of failure loads**

| Yield strength (MPa) | Failure load | | $\dfrac{q_P}{q_F}$ |
|---|---|---|---|
| | PPDM $q_P$ ($kN/m$) | FEM $q_F$ ($kN/m$) | |

| | | | |
|---|---|---|---|
| 350 | 5.90 | 6.21 | 0.95 |
| 450 | 6.29 | 6.46 | 0.97 |
| 550 | 7.40 | 6.75 | 1.10 |
| **Mean** | | | **1.01** |
| **S.D.** | | | **0.08** |

Table 6-7 suggests that the failure loads obtained from FEM and PPDM are in good agreement. The average ratio between PPDM and FEM is 1.01 and the standard deviation is 0.08.

## (2) Effects of cross section properties

A parametric study was conducted to examine the influence of cross-sectional dimensions on the plastic behaviour of the two-span sigma beams. The relationship between the deflection at the left mid-span point and the applied UDL is shown in Figs. 6-32 and 33, where the curves are divided into two groups based on different cross-sectional thickness and depth. Fig. 6-32 exhibits the effect of the thickness on the pre- and post-yield behaviour for three groups of sections with various depths, i.e. (a) 200mm, (b) 240mm, and (c) 300mm. It also shows that the thickness has a significant effect on the failure behaviour of the two-span sigma beams. As expected, the failure load increases as the thickness increases. According to Fig. 6-32 (a), the failure load for beam 120-20012, 120-20016, 120-20025 are 2.13kN/m, 3.25kN/m and 6.01kN/m, respectively, and this grows by 53% and 85% as the thickness increases from 1.2mm to 1.6mm, and from 1.6mm to 2.5mm respectively. The same conclusion can be drawn from Figs. 6-32 (b) and (c), where the load carrying capacity increases

by 75% in the 120-240 series with thickness increase from 1.5mm to 2.3mm, and by 72% in the 120-300 series with thickness increase from 1.8mm to 2.5mm. A common observation is that the gain in post-yield strength is higher when thicker walls are adopted.
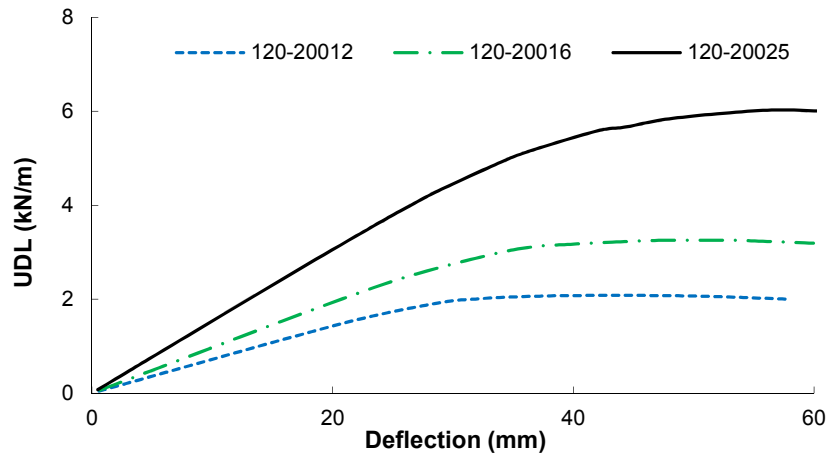


(a) 120-200xx series
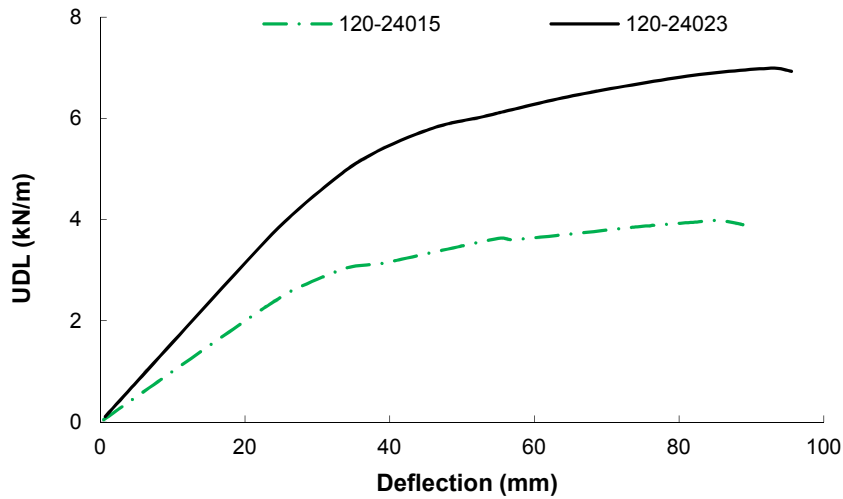


(b) 120-240xx series
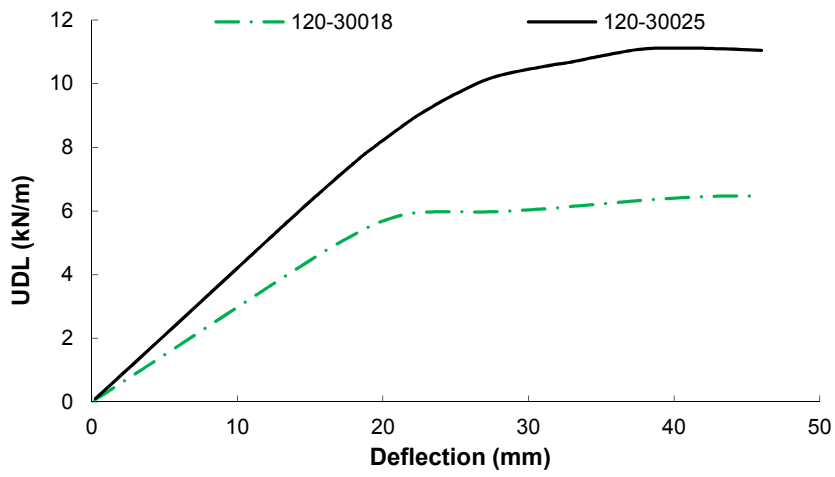
c) 120-300xx series

**Figure 6-32: Effect of thickness for two-span beam**
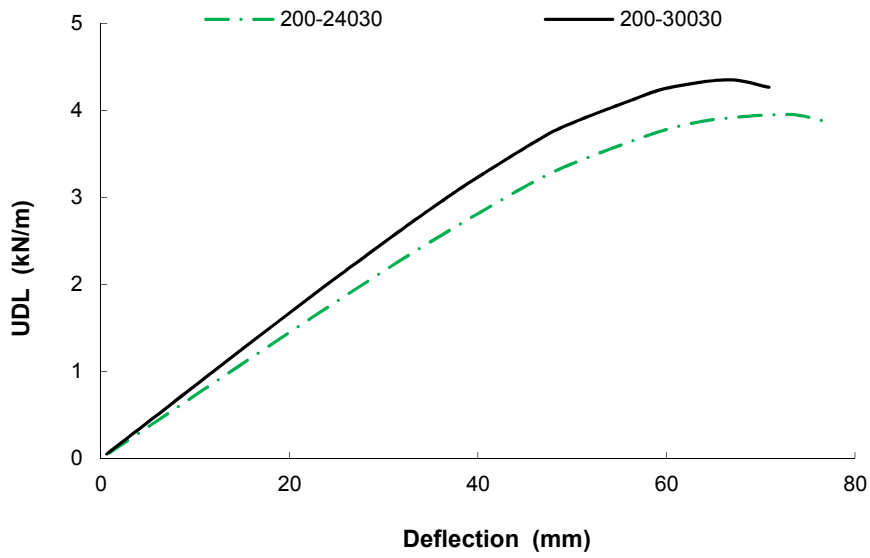


(a) 200-xxx30 series
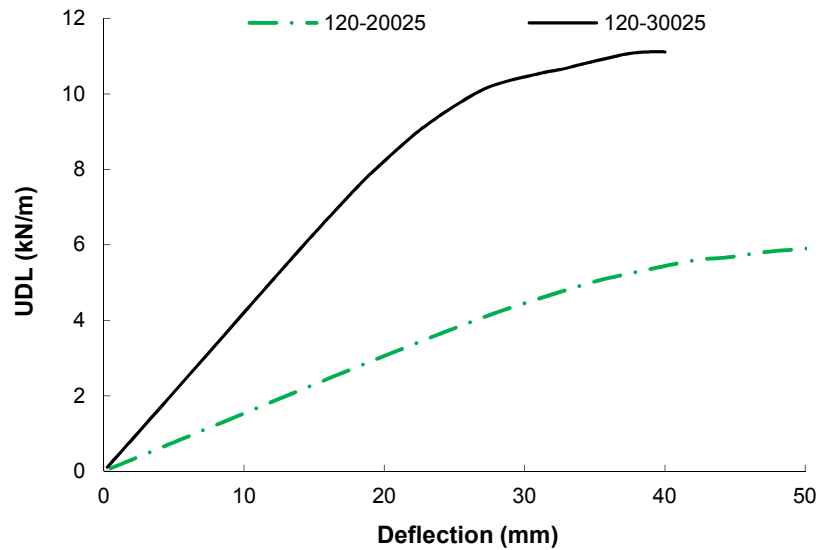
(b) 120-xxx25 series

**Figure 6-33: Effect of depth for two-span beam**

Similarly, Fig. 6-33 shows the effect of cross-sectional depth of two groups of beams with different span lengths. This group of studied examples all has relatively large wall thickness. Based on the results shown in Fig. 6-33, it suggests that in the long span length case (e.g. 10m span), the effect of depth on the pre- and post- yield behaviour is modest, which is evidenced by the observation of only a 10% increase when the section depth increases from 240mm (3.95kN/m) to 300mm (4.35kN/m). When the span length is reduced (e.g. to a 6m span), the deflection at failure for the deeper cross section is smaller than that for the shallow cross section. In this case, the failure load rises by 85% as the section depth increases from 200mm (6.01kN/m) to 300mm (11.12kN/m). In the same case, the post-yield strength gain in the 300mm depth is lower than the 200mm case, due to a lower $M_{pp}/M_e$ ratio for the former case.

In order to compare the results obtained using different design methods, as mentioned in the introduction, the values of predicted failure loads using FEM ($q_F$), DSM ($q_D$) and PPDM ($q_P$) and their calculated ratios are presented in Table 6-8. The critical buckling loads in the DSM are achieved by using the CUFSM package (Schafer and Ádány 2006, Li and Schafer 2010).

**Table 6-8: Comparison of failure loads obtained from different methods**

| Specimens | Failure load | | | $\dfrac{q_P}{q_D}$ | $\dfrac{q_P}{q_F}$ |
|---|---|---|---|---|---|
| | PPDM $q_P(kN/m)$ | DSM $q_D(kN/m)$ | FEM $q_F(kN/m)$ | | |
| 120-20012 | 2.26 | 1.60 | 2.13 | 1.41 | 1.06 |
| 120-20016 | 3.42 | 2.45 | 3.25 | 1.40 | 1.05 |
| 120-20025 | 6.49 | 4.76 | 6.01 | 1.36 | 1.08 |
| 200-20025 | N/A | 1.72 | 2.76 | N/A | N/A |
| 120-24015 | 4.07 | 2.89 | 4.00 | 1.41 | 1.02 |
| 120-24023 | 7.08 | 5.25 | 6.99 | 1.35 | 1.01 |
| 200-24030 | N/A | 2.75 | 3.95 | N/A | N/A |
| 120-30018 | 6.29 | 4.48 | 6.46 | 1.40 | 0.97 |
| 120-30025 | 10.03 | 7.30 | 10.23 | 1.37 | 0.98 |
| 200-30030 | N/A | 3.29 | 4.35 | N/A | N/A |
| **Mean** | | | | **1.39** | **1.02** |
| **S.D.** | | | | **0.03** | **0.04** |

*Note: N/A indicates that the PPDM method is not applicable to failure involves LTB.*

Table 6-8 demonstrates that the average ratio of the predicted failure loads between the PPDM and FEM methods is 1.02, with the maximum ratio being 1.08, whereas the average ratio between the PPDM and DSM methods is 1.39, with a maximum ratio being 1.41. It can be concluded that FEM shows a better agreement with PPDM. It

can also be seen that the PPDM method produces more favourable results than DSM. This is because the PPDM method is based on the plastic method, which allows the redistribution of moments in the beams by utilising the effective residual bending moment capacity of the CFS beams in the plastic hinge zone; and this will inherently lead to a more economic result.

## (3) Effect of span number and span length

Three-span and four-span continuous beams were further considered herein and the cross-section configuration, and material properties were the same as for the sigma specimen 120-30018. The overall geometric model of the two-span beam is illustrated in Fig. 6-34. Five identified cross sections (section A to E) that refer to the left mid-span, left internal support, mid-length, right internal support and right mid-span section, were selected as the characteristic sections to present the results.
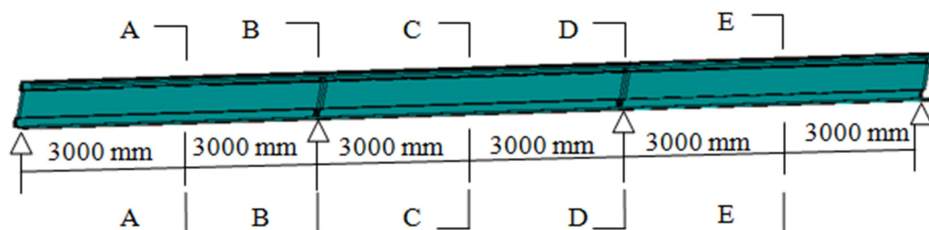


**Figure 6-34: Geometric dimensions of a three-span model**

The bending moment versus UDL curves for the identified sections of a three-span beam are shown in Fig. 6-35. It is worth noting that the absolute values are used for the hogging moment at internal supports in the following figures.
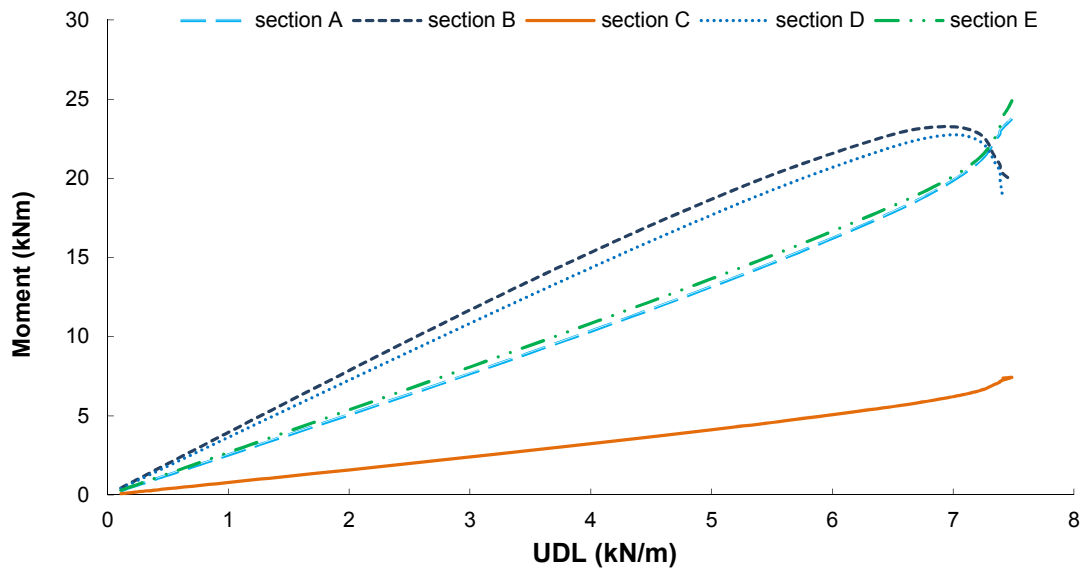
**Figure 6-35: Bending moment–UDL curves**

It can be seen from Fig. 6-35 that in the pre-yield stage, the bending moment at all sections increases with the applied load. For a perfect beam, the bending moment of sections B and D (or A and E) should be identical; however, due to the asymmetric caused by imperfection pattern, there is a slight discrepancy between these sections. When the UDL reached yield load (7.0kN/m), the bending moment at internal support B and D peaked at values of 23.2kNm and 22.8kNm, respectively. Then, with the continued increase in the applied load, the bending moment at B and D started to drop while the bending moment at A and E was still increasing, which indicates that the member was still in service until a sufficient number of plastic hinges had formed at the A or E section to create a mechanism. When the failure load 7.5kN/m was achieved, the maximum bending moment at the E section was 25.40kNm. It is worth noting that at the internal support where the hogging moment is present, the restraint

at the upper flange-web junction does not provide an effective restraining effect on the compression flange. This is why the peak moments at the internal supports are smaller than those at the mid-span sections.

A four-span continuous beam was further studied and comparisons of bending moment-UDL curves and UDL-deflection curves of beams with different span numbers are illustrated in Fig. 6-36 and 37. The section A, B and C mentioned in the figure are referred to the left mid-span section, left internal support section and middle section of the second span from left, respectively.
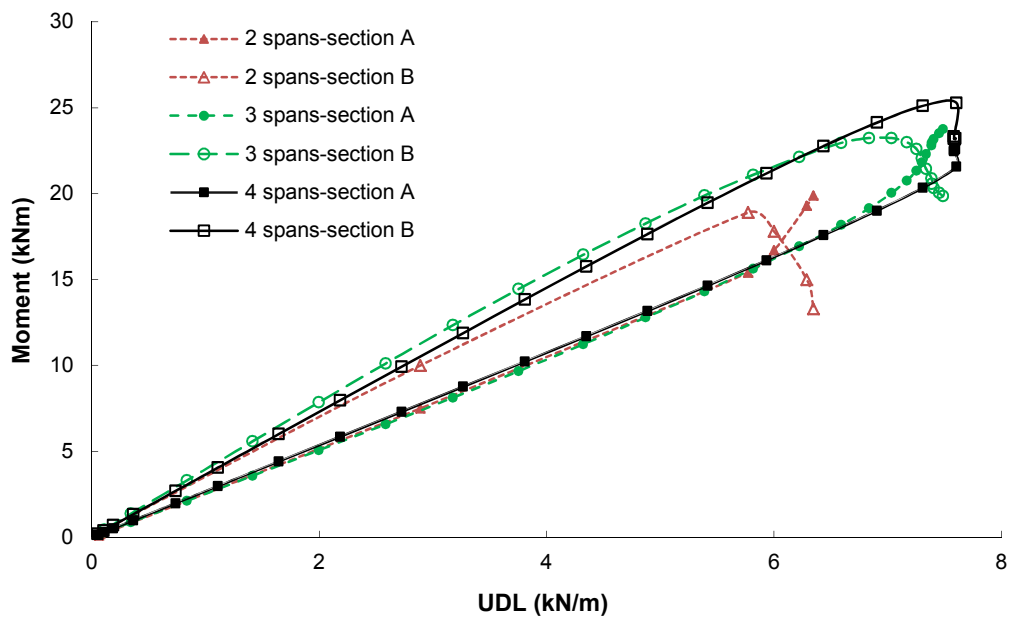


**Figure 6-36: Bending moment-UDL curves at section A and B**
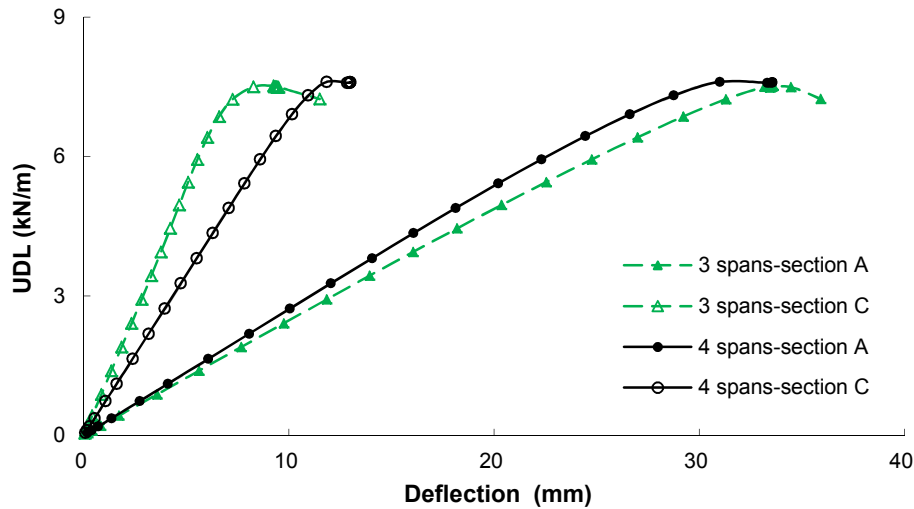
**Figure 6-37: UDL-Deflection curves at sections A and C**

According to Fig. 6-36, a similar failure pattern can be found in beams with different span numbers. When internal support section (section B) enters the yield stage, the peak moment at this section is attained and the plastic hinge is formed. The yield load for the two spans, three spans and four spans beam are 6.0kN/m, 7.0kN/m and 7.6kN/m, respectively. After the yield stage, the plastic hinge forms at the first mid-span section and the failure load of each beam are then reached. The effect of span number on the failure load is indicated by the failure load values of 6.5kN/m, 7.4kN/m and 7.6kN/m when the span number rises from 2 to 4. The deflection behaviour of section A and C of the three spans and four spans beams are presented in Fig. 6-37. As expected, the deflections at section A are greater than those at section C, and the deflections of the 3 span beam outweigh those 4 span beam at section A, but opposite trend is found at section C.

More two span beam models with different span lengths (4m, 5m, 6m, 7m and 8m) are presented for the parametric analysis. These models share the same cross-section geometric dimensions, material properties and boundary conditions with specimen 120-30018. The comparisons of the moment against UDL curves, and UDL against deflection curves at section A (left mid-span section) and B (internal support section) are demonstrated in Figs. 6-38 and 39.
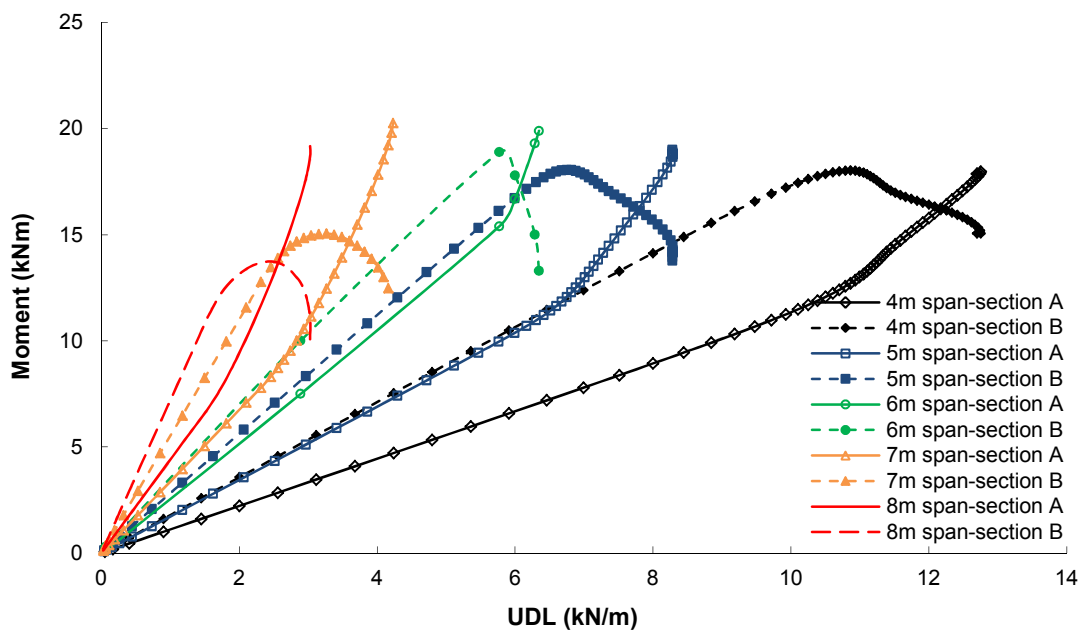


**Figure 6-38: Bending moment-UDL curves at section A and B**
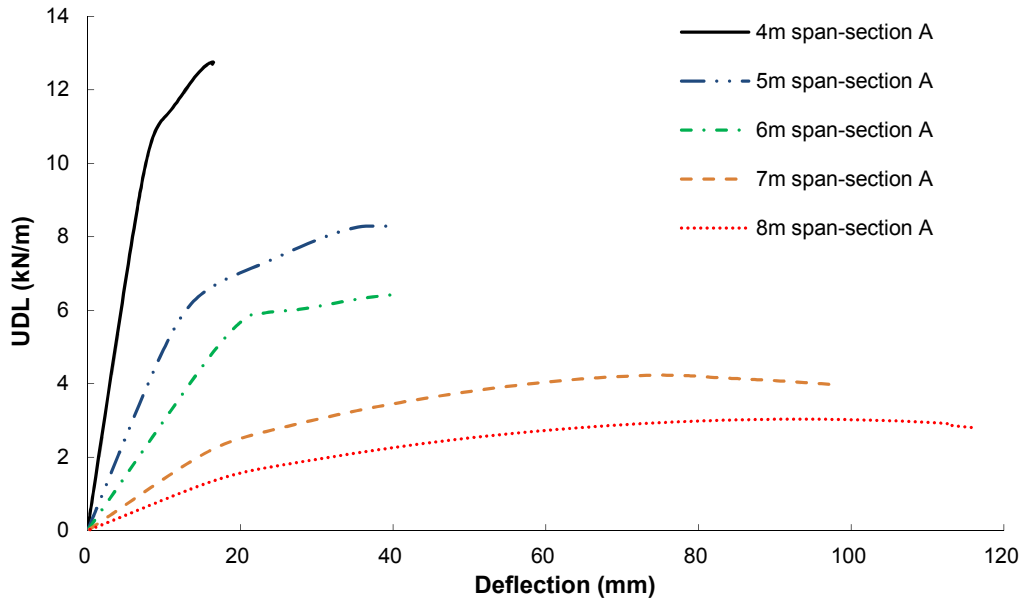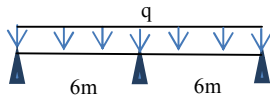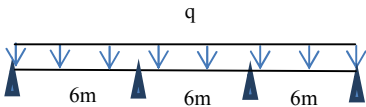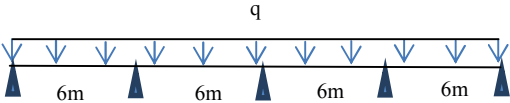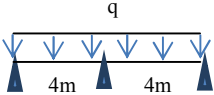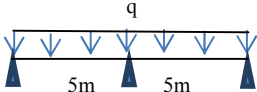
**Figure 6-39: UDL-Deflection curves at section A**
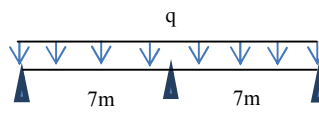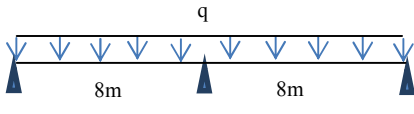
Fig. 6-38 illustrates that as the span length increases, the failure load decreases as expected. The value drops by 35% from the 4m span (12.72kN/m) to the 5m span (8.29kN/m), by 22% from the 5m span to the 6m span (6.46kN/m), by 34% from the 6m span to the 7m span (4.24kN/m), and by 32% from the 7m span to the 8m span (2.90kN/m). It seems that failure moment at section A is approximately constant (from 17.76kNm to 18.38kNm) for span length from 4m to 8m.The peak moment at section B drops 25% from 18.03kNm for the 4m span to 13.47kNm for the 8m span. This is because the effective length for the hogging moment is increased as the span length increases, and the distortional buckling mode in the restraint-free compression flange becomes increasingly evident when the span length increases. From Fig. 6-39, it is apparent that the deflection increases with an increase in span length. All the

deflection curves show a distinct 2-stage characteristic featuring the moment redistribution behaviour.

A comparison of predicted failure loads for continuous beams with different span numbers and span lengths is summarized in Table 6-9. The listed models have the same cross section (sigma 30018) and material properties (450MPa). The failure loads from PPDM and FEM and the ratios between two methods for each case are also presented in the Table.

**Table 6-9: Summary of PPDM and FEM results**

| Geometric model | Failure load | | $\dfrac{q_p}{q_F}$ |
| --- | --- | --- | --- |
| | PPDM | FEM | |
| | $q_p$(kN/m) | $q_F$(kN/m) | |
|  | 6.29 | 6.46 | 0.97 |
|  | 6.99 | 7.43 | 0.94 |
|  | 6.81 | 7.60 | 0.90 |
|  | 13.89 | 12.72 | 1.09 |
|  | 8.89 | 8.29 | 1.07 |

| | | | |
|---|---|---|---|
| q 7m ▲ 7m ▲ | 4.70 | 4.24 | 1.10 |
| q 8m ▲ 8m ▲ | 3.73 | 2.90 | 1.28 |

| | |
|---|---|
| **Mean** | **1.05** |

| | |
|---|---|
| **S.D.** | **0.09** |

It can be concluded from Table 6-9 that the failure loads from PPDM method are in good agreement with the FEM results in all of the cases studied. The average ratio of the failure load calculated using PPDM and that from FEM is found to be close to 1, with the minimum ratio being 0.90 and the maximum ratio being 1.28.

### 6.4 Summary

In the chapter, a series of FE models are established to investigate the effect of residual stress and strain hardening on the load resistance capacity of sigma beams. For investigating the impact of the roll forming process, continuous sigma beams at internal support are numerically studied and the comparisons are conducted between FE results and experimental data. The impact of coiling-uncoiling, press braking and the welding process is further investigated by comparing the load-deflection response of simply supported sigma beams with sheeting attachment between virgin model and the modified model. Moreover, continuous beams in sigma section are further studied

numerically for validating the PPDM approach. The results from the numerical analysis lead to the following conclusions.

1. The load-deflection response is sensitive to the effect of residual stresses and strain hardening. The existence of residual stress can decrease the stiffness of the sigma beam and the strain hardening can increase the peak load of sigma beams. For the roll formed sigma beams on internal support, the negative effect of residual stress is not negligible, and the enhancement induced by strain hardening is the dominate factor. A better agreement can be found between the test result and FE curve with RS, which also indicate the ignorance of cold work effect should lead to an inaccuracy outcome.

2. The effect of welding residual stress is insignificant to the load resistance of single-span sigma beam, but the load-deflection response is enhanced significantly by the effect of cold work, especially strain hardening. In the meanwhile, a good agreement can be found between test curves and curves with PB and W. The discrepancy between theoretical and FEM is insignificant (with the gap is 0.93 and 0.97, respectively), which indicates the accuracy and reliability of the numerical approach. The enhancement of load resistance by press braking process is achieved by comparing the FE enhanced model with the virgin model, and the average value is 1.13.

3. It can be found that the cold work in corner regions can improve the load resistance capability of simply supported sigma beam while the residual stress in flat portions

reduces the failure load of each specimen. The effect of strain hardening is dominant for the enhancement of load resistance capability of sigma beam with simply supported. The residual stress on the corner portion can increase the failure load while the cross-sectional residual stress will decrease the failure load.

4. Failure loads of specimens from FE models show a good agreement with the calculated results by using PPDM method, which indicates the PPDM approach is reliable for predicting load resistance capacity of sigma beams. Use of the PPDM method could lead to a more economical design for continuous cold-formed steel beams than some elastic analysis based methods, e.g. DSM.

5. Further analysis demonstrates that the PPDM method can also be used in continuous beams with a span number from 2 to 4, and a span length from 4m to 8m, and the PPDM method is applicable for beams with the nominal yield strength from 350MPa to 550MPa, which covers most practical applications.

# 7. CONCLUSIONS

## 7.1 General

The ultimate motivation of this thesis is to investigate the distribution and effect of residual stress in sigma sections. In order to fulfil the aim and objectives of the thesis, from Chapter 3 to Chapter 5, the efforts are made to conduct a series of analytical, experimental and numerical studies for exploring distribution of coiling-uncoiling, press braking, roll forming and welding residual stress. In Chapter 6, the effects of residual stress and strain hardening are further presented by comparing virgin models and modified models. The primary findings in each chapter are listed in section 7.2 to 7.5, respectively, and the recommendations for future works are highlighted in section 7.6.

## 7.2 Main findings of this thesis

1. The coiling-uncoiling residual stress in both directions decreases as the yield strength increases from 250MPa to 450MPa and as the thickness increases from 1.0mm to 1.8mm. The increasing of the roll radius will decrease the coiling-uncoiling residual stress in both directions. As the roll radius to sheet thickness radio approach to 1000 the residual stress in both direction close to zero, which means no plastic deformation occurs under such condition.

2. In the press braking process, the residual stress along the thickness is non-linear along the shell thickness and asymmetric to the neutral axis. For the corner portion, the maximum longitudinal residual stress occurs at 1/4 thickness position while the peak transverse residual stress occurs on the surface. For the flat region, the discrepancy of residual stress in two directions is insignificant. The transverse residual stress on the corner portion is found greater than the flat portion while the gap is quite limited for longitudinal residual stress.

3. In the roll forming process, both corner and flat portions residual stress are nonlinear distributed along the thickness and the curves are anti-symmetrical about the neutral axis. The peak value of transverse residual stress is higher than longitudinal residual stress at corner portion as the deformation mainly occurs in the transverse direction. The maximum longitudinal residual stress is found exceed transverse stress at the flat portion and the location of maximum stress along the thickness is located on $\pm 0.25$ of normalized thickness.

4. In the welding process, the maximum longitudinal residual stress is in tension and the longitudinal stress decreases drastically with increasing distance from the weld centreline. The maximum transverse residual stress is also in tension and greater than longitudinal stress around the weld bead; the value approaches zero almost 25mm away from the welding centreline and then tensile stress reverses to compressive stress.

5. The load-deflection response of sigma section is sensitive to the residual stresses and strain hardening effect. The existence of residual stress can decrease the stiffness of the beam and the strain hardening can increase the peak load of sigma beams. For the roll formed sigma beams on internal support, the effect of residual stress and strain hardening is not negligible and the enhancement induced by strain hardening is the dominant factor. The effect of welding residual stress is insignificant to the load resistance of single-span sigma beam. The load-deflection curves for all the specimens are enhanced by the effect of strain hardening during press braking. Other major findings are listed below in section 7.3 and 7.4.

## 7.3 Numerical prediction cold working and welding residual stress

1. The distribution of coiling and uncoiling residual stress is nonlinear along the shell thickness, and the curves are asymmetrical to the neutral axis in both directions. After the coiling process, the tensile stress is found on the outside surface and compression on the inside surface. The longitudinal residual stress is greater than stress in the transverse direction. At the final stage of the uncoiling process, the longitudinal residual stress acts as the dominant stress when compared with the transverse stress. The outside surface of the sheet is subjected to tension during the coiling process but turns to compression after uncoiling, which proves the coiling-uncoiling process is similar to a loading-unloading operation. A good agreement can be found between FEM results and analytical values.

2. The effect of roll radius is found the dominant factor in the coiling-uncoiling residual stress, followed by the effect of sheet thickness, and the change of yield strength has the least impact on the final residual stress.

3. For the press braking process, the effect of yield strength on residual stress in the longitudinal direction is insignificant; the transverse residual stress on the inside surface decreases with increasing yield strength. The effect of thickness on longitudinal residual stress on the surface of the corner portion is also insignificant while the transverse residual stress on the corner portion reduces as the increase of shell thickness.

4. During the roll forming process, the equivalent plastic strain is mainly occurred on the bending zone between innerweb and outerweb; the strain in the rest part is insignificant. The development of longitudinal strain indicates the arrangement of roll set in longitudinal direction is acceptable as the elongation is insignificant on the flat portion during the forming process. The transverse stress of the sheet increases continually as the increase of the bend angle in roll forming. The stress in both directions then has a decrease when the springback occurs at the final stage.

5. A good agreement is found between the FE achieved roll forming residual stress and experimental data obtained by using X-ray diffraction method. The comparison has validated the reliability and accuracy of the numerical model.

6. The temperature of weldment increases dramatically as approaching of the torch and then falling as torch leaves. The maximum temperature during heating is 1261℃, and the thermal field predicted by FEM is in good agreement with experimental measurement. The range of HAZ caused by torch is about 60mm in width, and the temperature on regions 30mm far from the HAZ is reduced to zero.

**7.4 Study of the influences of residual stresses on sigma beam**

1. A better agreement can be found between the test result and the FE model with RS, which also indicate the ignorance of cold work effect should lead to an inaccuracy outcome. The ratio of the failure load between SH model and FE virgin model is 1.06, which represents the effect of strain hardening in the failure load is not negligible. The ratio between RS model and FE virgin model is 0.98 and between RS-SH model and FE virgin model is 1.05, which indicates the enhancement induced by strain hardening is the dominate factor.

2. The effect of welding residual stresses on the load resistance of single-span sigma beams is negligible, but the load-deflection response is enhanced significantly by the effect of cold working in the corners, especially the strain hardening effect, particularly for relatively stocky sections. Meanwhile, a good agreement can be found between test curves and curves with PB and W. The discrepancy between theoretical and FEM is small (the average of numerical over experimental load resistance is 0.93 and 0.97, respectively), which indicates the accuracy and reliability of the numerical approach. The enhancement of load resistance by the press braking process is

quantified by comparing the FE enhanced model with the virgin model, and the average value is 1.13.

3. It can be found that the cold work in corner regions can improve the load resistance capability of simply supported sigma beam while the residual stress in flat portions reduces the failure load of each specimen. The effect of strain hardening is dominant for the enhancement of load resistance capability of sigma beam with simply supported ends. The residual stress field in the corner region can increase the failure load while the cross-sectional residual stress will decrease the failure load.

4. The numerically obtained failure loads show a good agreement with the predicted load resistance results using PPDM method, which indicates that the PPDM approach is reliable for predicting the load resistance of sigma beams. Use of the PPDM method could lead to a more economical design for continuous cold-formed steel beams than some elastic analysis based methods, e.g. DSM.

5. Further analysis demonstrates that the PPDM method can also be used in continuous beams with a span number from 2 to 4, and a span length from 4m to 8m, and the PPDM method is applicable for beams with the nominal yield strength from 350MPa to 550MPa, which covers most practical applications.

**7.5 Recommendations for future research**

This thesis has addressed some important problems in the distribution and effect of residual stress by using numerical and experimental methods. However, due to the limitation of financial and laboratory facility, many issues remain to be studied in the future:

1. The proposed numerical approach provides a rapid and economical alternative for predicting residual stress in cold-formed members. However, as the limitation of computation capability, the model of coiling-uncoiling and cold forming process is established separately. The advanced numerical approach is still required in the future to consider the multiple manufacturing processes (e.g. coiling-uncoiling and press braking, coiling-uncoiling and roll forming) simultaneously in an integrated model, by which the residual stress can be achieved in a more accuracy and efficiency way.

2. The effect of springback on the distribution of residual stress in sigma section has been considered in this thesis. However, the relationship between springback amplitude, cross-sectional geometrical dimension and configuration of roll forming system has not been fully discussed. Thus, comprehensive investigation of springback is recommended for further research.

3. In this study, the study of residual stress effect is focused on the nonlinear static analysis, however, residual stress, especially heat induced residual stress, is considered one of the primary causes of brittle fracture and lead to the deterioration of fatigue life of metal components. Therefore, more hysteresis research of steel members with welding residual stress is recommended for further study.

4. In the thesis, the numerical study of the continuous beam in cold formed sigma sections only considers the effects of span length and span number on load resistance capacity,  Other factors such as loading pattern also need to be investigated in future studies.

# APPENDIX

## 1 Tensile test for steel specimens with nominal yield strength of 450MPa

The tensile test was conducted at the Civil Engineering laboratory in the University of Birmingham. The nominal yield strength of test specimens was 450MPa and the tests were conducted by using SANS 20t test machine (see Fig. A.1-1). The measurement method and the achievement of properties such as Young's Modulus, 0.2% proof stress and ultimate stress for each specimen are according to the standard test method in BSI (2001).



**Figure A-1-1: Test device (SANS 20t test machine)**

The tensile strain of each specimen was measured by an extensometer which attached to the specimen with gauge length was 50mm (see Fig. A-1-2). Flat specimens were clamped by flat wedge-shaped jaws (see Fig. A-1-3a), and corner specimens were clamped by round jaws with short steel rods, which with greater stiffness than specimens, attached at both ends to make sure the good connection applied between specimen and clamps, as showed in Fig. A-1-3b.
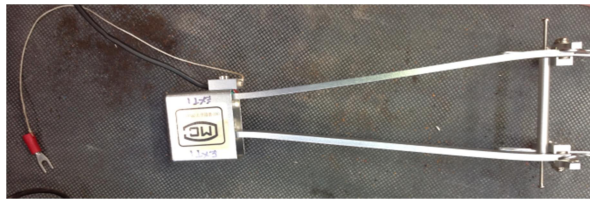


**Figure A-1-2: Extensometer**
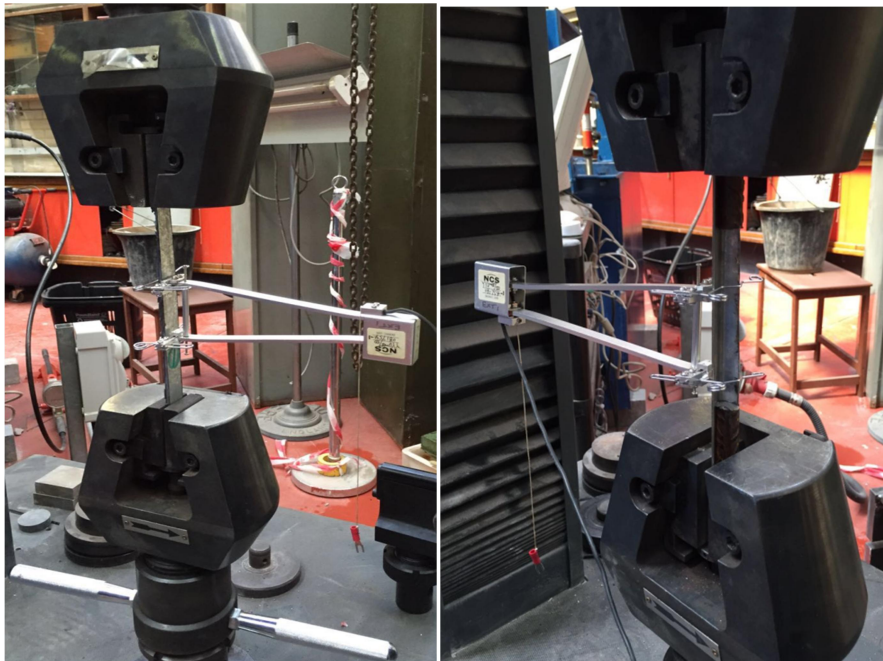


(a) Test setup for flat specimen      (b) Test setup for corner specimen

**Figure A-1-3: Test setup**

During the test, the load and strain history can be recorded automatically by the data acquisition system. Based on the measured dimensions of the samples, the engineering stress-strain relation of each specimen was achieved. It can be converted to true stress-strain relation by using the following equations:

$$\sigma_{true} = (1 + \varepsilon_e)\sigma_e \tag{1}$$

$$\varepsilon_{true} = \ln(1 + \varepsilon_e) \tag{2}$$

where $\sigma_e$ and $\varepsilon_e$ are engineering stress and strain.

The true stress-strain curves for each specimen are shown in Fig. A-1-4.

F-5

F-6

F-7

F-8

F-9

F-10
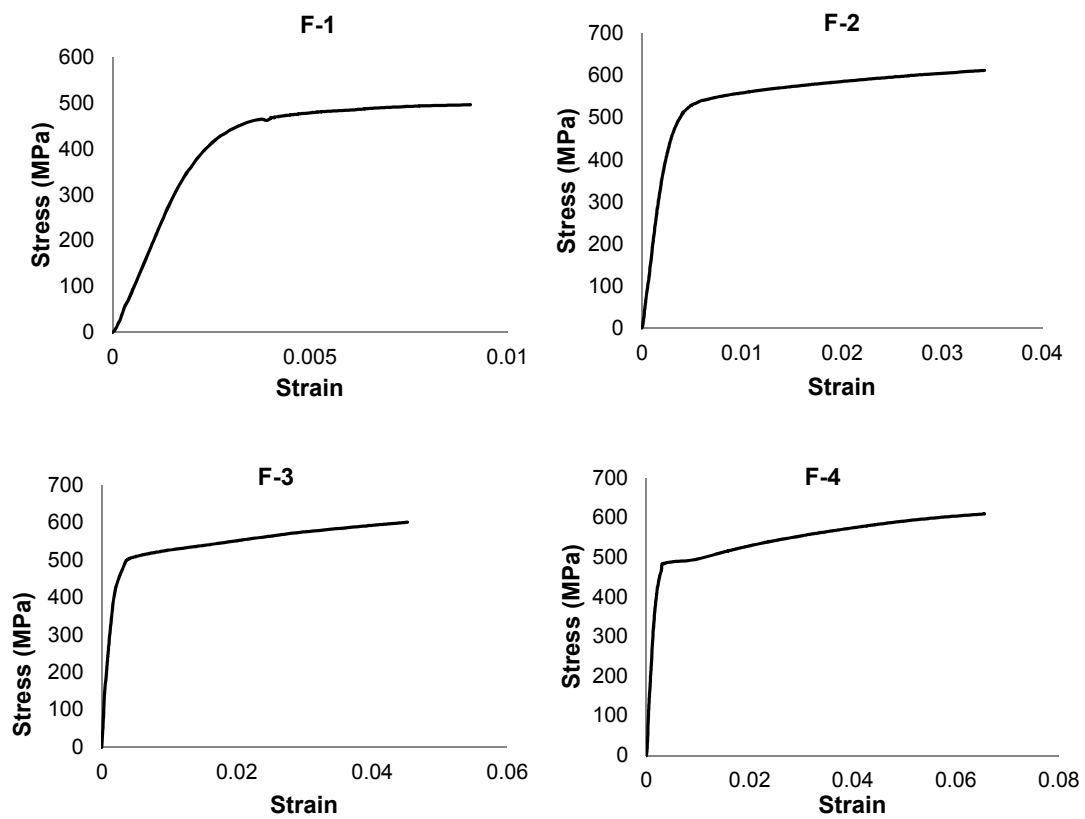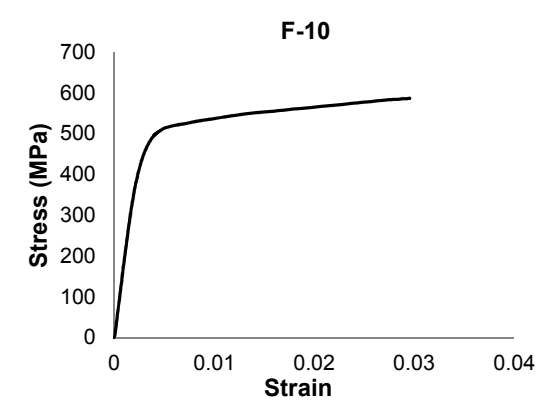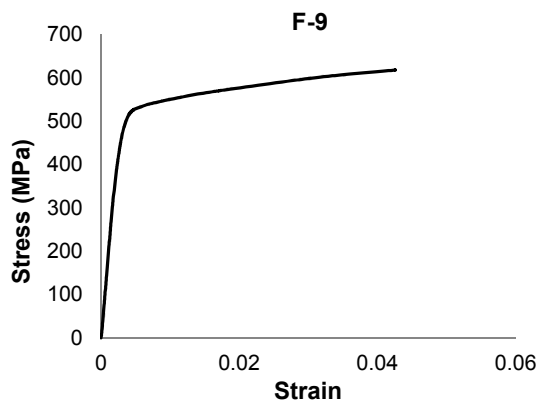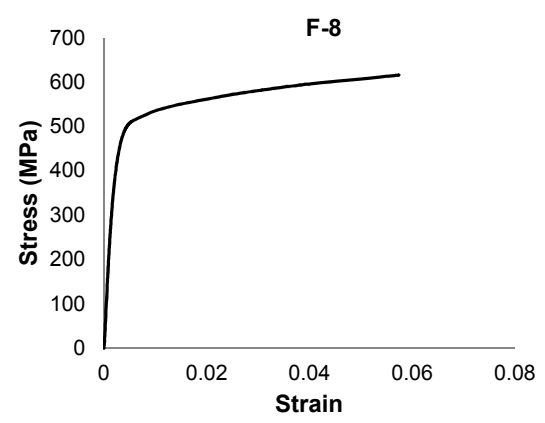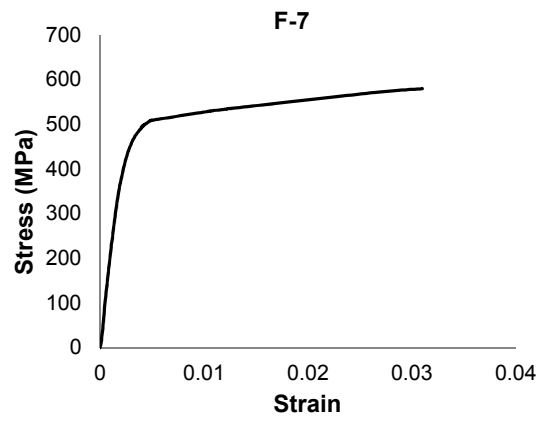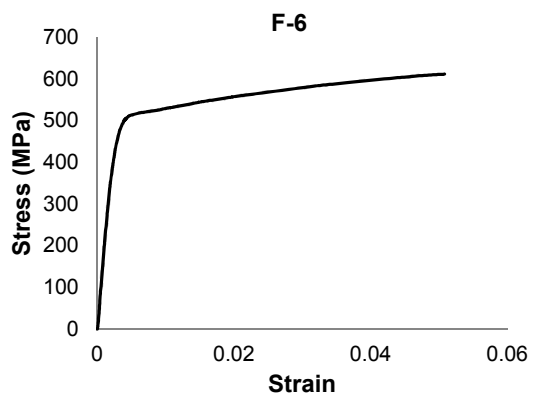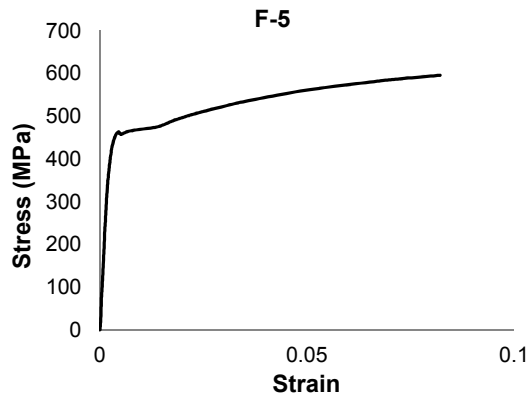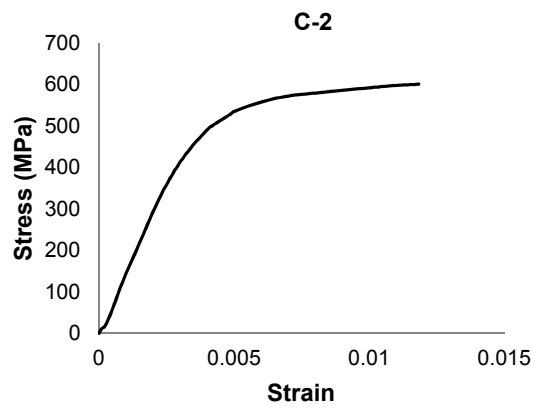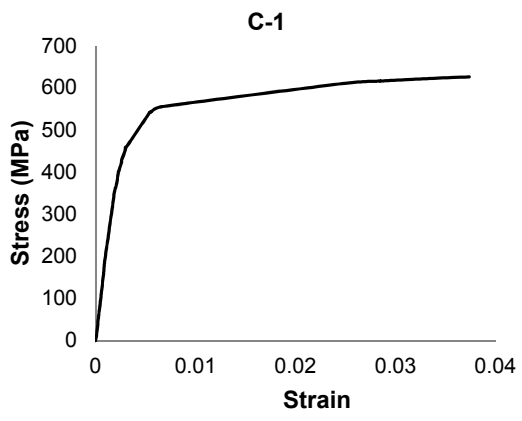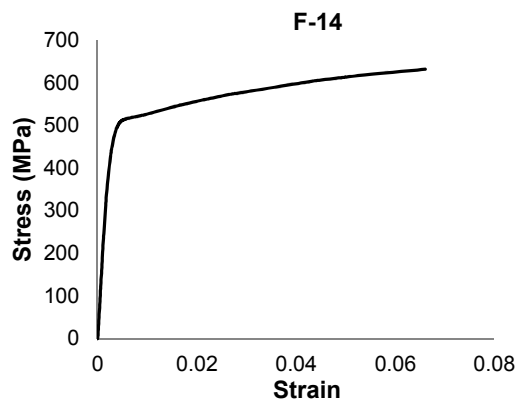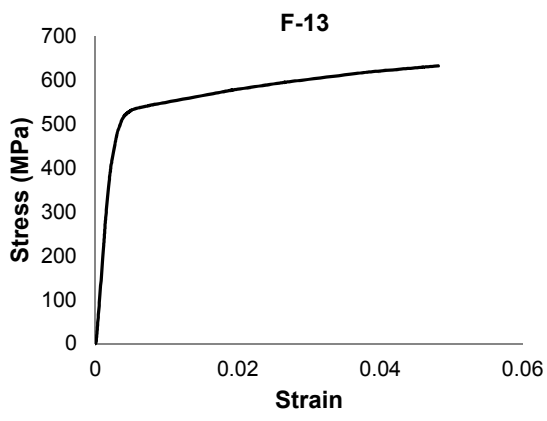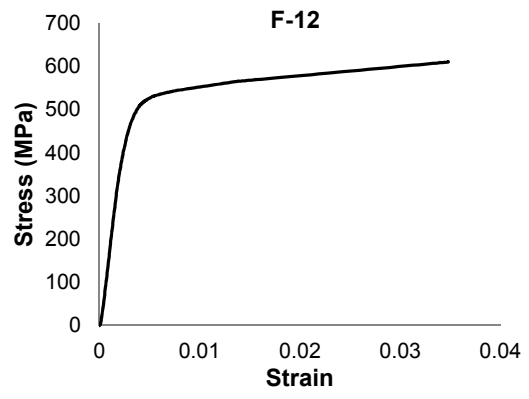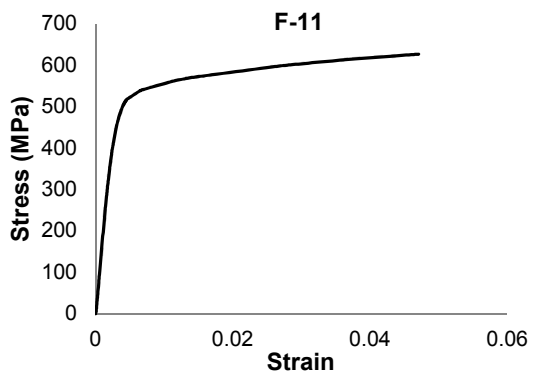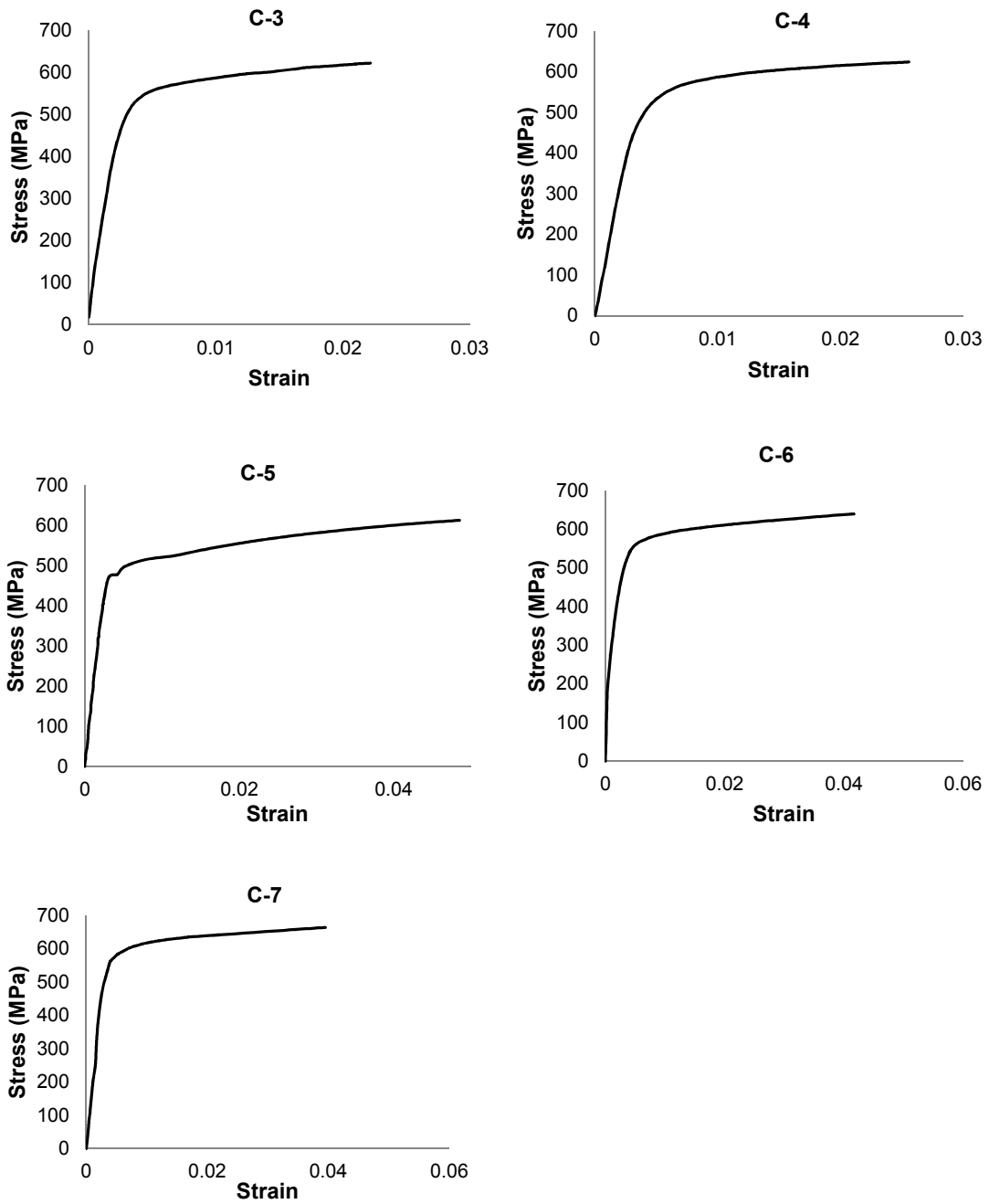
**Figure A-1-4: Tested true stress-strain curves for 450MPa specimens**

The measured strengths for flat and corner specimens at normal room temperature are summarized in Tables A-1-1 and A-1-2. The properties described in the table, except for the proportional limit, are defined in the conventional manner. The 0.2% offset

yield strength is used as proportional limit when referring to gradually yielding steels
and the lower yield point for sharply yielding steels.

**Table A-1-1: Summarize of test results – Flat specimens**

| Specimen No. | width (mm) | Length (mm) | Thickness (mm) | Elastic modulus E (Gpa) | 0.2%Proof strength $\sigma_{0.2}$ (Mpa) | ultimate strength $\sigma_u$ (Mpa) |
|---|---|---|---|---|---|---|
| Flat-1 | 19.0 | 235.0 | 1.2 | 195 | 460 | 520 |
| Flat-2 | 25.0 | 226.0 | 1.2 | 198 | 495 | 612 |
| Flat-3 | 18.0 | 218.0 | 1.2 | 203 | 470 | 601 |
| Flat-4 | 23.0 | 249.1 | 1.2 | 245 | 480 | 610 |
| Flat-5 | 22.8 | 240.1 | 1.2 | 200 | 455 | 596 |
| Flat-6 | 23.9 | 255.8 | 1.2 | 189 | 490 | 611 |
| Flat-7 | 21.5 | 235.2 | 1.2 | 210 | 480 | 580 |
| Flat-8 | 18.5 | 231.5 | 1.2 | 218 | 480 | 615 |
| Flat-9 | 25.9 | 229.1 | 1.2 | 184 | 520 | 619 |
| Flat-10 | 19.0 | 236.5 | 1.2 | 184 | 485 | 587 |
| Flat-11 | 18.1 | 259.2 | 1.2 | 197 | 490 | 627 |
| Flat-12 | 16.5 | 254.5 | 1.2 | 205 | 490 | 611 |
| Flat-13 | 17.6 | 254.1 | 1.2 | 201 | 495 | 633 |
| Flat-14 | 19.5 | 236.1 | 1.2 | 196 | 480 | 632 |
| **Mean** | | | | **202** | **484** | **604** |

**Table A-1-2: Summarize of test results – Corner specimens**

| Specimen No. | width (mm) | Length (mm) | Thickness (mm) | Elastic modulus E (Gpa) | 0.2%Proof strength $\sigma_{0.2}$ (Mpa) | ultimate strength $\sigma_u$ (Mpa) |
|---|---|---|---|---|---|---|
| Corner-1 | 32.0 | 225.0 | 1.2 | 204 | 510 | 626 |
| Corner-2 | 41.5 | 253.0 | 1.2 | 188 | 530 | 602 |
| Corner-3 | 29.0 | 251.5 | 1.2 | 200 | 540 | 621 |
| Corner-4 | 29.5 | 265.5 | 1.2 | 186 | 530 | 625 |
| Corner-5 | 32.5 | 258.0 | 1.2 | 200 | 530 | 612 |
| Corner-6 | 30.0 | 265.5 | 1.2 | 201 | 530 | 639 |
| Corner-7 | 33.5 | 233.0 | 1.2 | 191 | 560 | 664 |
| **Mean** | | | | **196** | **533** | **627** |

## 2 Tensile test for steel coupons with nominal yield strength of 235MPa

Twelve specimens with nominal yield strength 235MPa were also tested with the same devices and methods. The picture of tested specimens is shown in Fig. A-2-1, and the summary of test results is listed in Table A-2-1.



**Figure A-2-1: Specimens after test**

**Table A.2-1: Summary of the test results**

| Specimen No. | Measured width × thickness (mm) | Elastic modulus E (GPa) | 0.2% Proof stress $\sigma_{0.2}$ (MPa) | Ultimate tensile stress $\sigma_u$ (MPa) | Associated section thickness t (mm) |
|---|---|---|---|---|---|
| 1 | 20.87 × 1.22 | 205 | 180 | 354 | 1.2 |
| 2 | 20.83 × 1.18 | 200 | 175 | 334 | |
| 3 | 20.93 × 1.45 | 205 | 180 | 347 | 1.4 |
| 4 | 20.86 × 1.43 | 208 | 190 | 353 | |
| 5 | 20.89 × 2.00 | 201 | 179 | 349 | 2.0 |
| 6 | 20.91 × 2.03 | 200 | 170 | 344 | |
| 7 | 20.92 × 2.44 | 210 | 191 | 336 | |
| 8 | 20.87 × 2.40 | 215 | 213 | 372 | 2.4 |
| 9 | 20.61 × 2.43 | 212 | 200 | 347 | |
| 10 | 20.57 × 2.77 | 204 | 184 | 302 | |
| 11 | 20.27 × 2.78 | 215 | 202 | 344 | 3.0 |
| 12 | 21.11 × 2.78 | 199 | 172 | 326 | |
| **Mean** | | **206** | **186** | **342** | |

The true stress-strain curves obtained for each coupon are presented in the Fig. A-2-2.
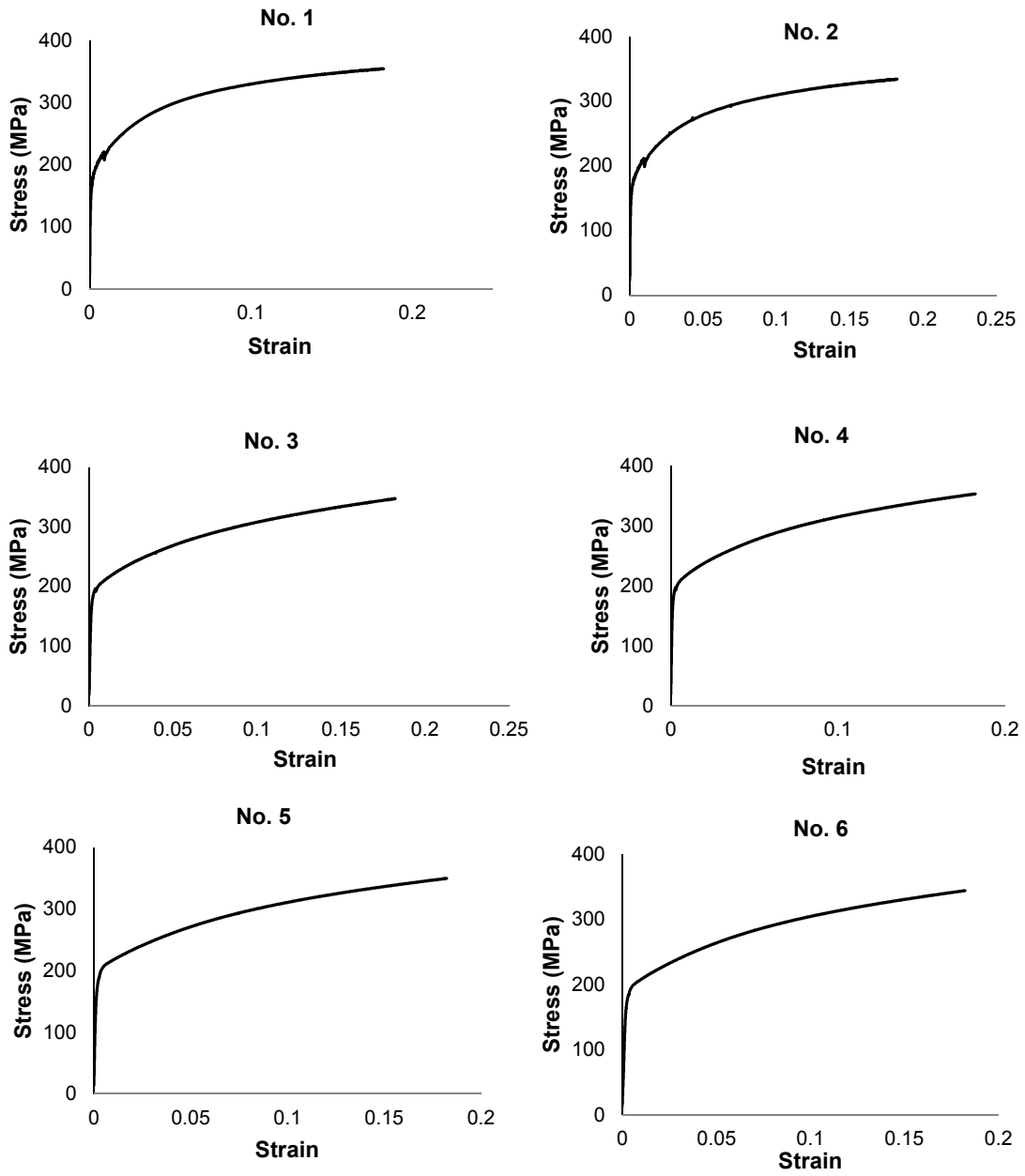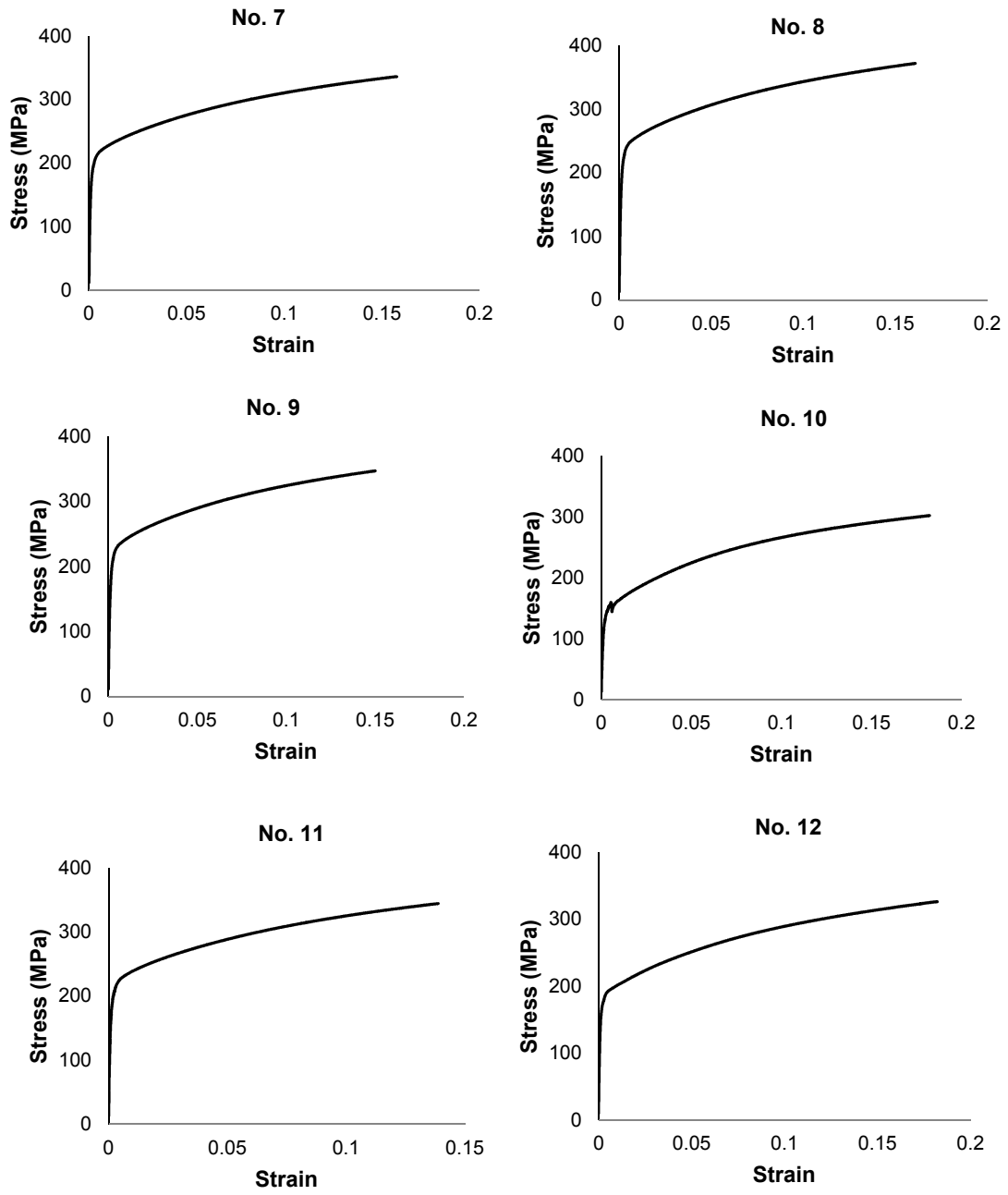
**Figure A-2-2: True stress-strain curves**

# References

**ABAQUS (2008)** Standard user's manual v6.10, Hibbitt, Karlsson and Sorensen Inc., United States.

**AISI (2007)** North American Specification for the Design of Cold formed Steel Structural Members. AISI S100-2007.

**Anis, A., Bjork, T. and Heinilla, S. (2012)** "Prediction of residual stresses in cold formed corners", *Journal of Advanced Science and Engineering Research*, 2, 252-264.

**ANSYS Commands Reference (2010)** "Elements Reference, Operations Guide, Basic Analysis Guide", Theory Reference for ANSYS.

**Argyris, J.H., Szimmat, J. and Willam, K.J. (1982)** "Computational aspects of welding stress analysis", *Computer Method in Applied Mechanics Engineering*, 33(1–3), 635–66.

**Ashraf, M., Gardner, L. and Nethercot, D.A. (2005)** "Strength enhancement of the corner regions of stainless steel cross-sections", *Journal of Construction Steel Research*, 61(1), 37–52.

**AS/NZS (2005).** Cold formed Steel Structures, AS/NZS 4600, Australian/New Zealand Standard, Standards Australia, Sydney.

**Barrans, S.M. and Muller, M. (2009)** "Finite element prediction of the ultimate axial load capacity of V-section band clamps", *The 7th International Conference on Modern Practice in Stress and Vibration Analysis*, Cambridge, UK.

**Bauschinger, J. (1881)** "Ueber die Veranderung der Elasticitatagrenze und dea Elasticitatamoduls verschiadener Metalle", Zivilingenieur, 27, 289–348.

**Beedle, L.S., and Tall, L. (1960)** "Basic Column Strength", *Journal of the Structural division*, ASCE, Vol. 86.

**Bhattacharyya, D., Smith, P.D., Yee, C.H. and Collins, I.F. (1984)** "The Prediction of deformation length in cold roll-forming", *Journal of Mechanical Working Technology*, 9, 181-191.

**Biempica, C.B., Diaz, J.J. del Coz, Nieto, P.J. Garcia and Sanchez I. P. (2009)** "Nonlinear analysis of residual stresses in a rail manufacturing process by FEM", *Journal of Applied Mathematical Modelling*, 33, 34-53.

**Bragg, W.L. (1912)** "The diffraction of short electromagnetic waves by a crystal", *Proceedings of the Cambridge Philosophical Society*, 17, 43.

**Brunet, M., Lay, B. and Pol, P. (1996)** "Computer aided design of roll-forming of channel sections", *Journal of Materials Processing Technology*, 60, 209-214.

**Brunet, M., Mguil, S. and Pol, P. (1998)** "Modelling of a roll-forming process with a combined 2D and 3D FEM code", *Journal of Materials Processing Technology*, 80-81, 213-219.

**BSI (2001).** Metallic materials-Tensile testing-Part 1: Method of test at ambient temperature, BS EN 10002-1:2001.

**BSI (2006).** Design of Steel Structures-Cold Formed Structures. BS EN 1993-1-3:2006.

**Bui, Q.V., Papelux, L. and Ponthot, J.P. (2004)** "Numerical simulation of springback using enhanced assumed strain elements", *Journal of Materials Processing Technology*, 153, 314-318.

**Bui, Q.V. and Ponthot, J.P. (2008)** "Numerical simulation of cold roll-forming processes", *Journal of Materials Processing Technology*, 275-282.

**Chakrabarty, J., Lee, W.B. and Chan, K.C. (2001)** "An exact solution for the elastic plastic bending of anisotropic", *International Journal of Mechanical Sciences*, 43, 1871-1880.

**Chakrabarty, J. (2006)** "Theory of plasticity (3rd edition)", Published by Elsevier Butterworth-Heinemann, Oxford, UK.

**Chajes, A., Britvec, S.J. and Winter, G. (1963)** "Effects of Cold-Straining on Structural Sheet Steels", *Journal of the Structural Division*, ASCE, 89, 1-32.

**Cheng, S.S., Kim, B. and Li, L.Y. (2013)** "Lateral– torsional buckling of cold formed channel sections subject to combined compression and bending*", Journal of Constructional Steel Research*, 80, 174-180.

**Chinnaraj, K., Sathya P.M. and Lakshmana R.C. (2014)** "Investigation of manufacturing residual stresses in cold formed truck frame rail sections", *International Journal of Engineering Research and Applicantings*, 4, 162-169.

**COPRA Software Manual (2012).** data M Sheet Metal Solutions.

**Cruise, R.B. and Gardner, L. (2008a)** "Residual stress analysis of structural stainless steel sections", *Journal of Constructional Steel Research*, 64, 352-366.

**Cruise, R.B. and Gardner, L. (2008b)** "Strength enhancements induced during cold forming of stainless steel sections", *Journal of Constructional Steel Research*, 64, 1310–1316.

**Davies, J.M. and Brown, B.A. (1996)** "Plastic Design to BS 5950", The Steel Construction Institute.

**Davis, J.M. and Raven, G.K. (1986)** "Design of cold formed steel purlins", *IABSE Thin-Walled Metal Structures in Buildings Colloquium*, Stockholm, 151-160.

**Davis, J.R. (1996)** ASM Specialty handbook–Carbon and alloy steels, Metals Park, OH: ASM International.

**Dattoma, V., De Giorgi, M. and Panella, F.W. (2002)** "Experimental and numerical evaluation of residual stresses and effect on fatigue life for longtudinal joints", *In: Proceedings of the First International Conference New Trends in Fatigue and Fracture*, Metz, France.

**Dattoma, V., De Giorgi, M.D. and Nobile, R. (2006)** "On the evolution of welding residual stress after milling and cutting machining", *Computers and Structures,* 84, 1965-1976.

**Deng, D. and Murakawa, H. (2006)** "Numerical simulation of temperature field and residual stress in multi-pass welds in stainless steel pipe and comparison with experimental measurements", *Computational Materials Science*, 37, 269–277.

**Deng, D., Murakawa, H. and Liang, W. (2008)** "Numerical and experimental investigations on welding residual stress in multi-pass butt-welded austenitic stainless steel pipe", *Computational Materials Science,* 42, 234–244.

**Deng, D. (2009)** "FEM prediction of welding residual stress and distortion in carbon steel considering phase transformation effects", *Materials and Design*, 30, 359–366.

**Dieter, G.E. (1988)** "Mechanical metallurgy", SI metric edition, McGraw-Hill, ISBN 0-07-100406-8.

**Dubina, D and Ungureanu, V. (2002)** "Effect of imperfections on numerical simulation of instability behaviour of cold formed steel members", *Thin-Walled Structures*, 40, 239–262.

**Edwards, L. and Endean, M. (1990)** "Manufacturing with materials", Butterworth Heinemann, ISBN 0-7506-2754-9.

**El-Khabeery, M.M. and Fattouh, M. (1989)** "Residual stress distribution caused by milling", *International Journal of Machine Tools and Manufacture*, 29(3), 391–401.

**Eom, J.G., Son, Y.H., Jeong, S.W., Ahn, S.T., Jang, S.M., Yoon, D.J. and Joun, M.S. (2014)** "Effect of strain hardening capability on plastic deformation behaviours of material during metal forming", *Materials and Design*, 54, 1010–101.

**Ferro, P., Bonollo, F. and Tiziani, A.** (2005) "Science and Technology of Welding and Joining", 10(3), 299.

**Gao, T. and Moen, C.D. (2010)** "The cold work of forming effect in steel structural members", *Stability and Ductility of Steel Structures*, Rio, Brazil.

**Gardner, L. and Nethercot, D. (2004)** "Experiments on stainless steel hollow sections- part 1: material and cross-sectional behaviour", *Journal of Constructional Steel Research*, 60(9), 1291–318.

**Gardner, L. and Cruise, R.B. (2009)** "Modelling of residual stresses in structural stainless steel sections", *Journal of Structural Engineering*, 135, 42-53.

**Gazzara, C.P. (1983)** "The measurement of residual stress with X-ray diffraction", *Army Materials and Mechanics Research Center*, Watertown, Massachusetts.

**Goladk, J., Chakravariti, A. and Bibby, M**. (1984) "A new finite element model for welding heat sources", *Metall Trans, B*15, 299–305.

**Gu, C.F., Toth, L.S. and Beausir,B. (2012)** "Modeling of large strain hardening during grain refinement", *Journal of Scripta Materialia*, 66, 250–3.

**Han, Z.W., Liu, C., Lu, W.P. and Ren, L.Q. (2002)** "Simulation of a multi-stand roll-forming process for thick channel section", *Journal of Materials Processing Technology*, 127, 382-387.

**Han, Z.W., Liu, C., Lu, W.P., Ren, L.Q. and Tong, J. (2005)** "Spline finite strip analysis of forming parameters in roll forming a channel section", *Journal of Materials Processing Technology*, 159, 383-388.

**Hattel, J.H., Nielsen, K.L. and Tutum, C.C. (2011)** "The effect of post-welding conditions in friction stir welds: from weld simulation to ductile failure", *European Journal of Mechanics—A/Solids*, 33, 67–74.

**Heinze, C., Schwenk, C. and Rethmeier, M. (2012)** "Numerical calculation of residual stress development of multi-pass gas metal arc welding under high restraint conditions", *Materials and Design*, 35, 201–209.

**Harvey, P.D. (1982)**. Engineering Properties of Steels. Metals Park, OH: American Society for Metals.

**Heinze, C., Schwenk, C. and Rethmeier, M. (2012)** "Numerical calculation of residual stress development of multi-pass gas metal arc welding", *Journal of Constructional Steel Research,* 72, 12–19.

**Heislitz, F., Livatyali, H., Ahmetoglua, M.A., Kinzel, G. L. and Altan, T. (1996)** "Simulation of roll forming process with the 3-D FEM code PAM-STAMP", *Journal of Materials Processing Technology*, 59, 59-67.

**Hertele, S., Waele, W.D., Denys, R. and Verstraete, M. (2012)** "Full-range stress–strain behaviour of contemporary pipeline steels: Part I. Model description", *International Journal of Pressure Vessels Piping*, 92, 34–40.

**Hill, H.N. (1944).** Determination of stress–strain relations from the offset yield strength values. Technical note no. 927. Washington (DC): National Advisory Committee for Aeronautics.

**Hill, R. (1950)** "The mathematical theory of plasticity", Oxford University Press, London.

**Hong, S., Lee, S. and Kim, N. (2001)** "A parametric study on forming length in roll forming", *Journal of Materials Processing Technology*, 113, 774–778.

**Ho, H. and Chung, K. (2004)** "Experimental investigation into the structural behaviour of lapped connections between cold formed steel Z sections", *Thin-Walled Structures*, 42, 1013-1033.

**Holloman, J.H. (1945)**. Tensile Deformation, *Transactions*, AIME, 162, 268-290.

**Hsu, Q.C. and Tran, C.T. (2011)** "Cold roll forming process design based on the induction of analytical knowledge by considering material and geometry effects", *Journal of Materials Science and Engineering*, A1, 210–218.

**Huber, A.W., and Beedle, L.S. (1954)** "Residual Stress and the Compressive Strength of Steel", *Welding Journal*, 33.

**Huber, A.W. (1956)** "The influence of residual stress on the instability of columns", Fritz Laboratory reports of Lehigh University, 1496.

**Huber, A.W. and Ketter, R.L. (1958)** "The influence of residual stress on the carrying capacity of eccentrically loaded columns", Fritz Laboratory reports of Lehigh University, 1503.

**Ingvarsson, L. (1975)** "Cold forming Residual Stress, Effect of Buckling", *3rd International Specialty Conference on Cold formed Steel Structures*, University of Missouri-Rolla, 85-119.

**Jacobus, K., De Vor R.E. and Kapoor, S.G. (2000)** "Machining-induced residual stress: Experimentation and modelling", *Journal of Manufacturing Science and Engineering*, 122, 20–31.

**Jameel, A.N., Nabeel, K. and Osama, F. (2010)** "Residual stress distribution for a single pass weld in pipe", *Journal of Engineering, Volume 16*.

**Jandera, M., Gardner, L. and Machacek, J. (2008)** "Residual stresses in cold-rolled stainless steel hollow sections", *Journal of Constructional Steel Research*, 64(11), 1255-1263.

**Jandera, M. and Machacek, J. (2014)** "Residual stress influence on material properties and column behaviour of stainless steel SHS", *Thin-Walled Structures*, 83, 12-18.

**Johnson, W. and Yu, T.X. (1981)** "Springback after the biaxial elastic-plastic pure bending of a rectangular plate-I", *International Journal of Mechanical Sciences*, 23 (10), 619-630.

**Joun, M.S., Eom, J.G. and Lee, M.C. (2008)** "A new method for acquiring true stress–strain curves over a large range of strains using a tensile test and finite element method", *Mechanics and Materials*, 40, 586–93.

**Karman, V. (1932)** "The Strength of Thin Plates in Compression", *Transactions, ASME*, 54-5.

**Ketter, R.L. (1958)** "The influence of residual stress on the strength of structural members", Fritz Laboratory reports of Lehigh University, 1500.

**Karren, K.W. (1967)** "Corner properties of cold formed steel shapes", *Journal of the Structural Division*, ASCE, 93, 401–32.

**Karren, K.W. and Winter, G. (1967)** "Effects of Cold forming on Light-Gage Steel Members", *Journal of the Structural Division*, ASCE, 93, 433-469.

**Kleiner, M., Krux, R. and Homberg, W. (2004)** "Analysis of Residual Stresses in High-Pressure Sheet Metal Forming", *CIRP Annals-Manufacturing Technology*, 53 (1), 211-214.

**Kim, W., Kawai, K., Koyama, H. and Miyazaki, D. (2007)** "Fatigue strength and residual stress of groove-rolled products", *Journal of Materials Processing Technology*, 194, 46-51.

**Kiuchi, M. (1989)** "CAD System for Cold Roll-Forming", *Manufacturing Technology*, 38(1), 283–286.

**Konter, A. (2005)** "Advanced finite element contact benchmarks", Glasgow: NAFEMS, 19.

**Kong, F., Ma, J. and Kovacevic, R. (2011)** "Numerical and experimental study of thermally induced residual stress in the hybrid laser–GMA welding process", *Journal of Materials Processing Technology*, 211, 1102-1111.

**Kumar, B.R., Singh, A.K., Das, S. and Bhattacharya, D.K. (2004)** "Cold rolling texture in AISI 304 stainless steel", *Materials Science and Engineering*, A364 (1-2), 132-139.

**Lee, G.C. and Ketter, R.L. (1958)** "The influence of residual stress on the strength of members of high strength steel", Fritz Laboratory reports of Lehigh University, 1725.

**Lee, C.K., Chiew, S.P. and Jiang, J. (2012)** "Residual stress study of welded high strength steel thin-walled plate-to-plate joints part 2: Numerical modelling", *Thin-Walled Structures*, 59, 120–131.

**Leggatt, R.H. (2008)** "Residual stresses in welded structures", *International Journal of Pressure Vessels and Piping,* 85, 144–151.

**Lindgren, M. (2007)** "An improved model for the longitudinal peak strain in the flange of a roll formed u-channel developed by FE-analysis", S*teel Research International*, 78(1), 82-87.

**Lindgren, M. (2007)** "Cold roll forming of a U-channel made of high strength steel", *Journal of Materials Processing Technology*, 186, 77-81.

**Liu, C., Zhang, J.X. and Xue, C.B. (2011)** "Numerical investigation on residual stress distribution and evolution during multi-pass narrow gap welding of thick-walled stainless steel pipes", *Fusion Engineering and Design*, 86, 288–295.

**Liu, C., Zhou, Y., and Lu, W. (1996)** "Numerical simulation of roll-forming by B-spline finite strip method", *Journal of Materials Processing Technology*, 60, 215-218.

**Liu, Q., Yang, J. and Li, L.Y. (2011a)** "Pseudo-plastic moment resistance of continuous beams with cold formed sigma sections at internal supports: experimental study", *Engineering Structures*, 33, 947-957.

**Liu, Q., Yang, J., Chan, H.C. and Li, L.Y. (2011b)** "Psuedo-plastic moment resistance of continuous beams with cold formed sigma sections at internal supports: A numerical study", *Thin-Walled structures*, 49(3), 1592-1604.

**Li, S.H., Zeng, G., Ma, Y.F., Guo, Y.J. and Lai, X.M. (2009)** "Residual stresses in roll-formed square hollow sections", *Thin-Walled Structures*, 47, 505–513.

**Li, Z. and Schafer, B.W. (2010)** "Buckling analysis of cold formed steel members with general boundary conditions using CUFSM: conventional and constrained finite strip methods", *20th International Specialty Conference on Cold formed Steel Structures*, Saint Louis, Missouri, USA.

**Luo, J., Li, M., Xu, W. and Li, H. (2010)** "The variation of strain rate sensitivity exponent and strain hardening exponent in isothermal compression of Ti–6Al–4V alloy", Journal of *Materials & Design*, 31, 741–8.

**Macdonald, M., Rhodes, J., Crawford, M. and Taylor, G.T. (1996)** "A study of the effect of cold forming on the yield strength of stainless steel type 304-hardness test approach", *Thirteenth International Specialty Conference on Cold formed Steel Structures*, St. Louis, Missouri U.S.A.

**Mackerle J. (1996)** "Finite element analysis and simulation of welding: A bibliography (1976–1996)", *Modelling and Simulation in Materials Science and Engineering*, 4, 501–33.

**Mackerle J. (2002)** "Finite element analysis and simulation of welding- An addendum: A bibliography (1996–2001)", *Modelling and Simulation in Materials Science and Engineering*, 10(3), 295–318.

**Majlessi, S.A. and Dadras, P. (1983)** "Pure plastic bending of sheet laminates under plane strain condition", *International Journal of Mechanical Sciences*, 25, 1-14.

**Magnucka, B.E. and Magnucki, K. (2010)** "Buckling and optimal design of cold formed thin-walled beams: Review of selected problems", *Thin-Walled structures*, 49(3), 554-561.

**Magnucki, K., Paczos, P. and Kasprzak, J. (2010)** "Elastic Buckling of Cold formed Thin-Walled Channel Beams with Drop Flanges", *Journal of Structural Engineering*, 136(7), 886-896.

**Masubuchi, K. (1983)** Residual stresses and distortion. Metals handbook. *Welding brazing and soldering*, 6, 856–95.

**Mathar, J. (1934)** "Determination of initial stresses by measuring the deformation around drilled holes", *Transactions, ASME*, 56(4), 249-254.

**Milad, M., Zreiba, N., Elhalouani, F. and Baradai, C. (2008)** "The effect of cold work on structure and properties of AISI 304 stainless steel", *Journal of Materials Processing Technology*, 203, 80-85.

**Mirambell, E. and Real, E. (2000)** "On the calculation of deflections in structural stainless steel beams: an experimental and numerical investigation", *Journal of Constructional Steel Research*, 54(1), 109–33.

**Moen, C.D., Igusa, T. and Schafer, B.W. (2008)** "Prediction of residual stresses and strains in cold formed steel members", *Thin-walled Structures*, 46, 1274-1289.

**Muller, M. and Barrans, S.M. (2009)** "Ultimate axial load capacity of V-band clamp joints", *Proceedings of Computing and Engineering Annual Researchers' Conference*, Huddersfield, UK, 14-18.

**Muller, M. and Barrans, S.M. (2010)** "Impact of flange geometry on the ultimate axial load capacity of V-band clamps", *9th International Conference on Turbochargers and Turbocharging*, London, UK.

**Murakawa, H., Beres, M., Vega, A., Rashed, S., Davies, C.M., Dye, D. and Nikbin, K.M. (2008)** "Effect of phase transformation onset temperature on residual stress in welded thin steel plates", *Transactions of JWRI*, 37, No. 2.

**Nadimi, S., Khoushehmehr, R.J., Rohani, B. and Mostafapour, A. (2008)** "Investigation and analysis of weld induced residual stresses in two dissimilar pipes by finite element modelling", *Journal of Applied Science*, 8 (6), 1014–1020.

**Nandini, P. and Kalyanaraman, V. (2010)** "Strength of cold formed lipped channel beams under interaction of loacl, distortional and lateral torsional buckling", *Thin-Walled Structures*, 49(2), 872-877.

**Nitta, A. and Thurlimann, B. (1960)** "Effect of cold bending on column strength", Fritz Laboratory reports of Lehigh University, page 1744.

**Papeleux, L. and Ponthot, J.P. (2002)** "Finite element simulation of springback in sheet metal forming", *Journal of Materials Processing Technology*, 785-791.

**Panton, S.M., Duncan, J.L. and Zhu, S.D. (1996)** "Longitudinal and shear strain development in clod roll forming", *Journal of Materials Processing Technology*, 60, 219-224.

**Paralikas, J., Salonitis, K. and Chryssolouris, G. (2009)** "Investigation of the effects of main roll forming process parameters on quality for a V-section profile from AHSS", *International Journal of Advanced Manufacturing Technology*, 44, 223-237.

**Paralikas, J., Salonitis, K. and Chryssolouris, G. (2010)** "Optimization of roll forming process parameters a semi-empirical approach", *International Journal of Advanced Manufacturing Technology*, 47, 1041-1052.

**Pastor, M.M., Bonada, J., Roure, F. and Casafont, M. (2013)** "Residual stresses and initial imperfections in non-linear analysis", *Engineering Structures*, 46, 493-507.

**Paulo, R.M.F., Carlone,P., Valente, R.A.F., Teixeira-Dias, F. and Palazzo, G.S. (2014)** "Influence of friction stir welding residual stresses on the compressive strength of aluminium alloy plates", *Thin-Walled Structures*, 74: 184–190.

**Peric, M., Tonkovic, Z., Rodic, A., Surjak, M., Garasic, I. and Boras, I. (2014)** "Numerical analysis and experimental investigation of welding residual stresses and distortions in a T-joint fillet weld", *Materials and designs*, 53, 1052-1063.

**Pham, C.H. and Hancock, G.J. (2009)** "Direct strength design of cold formed Purlins", *Journal of Structural Engineering*, 135 (3), 229-238.

**Quach, W.M., Teng, J.G. and Chung, K.F. (2004)** "Residual stresses in steel sheets due to coiling and uncoiling: a closed-form analytical solution", *Journal of Engineering Structures*, 26, 1249-1259.

**Quach, W.M., Teng, J.G. and Chung, K.F. (2006)** "Finite element predictions of residual stresses in press braked thin-walled steel sections", *Journal of Engineering Structures*, 28, 1609-1619.

**Quach, W.M., Teng, J.G. and Chung, K.F. (2009)** "Residual stresses in press braked stainless steel sections, I: Coiling and uncoiling of sheets", *Journal of Constructional Steel Research*, 65, 1803-1815.

**Quach, W.M., Teng, J.G. and Chung, K.F. (2009)** "Residual stresses in press braked stainless steel sections, II: Press-braking operations", *Journal of Constructional Steel Research*, 65, 1816-1826.

**Quach, W.M., Teng, J.G. and Chung, K.F. (2010)** "Effect of the manufacturing process on the behaviour of press braked thin-walled steel columns", *Engineering Structures*, 32, 3501–3515.

**Rahman, A.N. and Sivakumaran, K.S. (1996)** "Evaluation and modelling of the material properties for analysis of cold formed steel sections", *Thirteenth International Specialty Conference on Cold formed Steel Structures*, St. Louis, Missouri, U.S.A.

**Ramberg, W. and Osgood, W.R. (1943)** "Description of stress–strain curves by three parameters", Technical note No. 902, Washington (DC): National Advisory Committee for Aeronautics.

**Rasmussen, K.J.R. (2003)** "Full-range stress–strain curves for stainless steel alloys", *Journal of Constructional Steel Research*, 59(1), 47–61.

**Real, P.M.M.V., Cazeli, R. , Simoes, L. da Silva, Santiago, A. and Piloto, P. (2004)** "The effect of residual stresses in the lateral torsional buckling of steel I-beams at elevated temperature", *Journal of Constructional Steel Research*, 60, 783–793.

**Rogers, C.A. and Schuster, R.M. (1997).** "Flange/Web distortional buckling of cold formed steel sections in bending", *Thin-walled structures*, 27, 13-29.

**Rondal, J. (1987)** "Residual stresses in cold-rolled profiles", *Construction and Building Materials*, 1(3), 150-164.

**Roure, F. (2009)** "Simulation of the roll-forming process for the determination of the relevant residual stresses of cold formed steel members", *1st International Congress on Roll Forming. Bilbao: LABEIN*, 41-48.

**Rossi, B., Degee, H. and Pascon, F. (2009)** "Enhanced mechanical properties after cold process of fabrication of non-linear metallic profiles", *Thin-Walled Structures*, 47, 1575–1589.

**Rossi, B., Degee, H. and Boman, R. (2013)** "Numerical simulation of the roll forming of thin-walled sections and evaluation of corner strength enhancement", *Finite Elements in Analysis and Design*, 72: 13–20.

**Rossini, N.S., Dassisti, M., Benyounis, K.Y. and Olabi, A.G. (2012)** "Methods of measuring residual stresses in components", *Materials and Design*, 35, 572-588.

**Ruud, C.O. (1982)** "A review of selected non-destructive methods for residual stress measurement", *NDT International*, 15(1), 15-23.

**Schafer, B.W. and Peköz, T. (1998a).** "Direct strength prediction of cold formed steel members using numerical elastic buckling solutions", *Fourteenth international specialty conference on cold formed steel structures*, October 15-16, St. Louis, Missouri.

**Schafer, B.W. and Peköz, T. (1998b)** "Computational modelling of cold formed steel characterising geometric imperfections and residual stresses", *Journal of Constructional Steel Research*, 47(3), 193–210.

**Schafer, B.W. and Ádány, S. (2006)** "Buckling analysis of cold formed steel members using CUFSM: conventional and constrained finite strip methods", *18th International Specialty Conference on Cold formed Steel Structures*, Orlando, Florida.

**Schafer, B.W. (2008)** "The Direct Strength Method of cold formed steel member design", *Journal of Constructional Steel Research*, 64, 766-778.

**Senanayake, R. S., Cole, I. M. and Thiruvarudchelvan, S. (1994)** "The application of computational and experimental techniques to metal deformation in cold roll forming", *Journal of Material Processing Technology*, 45, 155-160.

**Shoghi, K., Barrans, S.M. and Rao, H.V. (2004)** "Stress in V-section band clamps", *Journal of Mechanical Engineering Science*, 218, 251-261.

**Sivakumaran, K.S. and Abdel-Rahman, N. (1998)** "A finite element analysis model for the behaviour of cold formed steel members", *Thin-Walled Structures*, 31, 305-324.

**Silvestre, N. and Camotim, D. (2006)** "Direct Strength Method for lipped channel columns and beams affected by local-plate/distortional interaction", *The Eighteenth International Specialty Conference on Cold Formed Steel Structures*, 17–37.

**Spoorenberg, R.C., Snijder, H.H., Hoenderkamp, J.C.D. and Bakker, M.C.M. (2009)** "Residual stresses in cold bent HE 100A steel arches", *Swedish Institute of Steel Constructi*on, 414-421.

**Spoorenberg, R.C., Snijder, H.H. and Hoenderkamp, J.C.D. (2010)** "Experimental investigation of residual stresses in roller bent wide flange steel sections", *Journal of Constructional Steel Research*, 66, 737-747.

**Spoorenberg, R.C., Snijder, H.H. and Hoenderkamp, J.C.D. (2011)** "Finite element simulation of residual stresses in roller bent wide flange sections", *Journal of Constructional Steel Research*, 67, 39-50.

**Taljat, B., Radhakrishnan B. and Zacharia, T. (1998)** "Numerical analysis of GTA welding process with emphasis on post-solidification phase transformation effects on residual stresses", *Materials Science and Engineering*, 246, 45 – 54.

**Tan, Z., Li, W.B. and Persson, B. (1994)** "On analysis and measurement of residual stresses in the bending of sheet metals", *International Journal of Mechanical Sciences*, 36 (5), 483-491.

**Tebedge, N., Alpsten, G.A. and Tall, L. (1973)** "Residual Stress Measurement by the Sectioning Method", *Journal of Experimental Mechanics,* 13(2), 88-96.

**Tehrani, M.S., Hartley, P., Naeini, H.M. and Khademizadeh, H. (2006)** "Localised edge buckling in cold roll-forming of symmetric channel section", *Thin-walled structures*, 44, 184-196.

**Teng, T.L., Chang, P.H. and Tseng, W.C. (2003)** "Effect of welding sequences on residual stresses", *Computers and Structures*, 81, 273–286.

**Telue, Y. and Mahendran, M. (2004)** "Numerical modelling and design of unlined cold formed steel wall frames", *Journal of Constructional Steel Research*, 60, 1241-1256.

**Thomopoulos, K.T., Mistakidis, E.S., Koltsakis, E.K. and Panagiotopoulos, P.D. (1995)** "Softening behaviour of continuous thin walled steel beams, two numerical methods", *Journal of Constructional Steel Research*; 36(1), 1-13.

**Timoshenko, S. (1956)** "Strength of Materials: Part II", 3rd Edition, New York: Van Nostrand Reinhold Company.

**Tong, L., Hou, G., Chen, Y., Zhou, F., Shen, K. and Yang, A. (2012)** "Experimental investigation on longitudinal residual stresses for cold formed thick-walled square hollow sections", *Journal of Constructional Steel Research*, 73, 105-116.

**Uribe, J. and Winter, G. (1969)** "Cold forming Effects in Thin-Walled Steel Members", Dept. of Structural Engineering, Cornell University.

**Van den Berg, G.J. and Van der Merwe, P. (1992)** "Prediction of corner mechanical properties for stainless steels due to cold forming", *The Eleventh International Specialty Conference on Cold Formed Steel Structures*, 571–86.

**Verguts, H. and Sowerby, R. (1975)** "The pure plastic bending of laminated sheet metal metals", *International Journal of Mechanical Sciences*, 17, 31.

**Vladimirov, I.N., Pietryga, M.P. and Reese, S. (2009)** "Prediction of springback in sheet forming by a new finite strain model with nonlinear kinematic and isotropic hardening", *Journal of Material Processing Technology*, 209, 4062-4075.

**Weng, C.C. and Peköz, T. (1990)** "Residual stresses in cold formed steel members", *Journal of Structural Division*, ASCE, 116(6), 1611-1625.

**Weng, C.C. and White, R.N. (1990)** "Residual Stresses in Cold-bent Thick Steel Plates", *Journal of Structural Engineering*, 116(1), 24-39.

**Weng, C.C. (1991)** "Effects of residual stress on cold formed steel column strength", *Journal of Structural Engineering*, 117, 1622-1640.

**White, D.W. (1993)** "Plastic-Hinge Methods for Advanced Analysis of Steel Frames", *Journal of Constructional Steel Research*, 24, 121-152.

**Wiebenga, J.H., Weiss, M., Rolfe, B. and van den Boogaard, A.H. (2013)** "Product defect compensation by robust optimization of a cold roll forming process", *Journal of Materials Processing Technology*, 213, 978–986.

**Yang, C.H., Beedle, L.S. and Johnston, B.G. (1952)** "Residual stress and the yield strength of steel beams", *Welding Journal*, 31(4), 205-229.

**Yang, J. and Liu, Q. (2012)** "Sleeve connections of cold formed steel sigma purlins", *Engineering Structures,* 43, 245-258.

**Ye, Z.M., Kettle, R.J., Li, L.Y. and Schafer, B.W. (2002)** "Buckling behaviour of cold formed zed-purlins partially restrained by steel sheeting", *Thin-walled structures*, 40, 853-864.

**Yu, W.W. (2003)** Cold formed steel design, 3rd edition, Missouri, US.

**Yaghi, A., Hyde, T.H., Becker, A.A., Sun, W. and Williams, J.A. (2006)** "Residual stress simulation in thin and thick-walled stainless steel pipe welds including pipe diameter effects", *International Journal of Pressure Vessels and Piping,* 83, 864–874.

**Zeng, G., Lai, X.M., Yu, Z.Q. and Lin, Z.Q. (2008a)** "Sensitivity analysis of parameters for multi-stand roll forming using a new booting model", *Journal of Shanghai University*, 13(6), 707–711.

**Zeng, J., Liu, Z., and Champliaud, H. (2008b)** "FEM dynamic simulation and analysis of the roll-bending process for forming a conical tube"*, Journal of Materials Processing Technology*, 198: 330-343.

**Zeng, G., Li, S.H., Yu, Z.Q. and Lai, X.M. (2009)** "Optimization design of roll profiles for cold roll forming based on response surface method", *Materials and Design*, 30(6), 1930–1938.

**Zeng, G., Lai, X.M., Yu, Z.Q. and Lin, Z.Q. (2009)** "Numerical simulation and sensitivity analysis of parameters for multi-stand roll forming of channel section with outer edge", *Journal of Iron and Steel Research*, 16 (1), 32–37.

**Zhang, L., Tan, N. and Liu, C. (2010)** "A New Model for Simulation of Cold Roll-Forming of Tubes by Using Spline Strip Method", *Journal of Shanghai Jiaotong University*, 15 (1), 70-75.

**Zhang, Z.T. and Hu, S.J. (1998)** "Stress and residual stress distributions in plane strain bending", *International Journal of Mechanical Sciences*, 40 (6), 533-543.

**Zhang, L. and Tong, G. (2008)** "Moment resistance and flexural rigidity of lapped connections in multi-span cold formed Z purlin systems", *Thin-Walled Structures*, 46, 551-560.

**Zhu, S.D., Panton, S.M. and Duncan, J. L. (1996)** "The effects of geometric variables in roll forming a channel section", *Proceedings of Institution of Mechanical Engineers*, 210, 127-134.

**Zhou, F., Chen, Y.Y. and Young, B. (2013)** "Cold formed high strength stainless steel cross-sections in compression considering interaction effects of constituent plate elements", *Journal of Constructional Steel Research*, 80, 32-41.